Analysis of seismic and aseismic deformation using shoreline-crossing observations

DISSERTATION

zur Erlangung des Doktorgrades an der
Mathematisch-Naturwissenschaftlichen Fakultät der
Christian-Albrechts-Universität zu Kiel

vorgelegt von

Florian Petersen

Kiel, 2021

Erste Gutachterin: Prof. Dr. Heidrun Kopp

Zweiter Gutachter: Prof. Dr. Ingo Grevemeyer

Tag der mündlichen Prüfung: 30.09.2021

Zum Druck genehmigt: 30.09.2021

Der Dekan

Erklärung

Hiermit erkläre ich, dass ich die vorliegende Doktorarbeit selbstständig und ohne Zuhilfenahme unerlaubter Hilfsmittel erstellt habe. Weder diese noch eine ähnliche Arbeit wurde an einer anderen Abteilung oder Hochschule im Rahmen eines Prüfungsverfahrens veröffentlicht oder zur Veröffentlichung vorgelegt. Ferner versichere ich, dass die Arbeit unter Einhaltung der Regeln guter wissenschaftlicher Praxis der Deutschen Forschungsgemeinschaft entstanden ist. Ich versichere, dass mir noch kein akademischer Titel entzogen wurde.

Ort, Datum Florian Petersen

Summary

Localized shear zones accommodate the deformation of the Earth's surface and are referred to as geological faults. Where the stress of tectonic plate movement or gravitational forces act on the internal strength of rocks or sediments and exceed certain shear stresses, rapid brittle deformation releases elastic energy, in the form of an earthquake. When physical properties, loading rate, or environmental conditions reduce the slip rate, no or long-period seismic energy is radiated and referred to as aseismic deformation. Varying fault slip behavior plays an essential role in the earthquake cycle and poses a significant risk to coastal populations, especially when occurring offshore due to potential cascading effects. The rigorous study of the seismic or aseismic behavior of faults involves the application of seafloor measurements and coastal observations to provide adequate assessments and mitigate future marine geohazards.

This thesis aims to analyze offshore seismic and aseismic deformation using different seismological and geodetic constraints from on- and offshore observations to better understand the spatial and temporal variations in fault slip behavior. The main methodology combines marine seismology and seafloor geodesy in a shoreline-crossing approach to estimate the spatio-temporal slip behavior along two major fault types. The behavior varies from seismic to radiation of elastic energy to aseismic (silent or slow slip), and is estimated to provide constraints on overarching tectonic or geological processes. To decipher slip variation along different fault types and to understand the underlying processes, three distinct settings are investigated: the offshore megathrust along the north Chilean subduction zone, the strike-slip North Anatolian Fault in the central Sea of Marmara and the southern limit of the unstable eastern flank of Europe's largest active volcano, Mount Etna.

The north Chilean subduction zone is characterized by the erosional underthrusting of the oceanic Nazca plate underneath the continental South American plate. The 2014 M_w 8.1 Iquique earthquake sheds light on the subduction processes of the shallow megathrust and the marine forearc. Analysis of an amphibious seismic network and multi-channel seismic data reveals a coupled process involving the seismic behavior at the seismogenic up-dip limit and shallow subduction erosion during the co- and postseismic phase.

Aseismic deformation of sub-seafloor faults is ubiquitous and requires the application of seafloor measurement techniques. Direct displacement monitoring using acoustic direct-path ranging is beneficial for in situ detection and discrimination of aseismic and seismic fault displacement. The analysis of seismic activity and deformation on the submerged strike-slip fault zone of the North Anatolian Fault using acoustic direct-path ranging with long-term monitoring revealed the locking state of the central Marmara segment and the implications of strain accumulation for the densely populated region.

Gravitational-driven fault displacement in the event of a submarine landslide poses a significant risk to inhabited coastal areas. The eastern flank of Mount Etna in Sicily has long been known for its instability, but offshore constraints were lacking. Analyses of the submerged eastern flank, which is limited by an onshore elongated strike-slip fault to the south, revealed aseismic slip behavior that includes slow slip and demonstrated the potential hazard of sudden flank movement in the Mediterranean Sea.

Zusammenfassung

Die Deformation der Erdoberfläche findet an örtlich begrenzten Scherzonen statt, welche als geologische Verwerfungen bezeichnet werden. Wirkt die Belastung durch tektonische Plattenbewegungen oder Gravitationskräfte auf die innere Festigkeit von Gesteinen oder Sedimenten ein und überschreitet diese bestimmte Scherspannungen, wird durch rasche spröde Verformung elastische Energie in Form von Erdbeben freigesetzt. Verringern physikalischen Eigenschaften, Belastungsrate und Umgebungsbedingungen die Gleitrate, wird keine oder eine langanhaltende seismische Energie abgestrahlt. Dies wird als aseismische Deformation bezeichnet. Das variable Gleitverhalten von Verwerfungen spielt eine wesentliche Rolle im Erdbebenzyklus und stellt eine erhebliche Gefahr für die Küstenbevölkerungen dar, insbesondere wenn es aufgrund möglicher Kaskadeneffekte vor der Küste auftritt. Die gründliche Untersuchung des seismischen oder aseismischen Verhaltens von Verwerfungen erfordert die Anwendung von Messverfahren am Meeresboden sowie Beobachtungen an der Küste, um in Zukunft eine angemessene Bewertung marinegeologischer Gefahren vornehmen zu können.

Ziel dieser Arbeit ist es, seismische und aseismische Deformation abseits der Küste mit Hilfe verschiedener seismologischer und geodätischer Daten aus Land und marinen Beobachtungen zu analysieren, zum besseren Verständnis der räumlichen und zeitlichen Variationen des Verwerfungsverhaltens. Die Hauptmethode kombiniert marine Seismologie und Meeresbodengeodäsie in einem küstenlinienübergreifenden Ansatz, der beitragen soll, das räumlich-zeitliche Gleitverhalten entlang zweier Hauptverwerfungstypen abzuschätzen. Die Deformation variiert von seismisch, über die Abstrahlung elastischer Energie, bis hin zu aseismisch, welches nicht notwendigerweise über Abstrahlung von Energie erfolgt (stilles oder langsames Gleiten). Das Untersuchen der verschiedenen Deformationen liefert Hinweise auf tektonische oder geologische Prozesse. Um die Gleitvariationen entlang verschiedener Verwerfungstypen zu entschlüsseln und die zugrundeliegenden Prozesse zu verstehen, werden in dieser Studie drei verschiedene Regionen untersucht: die submarine Plattengrenze entlang der nordchilenischen Subduktionszone, die Nordanatolische Horizontalverschiebung im zentralen Marmarameer und die südliche Grenze der instabilen Ostflanke von Europas größtem aktiven Vulkan, dem Ätna.

Die nordchilenische Subduktionszone ist durch das erosive Abtauchen der ozeanischen Nazca-Platte unter die kontinentale südamerikanische Platte gekennzeichnet. Das Iquique-

Erdbeben von 2014 mit einer Stärke von M_w 8,1 wirft ein Licht auf die aktiven Subduktionsprozesse der flachen Plattengrenze und des marinen Forearcs. Die Analyse eines amphibischen seismischen Netzwerks und mehrkanalreflexionsseismischer Daten weist auf einen gekoppelten Prozess hin, der das seismische Verhalten aufwärts der seismogenen Zone und die Subduktionserosion während der co- und post-seismischen Phase umfasst.

Die seismische Deformation von Verwerfungen am Meeresboden ist allgegenwärtig und erfordert die Anwendung von Messverfahren am Meeresboden. Die direkte Überwachung von Verschiebungen mit Hilfe von akustischem Distanzmessungen ist für die *in situ* Erkennung und Unterscheidung von aseismischen und seismischen Verwerfungen von Vorteil. Die Analyse der seismischen Aktivität und der Verformung an der unter Wasser liegenden Nordanatolischen Horizontalverschiebung, mit Hilfe von akustischen Distanzmessungen und Langzeitbeobachtungen, zeigte den Verriegelungszustand des zentralen Marmara-Segments und die Auswirkungen der Spannungsakkumulation auf die dicht besiedelte Region.

Schwerkraftbedingte Horizontalverschiebung, im Falle einer submarinen Hangrutschung, stellen eine erhebliches Risiko für besiedelte Küstenregionen dar. Die Ostflanke des Ätnas in Sizilien ist seit langem für ihre Instabilität bekannt, doch fehlte es an küstenfernen Beobachtungen. Analysen der submarinen Ostflanke, die durch eine langgestreckte Horizontalverschiebung an Land im Süden begrenzt ist, ergaben ein aseismisches Rutschverhalten, das langsames vorübergehendes Rutschen einschließt und die potenzielle Gefahr einer plötzlichen Flankenbewegung im Mittelmeer aufzeigt.

Contents

Abbreviations

AUV	autonomous underwater vehicle
gCMT	global centroid moment tensor
GNSS	Global Navigation Satellite System
GPS	Global Positioning System
cGPS	continuous Global Positioning System
InSAR	Interferometric Synthetic Aperture Radar
IPOC	Integrated Plate Boundary Observatory Chile
LEF	Low frequency earthquake
MCS	Multi-channel seismic
$\mathbf{M}_0$	Seismic moment
$\mathbf{M}_C$	Completeness magnitude
$\mathbf{M}_L$	Local magnitude
$\mathbf{M}_W$	Moment magnitude
NAF	North Anatolian Fault
OBS	Ocean Bottom Seismometer
QCF	Queen Charlotte Fault
SAF	San Andreas Fault
SSE	Slow-slip event
VLEF	Very low frequency earthquake

1 Motivation and Outline

1.1 Motivation

Globally, the proportion of people that live within 100 km of the coast is increasing and will reach 50 % of the world's population by 2030 (Small and Nicholls, 2003; Adger et al., 2005). These growing coastal populations are exposed to specific geohazards, including earthquakes, volcanic eruptions, submarine landslides and resulting tsunamis. In particular, great submarine earthquakes are among the most devastating natural disasters because of their potential to trigger cascading or cumulative effects, such as submarine landslides or tsunamis. The largest earthquakes on Earth occur where plate boundaries store and build up energy for centuries and then release it within minutes. Subduction zones have released 90 % of the total global seismic moment in the last century through large, shallow earthquakes, representing a significant portion of the Earth's seismic potential (Ruff and Kanamori, 1983; Pacheco and Sykes, 1992; Scholz and Campos, 1995). The most powerful of these earthquakes have the ability to propagate up-dip into the shallow subduction zone and thus can have exceptionally devastating consequences (e.g., the 2004 Sumatra earthquake). In particular, the sudden failure of the plate boundary at shallow depth, resulting in slow rupture propagation (Kanamori, 1972) can cause vertical movement of the seafloor and generate large tsunami waves that pose an even greater threat to coastal populations by destroying the infrastructure of coastal communities and causing significant loss of life (Stein and Okal, 2005; Newman et al., 2011; Simons et al., 2011; Lay et al., 2012). The short and incomplete historical seismic record since 1900 hinders an enhanced scientific estimation of event probability. In particular, the last decade has made us aware of how challenging calculating the probability of a major earthquakes is, especially for the rupture of earthquakes that were larger than expected (2011 Tohoku earthquake) or that occurred in regions where they were least expected (e.g., 2011 Christchurch earthquake, 2015 Illapel earthquake).

The tsunamigenic potential of submerged continental strike-slip fault zones has long been neglected because they generally cause mainly horizontal and limited vertical displacements (Elbanna et al., 2021; Scott, 2021). A recent review of strike-slip fault zones, however, revealed that transform plate boundaries have the ability to pose a significant tsunami potential, especially if supershear earthquakes are involved, where the rupture propagation velocity exceeds the shear wave velocity (Mai, 2019). Despite the disregarded tsunami potential, transform faults are able to release seismic energy with moment magnitudes above 8.5 (Meng et al., 2012). This knowledge demands a revised tsunami hazard assessments for affected populated coastal regions such as the Marmara Sea (Ambraseys, 2002) or the San Francisco Bay area (Song et al., 2008), where tsunamis have been recorded in the past (Elbanna et al., 2021).

Besides the risk for coastal populations, the world‘s industry is increasingly interested in the ocean floor and processes affecting it. Exploitation of the global seas and marine resources has increased over the last decade and is expected to grow, although the percentage from the oil and gas sector will decline in the next decade. In the future, seabed mining will rise to an essential component of the Blue Economy to meet the growing demand for materials of our rapidly developing technological world and to reach the objectives of e.g. the European Green Deal (compare The EU Blue Economy Report 2021; European Commission, 2021). Moreover, marine minerals and metals are frequently concentrated along tectonic plate boundaries and therefore inextricably linked to the geohazards posed by the sudden movement of boundary faults.

To provide adequate assessments and mitigate future geohazards, it is essential to determine the seismic potential of specific fault zones. Moreover, the spatio-temporal distribution of elastic strain accumulation, release of fault zones, and existence of different fault slip behaviors are crucial information for improving our understanding of the physics of earthquake phenomena and to recognize potential risks for coastal regions (Bürgmann et al., 2005; Harris, 2017; Uchida and Bürgmann, 2019). Varying fault slip behavior plays an important role in the earthquake cycle and associated geohazards (Lienert and Havskov, 1995). Tectonic faults that accommodate essential portions of their slip budget in an aseismic mode reduce the seismic hazard they pose, or act as precursory events and initiate or trigger earthquakes (Bürgmann, 2018). However, our knowledge and quantification of potential offshore geohazards is often limited by the coastline due to a lack of accurate information on the sub-seafloor domain. Assessing the heterogeneity of spatio-temporal faulting at submerged fault zones requires *in situ* ground truth determinations of their structures and properties. Consequently, the need for shoreline-crossing research approaches, combining land and marine seismology (Petersen et al., 2021) or linking Global Navigation Satellite System (GNSS) methods with seafloor geodesy techniques (Petersen et al., 2019) is immense (compare SZ4D Initiative, McGuire et al., 2017, and Helmholtz Research Program 2021-2027). Furthermore, shoreline-crossing approaches are crucial for a better understanding of slip behavior in offshore fault zones to constrain models (Tréhu, 2016), and for understanding and identifying the potential risks posed by geohazards.

1.2 Outline of this thesis

The thesis encompasses nine chapters, including six chapters dealing with the seismic and aseismic fault slip behavior at different fault zones and a concluding chapter. Finally, I will give an outlook on future challenges and recommendations of potential projects to enhance our understanding of fault slip characteristics. I authored three of the presented manuscripts, contributed substantial input to the manuscript of chapter eight, and contributed to the data acquisition, processing and discussion of the other manuscripts. All presented manuscripts have been published in or submitted to peer-reviewed journals.

Chapter 2 provides an overview of seismic and aseismic deformation characteristics, including a general introduction to the spatio-temporal behavior of subduction and strike-slip faults zones. Furthermore, this chapter examines measurement techniques for constraining sub-seafloor fault deformation by integrating shoreline-crossing observations.

Chapter 3 deals with the impact of active subduction erosion on the state of stress on the marine forearc of northern Chile. This chapter combines the results of two long-term ocean bottom seismometer (OBS) deployments on the marine forearc with long-offset multi-channel seismic data, and aims to provide insight into the seismo-tectonic structure of the 2014 M_w 8.1 Iquique earthquake rupture area. Based on the seismicity distribution along a wide stretch of the plate interface and upper plate, the chapter reveals that subduction erosion processes affect the base of the upper plate up-dip of the coseismic rupture. The transition from a fractured fluid-filled to a less deformed section of the upper plate witnesses active subduction erosion during the postseismic and possibly coseismic phases that leads to basal abrasion of the upper plate at the up-dip end of the seismogenic zone.

Author contributions: *DL, IG, EV, AT, HK designed the study. FP, DL, IG, HK, SB, ECR deployed and recovered the OBS. FP, MR, AT, ECR participated on MGL1610 cruise of RV Marcus G. Langseth during which the seismic reflection data was collected. FP processed the earthquake data and discussed the results with all co-authors. BM processed the multi-channel data with support of DK. FP produced the figures and wrote the paper supported by all co-authors. All co-authors contributed to the reviewing and editing of the paper.*

Chapter 3 is published in *Geophysical Research Letters* as:

Petersen, F., Lange, D., Ma, B., Grevemeyer, I., Geersen, J., Klaeschen, D., Contreras-Reyes, E., Barrientos, S., Tréhu, A. M., Vera, E., & Kopp, H. (2021). Relationship between subduction erosion and the up-dip limit of the 2014 mw 8.1 iquique earthquake. *Geophysical Research Letters*, *48*, e2020GL092207(9), https://doi.org/10.1029/2020GL092207.

Chapter 4 deals with the compelling observation of a spatial match between the rupture area of the 2014 Iquique earthquake and the coherent seismic reflectivity of the plate boundary using long-offset multi-channel seismic data. This chapter uses pre-stack depth migrated multi-channel seismic data covering the rupture area of partly unaffected segments north and south of the 2014 M_w 8.1 Iquique earthquake. We show that the aftershock distribution from Chapter 3 correlates spatially to the decrease in plate boundary reflection and supports our inference of a spatial relationship between the rupture area and the plate boundary reflectivity. Based on the sensitivity of seismic reflections to resolve fluid-pressure variations, this chapter suggests an interplay between the seismic rupture extent and coherent plate boundary reflection. The chapter concludes that the seismic reflection data may provide crucial information on seismic and tsunami hazards along active margins.

Author contributions: *DL, AT, HK designed the study. FP, MR, AT, ECR participated in cruise MGL1610 of RV Marcus G. Langseth during which the seismic reflection data were collected. BM processed the multi-channel data with support of DK. BM, JG, DL and HK discussed the results with all co-authors. FP processed the earthquake data. ECR, AT, MR, and YX contributed to the discussion of the seismic data. IG, DL, FP contributed to seismological topics. BM produced the figures. All co-authors contributed to the reviewing and editing of the paper.*

Chapter 4 is submitted to *Nature Geoscience* as:

Ma B., Geersen, J., Lange, D., Klaeschen, D., Grevemeyer, I., **Petersen, F.**, Riedel, M., Xia, Y., Tréhu, A. M., Contreras-Reyes, E., & Kopp, H. (submitted). Megathrust reflectivity matches the 2014 Iquique earthquake rupture. *Nature Geoscience.*

Chapter 5 deals with the analysis of repeating earthquakes from thirteen years of earthquake monitoring in the rupture area of the 2014 M_w 8.1 Iquique earthquake. This chapter uses multiple earthquake data sources, including the high-resolution aftershock catalog of Chapter 3, to determine an accurate resolved depth location of repeating earthquake sequences at the up-dip limit of the seismogenic zone. The study reveals repeating earthquake activity within the upper plate that correlates with the large-scale upper plate extensional faults identified in Chapter 3. Based on waveform coherency, repeaters indicate that upper plate fault slip begins during the foreshock period, characterized by thrust fault motion. The chapter concludes that the gradual unlocking of the plate interface during the long foreshock period induced weakening of the frontal upper plate by reverse activation of large-scale extensional faults and initiated subduction erosion.

Author contributions: *FP, DL, HK, IG designed the study. FP processed the earthquake data and discussed the results with all co-authors. SB provided the CSN earthquake catalog.*

FP produced the figures and wrote the paper supported by all co-authors. All co-authors contributed to the reviewing and editing of the paper.

Chapter 5 is submitted to the *Journal of Geophysical Research Solid Earth* as:

Petersen, F., Lange, D., Grevemeyer, I., Barrientos, S. & Kopp, H.(submitted). Repeating earthquakes reveal pre-seismic upper plate weakening by the 2014 Iquique foreshock sequence. *Journal of Geophysical Research Solid Earth.*

Chapter 6 reviews the emerging field of acoustic seafloor geodesy to study strain build-up by monitoring shallow seismic/aseismic fault displacement. We reviewed the recent development and progress in sea-going technology of long-term seafloor geodetic instrumentations, including the studies of the following Chapters 7 and 8 and analyzed potential effects of environmental influences on measurement precision. The method of acoustic direct-path ranging has proven to be a powerful tool by contributing essential information on the fault slip behavior of submarine fault zones. Further, the chapter examines the best approach to install acoustic ranging networks to achieve measurements precision at millimeter level, using recent seafloor geodetic studies of Chapters 7 and 8.

Author contributions: *FP, HK, DL, KH, MU designed the study. FP discussed the results with all co-authors. FP produced the figures and wrote the paper supported by all co-authors. All co-authors contributed to the reviewing and editing of the paper.*

Chapter 6 is published in the *Journal of Geodynamics* as:

Petersen, F., Kopp, H., Lange, D., Hannemann, K., & Urlaub, M. (2019). Measuring tectonic seafloor deformation and strain-build up with acoustic direct-path ranging. *Journal of Geodynamics*, *124*, 14–24, https://doi.org/10.1016/j.jog.2019.01.002.

Chapter 7 deals with the analysis of long-term monitoring for interseismic strain-build up on the North Anatolian Fault (NAF) in the Sea of Marmara. The chapter uses the acoustic direct-path ranging method, reviewed in Chapter 6, in collaboration of Turkish, French and German institutes to estimate the fault slip across the fault at the seafloor. Based on onshore GNSS ground displacement observations of the NAF and *in-situ* acoustic ranging slip measurements, the chapter provides strain rate sensitivity estimates using a theoretical dislocation model to assume the creeping depth below the seafloor geodetic observatory. Complemented by earthquake data from OBS and land data, the chapter shows that the central fault segment is in a locking state without transient aseismic displacement, thus accumulating strain. The result of an increasing slip-deficit poses a significant risk to the Istanbul metropolitan area.

Author contributions: *JYR, VB and HK funded and designed the experiment. DL, FP, KH, LYR, PH, VB, LG, PS deployed and collected the seafloor geodetic data. PH.*

implemented the analytical solution for the strain calculations, the modelling of strain was done by DL. The GPS land-stations and calculation of the water column parameters were done by SO, SE and FP. PS inverted the strike-slip rate from baseline data. The OBS data were processed by DL with input from LG, JB and ZC. The offshore geodetic data set was independently processed with a different software written by DL, FP who reached the same results. DL, HK produced the figures and drafted the manuscript supported by all co-authors. All co-authors contributed to the reviewing and editing of the paper.

Chapter 7 is published in *Nature Communications* as:

Lange, D., Kopp, H., Royer, J. Y., Henry, P., Cakir, Z., **Petersen, F.**, Sakic, P., Ballu, V., Bialas, J., Ozeren, M. S., Ergintav, S., & Geli, L. (2019). Interseismic strain build-up on the submarine north anatolian fault offshore istanbul. *Nature Communications*, *10*(1), 3006, https://doi.org/10.1038/ s41467-019-11016-z.

Chapter 8 deals with the observation of an aseismic slow-slip event along the southern limit of the eastern submerged flank of Mount Etna, Sicily. This chapter uses the acoustic direct-path ranging method reviewed in Chapter 6 linked with onshore GNSS/InSAR observations and high-resolution multi-channel seismic data to analyze the slip characteristics of the offshore-extending onshore faults. The chapter finds that the offshore fault slip has a similar character to the onshore fault, but total displacement exceeds the onshore counterpart, inferring a gravitational driven movement of the eastern volcanic flank.

Author contributions: *MU, FGross, GP, designed the study. FP, DL, MU, HK are responsible for the design of the seafloor network and formal data analysis. FP, FGross and SK participated in the acquisition of marine data. AB, FGuglielmino, and GO formally analyzed the onshore data. MU, FP, FGross, AB, and GP interpreted the data. MU, FP produced the figures. M.U. drafted and prepared the article supported by all co-authors. All co-authors contributed to the reviewing and editing of the paper.*

Chapter 8 is published in *Science Advances* as:

Urlaub, M., **Petersen, F.**, Gross, F., Bonforte, A., Puglisi, G., Guglielmino, F., Krastel, S., Lange, D., & Kopp, H. (2018). Gravitational collapse of mount etna's southeastern flank. *Science Advances*, *4*(10), eaat9700, https://doi.org/10.1126/sciadv.aat9700.

Chapter 9 summarizes the results and discussions of the previous chapters and provides an outlook for potential research with regard to yet unnoted fault systems, and suggests recommendations for future fault slip behavior related studies.

References

Adger, W. N., Hughes, T. P., Folke, C., Carpenter, S. R., & Rockstrom, J. (2005). Social-ecological resilience to coastal disasters. *Science*, *309*(5737), 1036–9, `https://doi.org/10.1126/science.1112122`.

Ambraseys, N. N. (2002). The seismic activity of the marmara sea region over the last 2000 years. *Bulletin of the Seismological Society of America*, *92*(1), 1–18, `https://doi.org/10.1785/0120000843`.

Bürgmann, R. (2018). The geophysics, geology and mechanics of slow fault slip. *Earth and Planetary Science Letters*, *495*, 112–134, `https://doi.org/10.1016/j.epsl.2018.04.062`.

Bürgmann, R., Kogan, M. G., Steblov, G. M., Hilley, G., Levin, V. E., & Apel, E. (2005). Interseismic coupling and asperity distribution along the kamchatka subduction zone. *Journal of Geophysical Research*, *110*(B7), `https://doi.org/10.1029/2005JB003648`.

Elbanna, A., Abdelmeguid, M., Ma, X., Amlani, F., Bhat, H. S., Synolakis, C., & Rosakis, A. J. (2021). Anatomy of strike-slip fault tsunami genesis. *Proceedings of the National Academy of Sciences*, *118*(19), `https://doi.org/10.1073/pnas.2025632118`.

European Commission (2021). The eu blue economy report 2021. *Publications Office of the European Union. Luxembourg.*, `https://doi.org/10.2771/8217`.

Harris, R. A. (2017). Large earthquakes and creeping faults. *Reviews of Geophysics*, *55*(1), 169–198, `https://doi.org/10.1002/2016rg000539`.

Kanamori, H. (1972). Mechanism of tsunami earthquakes. *Physics of the Earth and Planetary Interiors*, *6*(5), 346–359, `https://doi.org/10.1016/0031-9201(72)90058-1`.

Lay, T., Kanamori, H., Ammon, C. J., Koper, K. D., Hutko, A. R., Ye, L., Yue, H., & Rushing, T. M. (2012). Depth-varying rupture properties of subduction zone megathrust faults. *Journal of Geophysical Research: Solid Earth*, *117*(B04311), `https://doi.org/10.1029/2011jb009133`.

Lienert, B. R. & Havskov, J. (1995). A computer program for locating eathquakes both locally and globally. *Seismological Research Letters*, *66*(5).

Mai, P. M. (2019). Supershear tsunami disaster. *Nature Geoscience*, *12*(3), 150–151, `https://doi.org/10.1038/s41561-019-0308-8`.

McGuire, J. J., Plank, T., & et al. (2017). The sz4d initiative: Understanding the processes that underlie subduction zone hazards in 4d. vision document submitted to the national science foundation. *The IRIS Consortium*, (pp. 63 pp).

Meng, L., Ampuero, J. P., Stock, J., Duputel, Z., Luo, Y., & Tsai, V. C. (2012). Earthquake in a maze: compressional rupture branching during the 2012 m(w) 8.6 sumatra earthquake. *Science*, *337*(6095), 724–6, `https://doi.org/10.1126/science.1224030`.

Newman, A. V., Hayes, G., Wei, Y., & Convers, J. (2011). The 25 october 2010 mentawai tsunami earthquake, from real-time discriminants, finite-fault rupture, and tsunami excitation. *Geophysical Research Letters*, *38*(5), `https://doi.org/10.1029/2010gl046498`.

Pacheco, J. F. & Sykes, L. R. (1992). Seismic moment catalog of large shallow earthquakes, 1900 to 1989. *Bulletin of the Seismological Society of America*, *82*(3), 1306–1349.

Petersen, F., Kopp, H., Lange, D., Hannemann, K., & Urlaub, M. (2019). Measuring tectonic seafloor deformation and strain-build up with acoustic direct-path ranging. *Journal of Geodynamics*, *124*, 14–24, `https://doi.org/10.1016/j.jog.2019.01.002`.

Petersen, F., Lange, D., Ma, B., Grevemeyer, I., Geersen, J., Klaeschen, D., Contreras-Reyes, E., Barrientos, S., Tréhu, A. M., Vera, E., & Kopp, H. (2021). Relationship between subduction erosion and the up-dip limit of the 2014 mw 8.1 iquique earthquake. *Geophysical Research Letters*, *48, e2020GL092207*(9), `https://doi.org/10.1029/2020GL092207`.

Ruff, L. & Kanamori, H. (1983). Seismic coupling and uncoupling at subduction zones. *Tectonophysics*, *99*(2-4), 99–117, `https://doi.org/10.1016/0040-1951(83)90097-5`.

Scholz, C. H. & Campos, J. (1995). On the mechanism of seismic decoupling and back arc spreading at subduction zones. *Journal of Geophysical Research: Solid Earth*, *100*(B11), 22103–22115, `https://doi.org/10.1029/95jb01869`.

Scott, E. (2021). Strike-slip tsunamis. *Nature Reviews Earth and Environment*, *2*(6), 379–379, `https://doi.org/10.1038/s43017-021-00179-3`.

Simons, M., Minson, S. E., Sladen, A., Ortega, F., Jiang, J., Owen, S. E., Meng, L., Ampuero, J. P., Wei, S., Chu, R., Helmberger, D. V., Kanamori, H., Hetland, E., Moore, A. W., & Webb, F. H. (2011). The 2011 magnitude 9.0 tohoku-oki earthquake: mosaicking the megathrust from seconds to centuries. *Science*, *332*(6036), 1421–5, `https://doi.org/10.1126/science.1206731`.

Small, C. & Nicholls, R. J. (2003). A global analysis of human settlement in coastal zones. *J. Coast. Res.*, *19*, 584–599.

Song, S. G., Beroza, G. C., & Segall, P. (2008). A unified source model for the 1906 san francisco earthquake. *Bulletin of the Seismological Society of America*, *98*(2), 823–831, `https://doi.org/10.1785/0120060402`.

Stein, S. & Okal, E. A. (2005). Seismology: speed and size of the sumatra earthquake. *Nature*, *434*(7033), 581–2, `https://doi.org/10.1038/434581a`.

Tréhu, A. M. (2016). Measuring slow slip offshore. *Science*, *352*(6286), 654–5, `https://doi.org/10.1126/science.aaf6534`.

Uchida, N. & Bürgmann, R. (2019). Repeating earthquakes. *Annual Review of Earth and Planetary Sciences*, *47*(1), 305–332, `https://doi.org/10.1146/annurev-earth-053018-060119`.

2 Introduction

2.1 Seismic and aseismic slip characteristics

Geological faults are elongated discontinuities in rock formations that can host the lithospheric deformation through abrupt fast (seismic) slip and slower (aseismic) slip. Sudden fast seismic slip is characterized by a stick-slip behavior of involved rocks, which releases elastic energy. The elastic energy is radiated through the earth and along its surface in the form of seismic waves, which are recorded by seismometers. The amount of seismic energy is expressed by its moment magnitude, which depends on the shear module of involved rocks, the dimension of the fault plane and the average slip along the fault plane (Hanks and Kanamori, 1979). The mode of slip at faults is governed by a complex relationship between friction, slip velocity, duration and distance, also known as rate- and state-dependent friction (Dieterich, 1978, 1979; Ruina, 1983). For instance, if the decrease in frictional resistance to a fault movement exceeds the stress reduction of fault motion, sudden sliding with an associated stress drop occurs and seismic energy is released as elastic waves. Between sudden motions, periods of rest lead to the recharge of stress, known as stick-slip (Scholz, 1998). Seismic fault slip velocities that radiate high-frequency seismic waves range from 10^{-4} to 1 m/s (Bürgmann, 2018).

The existence of slow fault slip has been known for decades, but its significance and implications for hazard assessment were not recognized until GPS networks recorded such slow slip events in the early 90s (Linde et al., 1996; Peng and Gomberg, 2010). In general, slow fault slip is several orders of magnitude slower than seismic slip and can last for a few seconds to several years (Figure 2.1; Mallick et al., 2021). In the last two decades, slow seismic signals have been identified by a rapid increase in the number of permanently operated seismometers and campaign-type studies with temporarily deployed seismic sensors. Subsequent studies have uncovered a whole new class of earthquakes that occur unusually slow compared to seismic earthquakes (e.g., Beroza and Ide, 2011). In contrast to seismic slip, aseismic slip (slow slip), also frequently referred to as fault creep, is slow enough that inertial forces and seismic radiation are negligible, but there is no clear boundary between seismic and aseismic fault slip, and the rate of slow fault slip can be constant or vary over time. Since their discovery, various types of slower fault slip have been classified as tectonic tremor or episodic tremor and slip (ETS), low-frequency earthquakes (LEFs) (Shelly et al., 2006), very-low-frequency earthquakes (VLFEs) (Obara and Ito, 2005), with source durations of less than one second and a few tens of seconds, respectively. Among these signals, the most commonly observed are slow-slip events (SSEs), a slip phenomenon that is associated with an aseismic transient on a fault patch (Dragert et al., 2001; Ide et al., 2007; Peng and Gomberg, 2010; Beroza and Ide, 2011).

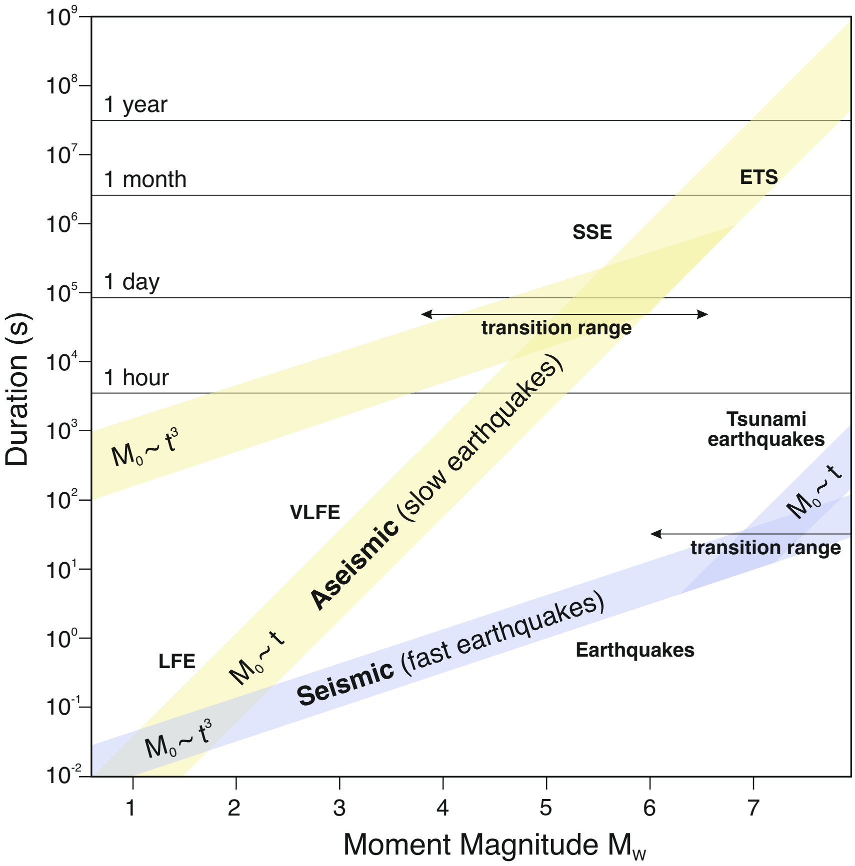

Figure 2.1: The moment magnitude M_w versus the characteristic duration t of various seismic and aseismic earthquakes (based on Ide et al., 2007; Gomberg et al., 2016). Letters refer to observed aseismic deformation: slow-slip events (SSE); low-frequency earthquakes (LEF); very low frequency earthquakes (VLFE) and episodic tremor and slip (ETS).

Aseismic or slow-slip fault deformation has also been documented on non-tectonic fault types, including glaciers (Wiens et al., 2008) and landslides (Urlaub et al., 2018), although the fault deformation is driven by gravity rather than plate motion. The study of such characteristic slow earthquakes have revealed that their moment magnitude is proportional to their characteristic duration (Figure 2.1), inferring that slow slip earthquakes are a different expression of the same occurrence (Ide et al., 2007). The proposed scaling law is expressed as seismic moment M_0 and duration t^n where n is 3 for seismic and 1 for aseismic deformation. However, dislocation models indicate that for both seismic and aseismic deformation appears to transition from $M_0 \sim t^3$ to $M_0 \sim t$ as slip zones are confined at their up-dip and down-dip limits (Gomberg et al., 2016).

The phenomenom of SSE, which are accelerated episodes of slip (Ide et al., 2007), has been most commonly observed at subduction zones, particularly in the circum-Pacific region, and has generated tremendous interest in the physical processes that control fault slip (Beroza and Ide, 2011; Wallace, 2020). To allow slow fault motion, a strengthening mechanism is required that slows the speed of faulting down to sub-seismogenic slip velocities (Bürgmann, 2018). In general, the increase of fault strength with growing slip prevents fast earthquake rupture and promotes fault creep (velocity-strengthening). In contrast, faults that weaken with increasing slip rate are referred to as velocity weakening and can enter seismic stick-slip behavior and radiate elastic waves (Scholz, 1998).

Active plate tectonics and their restless boundaries are the main driver for changing slip behaviors. Furthermore, the interaction between the two moving tectonic plates is accommodated by a combination of interseismic slow slip, seismic rupture and postseismic deformation. In general, plate boundaries are classified as either divergent (e.g., mid ocean ridges), convergent (subduction thrust) or transform faults (strike-slip faults). The region of the plate boundary exhibiting stick-slip (velocity-weakening) behavior and capable of generating large earthquakes is referred to as the seismogenic zone. This zone is bounded by regions that are dominated by a frictional transition from unstable to stable sliding (velocity-strengthening). However, the extent and width of the seismogenic zone varies spatially along the plate boundary (Figures 2.2 and 2.3; e.g., Schmidt et al., 2005; Lay et al., 2012; Yamamoto et al., 2017). Such fault zones with varying slip modes are referred to as partially coupled, where fault coupling defines the degree to which slip on a fault is determined by seismic vs. aseismic slip (Wang and Dixon, 2004). The coupling ratio ranges from 0 to 1, but coupling ratios are highly dependent on the length of the observation period. For instance, the observation of short period fault slip at a rate faster than the overall plate convergence rate causes a coupling ratio of < 0 and is not unlikely (Wang and Dixon, 2004). However, a coupling ratio of > 1 implies a backward motion compared to the long-term fault slip motion and seems physically impossible (Wang and Dixon, 2004).

2.2 Observational constraints on offshore seismic and aseismic deformation

The first observations of slower fault slip date back more than 60 years. They were made on onshore tectonic strike-slip faults including the San Andreas fault (Steinbrugge et al., 1960), Hayward fault (Louderback, 1942), and the North Anatolian Fault (Ambraseys, 1970) by observing the slowly increasing offset of artificial structures (Harris, 2017). Subsequently, the comparison of global seismic moment release and the distribution of estimated fully coupled areas indicated that large portions of plate boundaries, including tectonic strike-slip faults, may slip aseismically (Pacheco et al., 1993; Tichelaar and Ruff, 1993; Bird and Kagan, 2004). Early measurements of slow fault movements were restricted to the shallow near surface shear zone, but precise and fault distance-dependent motion measurements allowed aseismic and fully coupled fault patches, i.e. at the San Andreas Fault (Harris and Segall, 1987), to be modelled. Today, geophysical observations of slow fault slip are mainly carried out using geodetic methods; for instance, continuous GNSS monitoring or Interferometric Synthetic Aperture Radar (InSAR) with a high spatial resolution at a millimeter level. To directly measure fault displacement, creepmeters cross fault traces and are able to resolve movements at sub-millimeter accuracy (e.g., Victor et al., 2018). Slip on submarine fault systems is more difficult to measure due to the lower resolution of slip observations, as well as coupling models being based only on terrestrial geodetic observations (e.g., Chlieh et al., 2008; Loveless and Meade, 2011; Métois et al., 2013). Networks of short- and long-period ocean-bottom seismometers are used to estimate accurate hypocenter locations far offshore and to reveal the seismogenic properties of the megathrust zone (e.g., Husen and Kissling, 2001; Petersen et al., 2021) or the seismic structure of faults (Lange et al., 2010; Yamamoto et al., 2017). OBS station runtimes, however, are highly dependent on battery life and are only able to record seismic deformation. Consequently, in situ ground-truthing of aseismic deformation requires the use of seafloor measurement techniques to directly observe aseismic deformation and determine fault coupling (Bürgmann and Chadwell, 2014; Petersen et al., 2019). The following have proven to be powerful tools for revealing shallow offshore slip and inter-seismic strain build-up: acoustic direct-path ranging arrays (Urlaub et al., 2018; Lange et al., 2019; Petersen et al., 2019; Yamamoto et al., 2019); GNSS-acoustic sensors (Gagnon et al., 2005; Yokota and Ishikawa, 2020); ocean bottom pressure sensors (Wallace et al., 2016); on- and offshore linked earthquake observations (e.g., Lieser et al., 2014; Petersen et al., 2021); and boreholes pore–pressure measurements (Araki et al., 2017).

Although the occurrence of aseismic or slow slip is by definition silent, seismic signals and methods can be used to reveal its existence and provide additional information about the spatio-temporal distribution of slow slip along faults (Uchida and Bürgmann, 2019). Earthquakes that have nearly identical waveforms are referred to as repeating earthquakes that occur at the same fault by repeated rupturing of small asperities that catch up with surrounding aseismic slip (Nadeau and McEvilly, 1999; Uchida and Bürgmann, 2019). These repeated seismic moment releases are used to analyze and estimate the slow slip of faults in time through the geodetically calibrated magnitude-slip empirical relationship (Nadeau and Johnson, 1998; Igarashi et al., 2003). Repeating earthquakes have been found at extensional faults (Valoroso et al., 2017; Vuan et al., 2017; Duverger et al., 2018), thrust faults (Chen et al., 2008), subduction related megathrust faults (Chen et al., 2007; Uchida and Matsuzawa, 2013; Kato and Nakagawa, 2014) and transform plate boundaries (Nadeau and Johnson, 1998; Peng, 2005; Turner et al., 2015; Bohnhoff et al., 2017). The occurrence and analysis of their cumulative slip, spatial distribution and recurrence have improved our understanding of fault slip characteristics, event triggering and the predictability of earthquakes. However, the lack of repeating earthquakes along silent fault zones does not imply the absence of aseismic/slow slip (Uchida and Bürgmann, 2019). Constraints on the occurrence of aseismic/slow slip can also be provided by swarm-like earthquake sequences, which do not have a clear relationship between the main and aftershocks and do not show a decay in time according to standard aftershock scaling laws (e.g., Omori law-type). However, a lack of constraining geophysical data means that their driving processes are often unclear (Roland and McGuire, 2009).

2.3 Subduction zone deformation modes

At convergent plate boundaries, the far-field motion of two different tectonic plates is accommodated on a localized zone of deformation. The interface between the subducting and overriding plate is referred to as a megathrust fault (Figure 2.2). The megathrust is thought to be a shear zone rather than a single surface (Calahorrano et al., 2008; Vannucchi et al., 2008). Comparisons of seismic moment release and estimated fully coupled subduction zones indicate that large portions of convergent plate boundaries may slip aseismically (Pacheco and Sykes, 1992; Pacheco et al., 1993). Based on the analysis of large and great earthquakes in the last century, the seismogenic zone where great earthquakes nucleate includes certain depth-dependent rupture variations. The shallow megathrust (0 - 55 km depth) is separated into faulting domains (Figure 2.2). The very shallow part of the plate interface extends from the trench toe to the up-dip limit of the seismogenic zone. The up-dip limit of the seismogenic zone that confines the shallow part is suggested to be related to forearc structure and morphology (Wang and Hu, 2006; Tilmann et al., 2010); metamorphic processes (Moore and Saffer, 2001); or thermal properties (Oleskevich et al., 1999; Moore and Saffer, 2001). This shallow region has long been considered to exhibit a major aseismic behavior, but recent developments in offshore instrumentation revealed that modes of slip similar to other shallow fault zones, including SSE (e.g., Song et al., 2009) LFE and VLFE (e.g., Ito and Obara, 2006), tectonic tremor with or without slow slip (e.g., Shelly et al., 2006) are a common feature along the shallow subduction zone megathrust (Figure 2.2; Bilek and Lay, 2018; Yokota and Ishikawa, 2020). However, slip behavior within the shallow subduction zone indicates very large spatial and temporal variations, so that some regions may undergo stable sliding that prevents significant strain accumulation (Hu and Wang, 2008). It has been suggested that geological features, such as disparities in interface roughness or subducting seamounts, evoke shallow fault creep and impact the deeper seismogenic zone of the plate interface (Wang and Bilek, 2014; Edwards et al., 2018). Further along-dip, a transition zone of conditional stable sliding prevails, defining the up-dip limit of the seismogenic zone until unstable sliding predominates (nucleation of large earthquakes) (Scholz, 1998).

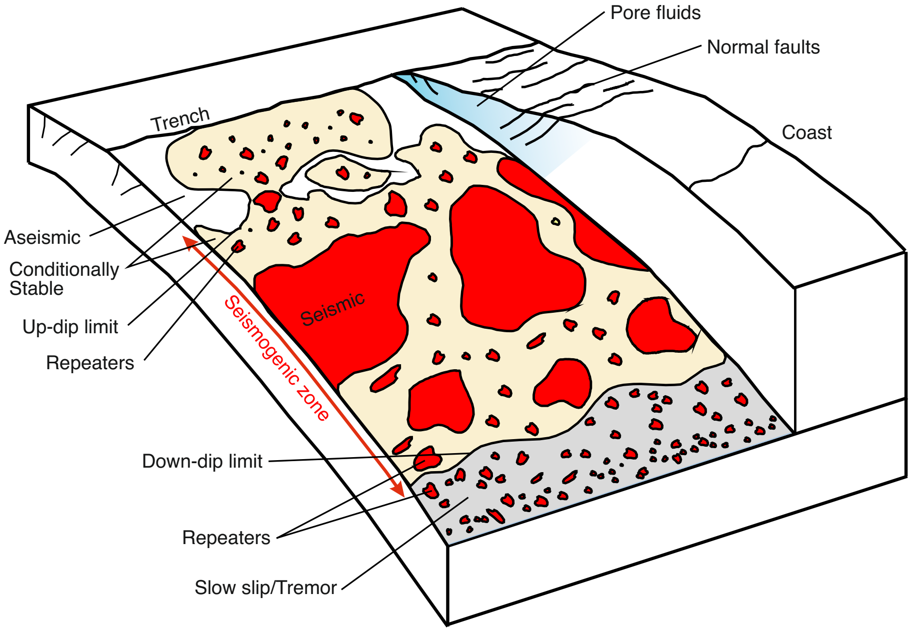

Figure 2.2: Fault structure and slip behavior of an example subduction thrust fault on a predominantly erosional convergent margin (based on Lay et al., 2012).

In the seismogenic zone, a twofold earthquake rupture pattern has been observed, comprised of an area of large coseismic slip with low short-period energy earthquakes and, further down-dip, an area of high short-period energy with intermediate slip earthquakes (Figure 2.2; Lay et al., 2012). Great earthquakes ($M \geq 8$) with large fault slip tend to rupture at depths between 15 to 35 km, whereas large earthquakes ($M \geq 7$) rupture at greater depth between 35 - 55 km. Down-dip of the seismogenic zone, a second transitional region appears where slow slip phenomena have been documented and ductile flow in the mantle wedge sets in (Bilek and Lay, 2018). In this second transitional region, high temperatures and pressures at the megathrust shear zone allow slow fault motion and continuous shearing (Avouac, 2015). With increasing temperature at depth, the accompanying transition from conditional sliding to velocity-strengthening frictional behavior is believed to be responsible for the termination of earthquakes, with stable sliding accommodating plate motion (Figure 2.2; Schwartz and Rokosky, 2007). In this deep part of the subduction zone, slow earthquakes and subduction associated deep-situated fault creep was first observed using land-based seismometers and GNSS stations two decades ago at two extremely well monitored subduction zones: Cascadia (Dragert et al., 2001) and Nankai (Hirose et al., 1999; Obara, 2002).

Investigations of the shallow offshore located subduction thrust, using on- and offshore geodetic and seismological techniques enable an improvement in the understanding of subduction erosion and accretion, splay fault activity, interface coupling ratios, delimitation of large interface asperities, state of stress of the overriding plate, and bend fault activity. In particular, the up-dip end of the seismogenic zone where frictional transition from unstable to conditional and stable sliding occurs has important implications for tsunami generation. Although great earthquakes nucleate at greater depth, megathrust ruptures characterized by long durations with moderate magnitudes can propagate to the trench as a result of conditional stability of fault friction (Scholz, 1998; Hu and Wang, 2008) and produce disproportionally large tsunamis (Kanamori, 1972; Kanamori and Kikuchi, 1993; Satake, 1994; Newman et al., 2011).

2.4 Strike-slip deformation modes

Transform plate boundaries are characterized by two tectonic plates that slide past one another in a predominantly horizontal motion. Most strike-slip faults occur at mid ocean ridges, where they are referred to as transform faults; however continental transform faults have been intensively studied over the last decades, using creepmeters, InSAR, near-field GNSS and/or terrestrial surveying, geological field studies, and strainmeters. These studies, especially at the San Andreas Fault and North Anatolian Fault have led to an improved resolution of the distribution of locked and creeping fault areas on continental strike-slip fault zones. Offshore strike-slip fault investigations, conversely, depend on the use of sophisticated measurement technology, including seafloor acoustic ranging; near-field ocean bottom pressure; and borehole pore pressure, strain- and tiltmeters (Harris, 2017; Bürgmann, 2018).

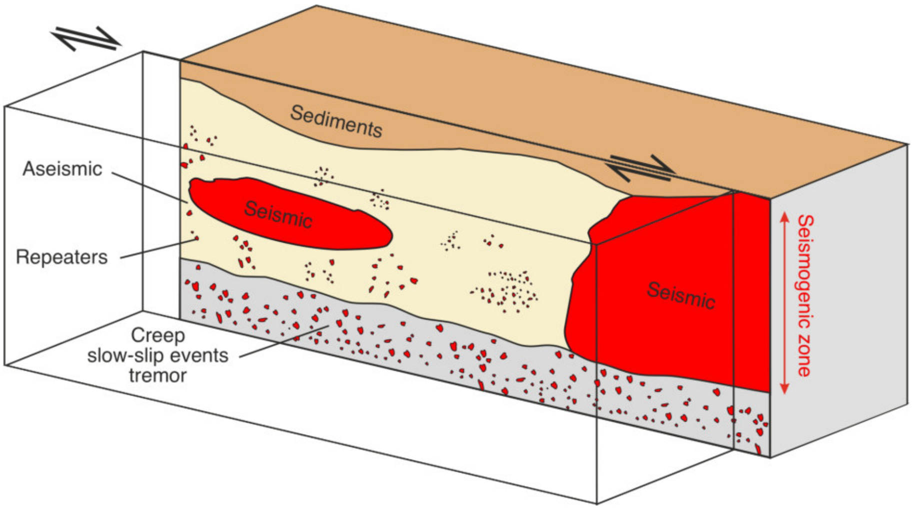

Figure 2.3: Fault structure and seismic behavior of an example strike-slip fault zone (based on Bürgmann, 2018).

In general, strike-slip fault zones are characterized at depth by a brittle to ductile transition that induces velocity-strengthening frictional behavior, creep, slow-slip events and tremors. Above a certain temperature (300 - 360 °C), the rate-and-state frictional behavior changes from aseismic to seismic deformation and large earthquakes are able to nucleate (unstable sliding) (e.g., Cole et al., 2007; Fagereng and Toy, 2011). The seismogenic zone along the fault zone varies, with large asperities adjacent to creeping segments and smaller asperities, including repeating earthquakes (Figure 2.3). Large distributed aseismic deformation along fault segments that extend to greater depth may impact the earthquake timing and magnitude (Harris, 2017). The shallow fault zone can exhibit zones of distributed shearing and slip partitioning, expressed through complex surface faulting and secondary faults, which accommodate displacement through stable frictional behavior (aseismic). Tensional stresses on the strike-slip fault create trans-tensional normal faults, resulting in basins such as the Sea of Marmara. On the contrary, compressional stresses create transpressional reverse faults and cause small-scale mountain building. Fault systems that splay off with tensional or compressional stresses and create secondary faulting are known as flower structures, which are characterized by numerous fault exposures at the surface. When features below the seafloor have complex strain distribution, seafloor measurements struggle to reveal the degree of local locking and to estimate the seismic potential (Petersen et al., 2019). Lateral displacement also occurs where gravity acts on large masses and triggers large submarine landslides (Urlaub et al., 2018) or drives the movement of glaciers (Wiens et al., 2008).

References

Ambraseys, N. N. (1970). Some characteristic features of the anatolian fault zone. *Tectonophysics*, *9*(2-3), 143–165, `https://doi.org/10.1016/0040-1951(70)90014-4`.

Araki, E., Saffer, D. M., Kopf, A. J., Wallace, L. M., Kimura, T., Machida, Y., Ide, S., Davis, E., & scientists, I. E. . s. (2017). Recurring and triggered slow-slip events near the trench at the nankai trough subduction megathrust. *Science*, *356*(6343), 1157–1160, `https://doi.org/10.1126/science.aan3120`.

Avouac, J.-P. (2015). From geodetic imaging of seismic and aseismic fault slip to dynamic modeling of the seismic cycle. *Annual Review of Earth and Planetary Sciences*, *43*(1), 233–271, `https://doi.org/10.1146/annurev-earth-060614-105302`.

Beroza, G. C. & Ide, S. (2011). Slow earthquakes and nonvolcanic tremor. *Annual Review of Earth and Planetary Sciences*, *39*(1), 271–296, `https://doi.org/10.1146/annurev-earth-040809-152531`.

Bilek, S. L. & Lay, T. (2018). Subduction zone megathrust earthquakes. *Geosphere*, *14*(4), 1468–1500, `https://doi.org/10.1130/ges01608.1`.

Bird, P. & Kagan, Y. Y. (2004). Plate-tectonic analysis of shallow seismicity: Apparent boundary width, beta, corner magnitude, coupled lithosphere thickness, and coupling in seven tectonic settings. *Bulletin of the Seismological Society of America*, *94*(6), 2380–2399, `https://doi.org/10.1785/0120030107`.

Bohnhoff, M., Wollin, C., Domigall, D., Küperkoch, L., Martínez-Garzón, P., Kwiatek, G., Dresen, G., & Malin, P. E. (2017). Repeating marmara sea earthquakes: indication for fault creep. *Geophysical Journal International*, *210*(1), 332–339, `https://doi.org/10.1093/gji/ggx169`.

Bürgmann, R. (2018). The geophysics, geology and mechanics of slow fault slip. *Earth and Planetary Science Letters*, *495*, 112–134, `https://doi.org/10.1016/j.epsl.2018.04.062`.

Bürgmann, R. & Chadwell, D. (2014). Seafloor geodesy. *Annual Review of Earth and Planetary Sciences*, *42*(1), 509–534, `https://doi.org/10.1146/annurev-earth-060313-054953`.

Calahorrano, A., Sallares, V., Collot, J., Sage, F., & Ranero, C. (2008). Nonlinear variations of the physical properties along the southern ecuador subduction channel: Results from depth-migrated seismic data. *Earth and Planetary Science Letters*, *267*(3-4), 453–467, `https://doi.org/10.1016/j.epsl.2007.11.061`.

Chen, K. H., Nadeau, R. M., & Rau, R.-J. (2007). Towards a universal rule on the recurrence interval scaling of repeating earthquakes? *Geophysical Research Letters*, *34*(16), `https://doi.org/10.1029/2007gl030554`.

Chen, K. H., Nadeau, R. M., & Rau, R.-J. (2008). Characteristic repeating earthquakes in an arc-continent collision boundary zone: The chihshang fault of eastern taiwan. *Earth and Planetary Science Letters*, *276*(3-4), 262–272, `https://doi.org/10.1016/j.epsl.2008.09.021`.

Chlieh, M., Avouac, J. P., Sieh, K., Natawidjaja, D. H., & Galetzka, J. (2008). Heterogeneous coupling of the sumatran megathrust constrained by geodetic and paleogeodetic measurements. *Journal of Geophysical Research*, *113*(B5), `https://doi.org/10.1029/2007jb004981`.

Cole, J., Hacker, B., Ratschbacher, L., Dolan, J., Seward, G., Frost, E., & Frank, W. (2007). Localized ductile shear below the seismogenic zone: Structural analysis of an exhumed strike-slip fault, austrian alps. *Journal of Geophysical Research*, *112*(B12), `https://doi.org/10.1029/2007jb004975`.

Dieterich, J. H. (1978). *Time-Dependent Friction and the Mechanics of Stick-Slip*, volume 6, book section Chapter 15, (pp. 790–806).

Dieterich, J. H. (1979). Modeling of rock friction: 1. experimental results and constitutive equations. *Journal of Geophysical Research*, *84*(B5), `https://doi.org/10.1029/JB084iB05p02161`.

Dragert, G., Wang, K., & James, T. S. (2001). A silent slip event on the deeper cascadia subduction interface. *Science*, *292*(5521), 1525–8, `https://doi.org/10.1126/science.1060152`.

Duverger, C., Lambotte, S., Bernard, P., Lyon-Caen, H., Deschamps, A., & Nercessian, A. (2018). Dynamics of microseismicity and its relationship with the active structures in the western corinth rift (greece). *Geophysical Journal International*, *215*(1), 196–221, `https://doi.org/10.1093/gji/ggy264`.

Edwards, J. H., Kluesner, J. W., Silver, E. A., Brodsky, E. E., Brothers, D. S., Bangs, N. L., Kirkpatrick, J. D., Wood, R., & Okamoto, K. (2018). Corrugated megathrust revealed offshore from costa rica. *Nature Geoscience*, *11*(3), 197–202, `https://doi.org/10.1038/s41561-018-0061-4`.

Fagereng, A. & Toy, V. G. (2011). Geology of the earthquake source: an introduction. *Geological Society, London, Special Publications*, *359*(1), 1–16, `https://doi.org/10.1144/sp359.1`.

Gagnon, K., Chadwell, C. D., & Norabuena, E. (2005). Measuring the onset of locking in the peru-chile trench with gps and acoustic measurements. *Nature*, *434*(7030), 205–8, `https://doi.org/10.1038/nature03412`.

Gomberg, J., Wech, A., Creager, K., Obara, K., & Agnew, D. (2016). Reconsidering earthquake scaling. *Geophysical Research Letters*, *43*(12), 6243–6251, `https://doi.org/10.1002/2016gl069967`.

Hanks, T. C. & Kanamori, H. (1979). A moment magnitude scale. *Journal of Geophysical Research*, *84*(B5), `https://doi.org/10.1029/JB084iB05p02348`.

Harris, R. A. (2017). Large earthquakes and creeping faults. *Reviews of Geophysics*, *55*(1), 169–198, `https://doi.org/10.1002/2016rg000539`.

Harris, R. A. & Segall, P. (1987). Detection of a locked zone at depth on the parkfield, california, segment of the san andreas fault. *Journal of Geophysical Research*, *92*(B8), `https://doi.org/10.1029/JB092iB08p07945`.

Hirose, H., Hirahara, K., Kimata, F., Fujii, N., & Miyazaki, S. (1999). A slow thrust slip event following the two 1996 hyuganada earthquakes beneath the bungo channel, southwest japan. *Geophysical Research Letters*, *26*(21), 3237–3240, `https://doi.org/10.1029/1999gl010999`.

Hu, Y. & Wang, K. (2008). Coseismic strengthening of the shallow portion of the subduction fault and its effects on wedge taper. *Journal of Geophysical Research*, *113*(B12), `https://doi.org/10.1029/2008jb005724`.

Husen, S. & Kissling, E. (2001). Postseismic fluid flow after the large subduction earthquake of antofagasta, chile. *Geology*, *29*(9), `https://doi.org/10.1130/0091-7613(2001)029<0847:Pffatl>2.0.Co;2`.

Ide, S., Beroza, G. C., Shelly, D. R., & Uchide, T. (2007). A scaling law for slow earthquakes. *Nature*, *447*(7140), 76–9, `https://doi.org/10.1038/nature05780`.

Igarashi, T., Matsuzawa, T., & Hasegawa, A. (2003). Repeating earthquakes and interplate aseismic slip in the northeastern japan subduction zone. *Journal of Geophysical Research: Solid Earth*, *108*(B5), `https://doi.org/10.1029/2002jb001920`.

Ito, Y. & Obara, K. (2006). Very low frequency earthquakes within accretionary prisms are very low stress-drop earthquakes. *Geophysical Research Letters*, *33*(9), `https://doi.org/10.1029/2006gl025883`.

Kanamori, H. (1972). Mechanism of tsunami earthquakes. *Physics of the Earth and Planetary Interiors*, *6*(5), 346–359, `https://doi.org/10.1016/0031-9201(72)90058-1`.

Kanamori, H. & Kikuchi, M. (1993). The 1992 nicaragua earthquake: a slow tsunami earthquake associated with subducted sediments. *Nature*, *361*(6414), 714–716, `https://doi.org/10.1038/361714a0`.

Kato, A. & Nakagawa, S. (2014). Multiple slow-slip events during a foreshock sequence of the 2014 iquique, chile mw 8.1 earthquake. *Geophysical Research Letters*, *41*(15), 5420–5427, `https://doi.org/10.1002/2014gl061138`.

Lange, D., Kopp, H., Royer, J. Y., Henry, P., Cakir, Z., Petersen, F., Sakic, P., Ballu, V., Bialas, J., Ozeren, M. S., Ergintav, S., & Geli, L. (2019). Interseismic strain build-up on the submarine north anatolian fault offshore istanbul. *Nat Commun*, *10*(1), 3006, `https://doi.org/10.1038/s41467-019-11016-z`.

Lange, D., Tilmann, F., Rietbrock, A., Collings, R., Natawidjaja, D. H., Suwargadi, B. W., Barton, P., Henstock, T., & Ryberg, T. (2010). The fine structure of the subducted investigator fracture zone in western sumatra as seen by local seismicity. *Earth and Planetary Science Letters*, *298*(1-2), 47–56, `https://doi.org/10.1016/j.epsl.2010.07.020`.

Lay, T., Kanamori, H., Ammon, C. J., Koper, K. D., Hutko, A. R., Ye, L., Yue, H., & Rushing, T. M. (2012). Depth-varying rupture properties of subduction zone megathrust faults. *Journal of Geophysical Research: Solid Earth*, *117*(B04311), `https://doi.org/10.1029/2011jb009133`.

Lieser, K., Grevemeyer, I., Lange, D., Flueh, E., Tilmann, F., & Contreras-Reyes, E. (2014). Splay fault activity revealed by aftershocks of the 2010 mw 8.8 maule earthquake, central chile. *Geology*, *42*(9), 823–826, `https://doi.org/10.1130/g35848.1`.

Linde, A. T., Gladwin, M. T., Johnston, M. J. S., Gwyther, R. L., & Bilham, R. G. (1996). A slow earthquake sequence on the san andreas fault. *Nature*, *383*(6595), 65–68, `https://doi.org/10.1038/383065a0`.

Louderback, G. D. (1942). Faults and earthquakes. *Bulletin of the Seismological Society of America*, *32*(4), 305–330, `https://doi.org/10.1785/bssa0320040305`.

Loveless, J. P. & Meade, B. J. (2011). Spatial correlation of interseismic coupling and coseismic rupture extent of the 2011 mw= 9.0 tohoku-oki earthquake. *Geophysical Research Letters*, *38*(17), `https://doi.org/10.1029/2011gl048561`.

Mallick, R., Meltzner, A. J., Tsang, L. L. H., Lindsey, E. O., Feng, L., & Hill, E. M. (2021). Long-lived shallow slow-slip events on the sunda megathrust. *Nature Geoscience*, `https://doi.org/10.1038/s41561-021-00727-y`.

Moore, J. C. & Saffer, D. (2001). Updip limit of the seismogenic zone beneath the accretionary prism of southwest japan: An effect of diagenetic to low-grade metamorphic processes and increasing effective stress. *Geology*, *29*(2), `https://doi.org/10.1130/0091-7613(2001)029<0183:Ulotsz>2.0.Co;2`.

Métois, M., Socquet, A., Vigny, C., Carrizo, D., Peyrat, S., Delorme, A., Maureira, E., Valderas-Bermejo, M. C., & Ortega, I. (2013). Revisiting the north chile seismic gap segmentation using gps-derived interseismic coupling. *Geophysical Journal International*, *194*(3), 1283–1294, `https://doi.org/10.1093/gji/ggt183`.

Nadeau, R. M. & Johnson, L. R. (1998). Seismological studies at parkfield vi: Moment release rates and estimates of source parameters for small repeating earthquakes. *Bulletin of the Seismological Society of America*, *88*(3), 790–814.

Nadeau, R. M. & McEvilly, T. V. (1999). Fault slip rates at depth from recurrence intervals of repeating microearthquakes. *Science*, *285*(5428), 718–21, `https://doi.org/10.1126/science.285.5428.718`.

Newman, A. V., Hayes, G., Wei, Y., & Convers, J. (2011). The 25 october 2010 mentawai tsunami earthquake, from real-time discriminants, finite-fault rupture, and tsunami excitation. *Geophysical Research Letters*, *38*(5), `https://doi.org/10.1029/2010gl046498`.

Obara, K. (2002). Nonvolcanic deep tremor associated with subduction in southwest japan. *Science*, *296*(5573), 1679–81, `https://doi.org/10.1126/science.1070378`.

Obara, K. & Ito, Y. (2005). Very low frequency earthquakes excited by the 2004 off the kii peninsula earthquakes: A dynamic deformation process in the large accretionary prism. *Earth, Planets and Space*, *57*(4), 321–326, `https://doi.org/10.1186/bf03352570`.

Oleskevich, D. A., Hyndman, R. D., & Wang, K. (1999). The updip and downdip limits to great subduction earthquakes: Thermal and structural models of cascadia, south alaska, sw japan, and chile. *Journal of Geophysical Research: Solid Earth*, *104*(B7), 14965–14991, `https://doi.org/10.1029/1999jb900060`.

Pacheco, J. F. & Sykes, L. R. (1992). Seismic moment catalog of large shallow earthquakes, 1900 to 1989. *Bulletin of the Seismological Society of America*, *82*(3), 1306–1349.

Pacheco, J. F., Sykes, L. R., & Scholz, C. H. (1993). Nature of seismic coupling along simple plate boundaries of the subduction type. *Journal of Geophysical Research: Solid Earth*, *98*(B8), 14133–14159, `https://doi.org/10.1029/93jb00349`.

Peng, Z. (2005). Systematic variations in recurrence interval and moment of repeating aftershocks. *Geophysical Research Letters*, *32*(15), `https://doi.org/10.1029/2005gl022626`.

Peng, Z. & Gomberg, J. (2010). An integrated perspective of the continuum between earthquakes and slow-slip phenomena. *Nature Geoscience*, *3*(9), 599–607, `https://doi.org/10.1038/ngeo940`.

Petersen, F., Kopp, H., Lange, D., Hannemann, K., & Urlaub, M. (2019). Measuring tectonic seafloor deformation and strain-build up with acoustic direct-path ranging. *Journal of Geodynamics*, *124*, 14–24, `https://doi.org/10.1016/j.jog.2019.01.002`.

Petersen, F., Lange, D., Ma, B., Grevemeyer, I., Geersen, J., Klaeschen, D., Contreras-Reyes, E., Barrientos, S., Tréhu, A. M., Vera, E., & Kopp, H. (2021). Relationship between subduction erosion and the up-dip limit of the 2014 mw 8.1 iquique earthquake. *Geophysical Research Letters*, *48, e2020GL092207*(9), `https://doi.org/10.1029/2020GL092207`.

Roland, E. & McGuire, J. J. (2009). Earthquake swarms on transform faults. *Geophysical Journal International*, *178*(3), 1677–1690, `https://doi.org/10.1111/j.1365-246X.2009.04214.x`.

Ruina, A. (1983). Slip instability and state variable friction laws. *Journal of Geophysical Research: Solid Earth*, *88*(B12), 10359–10370, `https://doi.org/10.1029/JB088iB12p10359`.

Satake, K. (1994). Mechanism of the 1992 nicaragua tsunami earthquake. *Geophysical Research Letters*, *21*(23), 2519–2522, `https://doi.org/10.1029/94gl02338`.

Schmidt, D. A., Burgmann, R., Nadeau, R. M., & d'Alessio, M. (2005). Distribution of aseismic slip rate on the hayward fault inferred from seismic and geodetic data. *Journal of Geophysical Research-Solid Earth*, *110*(B8), `https://doi.org/10.1029/2004jb003397`.

Scholz, C. H. (1998). Earthquakes and friction laws. *Nature*, *391*, 37–42, `https://doi.org/10.1038/34097`.

Schwartz, S. Y. & Rokosky, J. M. (2007). Slow slip events and seismic tremor at circum-pacific subduction zones. *Reviews of Geophysics*, *45*(3), `https://doi.org/10.1029/2006rg000208`.

Shelly, D. R., Beroza, G. C., Ide, S., & Nakamula, S. (2006). Low-frequency earthquakes in shikoku, japan, and their relationship to episodic tremor and slip. *Nature*, *442*(7099), 188–91, `https://doi.org/10.1038/nature04931`.

Song, T. R., Helmberger, D. V., Brudzinski, M. R., Clayton, R. W., Davis, P., Perez-Campos, X., & Singh, S. K. (2009). Subducting slab ultra-slow velocity layer coincident with silent earthquakes in southern mexico. *Science*, *324*(5926), 502–6, `https://doi.org/10.1126/science.1167595`.

Steinbrugge, K. V., Zacher, E. G., Tocher, D., Whitten, C. A., & Claire, C. N. (1960). Creep on the san andreas fault. *Bulletin of the Seismological Society of America*, *50*(3), 389–415.

Tichelaar, B. W. & Ruff, L. J. (1993). Depth of seismic coupling along subduction zones. *Journal of Geophysical Research: Solid Earth*, *98*(B2), 2017–2037, `https://doi.org/10.1029/92jb02045`.

Tilmann, F. J., Craig, T. J., Grevemeyer, I., Suwargadi, B., Kopp, H., & Flueh, E. (2010). The updip seismic/aseismic transition of the sumatra megathrust illuminated by aftershocks of the 2004 aceh-andaman and 2005 nias events. *Geophysical Journal International*, `https://doi.org/10.1111/j.1365-246X.2010.04597.x`.

Turner, R. C., Shirzaei, M., Nadeau, R. M., & Bürgmann, R. (2015). Slow and go: Pulsing slip rates on the creeping section of the san andreas fault. *Journal of Geophysical Research: Solid Earth*, *120*(8), 5940–5951, `https://doi.org/10.1002/2015jb011998`.

Uchida, N. & Bürgmann, R. (2019). Repeating earthquakes. *Annual Review of Earth and Planetary Sciences*, *47*(1), 305–332, `https://doi.org/10.1146/annurev-earth-053018-060119`.

Uchida, N. & Matsuzawa, T. (2013). Pre- and postseismic slow slip surrounding the 2011 tohoku-oki earthquake rupture. *Earth and Planetary Science Letters*, *374*, 81–91, `https://doi.org/10.1016/j.epsl.2013.05.021`.

Urlaub, M., Petersen, F., Gross, F., Bonforte, A., Puglisi, G., Guglielmino, F., Krastel, S., Lange, D., & Kopp, H. (2018). Gravitational collapse of mount etna's southeastern flank. *Sci Adv*, *4*(10), eaat9700, `https://doi.org/10.1126/sciadv.aat9700`.

Valoroso, L., Chiaraluce, L., Di Stefano, R., & Monachesi, G. (2017). Mixed-mode slip behavior of the altotiberina low-angle normal fault system (northern apennines, italy) through high-resolution earthquake locations and repeating events. *Journal of Geophysical Research: Solid Earth*, *122*(12), 10,220–10,240, `https://doi.org/10.1002/2017jb014607`.

Vannucchi, P., Remitti, F., & Bettelli, G. (2008). Geological record of fluid flow and seismogenesis along an erosive subducting plate boundary. *Nature*, *451*(7179), 699–703, `https://doi.org/10.1038/nature06486`.

Victor, P., Oncken, O., Sobiesiak, M., Kemter, M., Gonzalez, G., & Ziegenhagen, T. (2018). Dynamic triggering of shallow slip on forearc faults constrained by monitoring surface displacement with the ipoc creepmeter array. *Earth and Planetary Science Letters*, *502*, 57–73, `https://doi.org/10.1016/j.epsl.2018.08.046`.

Vuan, A., Sugan, M., Chiaraluce, L., & Di Stefano, R. (2017). Loading rate variations along a midcrustal shear zone preceding the mw 6.0 earthquake of 24 august 2016 in central italy. *Geophysical Research Letters*, *44*(24), `https://doi.org/10.1002/2017gl076223`.

Wallace, L. M. (2020). Slow slip events in new zealand. *Annual Review of Earth and Planetary Sciences*, *48*(1), 175–203, `https://doi.org/10.1146/annurev-earth-071719-055104`.

Wallace, L. M., Webb, S. C., Ito, Y., Mochizuki, K., Hino, R., Henrys, S., Schwartz, S. Y., & Sheehan, A. F. (2016). Slow slip near the trench at the hikurangi subduction zone, new zealand. *Science*, *352*(6286), 701–4, `https://doi.org/10.1126/science.aaf2349`.

Wang, K. & Bilek, S. L. (2014). Invited review paper: Fault creep caused by subduction of rough seafloor relief. *Tectonophysics*, *610*, 1–24, `https://doi.org/10.1016/j.tecto.2013.11.024`.

Wang, K. & Dixon, T. (2004). "coupling" semantics and science in earthquake research. *Eos, Transactions American Geophysical Union*, *85*(18), 180–180, `https://doi.org/10.1029/2004EO180005`.

Wang, K. & Hu, Y. (2006). Accretionary prisms in subduction earthquake cycles: The theory of dynamic coulomb wedge. *Journal of Geophysical Research: Solid Earth*, *111*(B6), `https://doi.org/10.1029/2005jb004094`.

Wiens, D. A., Anandakrishnan, S., Winberry, J. P., & King, M. A. (2008). Simultaneous teleseismic and geodetic observations of the stick-slip motion of an antarctic ice stream. *Nature*, *453*(7196), 770–4, `https://doi.org/10.1038/nature06990`.

Yamamoto, R., Kido, M., Ohta, Y., Takahashi, N., Yamamoto, Y., Pinar, A., Kalafat, D., Özener, H., & Kaneda, Y. (2019). Seafloor geodesy revealed partial creep of the north anatolian fault submerged in the sea of marmara. *Geophysical Research Letters*, *46*(3), 1268–1275, `https://doi.org/10.1029/2018gl080984`.

Yamamoto, Y., Takahashi, N., Pinar, A., Kalafat, D., Citak, S., Comoglu, M., Polat, R., & Kaneda, Y. (2017). Geometry and segmentation of the north anatolian fault beneath the marmara sea, turkey, deduced from long-term ocean bottom seismographic observations. *Journal of Geophysical Research: Solid Earth*, *122*(3), 2069–2084, `https://doi.org/10.1002/2016jb013608`.

Yokota, Y. & Ishikawa, T. (2020). Shallow slow slip events along the nankai trough detected by gnss-a. *Sci Adv*, *6*(3), eaay5786, `https://doi.org/10.1126/sciadv.aay5786`.

3 Relationship between subduction erosion and the up-dip limit of the 2014 Mw 8.1 Iquique earthquake

Florian Petersen[1], Dietrich Lange[1], Bo Ma[1], Ingo Grevemeyer[1], Jacob Geersen[2], Dirk Klaeschen[2], Eduardo Contreras-Reyes[3], Sergio Barrientos[4], Anne M. Tréhu[5], Emilio Vera[3] and Heidrun Kopp[1,2]

1) GEOMAR Helmholtz Centre for Ocean Research Kiel, Kiel, Germany.
2) Institute of Geosciences, Kiel University, Kiel, Germany.
3) Departamento de Geofísica, Facultad de Ciencias Físicas y Matemáticas, Universidad de Chile, Santiago, Chile.
4) Centro Sismológico Nacional, Facultad de Ciencias Físicas y Matemáticas, Universidad de Chile, Santiago, Chile.
5) Oregon State University, College of Earth, Ocean, and Atmospheric Sciences, Corvallis, USA

Published in **Geophysical Research Letters**, May 2021.

DOI: 10.1029/2020GL092207

Key Points

- We investigate structure and seismicity at the up-dip end of the 2014 Iquique earthquake rupture using amphibious seismic data.
- Seismicity up-dip of the 2014 Iquique earthquake occurs over a broad range likely interpreted to be related to the basal erosion processes.
- Coseismic stress changes and aftershocks activate extensional faulting of the upper plate and subduction erosion.

Abstract

The aftershock distribution of the 2014 M_w 8.1 Iquique earthquake offshore northern Chile, identified from a long-term deployment of ocean bottom seismometers installed eight months after the mainshock, in conjunction with seismic reflection imaging, provides insights into the processes regulating the up-dip limit of coseismic rupture propagation. Aftershocks up-dip of the mainshock hypocenter frequently occur in the upper plate and are associated with normal faults identified from seismic reflection data. We propose that aftershock seismicity near the plate boundary documents subduction erosion that removes mass from the base of the wedge and results in normal faulting in the upper plate. The combination of very little or no sediment accretion and subduction erosion over millions of years has resulted in a very weak and aseismic frontal wedge. Our observations thus link the shallow subduction zone seismicity to subduction erosion processes that control the evolution of the overriding plate.

Plain Language Summary

To better understand the controls on shallow seismicity and subduction erosion following large subduction earthquakes, we use marine recordings of the M_w 8.1 2014 Iquique earthquake aftershocks and long-offset multi-channel seismic data. By comparing the aftershock locations and seismic imaging, we observe that most aftershocks occurred in the upper continental plate and abruptly stopped in the frontal forearc. The amplitude characteristics of upper-crust reflections indicate a fractured and fluid-filled outer forearc, which is associated with the absence of aftershocks. Large-scale faulting, as evidenced by disrupted reflections in the seismic image, can be correlated to upper plate seismicity. We propose that the aftershocks up-dip of the main earthquake area reflect active subduction erosion processes.

3.1 Introduction

The largest earthquakes on the globe occur along convergent plate margins, rupturing the boundary between upper overriding and lower subducting plates. For most subduction zones, the precise location of the far offshore located up-dip limit of coseismic slip and its controlling parameters remain poorly resolved, despite being of fundamental importance for earthquake hazard assessment. Controls on the up-dip limit were suggested to be related to forearc structure and morphology (Wang and Hu, 2006; Tilmann et al., 2010), metamorphic processes (Moore and Saffer, 2001), or thermal properties (Oleskevich et al., 1999; Moore and Saffer, 2001). Earthquake ruptures that extend into the shallow frontal subduction domain cause larger seafloor displacement and hence trigger potentially large tsunamis as evidenced by a historical slip-to-trench megathrust event offshore Costa Rica (Vannucchi et al., 2017) or exemplified by the 2011 M_w 9.0 Tohoku-Oki earthquake and associated tsunami (Simons et al., 2011; Kodaira et al., 2012). Knowledge of the seismogenic up-dip limit and its controlling factors are thus essential for assessing subduction zone hazards. Material transfer at subduction zones is primarily governed by either frontal or basal accretion of oceanic sediments or by tectonic erosion at the front and base of the upper plate (hereafter referred to as subduction erosion).

A slight majority of subduction zones worldwide are of erosive nature (Scholl and von Huene, 2007; Straub et al., 2020). It has been suggested that subduction erosion and the occurrence of seismicity along subduction zone megathrusts and in the upper overriding plates are inherently related (Wang et al., 2010). Long-term permanent subsidence of the forearc (von Huene and Lallemand, 1990) and the landward migration of the trench and the volcanic arc (Rutland, 1971) have been linked to subduction erosion (Clift and Vannucchi, 2004). Two modes of subduction erosion have been identified: (1) frontal erosion as commonly caused by the underthrusting of rough seafloor topography, like bending related horst-and-grabens or seamounts colliding with the lower slope (Ranero and von Huene, 2000; Sallarès and Ranero, 2005) and (2) basal erosion by the continuous removal of material from the base of the overriding plate (von Huene et al., 2004). The latter directly impacts the structural development of the plate boundary and might be essential to understand the up-dip limit of seismic rupture during megathrust earthquakes and the onset of seismicity at the seismogenic up-dip end (Byrne et al., 1988; Wang et al., 2010). The offshore location of the shallow subduction interface complicates the recording of earthquake-related processes by geophysical data, causing a gap in our understanding of the structural configuration of the plate boundary, overriding plate and subducting plate. Hence, the slip-rate deficit (kinematic coupling ratio) and the detailed seismicity are not accurately resolved during the seismic cycle. However, the extent and termination of coseismic slip are frequently revealed through the spatial distribution of seismicity after the mainshock, (Mendoza and Hartzell, 1988), therefore, the postseismic period offers the opportunity to study postseismic processes (Husen et al., 1999; Tilmann et al., 2010).

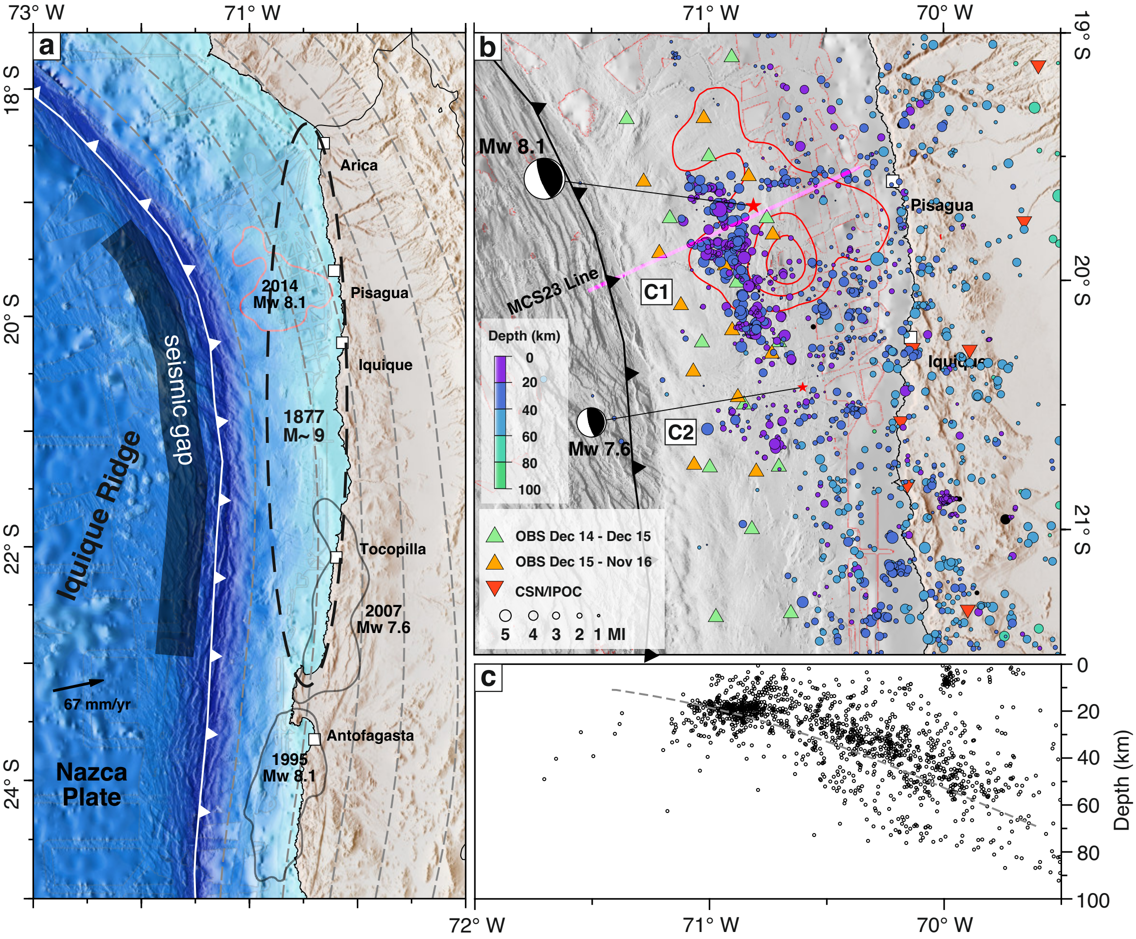

Figure 3.1: (a) Map of historical earthquakes along northern Chile. The 2014 Iquique earthquake is sketched in red by the 2 m slip contour line Duputel et al. (2015). The 1877 M ~9 North Chilean earthquake is displayed as an dashed ellipse (Comte and Pardo, 1991), the rupture area of the M8.1 1995 Antofagasta (Chlieh et al., 2004) and the 2007 M7.7 Tocopilla earthquake (Schurr et al., 2012) are outlined by 0.5 m slip contours. Depths of the plate interface (Slab2; Hayes et al., 2018) are shown with dashed gray lines and 20 km depth intervals. Plate convergence rate is shown as a black arrow (Angermann et al., 1999). Bathymetry from Geersen et al. (2018a) combined with GEBCO, SRTM Topography from Farr et al. (2007). (b) Map of the aftershock hypocenter distribution (1,471 events) of the M_w 8.1 2014 Iquique earthquake from 9th December, 2014, until 31^{st} October 2016, recorded by Ocean Bottom Seismometers (OBS) and land stations from the CSN and IPOC networks. C1 marks the up-dip cluster of the aftershock seismicity and C2 the up-dip cluster of seismicity following the greatest aftershock with M_w 7.6. The green line indicates the MC23 profile (Tréhu et al., 2017) shown in Figure 3.2a. gCMT solutions indicate the M_w 8.1 2014 Iquique mainshock and the largest M7.6 aftershock. (c) Seismicity cross section of depth versus latitude.

The South American subduction zone off the coast of northern Chile is a convergent margin dominated by subduction erosion since Mesozoic times (Rutland, 1971; von Huene and Scholl, 1991). This is manifested in the landward migration of the volcanic arc and pervasive extensional faulting of the terrestrial (Armijo and Thiele, 1990; Allmendinger and González, 2010) and marine forearc (von Huene et al., 1999; von Huene and Ranero, 2003; Geersen et al., 2018b). Further, erosional systems are characterized by the sediment-starved trenches, lacking accretionary prisms and vast amount of trench sediments (Clift and Vannucchi, 2004; Geersen et al., 2018a). The 2014 Iquique earthquake on 1st April broke a central segment between 19 °S and 21 °S of the north Chilean seismic gap, which previously ruptured in 1877 during a M~9 earthquake (Figure 3.1; Comte and Pardo, 1991). A long precursory phase preceded the 2014 mainshock (e.g., Bedford et al., 2015) and devolved into an intense foreshock series before the 2014 Iquique mainshock (Brodsky and Lay, 2014; Schurr et al., 2014; Yagi et al., 2014; Cesca et al., 2016; Herman et al., 2016; León-Ríos et al., 2016). The 2014 Iquique earthquake did not result in enough shallow rupture to trigger a significant tsunami in the Pacific Ocean (An et al., 2014; Lay et al., 2014).

To study the processes that govern the up-dip limit of seismic rupture in the northern Chilean subduction zone, we combine data from amphibious seismic observations from the postseismic phase of the 2014 Iquique earthquake with multi-channel seismic reflection data of the marine forearc acquired in 2016. We suggest that the up-dip limit of the 2014 Iquique earthquake activates subduction erosion at the up-dip limit of the seismogenic zone during the postseismic and possibly the coseismic phase, which leads to extensive faulting of the upper plate, thereby manifesting the location of the up-dip limit over many earthquake cycles.

3.2 Data and Methods

We installed two temporary passive seismic networks on the marine forearc. The first deployment was an array of 15 short period ocean bottom seismometers (OBS) eight months after the 1st April 2014 Iquique mainshock, using the Chilean Navy vessel *OVP Toro*. After one year, the seismic network was recovered and 14 OBS were redeployed during *R/V SONNE* cruise SO244/2 in December 2015 and subsequently with a denser station distribution to focus on the up-dip aftershock distribution (Figure 3.1)Furthermore, we used waveform data of the permanent seismic network of the Centro Seismológico Nacional (CSN, `www.sismologia.cl`) and the Integrated Plate Boundary Observatory Chile (IPOC, `www.ipoc-network.org`).

Earthquakes were detected with the scanloc module of SeisComP3 (GFZ and gempa GmbH, 2008) using a cluster search algorithm to associate phase detections to one or many potential earthquake sources. Source scanning was done with the local 1-D velocity model from Husen et al. (1999). Next, P-phases (Aldersons, 2004; Lange et al., 2012) and S-phases were picked automatically (Diehl et al., 2009), however, automated phase picking on OBS data proved to be unsatisfactory on small magnitude events due to the elevated noise level on some waveform data. Therefore, we manually revised the P- and S-phase onsets of all offshore events.

We calculated a minimum 1D velocity model (Kissling et al., 1995; Husen et al., 1999) and a local 2D earthquake tomography for vp and vs across the South American margin at 20 °S from 71.5 °W to 69.4 °W using SIMUL2000 (Thurber, 1983, 1992). Subsequently, we estimated absolute locations based on the 2D velocity model with NonLinLoc (Lomax et al., 2000). The velocity model used was constructed from the 2D model transposing it across the whole study region by following the geometry of the trench. Relative hypocenter locations were estimated using a double-difference location scheme (Waldhuser and Ellsworth, 2000). After the final relocation, seismicity in the up-dip area forms distinct clusters compared to previous processing steps.

Finally, we calculated moment magnitudes (Ottemoller and Havskov, 2003) and local magnitudes (Hutton and Boore, 1987), followed by the calculation of focal mechanisms for 98 stronger events (Reasenberg et al., 1985). We used focal mechanisms from the Global Centroid Moment Tensor catalog (Dziewonski et al., 1981; Ekström et al., 2012) for the largest events as those overloaded our data loggers, in turn, causing problems in identifying first motion polarities. Additional details on the seismological data processing are given in the supporting information and Figures 3.4 - 3.15.

To provide additional structural context for the seismicity analysis, we use a multi-channel reflection seismic (MCS) line MC23 acquired during the *R/V Marcus Langseth* cruise MGL1610 in November 2016 (Tréhu et al., 2017). The along-dip MCS profile is processed up to pre-stack depth migration (Ma et al., 2020) and images the structure around the Iquique mainshock down to 35 km depth (Figure 3.2a). The MCS data were collected with an 8-km long, 640 channel streamer and 6600 cubic inch airgun array and resolve the plate boundary and the internal structure of the marine forearc in greater detail and to a greater depth than available from previous seismic reflection studies of the northern Chilean margin (Coulbourn and Moberly, 1977; Moberly et al., 1982; von Huene et al., 1999; von Huene and Ranero, 2003; Geersen et al., 2015).

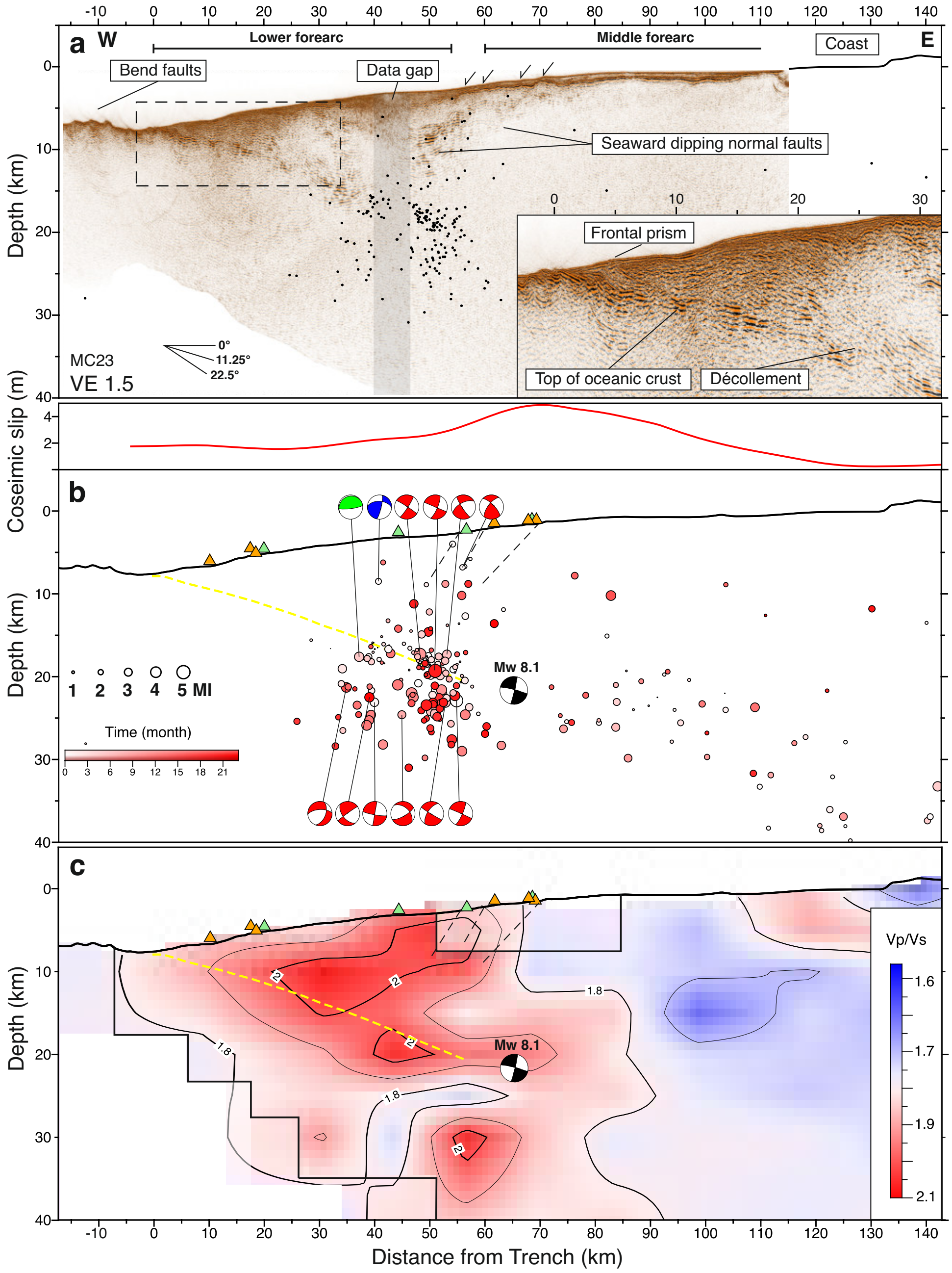

Figure 3.2: Seismogenic up-dip limit crossing profile illustrated by different datasets. Subplots A - C showing the same seismicity MCS profile of Figure 3.1. (a) Pre-stack depth migrated multi-channel seismic reflection line MC23. (b) coseismic slip from Duputel et al. (2015) above the aftershock distribution (287 events) using a 15 km swath on each side of the seismic profile. The aftershocks are colored according to the time scale from 9th December until the end of the operation in October 2016. Focal mechanisms from FPFIT and gCMT are classified by faulting type in thrust (red), normal (green), strike-slip (yellow), or oblique (blue) fault mechanism. OBS station locations are marked as green and orange triangles. The M_w 8.1 Iquique mainshock hypocenter is indicated by the black focal mechanism. (c) Projection of vp/vs ratio from 2D local earthquake tomography to the MCS profile of panel a using the hypocenters from panel b. Black solid line indicates the region of good resolution.

3.3 Results

3.3.1 Aftershock distribution in the marine forearc

Our final seismicity catalog spans 23 months and starts eight months after the mainshock occurred (Figure 3.1). Since we focus on the marine forearc, our local seismic catalog covers the region between 72 ° W and 69.5 °W in longitude and between 22 °S and 19 °S in latitude, comprising 1,778 local earthquakes (Figure 3.4). Aftershocks outside this region and deeper than 40 km will be excluded from the following discussion. Generally, the majority of hypocenters are widely distributed, occurring along the plate interface, in the subducting slab, and the overriding plate (Figure 3.2). However, a significant number of events with higher magnitudes occurred up-dip of the mainshock and the largest aftershock. These occurred in two major clusters, marked as C1 and C2 in Figure 3.1, which are separated by a zone of low aftershock activity. C1 forms an NNW-SSE trending band, whereas C2 trends west to east, forming a less focused cluster of smaller magnitude earthquakes. Similar elevated aftershock seismicity up-dip of the mainshock area has been reported for other subduction zones (e.g., Tilmann et al., 2010) and has elsewhere been correlated to changes in the slope or subducting plate topography interacting with the upper plate (Wang and Bilek, 2014). The elevated Iquique aftershock activity in the shallow marine forearc was previously described in studies using land stations only (León-Ríos et al., 2016; Soto et al., 2019; Schurr et al., 2020; Sippl et al., 2018). However, the seismicity of the marine forearc occurs far outside the land network, resulting in increased uncertainties and a systematic bias in hypocenters for offshore earthquakes. We compare our seismicity with the catalog from Soto et al. (2019). Both catalogs have 23 days and 425 events in common. Soto et al. (2019) observe several west-east striking seismicity streaks interpreted as markers of surrounding aseismic creep along the plate interface. We do not observe the east-west striking seismicity clusters, and offshore our events tend to be located in the continental crust. In general, the horizontal location discrepancies increase with increasing distance from the coast and are largest at the seismogenic up-dip limit, where the OBS are located (see Figure 3.11; Soto et al., 2019, Figure 3.5). We explain the difference between the catalogs by the much better coverage of the forearc seismicity with the OBS stations. Furthermore, we use a more accurate 2D velocity model derived from the offshore seismicity

The depth uncertainties, estimated by absolute locations, of events in C1, on which the following discussion focusses, shows a range between 0.5 km and 2 km (Figure 3.6) and thus indicates to be a smaller depth error compared to previous seismicity studies offshore Iquique (Sippl et al., 2018; Soto et al., 2019). The observed seismicity in the forearc cross-section of Figure 3.2 will be described from west to east following the subduction direction. Beneath the outer rise, westward of the trench, no significant seismic activity was detected during the 23 months of OBS recording. Elsewhere outer rise aftershock seismicity has been correlated to slip during large earthquakes that extend to the trench (Sladen and Trevisan, 2018). East of the trench, a ~35 km wide zone with very sparse seismicity is observed. Further East of the observed aseismic zone (>35 km), a large number of events are located within 5 km distance of the plate boundary, that is derived from the multi-channel seismic data. Below the plate interface, seismicity occurred between 20 and 30 km depth, indicating earthquakes are located in the lower plate. Above the plate interface, several earthquakes occurred in the upper plate during the entire observations period. The local earthquake tomography (LET) reveals an elevated vp/vs ratio in the upper crust that decreases towards the inner forearc (Figure 3.2 and Figure 3.8). East of the mainshock, the aftershocks are diffusely distributed in the upper crust with local magnitudes mostly lower than 3. The vast majority of focal mechanisms at the seismogenic up-dip end indicate thrust faulting with one focal plane oriented subparallel to slab dip (Figure 3.13).

3.3.2 Marine forearc structure and active tectonics in the 2014 Iquique earthquake region

The multi-channel seismic profile MC23 crosses the epicentral region of the 2014 Iquique earthquake (Figure 3.1) and images the structure of the incoming and subducting oceanic plate and the marine forearc (Figure 3.2). On the incoming plate, the crust of the oceanic Nazca Plate is repeatedly offset by up to 500 m along bending related landward and seaward dipping normal faults (Geersen et al., 2018a). The trench is characterized by less than 500 m of sediment cover. Landward of the trench, a series of shallow, landward-dipping reflections indicates a ca. 7 km wide frontal prism (Figure 3.2). Below the frontal prism, the top of the subducting oceanic basement has a landward dip of ~12°. The high reflectivity of the oceanic basement under the marine forearc can be observed down to depths of ~17 km at 35 km from the trench, where aftershock seismicity commences. Between 50 and 70 km from the trench, a series of pronounced seaward dipping normal faults cut from the seafloor into the framework rock of the upper plate (dashed lines; Figure 3.2b). Their locations correlate to some of the aftershock hypocenters in the upper plate (also compare Reginato et al., 2020).

3.4 Discussion

The combined analysis of the 2014 Iquique aftershocks and the seismic reflection image of the marine forearc within the rupture area offers the possibility to link short term deformation associated with a single seismic cycle to the permanent deformation history of an erosive convergent margin. Previous studies of the marine forearc structure of the

2014 Iquique earthquake related the up-dip aftershock seismicity to postseismic processes, including postseismic relaxation or afterslip (Cesca et al., 2016; León-Ríos et al., 2016; Soto et al., 2019). In contrast to Soto et al. (2019), our aftershock catalog, which is based on 23 months of amphibious and deep crustal MCS data, does not resolve any E-W elongated streaks of seismicity. Instead, we find a broad band of seismicity with individual earthquake clusters up-dip of the coseismic rupture in the upper and lower plate, besides the plate interface related seismicity. Similar lower plate aftershocks related to the up-dip limit were observed in Costa Rica (Bilek and Lithgow-Bertelloni, 2005) and Japan (Obana et al., 2013). Obana et al. (2013) related oceanic upper crustal events to bending of the incoming plate since they observed normal faulting events in the oceanic plate. Since we observe few thrust mechanisms at the Iquique up-dip limit and below the plate interface (in the oceanic plate) this might be similar to thrust faulting in the downgoing plate as observed by Nippress and Rietbrock (2007) after the 1995 Antofagasta earthquake (Figure 3.1). The thrust faulting in the oceanic crust and mantle was suggested to be associated with the re-activation of horst and graben structures from the plate bending at the outer rise bend (Nippress and Rietbrock, 2007). Above the lower plate seismicity, we document an up-dip limit of aftershock seismicity that is correlated with crustal reflectivity (Figure 3.1 and Figure 3.2), indicative of long-term along-dip seismo-tectonic segmentation of the subduction zone.

If the up-dip limit of plate-boundary seismicity is stable in space over many earthquake cycles, it can induce permanent forearc deformation expressed in first-order topographic changes (Rosenau and Oncken, 2009). Indeed, at other subduction zones, similar intense up-dip clusters of seismicity often correlate with structural or topographic changes of the forearc (Lange et al., 2007; Tilmann et al., 2010; Lieser et al., 2014; Tréhu et al., 2019). Furthermore, such up-dip seismicity occurs predominantly along the plate boundary. The aftershocks associated with the 2014 Iquique earthquake in northern Chile show a very different pattern. Most aftershocks occur in a narrow band roughly up-dip of the main coseismic rupture (upper panel in Figure 3.2b), implying postseismic deformation at the seismic-to-aseismic transition. These aftershocks are, however, not associated with a structural or topographic change of the forearc (Figure 3.2). They are further not limited to the megathrust fault but also occur in the upper overriding and lower subducting plates (Figure 3.2b).

We interpret the striking aftershock sequence at the up-dip limit of seismic rupture following the 2014 Iquique earthquake as an indication of active subduction erosion during the coseismic and early postseismic phase. From fossil subduction zones, we have learned that a wide shear zone, as exemplified by the different depths of the 2014 Iquique aftershocks, is characteristic for margins dominated by subduction erosion (Vannucchi et al., 2008). In the concept of subduction erosion, fracturing at the base of the upper plate starts at the up-dip limit of the seismogenic zone and increases towards the shallow plate interface up to the frontal prism (von Huene et al., 2004). This basal erosion induced by the 2014 Iquique earthquake is indicated by the high number of aftershocks that occur at or slightly above the plate boundary (Figure 3.2b). Such abrasion of material from the underside of the upper plate is expected to be in a dynamic equilibrium between the removal of material and steepening of forearc slope (von Huene et al., 2004). The associated deformation of the entire upper plate is illustrated by the overall fewer but still significant number of aftershocks above the up-dip limit of seismic rupture (Figure 3.2b). These aftershocks seem to occur along seaward dipping planes that match the location of seismically imaged normal faults within the upper plate (Figure 3.2a). This implies that the faults have moved in the postseismic phase of the 2014 Iquique earthquake. Although the absolute depths of the normal faults are not fully resolved by the seismic data, data from other erosive convergent margins suggest that they may cut to the plate boundary (Ranero et al., 2008; Kodaira et al., 2012; Contreras-Reyes et al., 2015).

While the aftershocks of the 2014 Iquique earthquake represent forearc deformation during the early postseismic phase of one earthquake, the seismically imaged structure of the marine forearc is a result of forearc deformation from hundreds to thousands of seismic cycles (Scholz, 1998). Repeated coseismic and postseismic deformation and associated subduction erosion force extensive faulting and pervasive fracturing at the up-dip limit of seismic rupture. Deformation is not limited to the plate boundary but active throughout the entire upper plate from the plate boundary to the seafloor (compare Geersen et al., 2018a). This is consistent with earlier studies based on numerical and analog modeling and conceptional considerations on the relationship between long-term forearc deformation of the overriding plate and earthquake behavior of subduction zone forearcs (Wang and Hu, 2006; Rosenau and Oncken, 2009). Northern Chile is an end-member margin in terms of trench sediment thickness, and subduction erosion is likely the dominant tectonic mode since at least Mesozoic times (Rutland, 1971). This is manifested in about 250 km loss of overriding continental plate since 150 Ma (Scheuber and Reutter, 1992) and associated eastward migration of the trench and volcanic arc. Over time, tectonic erosion of the upper plate (von Huene and Ranero, 2003) causes the up-dip limit to migrate landwards, mimicking the migration of the volcanic arc and the trench.

In the Iquique region of the 2014 Iquique earthquake, long-term upper plate faulting and fracturing at the up-dip limit of the seismogenic zone are manifested in the permanent deformation pattern of the marine forearc seaward of the 2014 Iquique aftershocks. This part of the marine forearc between the trench and the current up-dip limit (40 km distance) has migrated through the up-dip limit over the last millions of years. It is heavily faulted as indicated by discontinuous seismic reflections. The overall high reflection amplitudes in this region further support a high degree of fracturing and possibly fluids within the fractures.

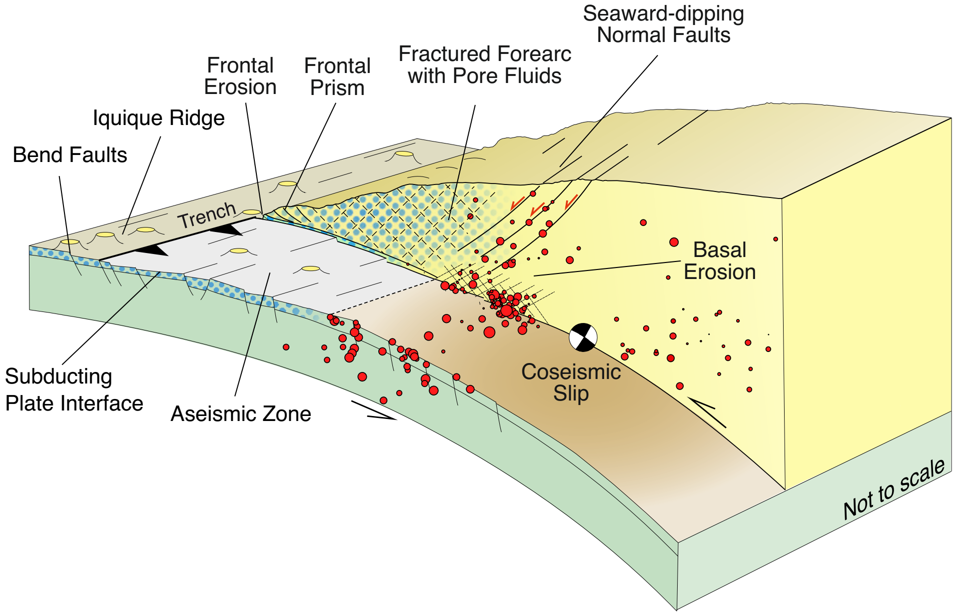

Figure 3.3: Conceptional model of seismotectonic segmentation and basal erosion of the North Chilean margin offshore Iquique. Pore-fluid extent marks the region of increased vp/vs ratio.

The elevated vp/vs ratio in the upper plate recognized from local earthquake tomography (Figure 3.2c) further supports the presence of fluids in the highly fractured outermost marine forearc (Popp and Kern, 1994; Wang et al., 2012). The fractured and fluid-rich outermost marine forearc, seaward of the 2014 Iquique earthquake rupture is likely too weak (and heavily deformed) to store sufficient elastic energy to nucleate a great earthquake. Further down-dip, the decrease in faulting and fluid content in the marine forearc, together with the onset of aftershock seismicity, indicates an increase in strength of the overriding plate that allows the storing of elastic energy (Figure 3.3). A similar down-dip segmentation of the North Chilean forearc that can build up elastic energy and rupture during great earthquakes has been previously suggested based on gravity data and seismic velocity structure (Sallarès and Ranero, 2005; Contreras-Reyes et al., 2012; Maksymowicz et al., 2018). The segmentation is in-line with our amphibious aftershock observation of the 2014 Iquique earthquake rupture. It is further supported by the decrease of coseismic rupture at the transition from the heavily deformed outermost marine forearc to the less deformed section of the forearc between the coast and the up-dip limit of the seismic rupture (Schurr et al., 2014; Duputel et al., 2015; Jara et al., 2018).

3.5 Conclusion

Combining two years of local seismicity observations following the 2014 Iquique earthquake and structural constraints on forearc architecture derived from MCS data, we provide evidence for the interplay of plate boundary rupture and upper plate deformation in the context of long-term subduction erosion. The majority of aftershocks of the 2014 Iquique earthquake occurred up-dip of the coseismic slip and ~32 - 60 km landward of the trench. Although most of the seismicity was within ~5 km of the plate boundary, earthquakes extended through the upper plate, defining a seaward dipping zone that coincides with seaward dipping normal faults imaged in the MCS data. The up-dip band of aftershock seismicity separates a pervasively fractured and likely fluid-filled marine forearc farther seaward from a less deformed section of the upper plate forearc. At the transition, active subduction erosion during the postseismic and possibly coseismic phases leads to basal abrasion of the upper plate and associated extensional faulting of the upper plate at the up-dip end of the seismogenic zone. Landward migration of the up-dip end of the seismogenic zone, at similar rates compared to the trench and the volcanic arc, preconditions the structural setting of the heavily fractured, fluid-filled and therefore weak and aseismic outermost marine forearc.

Acknowledgments

This publication is funded by the German Research Foundation (DFG) under grant LA2970/4-1. We greatly appreciate the support from the Armada de Chile and SHOA, providing ship time on the *OPV Toro* to deploy the OBS in December 2014. GEOMAR's OCEANS program funded the OBS deployment. The SO244 cruise in 2015 was financed in the scope of the project GeoSEA by the German Federal Ministry for Education and Research (Bundesministerium für Bildung und Forschung/BMBF) under grant No. 03G0244A. The authors gratefully acknowledge the de-installation of the OBS with RV Langseth in 2016 (Oregon State University, grant OCE-1459368). We acknowledge the excellent sea-going support provided by all captains and their crews. ECR acknowledges the support of the Chilean National Research Agency (ANID, grant FONDECYT 1170009). We thank Soto et al. (2019) for providing their event catalog and Z. Duputel for providing the coseismic slip maps. Figures were created using Generic Mapping Tools (Wessel et al., 2013). We gratefully acknowledge the comments by P. Vannucchi and one anonymous reviewer in improving the manuscript.

Data Availability Statement

The seismic waveform data from network CX are available from GFZ and CNRS-INSU (2006). OBS seismic catalog and waveform data are available from PANGAEA `https://doi.pangaea.de/10.1594/PANGAEA.929899`. Arrival times from the permanent land network were provided by the CSN (Barrientos, 2018). Earthquake focal mechanisms were obtained from Global Centroid-Moment-Tensor catalog (`https://www.globalcmt.org/`). Multibeam data from Geersen et al. (2018a) can be accessed via `https://doi.pangaea.de/10.1594/PANGAEA.893034`.

References

Aldersons, F. (2004). *Toward a Three-Dimensional Crustal Structure of the Dead Sea region from Local Earthquake Tomography*. Ph.d. thesis.

Allmendinger, R. W. & González, G. (2010). Invited review paper: Neogene to quaternary tectonics of the coastal cordillera, northern chile. *Tectonophysics*, *495*(1-2), 93–110, `https://doi.org/10.1016/j.tecto.2009.04.019`.

An, C., Sepúlveda, I., & Liu, P. L. F. (2014). Tsunami source and its validation of the 2014 iquique, chile, earthquake. *Geophysical Research Letters*, *41*(11), 3988–3994, `https://doi.org/10.1002/2014gl060567`.

Angermann, D., Klotz, J., & Reigber, C. (1999). Space-geodetic estimation of the nazca-south america euler vector. *Earth and Planetary Science Letters*, *171*(3), 329–334, `https://doi.org/10.1016/s0012-821x(99)00173-9`.

Armijo, R. & Thiele, R. (1990). Active faulting in northern chile: ramp stacking and lateral decoupling along a subduction plate boundary? *Earth and Planetary Science Letters*, *98*(1), 40–61, `https://doi.org/10.1016/0012-821x(90)90087-e`.

Barrientos, S. (2018). The seismic network of chile. *Seismological Research Letters*, *89*(2A), 467–474, `https://doi.org/10.1785/0220160195`.

Bedford, J., Moreno, M., Schurr, B., Bartsch, M., & Oncken, O. (2015). Investigating the final seismic swarm before the iquique-pisagua 2014 mw 8.1 by comparison of continuous gps and seismic foreshock data. *Geophysical Research Letters*, *42*(10), 3820–3828, `https://doi.org/10.1002/2015gl063953`.

Bilek, S. L. & Lithgow-Bertelloni, C. (2005). Stress changes in the costa rica subduction zone due to the 1999 mw=6.9 quepos earthquake. *Earth and Planetary Science Letters*, *230*(1-2), 97–112, `https://doi.org/10.1016/j.epsl.2004.11.020`.

Brodsky, E. E. & Lay, T. (2014). Recognizing foreshocks from the 1 april 2014 chile earthquake. *Science*, *344*(6185), 700–2, `https://doi.org/10.1126/science.1255202`.

Byrne, D. E., Davis, D. M., & Sykes, L. R. (1988). Loci and maximum size of thrust earthquakes and the mechanics of the shallow region of subduction zones. *Tectonics*, *7*(4), 833–857, `https://doi.org/10.1029/TC007i004p00833`.

Cesca, S., Grigoli, F., Heimann, S., Dahm, T., Kriegerowski, M., Sobiesiak, M., Tassara, C., & Olcay, M. (2016). The mw8.1 2014 iquique, chile, seismic sequence: a tale of foreshocks and aftershocks. *Geophysical Journal International*, *204*(3), 1766–1780, `https://doi.org/10.1093/gji/ggv544`.

Chlieh, M., de Chabalier, J. B., Ruegg, J. C., Armijo, R., Dmowska, R., Campos, J., & Feigl, K. L. (2004). Crustal deformation and fault slip during the seismic cycle in the north chile subduction zone, from gps and insar observations. *Geophysical Journal International*, *158*(2), 695–711, `https://doi.org/10.1111/j.1365-246X.2004.02326.x`.

Clift, P. & Vannucchi, P. (2004). Controls on tectonic accretion versus erosion in subduction zones: Implications for the origin and recycling of the continental crust. *Reviews of Geophysics*, *42*(2), `https://doi.org/10.1029/2003rg000127`.

Collings, R., Lange, D., Rietbrock, A., Tilmann, F., Natawidjaja, D., Suwargadi, B., Miller, M., & Saul, J. (2012). Structure and seismogenic properties of the mentawai segment of the sumatra subduction zone revealed by local earthquake traveltime tomography. *Journal of Geophysical Research: Solid Earth*, *117*(B1), `https://doi.org/10.1029/2011jb008469`.

Comte, D. & Pardo, M. (1991). Reappraisal of great historical earthquakes in the northern chile and southern peru seismic gaps. *Natural Hazards*, *4*(1), 23–44, `https://doi.org/10.1007/bf00126557`.

Contreras-Reyes, E., Jara, J., Grevemeyer, I., Ruiz, S., & Carrizo, D. (2012). Abrupt change in the dip of the subducting plate beneath north chile. *Nature Geoscience*, *5*(5), 342–345, `https://doi.org/10.1038/ngeo1447`.

Contreras-Reyes, E., Ruiz, J. A., Becerra, J., Kopp, H., Reichert, C., Maksymowicz, A., & Arriagada, C. (2015). Structure and tectonics of the central chilean margin (31°–33°s): implications for subduction erosion and shallow crustal seismicity. *Geophysical Journal International*, *203*(2), 776–791, `https://doi.org/10.1093/gji/ggv309`.

Coulbourn, W. T. & Moberly, R. (1977). Structural evidence of the evolution of fore-arc basins off south america. *Canadian Journal of Earth Sciences*, *14*(1), 102–116, `https://doi.org/10.1139/e77-011`.

Diehl, T., Deichmann, N., Kissling, E., & Husen, S. (2009). Automatic s-wave picker for local earthquake tomography. *Bulletin of the Seismological Society of America*, *99*(3), 1906–1920, `https://doi.org/10.1785/0120080019`.

Duputel, Z., Jiang, J., Jolivet, R., Simons, M., Rivera, L., Ampuero, J. P., Riel, B., Owen, S. E., Moore, A. W., Samsonov, S. V., Ortega Culaciati, F., & Minson, S. E. (2015). The iquique earthquake sequence of april 2014: Bayesian modeling accounting for prediction uncertainty. *Geophysical Research Letters*, *42*(19), 7949–7957, `https://doi.org/10.1002/2015gl065402`.

Dziewonski, A. M., Chou, T. A., & Woodhouse, J. H. (1981). Determination of earthquake source parameters from waveform data for studies of global and regional seismicity. *Journal of Geophysical Research: Solid Earth*, *86*(B4), 2825–2852, `https://doi.org/10.1029/JB086iB04p02825`.

Ekström, G., Nettles, M., & Dziewoński, A. M. (2012). The global cmt project 2004–2010: Centroid-moment tensors for 13,017 earthquakes. *Physics of the Earth and Planetary Interiors*, *200-201*, 1–9, `https://doi.org/10.1016/j.pepi.2012.04.002`.

Farr, T. G., Rosen, P. A., Caro, E., Crippen, R., Duren, R., Hensley, S., Kobrick, M., Paller, M., Rodriguez, E., Roth, L., Seal, D., Shaffer, S., Shimada, J., Umland, J., Werner, M., Oskin, M., Burbank, D., & Alsdorf, D. (2007). The shuttle radar topography mission. *Reviews of Geophysics*, *45*(2), `https://doi.org/10.1029/2005rg000183`.

Frohlich, C. (1992). Triangle diagrams: ternary graphs to display similarity and diversity of earthquake focal mechanisms. *Physics of the Earth and Planetary Interiors*, *75*(1-3), 193–198, `https://doi.org/10.1016/0031-9201(92)90130-n`.

Geersen, J., Ranero, C. R., Barckhausen, U., & Reichert, C. (2015). Subducting seamounts control interplate coupling and seismic rupture in the 2014 iquique earthquake area. *Nat Commun*, *6*, 8267, `https://doi.org/10.1038/ncomms9267`.

Geersen, J., Ranero, C. R., Klaucke, I., Behrmann, J. H., Kopp, H., Tréhu, A. M., Contreras-Reyes, E., Barckhausen, U., & Reichert, C. (2018a). Active tectonics of the north chilean marine forearc and adjacent oceanic nazca plate. *Tectonics*, *37*(11), 4194–4211, `https://doi.org/10.1029/2018tc005087`.

Geersen, J., Ranero, C. R., Kopp, H., Behrmann, J. H., Lange, D., Klaucke, I., Barrientos, S., Diaz-Naveas, J., Barckhausen, U., & Reichert, C. (2018b). Does permanent extensional deformation in lower forearc slopes indicate shallow plate-boundary rupture? *Earth and Planetary Science Letters*, *489*, 17–27, `https://doi.org/10.1016/j.epsl.2018.02.030`.

GFZ & CNRS-INSU (2006). Ipoc seismic network. integrated plate boundary observatory chile - ipoc. *Other/Seismic Network*, `https://doi.org/10.14470/ PK615318`.

GFZ & gempa GmbH (2008). The seiscomp seismological software package. *GFZ Data Services*, `https://doi.org/10.5880/GFZ.2.4.2020.003`.

Haberland, C., Rietbrock, A., Lange, D., Bataille, K., & Dahm, T. (2009). Structure of the seismogenic zone of the southcentral chilean margin revealed by local earthquake traveltime tomography. *Journal of Geophysical Research: Solid Earth*, *114*(B1), `https://doi.org/10.1029/2008jb005802`.

Havskov, J., Voss, P. H., & Ottemoller, L. (2020). Seismological observatory software: 30 yr of seisan. *Seismological Research Letters*, *91*(3), 1846–1852, `https://doi.org/10.1785/0220190313`.

Hayes, G. P., Moore, G. L., Portner, D. E., Hearne, M., Flamme, H., Furtney, M., & Smoczyk, G. M. (2018). Slab2, a comprehensive subduction zone geometry model. *Science*, *362*(6410), 58–61, `https://doi.org/10.1126/science.aat4723`.

Herman, M. W., Furlong, K. P., Hayes, G. P., & Benz, H. M. (2016). Foreshock triggering of the 1 april 2014 mw 8.2 iquique, chile, earthquake. *Earth and Planetary Science Letters*, *447*, 119–129, `https://doi.org/10.1016/j.epsl.2016.04.020`.

Husen, S., Kissling, E., Flueh, E. R., & Asch, G. (1999). Accurate hypocentre determination in the seismogenic zone of the subducting nazca plate in northern chile using a combined on-/offshore network. *Geophysical Journal International*, *138*(3), 687–701, `https://doi.org/10.1046/j.1365-246x.1999.00893.x`.

Husen, S. & Smith, R. B. (2004). Probabilistic earthquake relocation in three-dimensional velocity models for the yellowstone national park region, wyoming. *Bulletin of the Seismological Society of America*, *94*(3), 880–896, `https://doi.org/10.1785/0120030170`.

Hutton, L. K. & Boore, D. M. (1987). The ml scale in southern california. *Bulletin of the Seismological Society of America*, *77*(6), 2074–2094.

Jara, J., Sánchez-Reyes, H., Socquet, A., Cotton, F., Virieux, J., Maksymowicz, A., Díaz-Mojica, J., Walpersdorf, A., Ruiz, J., Cotte, N., & Norabuena, E. (2018). Kinematic study of iquique 2014 m 8.1 earthquake: Understanding the segmentation of the seismogenic zone. *Earth and Planetary Science Letters*, *503*, 131–143, `https://doi.org/10.1016/j.epsl.2018.09.025`.

Kissling, E., Kradolfer, U., & Maurer, H. (1995). *Program VELEST user's Guide-Short Introduction.* Report.

Kodaira, S., No, T., Nakamura, Y., Fujiwara, T., Kaiho, Y., Miura, S., Takahashi, N., Kaneda, Y., & Taira, A. (2012). Coseismic fault rupture at the trench axis during the 2011 tohoku-oki earthquake. *Nature Geoscience*, *5*(9), 646–650, `https://doi.org/10.1038/ngeo1547`.

Lange, D., Rietbrock, A., Haberland, C., Bataille, K., Dahm, T., Tilmann, F., & Flüh, E. R. (2007). Seismicity and geometry of the south chilean subduction zone (41.5°s–43.5°s): Implications for controlling parameters. *Geophysical Research Letters*, *34*(6), `https://doi.org/10.1029/2006gl029190`.

Lange, D., Tilmann, F., Barrientos, S. E., Contreras-Reyes, E., Methe, P., Moreno, M., Heit, B., Agurto, H., Bernard, P., Vilotte, J.-P., & Beck, S. (2012). Aftershock seismicity of the 27 february 2010 mw 8.8 maule earthquake rupture zone. *Earth and Planetary Science Letters*, *317-318*, 413–425, `https://doi.org/10.1016/j.epsl.2011.11.034`.

Lay, T., Yue, H., Brodsky, E. E., & An, C. (2014). The 1 april 2014 iquique, chile, mw 8.1 earthquake rupture sequence. *Geophysical Research Letters*, *41*(11), 3818–3825, `https://doi.org/10.1002/2014gl060238`.

León-Ríos, S., Ruiz, S., Maksymowicz, A., Leyton, F., Fuenzalida, A., & Madariaga, R. (2016). Diversity of the 2014 iquique's foreshocks and aftershocks: clues about the complex rupture process of a mw 8.1 earthquake. *Journal of Seismology*, *20*(4), 1059–1073, `https://doi.org/10.1007/s10950-016-9568-6`.

Lieser, K., Grevemeyer, I., Lange, D., Flueh, E., Tilmann, F., & Contreras-Reyes, E. (2014). Splay fault activity revealed by aftershocks of the 2010 mw 8.8 maule earthquake, central chile. *Geology*, *42*(9), 823–826, `https://doi.org/10.1130/g35848.1`.

Lomax, A., Virieux, J., Volant, P., & Berge-Thierry, C. (2000). *Probabilistic Earthquake Location in 3D and Layered Models*, volume 18 of *Modern Approaches in Geophysics*, book section Chapter 5, (pp. 101–134).

Ma, B., Klaeschen, D., Kopp, H., Geersen, J., & Tréhu, A. M. (2020). Variations in plate interface reflectivity within the rupture zone of the 2014 iquique earthquake sequence: evidence from seismic and bathymetric data. *AGU Fall Meeting 2020.*

Maksymowicz, A., Ruiz, J., Vera, E., Contreras-Reyes, E., Ruiz, S., Arraigada, C., Bonvalot, S., & Bascuñan, S. (2018). Heterogeneous structure of the northern chile marine forearc and its implications for megathrust earthquakes. *Geophysical Journal International*, *215*(2), 1080–1097, `https://doi.org/10.1093/gji/ggy325`.

Mendoza, C. & Hartzell, S. (1988). Aftershock patterns and main shock faulting. *Bull. Seismol. Soc. Am.*, *78*(4), 1438–1449.

Moberly, R., Shepherd, G. L., & Coulbourn, W. T. (1982). Forearc and other basins, continental margin of northern and southern peru and adjacent ecuador and chile. *Geological Society, London, Special Publications*, *10*(1), 171–189, `https://doi.org/10.1144/gsl.Sp.1982.010.01.11`.

Moore, J. C. & Saffer, D. (2001). Updip limit of the seismogenic zone beneath the accretionary prism of southwest japan: An effect of diagenetic to low-grade metamorphic processes and increasing effective stress. *Geology*, *29*(2), `https://doi.org/10.1130/0091-7613(2001)029<0183:Ulotsz>2.0.Co;2`.

Nippress, S. E. J. & Rietbrock, A. (2007). Seismogenic zone high permeability in the central andes inferred from relocations of micro-earthquakes. *Earth and Planetary Science Letters*, *263*(3-4), 235–245, `https://doi.org/10.1016/j.epsl.2007.08.032`.

Obana, K., Kodaira, S., Shinohara, M., Hino, R., Uehira, K., Shiobara, H., Nakahigashi, K., Yamada, T., Sugioka, H., Ito, A., Nakamura, Y., Miura, S., No, T., & Takahashi, N. (2013). Aftershocks near the updip end of the 2011 tohoku-oki earthquake. *Earth and Planetary Science Letters*, *382*, 111–116, `https://doi.org/10.1016/j.epsl.2013.09.007`.

Oleskevich, D. A., Hyndman, R. D., & Wang, K. (1999). The updip and downdip limits to great subduction earthquakes: Thermal and structural models of cascadia, south alaska, sw japan, and chile. *Journal of Geophysical Research: Solid Earth*, *104*(B7), 14965–14991, `https://doi.org/10.1029/1999jb900060`.

Ottemoller, L. & Havskov, J. (2003). Moment magnitude determination for local and regional earthquakes based on source spectra. *Bulletin of the Seismological Society of America*, *93*(1), 203–214, `https://doi.org/10.1785/0120010220`.

Popp, T. & Kern, H. (1994). The influence of dry and water saturated cracks on seismic velocities of crustal rocks - a comparison of experimental data with theoretical model. *Surveys in Geophysics*, *15*(5), 443–465, `https://doi.org/10.1007/bf00690169`.

Ranero, C. R., Grevemeyer, I., Sahling, H., Barckhausen, U., Hensen, C., Wallmann, K., Weinrebe, W., Vannucchi, P., von Huene, R., & McIntosh, K. (2008). Hydrogeological system of erosional convergent margins and its influence on tectonics and interplate seismogenesis. *Geochemistry, Geophysics, Geosystems*, *9*(3), `https://doi.org/10.1029/2007gc001679`.

Ranero, C. R. & von Huene, R. (2000). Subduction erosion along the middle america convergent margin. *Nature*, *404*(6779), 748–52, `https://doi.org/10.1038/35008046`.

Reasenberg, P., Oppenheimer, D., & USGS (1985). *FPFIT, FPPLOT and FPPAGE Fortran computer programs for calculating and displaying earthquake fault-plane solutions*. Report.

Reginato, G., Vera, E., Contreras-Reyes, E., Tréhu, A. M., Maksymowicz, A., Bello-González, J. P., & González, F. (2020). Seismic structure and tectonics of the continental wedge overlying the source region of the iquique mw8.1 2014 earthquake. *Tectonophysics*, *796*, `https://doi.org/10.1016/j.tecto.2020.228629`.

Rosenau, M. & Oncken, O. (2009). Fore-arc deformation controls frequency-size distribution of megathrust earthquakes in subduction zones. *Journal of Geophysical Research*, *114*(B10), `https://doi.org/10.1029/2009jb006359`.

Rutland, R. W. (1971). Andean orogeny and ocean floor spreading. *Nature*, *233*(5317), 252–5, `https://doi.org/10.1038/233252a0`.

Sallarès, V. & Ranero, C. (2005). Structure and tectonics of the erosional convergent margin off antofagasta, north chile (23°30ś). *Journal of Geophysical Research*, *110*(B6), `https://doi.org/10.1029/2004jb003418`.

Scheuber, E. & Reutter, K.-J. (1992). Magmatic arc tectonics in the central andes between 21° and 25°s. *Tectonophysics*, *205*(1-3), 127–140, `https://doi.org/10.1016/0040-1951(92)90422-3`.

Scholl, D. & von Huene, R. (2007). *Crustal recycling at modern subduction zones applied to the past—Issues of growth and preservation of continental basement crust, mantle geochemistry, and supercontinent reconstruction*. 4-D Framework of Continental Crust. Geological Society of America.

Scholz, C. H. (1998). Earthquakes and friction laws. *Nature*, *391*, 37–42, `https://doi.org/10.1038/34097`.

Schurr, B., Asch, G., Hainzl, S., Bedford, J., Hoechner, A., Palo, M., Wang, R., Moreno, M., Bartsch, M., Zhang, Y., Oncken, O., Tilmann, F., Dahm, T., Victor, P., Barrientos, S., & Vilotte, J. P. (2014). Gradual unlocking of plate boundary controlled initiation of the 2014 iquique earthquake. *Nature*, *512*(7514), 299–302, `https://doi.org/10.1038/nature13681`.

Schurr, B., Asch, G., Rosenau, M., Wang, R., Oncken, O., Barrientos, S., Salazar, P., & Vilotte, J. P. (2012). The 2007 m7.7 tocopilla northern chile earthquake sequence: Implications for along-strike and downdip rupture segmentation and megathrust frictional behavior. *Journal of Geophysical Research: Solid Earth*, *117*(B5), `https://doi.org/10.1029/2011jb009030`.

Schurr, B., Moreno, M., Tréhu, A. M., Bedford, J., Kummerow, J., Li, S., & Oncken, O. (2020). Forming a mogi doughnut in the years prior to and immediately before the 2014 mw8.1 iquique, northern chile, earthquake. *Geophysical Research Letters*, *47*(16), `https://doi.org/10.1029/2020gl088351`.

Sielfeld, G., Lange, D., & Cembrano, J. (2019). Intra-arc crustal seismicity: Seismotectonic implications for the southern andes volcanic zone, chile. *Tectonics*, *38*(2), 552–578, `https://doi.org/10.1029/2018tc004985`.

Simons, M., Minson, S. E., Sladen, A., Ortega, F., Jiang, J., Owen, S. E., Meng, L., Ampuero, J. P., Wei, S., Chu, R., Helmberger, D. V., Kanamori, H., Hetland, E., Moore, A. W., & Webb, F. H. (2011). The 2011 magnitude 9.0 tohoku-oki earthquake: mosaicking the megathrust from seconds to centuries. *Science*, *332*(6036), 1421–5, `https://doi.org/10.1126/science.1206731`.

Sippl, C., Schurr, B., Asch, G., & Kummerow, J. (2018). Seismicity structure of the northern chile forearc from >100,000 double-difference relocated hypocenters. *Journal of Geophysical Research: Solid Earth*, *123*(5), 4063–4087, `https://doi.org/10.1002/2017jb015384`.

Sladen, A. & Trevisan, J. (2018). Shallow megathrust earthquake ruptures betrayed by their outer-trench aftershocks signature. *Earth and Planetary Science Letters*, *483*, 105–113, `https://doi.org/10.1016/j.epsl.2017.12.006`.

Soto, H., Sippl, C., Schurr, B., Kummerow, J., Asch, G., Tilmann, F., Comte, D., Ruiz, S., & Oncken, O. (2019). Probing the northern chile megathrust with seismicity: The 2014 m8.1 iquique earthquake sequence. *Journal of Geophysical Research: Solid Earth*, *124*(12), 12935–12954, `https://doi.org/10.1029/2019jb017794`.

Straub, S. M., Gómez-Tuena, A., & Vannucchi, P. (2020). Subduction erosion and arc volcanism. *Nature Reviews Earth and Environment*, *1*(11), 574–589, `https://doi.org/10.1038/s43017-020-0095-1`.

Thurber, C. H. (1983). Earthquake locations and three-dimensional crustal structure in the coyote lake area, central california. *Journal of Geophysical Research*, *88*(B10), `https://doi.org/10.1029/JB088iB10p08226`.

Thurber, C. H. (1992). Hypocenter-velocity structure coupling in local earthquake tomography. *Physics of the Earth and Planetary Interiors*, *75*(1-3), 55–62, `https://doi.org/10.1016/0031-9201(92)90117-e`.

Tilmann, F. J., Craig, T. J., Grevemeyer, I., Suwargadi, B., Kopp, H., & Flueh, E. (2010). The updip seismic/aseismic transition of the sumatra megathrust illuminated by aftershocks of the 2004 aceh-andaman and 2005 nias events. *Geophysical Journal International*, `https://doi.org/10.1111/j.1365-246X.2010.04597.x`.

Tréhu, A. M., Hass, B., de Moor, A., Maksymowicz, A., Contreras-Reyes, E., Vera, E., & Tryon, M. D. (2019). Geologic controls on up-dip and along-strike propagation of slip during subduction zone earthquakes from a high-resolution seismic reflection survey across the northern limit of slip during the 2010 mw 8.8 maule earthquake, offshore chile. *Geosphere*, *15*(6), 1751–1773, `https://doi.org/10.1130/ges02099.1`.

Tréhu, A. M., Vera, E., & Riedel, M. (2017). *PICTURES: Pisagua/Iquique crustal tomography to understand the region of the earthquake source.* Report.

Vannucchi, P., Remitti, F., & Bettelli, G. (2008). Geological record of fluid flow and seismogenesis along an erosive subducting plate boundary. *Nature*, *451*(7179), 699–703, `https://doi.org/10.1038/nature06486`.

Vannucchi, P., Spagnuolo, E., Aretusini, S., Di Toro, G., Ujiie, K., Tsutsumi, A., & Nielsen, S. (2017). Past seismic slip-to-the-trench recorded in central america megathrust. *Nature Geoscience*, *10*(12), 935–940, `https://doi.org/10.1038/s41561-017-0013-4`.

von Huene, R. & Lallemand, S. (1990). Tectonic erosion along the japan and peru convergent margins. *Geological Society of America Bulletin*, *102*(6), 704–720, `https://doi.org/10.1130/0016-7606(1990)102<0704:TEATJA>2.3.CO;2`.

von Huene, R. & Ranero, C. R. (2003). Subduction erosion and basal friction along the sediment-starved convergent margin off antofagasta, chile. *Journal of Geophysical Research: Solid Earth*, *108*(B2), `https://doi.org/10.1029/2001jb001569`.

von Huene, R., Ranero, C. R., & Vannucchi, P. (2004). Generic model of subduction erosion. *Geology*, *32*(10), `https://doi.org/10.1130/g20563.1`.

von Huene, R. & Scholl, D. W. (1991). Observations at convergent margins concerning sediment subduction, subduction erosion, and the growth of continental crust. *Reviews of Geophysics*, *29*(3), `https://doi.org/10.1029/91rg00969`.

von Huene, R., Weinrebe, W., & Heeren, F. (1999). Subduction erosion along the north chile margin. *Journal of Geodynamics*, *27*(3), 345–358, `https://doi.org/10.1016/s0264-3707(98)00002-7`.

Waldhuser, F. & Ellsworth, W. L. (2000). A double-difference earthquake location algorithm method and application to the northern hayward fault, california. *Bulletin of the Seismological Society of America*, *90*(6), 1253–1368, `https://doi.org/10.1785/0120000006`.

Wang, K. & Bilek, S. L. (2014). Invited review paper: Fault creep caused by subduction of rough seafloor relief. *Tectonophysics*, *610*, 1–24, `https://doi.org/10.1016/j.tecto.2013.11.024`.

Wang, K. & Hu, Y. (2006). Accretionary prisms in subduction earthquake cycles: The theory of dynamic coulomb wedge. *Journal of Geophysical Research: Solid Earth*, *111*(B6), `https://doi.org/10.1029/2005jb004094`.

Wang, K., Hu, Y., von Huene, R., & Kukowski, N. (2010). Interplate earthquakes as a driver of shallow subduction erosion. *Geology*, *38*(5), 431–434, `https://doi.org/10.1130/g30597.1`.

Wang, X. Q., Schubnel, A., Fortin, J., David, E. C., Guéguen, Y., & Ge, H. K. (2012). High vp/vs ratio: Saturated cracks or anisotropy effects? *Geophysical Research Letters*, *39*(L11307), `https://doi.org/10.1029/2012GL051742`.

Wessel, P., Smith, W. H. F., Scharroo, R., Luis, J., & Wobbe, F. (2013). Generic mapping tools: Improved version released. *Eos, Transactions American Geophysical Union*, *94*(45), 409–410, `https://doi.org/10.1002/2013eo450001`.

Yagi, Y., Okuwaki, R., Enescu, B., Hirano, S., Yamagami, Y., Endo, S., & Komoro, T. (2014). Rupture process of the 2014 iquique chile earthquake in relation with the foreshock activity. *Geophysical Research Letters*, *41*(12), 4201–4206, `https://doi.org/10.1002/2014GL060274`.

Supporting Information

Introduction

This appendix provides supporting information on the methods we used to investigate the local seismicity following the 2014 M_w 8.1 Iquique earthquake. We used the continuous waveform data from two subsequent Ocean Bottom Seismometer installations and the permanent land stations from CSN (Barrientos, 2018) and IPOC (GFZ and CNRS-INSU, 2006) between December 9, 2014, and October 31, 2016.

Our local seismic catalog covers the region between 72 °W and 69.5 °W and between 22 °S and 19 °S. In total, the amphibious catalog comprises 1,990 earthquakes observed on at least eight stations (Figure S1), including 27,877 P-phase picks and 7,229 S-phases. The entire seismic catalog and waveform data are available from the PANGAEA archive (`https://www.pangaea.de`). The local magnitude of completeness is M_l 1.75 in the first year and M_l 2.5 in the second year. The decrease in the magnitude of completeness results from less operating OBS in the second year.

Earthquake detection and picking of P-phases

Earthquakes were detected with the scanloc module of SeisComP3 (GFZ and gempa GmbH, 2008) using a cluster search algorithm to associate phase detections to one or many potential earthquake sources. Source scanning was done with the local 1-D velocity model from Husen et al. (1999) (Figure 3.4). In the next step, the SeisComP3 estimated P-phase picks were used to re-pick P-phases onsets using the automatic Manneken Pix (MPX) algorithm (Aldersons, 2004) following the procedure of (Lange et al., 2012). All phase picks manually revised and associated with uncertainty from 0 to 4 according to their quality and re-picked using the SEISAN software (Havskov et al., 2020).

Picking of S-phases

In the next step, S-phases were picked for all events with more than 8 P picks using the S-phase pick algorithm of Diehl et al. (2009). All phase picks are associated with uncertainty from 0 to 4 according to their quality, and we removed all phases with a ratio of station residual to epicentral distance higher than 0.05 s/km. However, automated phase picking on OBS data turned out to be unsatisfactory due to increased noise on the waveform data. Hence, we manually revised the phase picks on the OBS data.

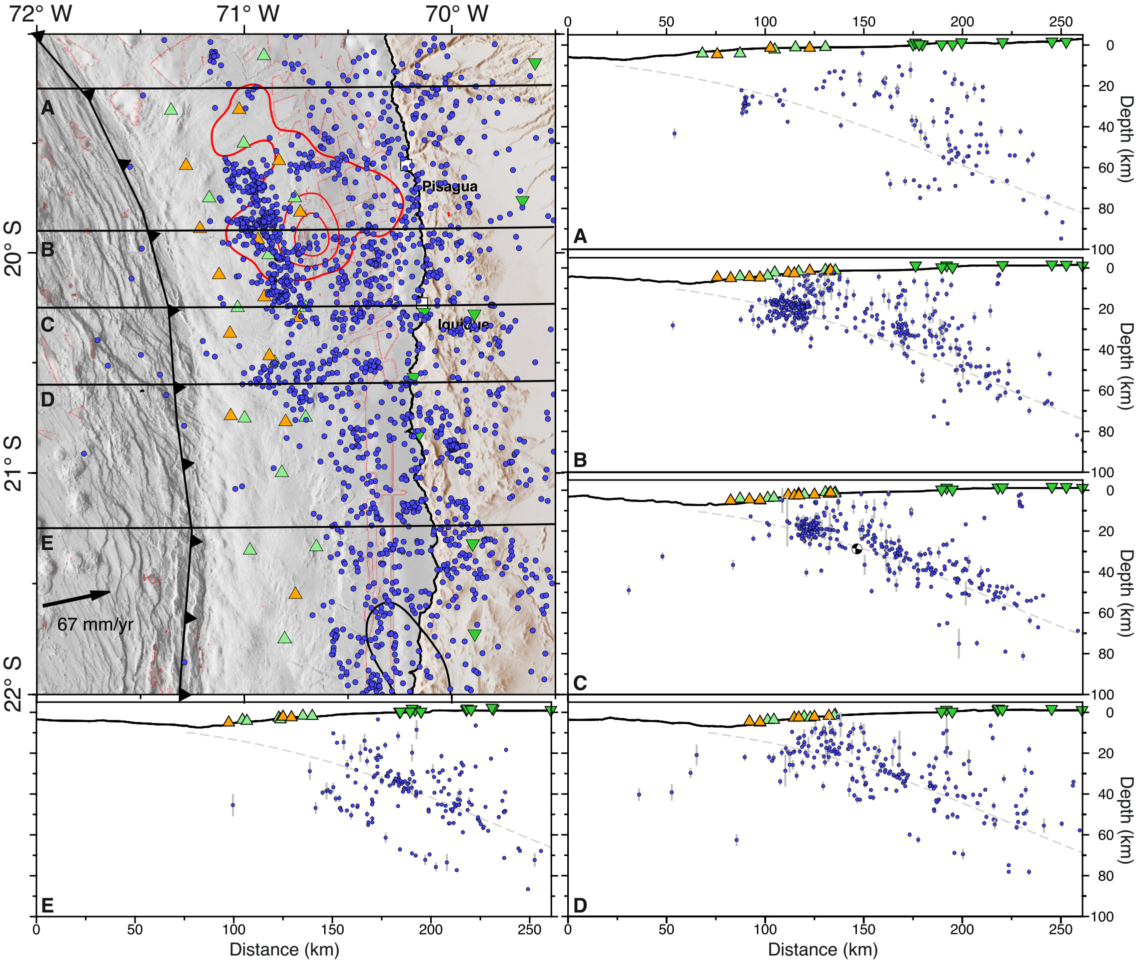

Figure 3.4: (Left) Map view of the total seismic catalog from December 9, 2014, until October 31, 2016. Coseismic slip model from Duputel et al. (2015) (Right) Profiles A-C crossing the rupture area of the 2014 Iquique earthquake. Blue dots indicate earthquakes located within the two-dimensional local earthquake tomography velocity model. Triangles mark the locations of the OBS deployments and land stations of CSN/IPOC, respectively.

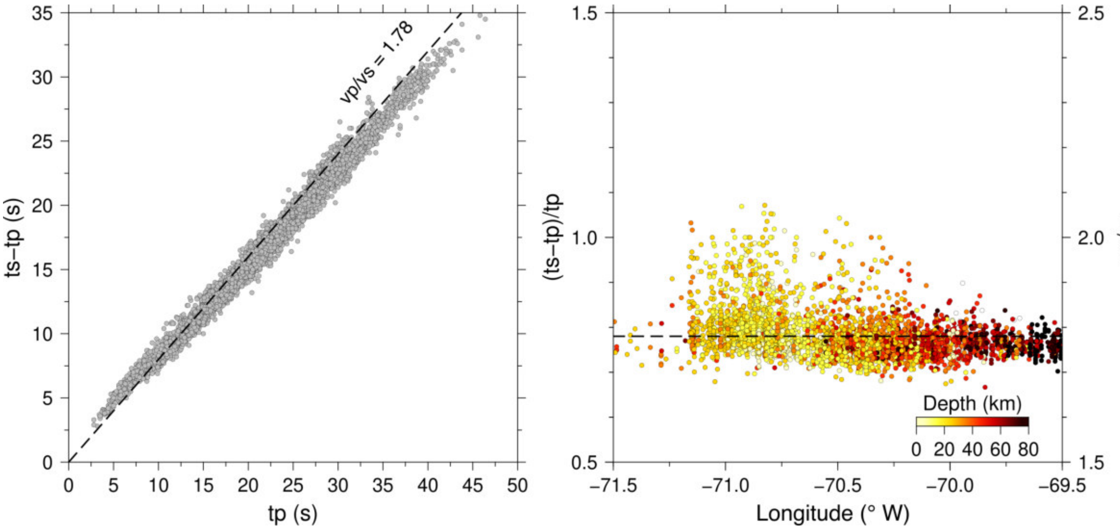

Figure 3.5: (Left) Wadati diagram of all events detected OBS06, located in the center of the OBS network. The dashed line marks the *vp/vs* ratio of 1.78. (Right) Plot of *vp/vs* ratios versus hypocenter longitudes (e.g., Haberland et al., 2009). Events east of 70.5 °W show an increase in the *vp/vs* ratio.

1D minimum Velocity Model

We selected 520 events from our local earthquake catalog with a gap of less than 180° and more than 12 P-wave arrivals and 8 S-wave arrivals to calculate local one-dimensional (1D) *vp* models and 1D *vp/vs* velocity models. The inversion is performed with VELEST (Kissling et al., 1995) using the staggered approach for inverting *vp* and *vp/vs* 1D velocity models (Husen et al., 1999) using a wide range of input velocity models (e.g., Sielfeld et al., 2019). The 1D velocity models are shown in Figure 3.6).

2D-tomography

The 1D models are then used as input for the 2D local earthquake tomography (LET) using SIMUL2000 (e.g., Thurber, 1983, 1992) following the procedure of Collings et al. (2012). The earthquake locations from the minimum 1D velocity model and the one-dimensional input velocity model were used for the 2D tomography (Figure 3.8). The resolution matrix contains at each row an averaging vector for a single model parameter and reflects how individual model parameters are dependent on all other model parameters (Collings et al., 2012). High resolution and large diagonal elements result in a low spread value (Figure 3.9). The two-dimensional tomography resolution indicates good resolution for the updip region and the coastal area for both *vp* and *vp/vs*. The marine forearc basin is poorly resolved because of a small amount of shallow seismic activity and no station coverage. The 2D velocity model was used to relocate the entire catalog using NonLinLoc (Lomax et al., 2000).

Magnitudes

We calculated moment magnitudes after Ottemoller and Havskov (2003) using standard values for geometric spreading and local magnitudes after Hutton and Boore (1987) using the maximum amplitudes of horizontal components of OBS and land stations. The instrument responses of OBS sensors are calibrated to match event magnitudes from land stations of the CSN (Figure 3.12) and result in similar magnitudes.

Earthquake locations and uncertainties

Hypocenter locations were determined using the non-linear oct-tree search algorithm NonLinLoc (Lomax et al., 2000). The maximum likelihood location is chosen as the preferred location from the probability density functions of event scatter samples. Furthermore, the oct-tree algorithm estimates hypocenter uncertainties based on a 3D error ellipsoid (68 % confidence). The distribution of the obtained location errors was averaged in the latitude, longitude and depth for all the events within each of the spatial 0.1° x 0.1° grid cells in which we subdivided the study region. To classify hypocenter locations in best (A), good (B), and fair (C) events, we use the procedure from Husen and Smith, 2004. We only consider the highest two classes, A and B with the most reliable earthquake locations (Husen and Smith, 2004).

Double-difference locations

To obtain precise relative relocations and to investigate the internal seismicity structure of the marine forearc, we applied the double-difference algorithm (HypoDD, Waldhuser and Ellsworth, 2000) on our local earthquake catalog with events relocated using the 2D local earthquake tomography (section 3.5). The algorithm minimizes the residual between observed and theoretical travel time differences based on waveform cross-correlations between two nearby earthquakes at the same station that recorded both events. Cross-correlations for events pairs with calculated time differences are considered with a maximum distance of 10 km and a cross-correlation coefficient greater than 0.8. The local catalog now encompasses 916 earthquakes relocated using the double-difference algorithm HypoDD

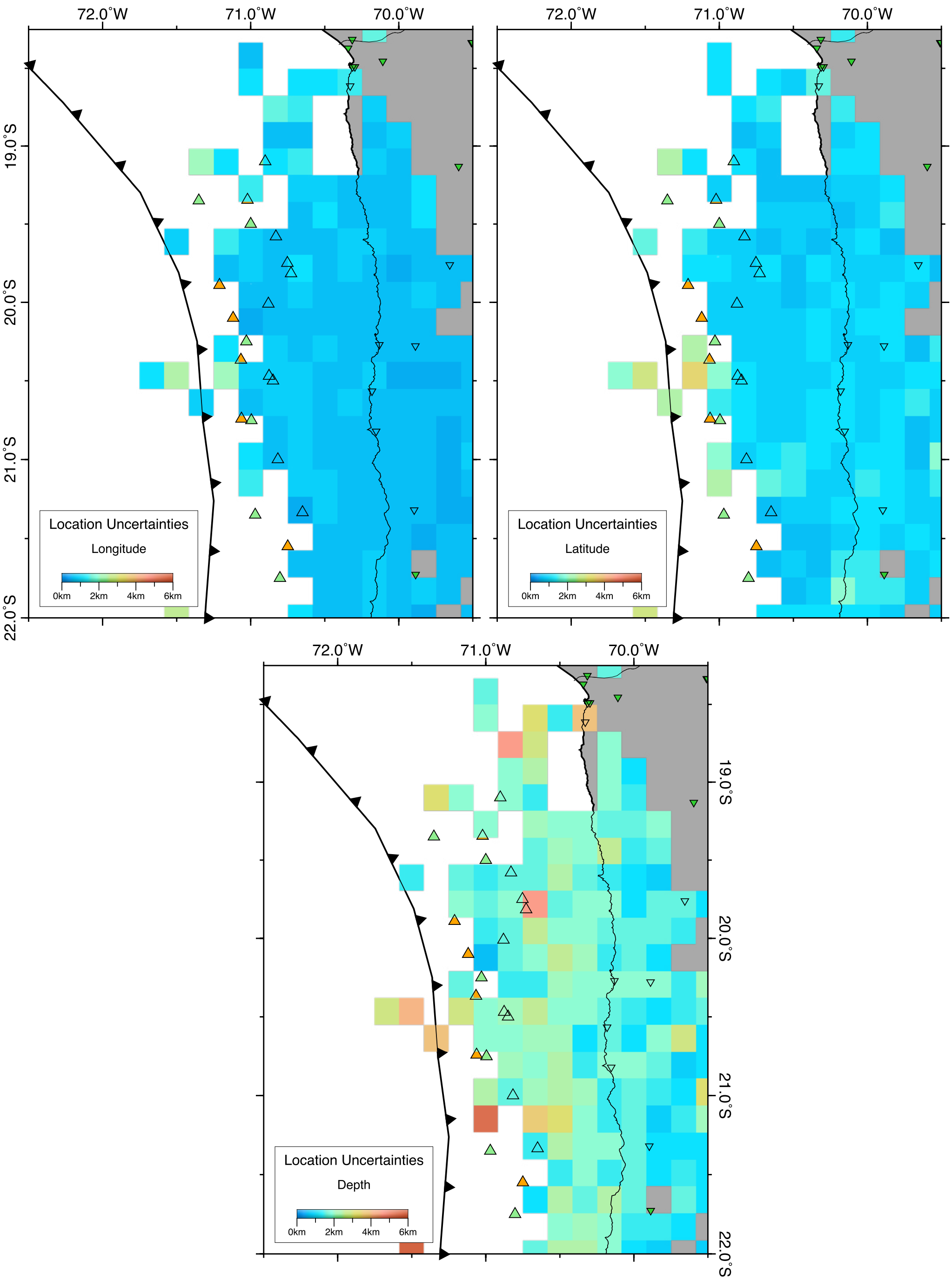

Figure 3.6: Location uncertainties from average event locations for hypocenters at 0 – 60 km depth for 0.25° × 0.25° squares. Uncertainties estimated using the oct-tree algorithm of the probabilistic location scheme of NonLinLoc. Error ellipsoids (68 % confidence) in three components x (longitude), y (latitude) and z (depth). Depth errors for shallow events outside the station network are not comparable to the large horizontal errors as the oct-tree search algorithm only explores the PDF within the pre-defined grid (e.g., no air-quakes).

(Waldhuser and Ellsworth, 2000) and 862 earthquakes located using the non-linear oct-tree search algorithm NonLinLoc (Lomax et al., 2000) with the quality classes A and B (Husen and Smith, 2004).

Catalog comparison

The aftershock seismic catalog presented here overlaps in 23 days with the local seismicity catalog from Soto et al. (2019), starting on December 9, 2014, with the deployment of the first Ocean Bottom Seismometer (OB01) (Figure 3.11). We compared both catalogs and searched the OBS data for missing events by comparing the origin times. Both catalogs have 425 events in common, but we could not locate 25 events from Soto et al. (2019) in our OBS data (Figure 3.11) due to a low signal-to-noise ratio on OBS waveforms. Our OBS network detected additional 58 events missing in the catalog from Soto et al. (2019). These 58 events are mainly located offshore at the seismogenic up-dip limit. In contrast, the 25 events observed only by Soto et al. (2019) are primarily located in the down-dip region of the Iquique earthquake. The earthquake locations from the Soto et al. (2019) catalog are biased 1.6 ± 0.04 km southwards, 3.27 ± 0.02 km westwards and 0.9 ± 0.06 km in depth relative to the locally determined hypocenters (Figure 3.11).

Focal mechanisms

Focal mechanisms of 98 events are calculated based on revised first motion P phase polarities of events with more than 20 P polarities (FPFIT, Reasenberg et al., 1985). Unique solutions are considered, which are based on event azimuths and take-off angles from hypocenters. Besides, we used focal mechanisms from the Global Centroid Moment Tensor (gCMT) catalog (`www.globalcmt.org`) (Dziewonski et al., 1981; Ekström et al., 2012), which comprises 20 earthquakes ($M_w > 4.7$) that occurred during the two years of the OBS deployment. CMT and focal mechanisms of the marine forearc are shown in Figure 3.13). In addition, we compared the focal mechanisms from FPFIT with three larger events of the global CMT catalog. We identified the largest discrepancy in the strike angle of the focal mechanisms (Figure 3.15). We calculated the bias in location as a weighted average for the events that the gCMT catalog and the local aftershock catalog have in common to compare the focal mechanism locations. The global gCMT catalog is displaced by 25 ± 0.5 km in the North direction and 2.9 ± 0.5 km in the East direction and 8 km deeper relative to our local catalog based on amphibious data.

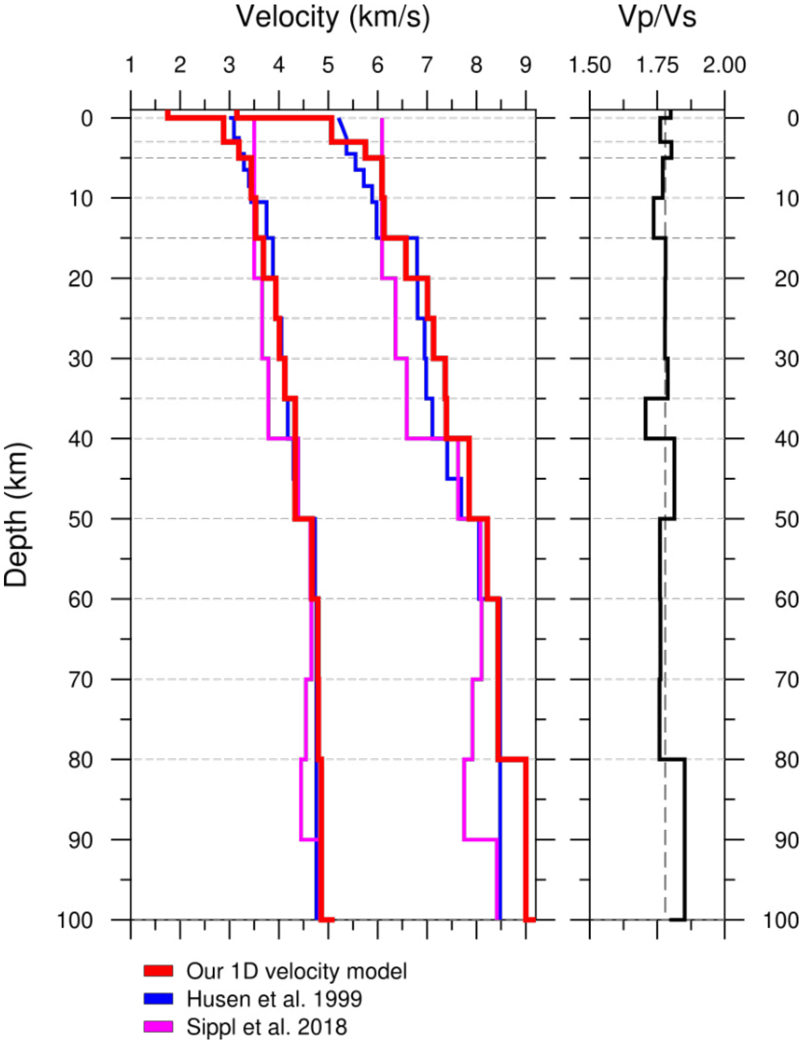

Figure 3.7: Minimum 1D velocity model for the marine forearc. The red line indicates the velocity model calculated with the offshore recorded Iquique aftershock sequence determined using VELEST (Kissling et al., 1995). The upper layers up to 15 km are not well constrained due to the near-vertical ray paths below the seismic network (Sippl et al., 2018; Husen et al., 1999).

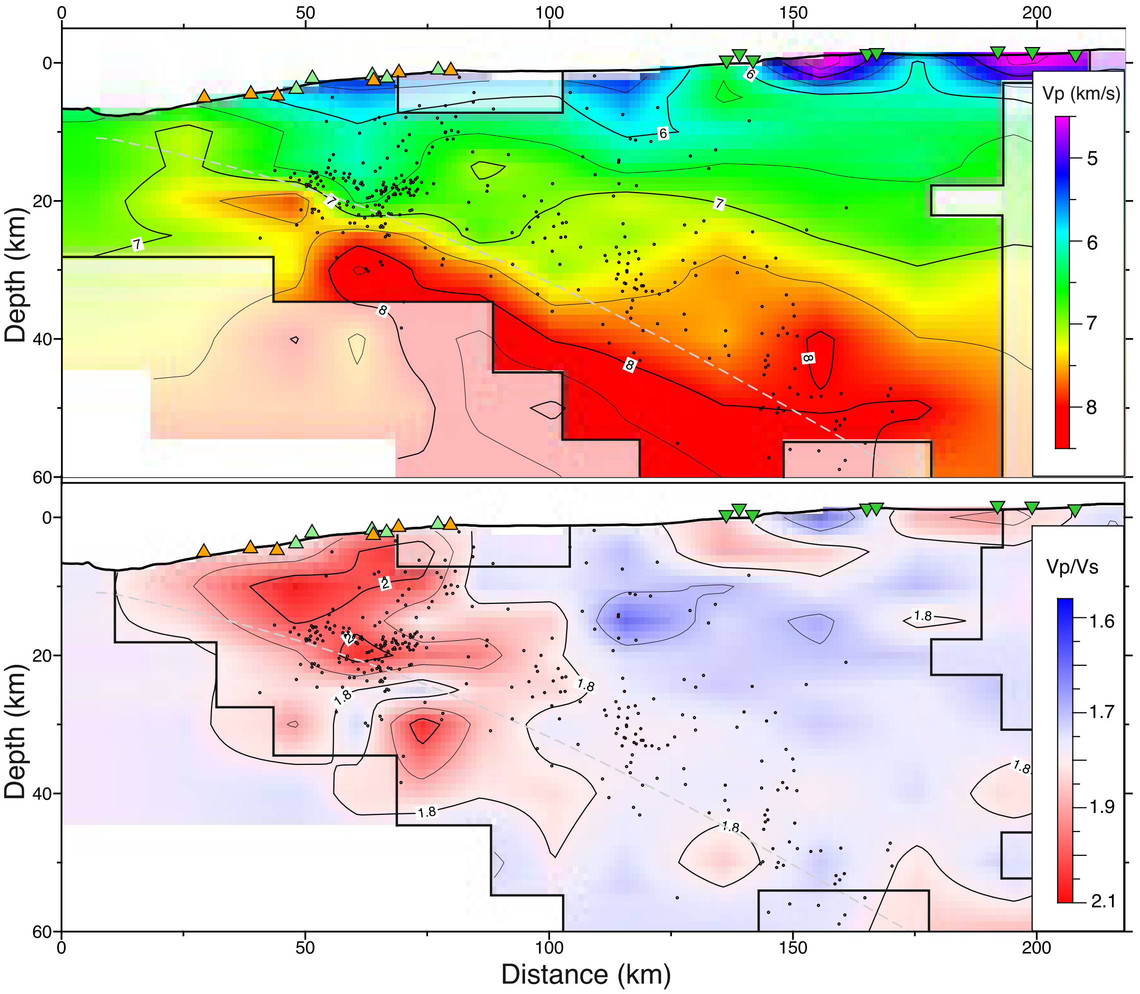

Figure 3.8: Local earthquake tomography at 20 °S west to east starting at 71.49 °W using SIMUL2000 (e.g., Thurber, 1983) and aftershock seismicity. The grey dashed line indicated the Slab2 model by (Hayes et al., 2018). OBS locations on the marine forearc are marked as triangles with defined color codes as in Figure 3.1 of the main manuscript. (Top) the vp model, (Bottom) vp/vs ratio. Black solid line encircles the region of good resolution.

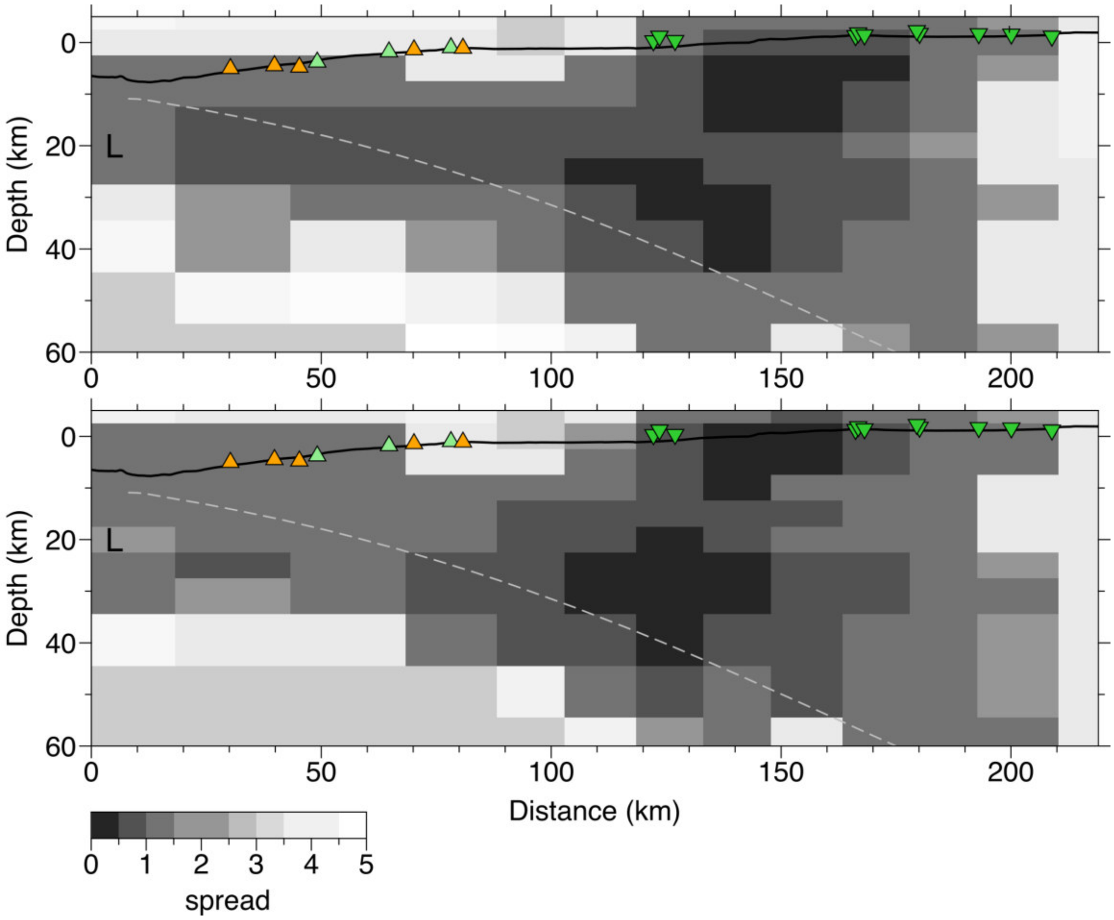

Figure 3.9: Spread of the two-dimensional local earthquake tomography model for *vp* (top) and *vp/vs* (bottom). Estimates are based on the analysis of the resolution matrix with gray shading following the spread function values.

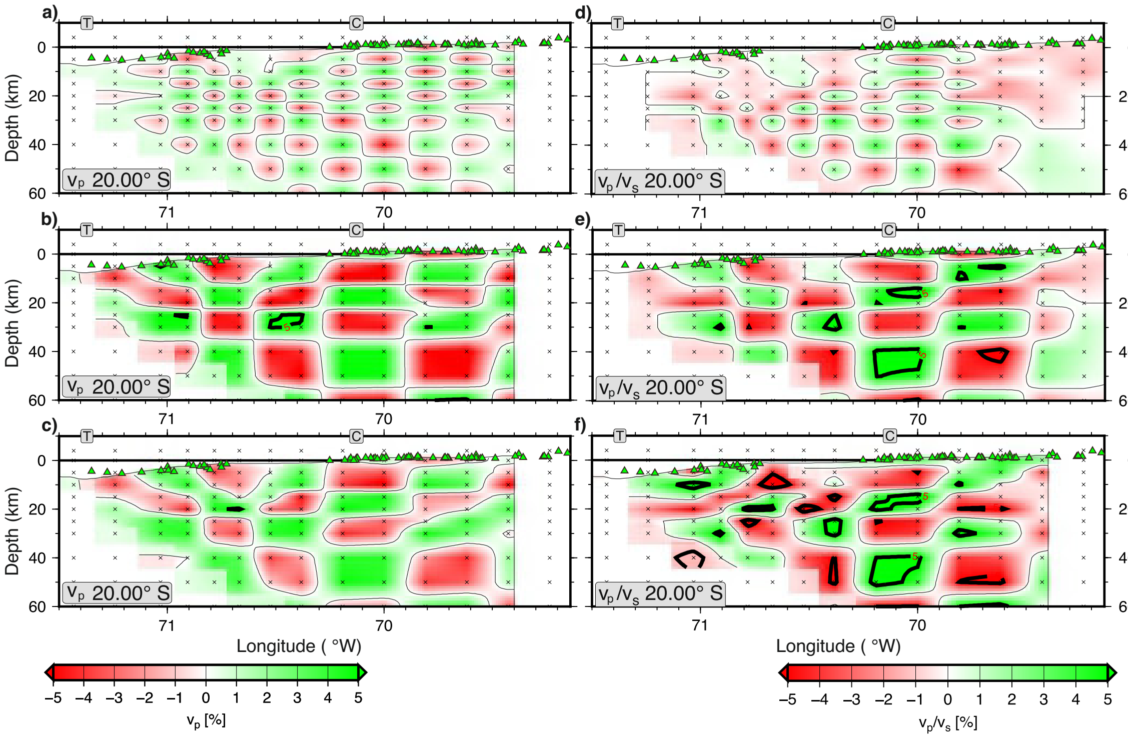

Figure 3.10: Checkerboards from the 2D local earthquake tomography. The profiles are oriented east west at 20 °S. Stations are shown with green triangles at their real depths (projected onto the profile at 20 °S. Contours lines exceeding the 5 % of the input checkerboard are indicated with black thick lines and are labelled. Nodes are indicated with crosses. The location of the coast (trench) is marked with C and T, respectively. (Left) (a) 1x1 checkerboard test vp, without noise; (b) 2x2 checkerboard test vp, without noise; (c) 2x2 checkerboard test vp, with noise dependent on the uncertainties of the different qualities of the picked phases. (Right) (d) 1x1 checkerboard test *vp/vs*, without noise; (e) 2x2 checkerboard test vp/vs, without noise; (f) 2x2 checkerboard test *vp/vs*, with noise dependent on the uncertainties of the different qualities of the picked phases.

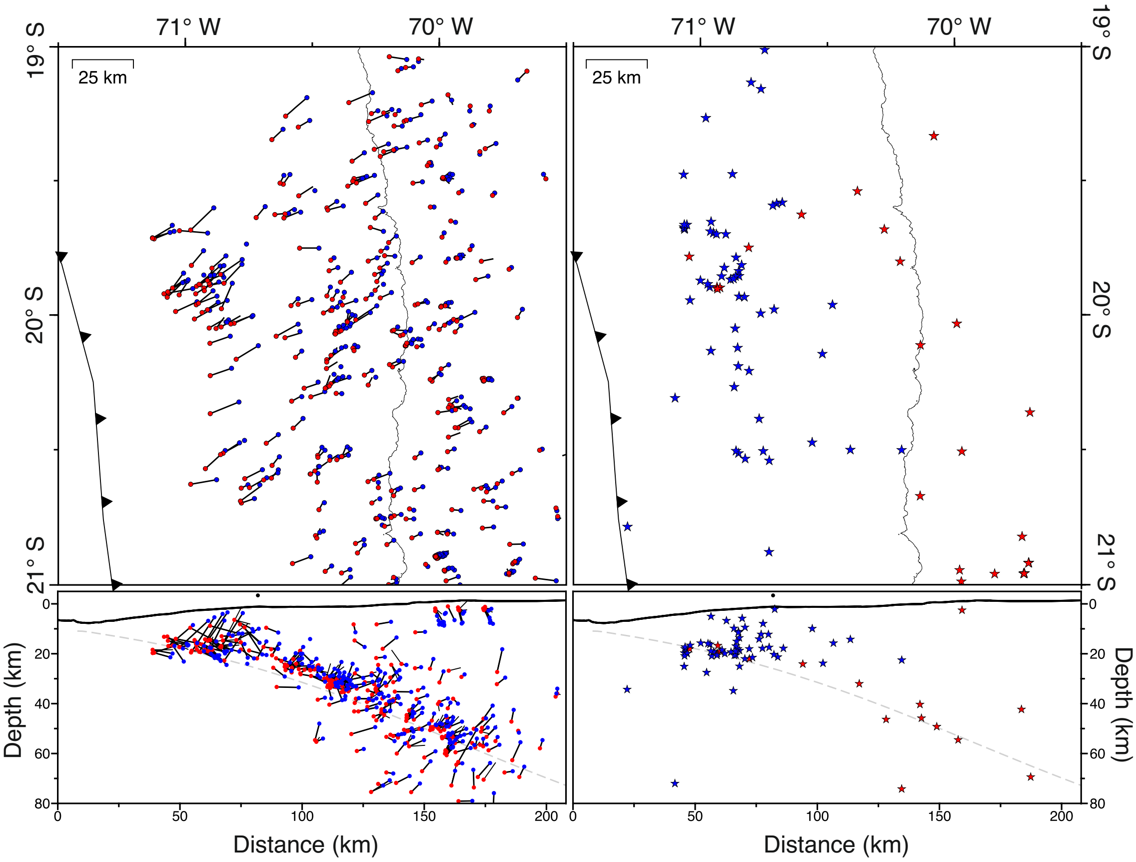

Figure 3.11: Difference between the OBS catalog of this study (blue dots/stars) and the catalog based on land stations from Soto et al. (2019) (red dots/stars). Both Catalogs overlapping 23 days in December 2014 and have 425 in common. (Right) Common events in both catalogs with the epicentral difference displayed as a black line. (Left) Blue stars indicate event locations that appear only in the amphibious catalog and red stars indicate event locations in the catalog of Soto et al. (2019).

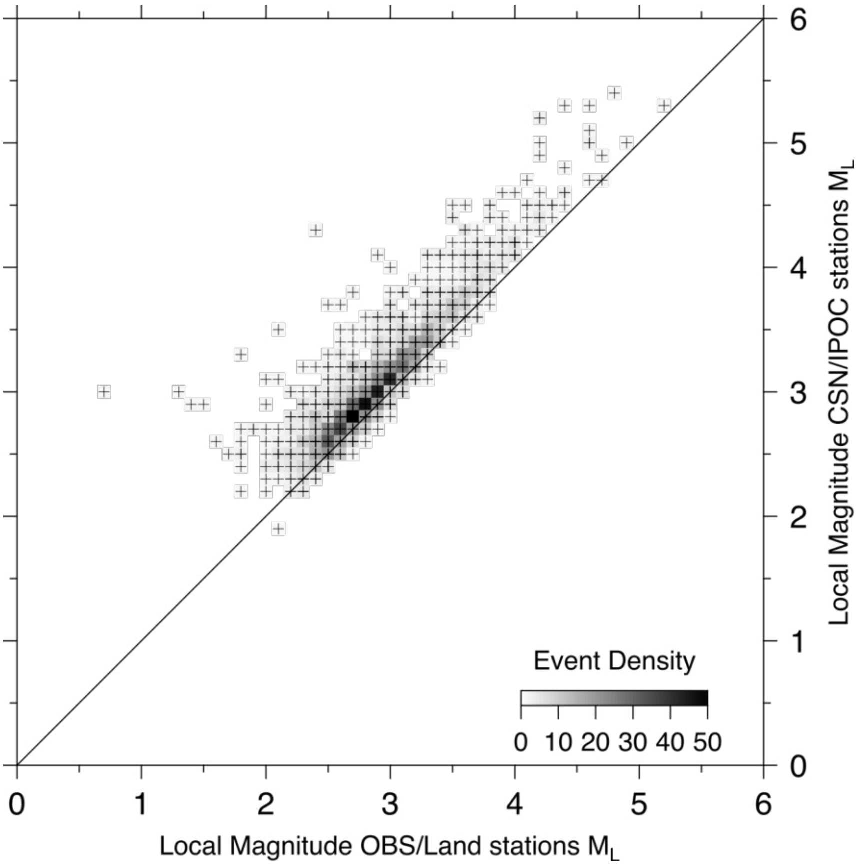

Figure 3.12: Local magnitudes of our catalog versus the local magnitudes of the CSN catalog (Barrientos, 2018).

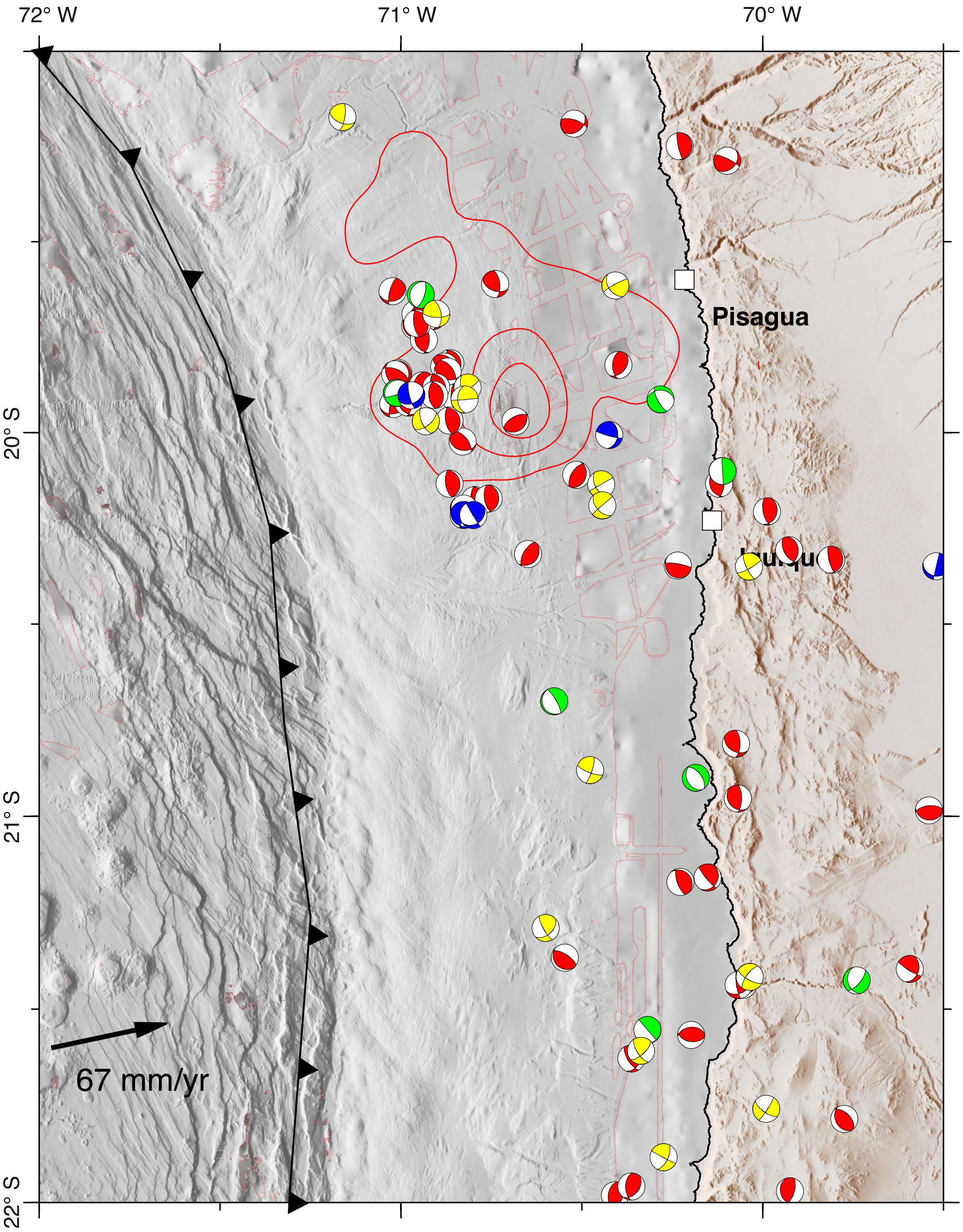

Figure 3.13: Focal mechanisms from FPFIT shown together with moment tensors from the gCMT catalogs (`www.globalcmt.org`). Beachballs are color-coded by faulting type in thrust (red), normal (green), strike-slip (yellow), or oblique (blue) fault mechanisms.

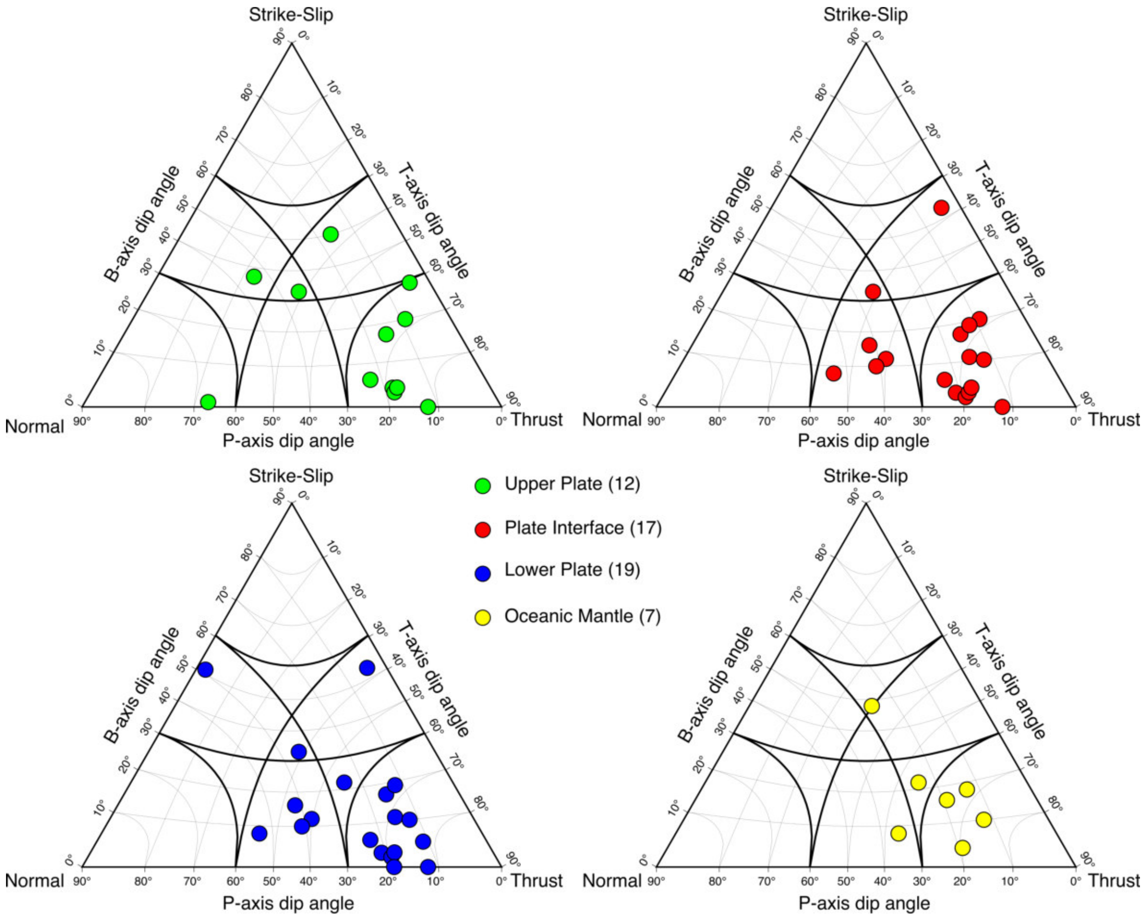

Figure 3.14: Ternary azimuthal gnomonic projection for the classification of focal mechanisms (Frohlich, 1992). Red circles indicate earthquakes with vertical distances to the plate interface of 5 km on either side of the plate interface of the global Slab2 model (Hayes et al., 2018). Blue circles are focal mechanisms of earthquakes in the subducting lower plate and orange circles are focal mechanisms deeper 10 km below the global Slab2 model.

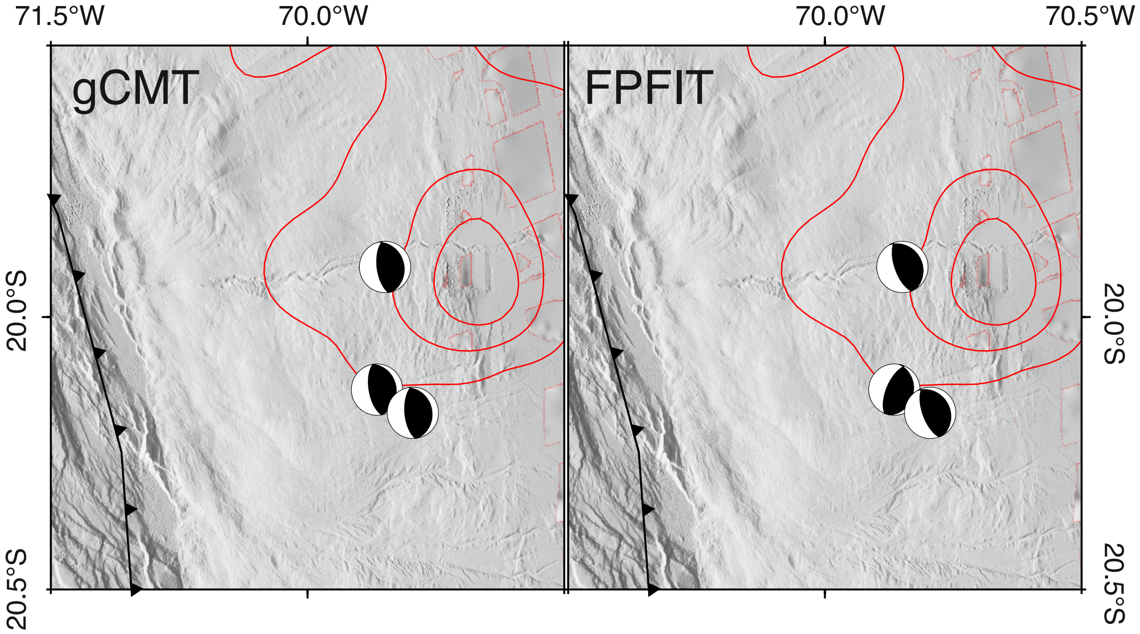

Figure 3.15: Comparison of focal mechanisms between the (left) global gCMT catalog solutions and (right) our FPFIT solutions (Reasenberg et al., 1985).

4 Megathrust reflectivity reveals the updip limit of the 2014 Iquique earthquake rupture

Bo Ma[1], Jacob Geersen[2], Dietrich Lange[1], Dirk Klaeschen[1], Ingo Grevemeyer[1], **Florian Petersen**[1], Michael Riedel[1], Yueyang Xia[1], Anne M. Tréhu[3], Eduardo Contreras-Reyes[4], and Heidrun Kopp[1,2]

1) GEOMAR Helmholtz Centre for Ocean Research Kiel, Kiel, Germany
2) Institute of Geosciences, Kiel University, Kiel, Germany
3) Oregon State University, College of Earth, Ocean, and Atmospheric Sciences, Corvallis, USA
4) Departamento de Geofísica, Facultad de Ciencias Físicas y Matemáticas, Universidad de Chile, Santiago, Chile

Submitted to **Nature Geoscience**, August 2021.

Abstract

The updip limit of seismic rupture during a megathrust earthquake exerts a major control on the size of the resulting tsunami. Offshore Northern Chile, the 2014 M_w 8.1 Iquique earthquake ruptured the plate boundary between 19.5 °S - 21 °S. Rupture terminated under the mid-continental slope and did not propagate updip to the trench. Here, we use state-of-the-art seismic reflection data to investigate the tectonic setting associated with the apparent updip arrest of rupture propagation at 15 km depth during the Iquique earthquake. We document a spatial correspondence between the rupture area and the seismic reflectivity of the plate boundary. North and updip of the rupture area, a coherent, highly reflective plate boundary indicates excess fluid pressure, which may prevent the accumulation of elastic strain. In contrast, the rupture area is characterized by the absence of plate boundary reflectivity, which suggests low fluid pressure that result in stress accumulation and thus control the extent of earthquake rupture. Generalizing these results, seismic reflection data can provide insights into the physical state of the shallow plate boundary and help to assess the potential for future shallow rupture in the absence of direct measurements of interplate deformation from most outermost forearc slopes.

4.1 Introduction

Megathrust earthquakes result from the sudden failure of the plate boundary in a region where elastic strain has accumulated prior to the event. Fluid pressure is a critical parameter that determines the strength of the megathrust and therefore exerts a main control on where and how seismic moment is released (Hubbert and Rubey, 1959; Saffer and Tobin, 2011). Pore fluid pressure in excess of hydrostatic pressure diminishes fault strength (Hubbert and Rubey, 1959). The key processes that release water in shallow subduction zones, and thus control fluid pressure, are compaction dewatering and clay and opal dehydration reactions in subducting sediments and the upper oceanic basement(Moore and Saffer, 2001; Ranero et al., 2008; Saffer and Tobin, 2011; Kameda et al., 2011). These processes take place under low temperatures and low confining pressures (Hubbert and Rubey, 1959; Kastner et al., 1991), so that excess pore pressures are expected in areas of low overburden, such as the shallow plate-boundary. Seismic reflection data are sensitive to the high acoustic impedance contrast generated by fluids and thus seismic reflection studies have proven powerful to investigate spatial variations in plate boundary fluid pressure, at least in a qualitative manner (Shipley et al., 1994; Casey Moore et al., 1998; Hurowitz and McLennan, 2007; Ranero et al., 2008; Spinelli and Wang, 2008; Tobin and Saffer, 2009; Bell et al., 2010; Bangs et al., 2015).

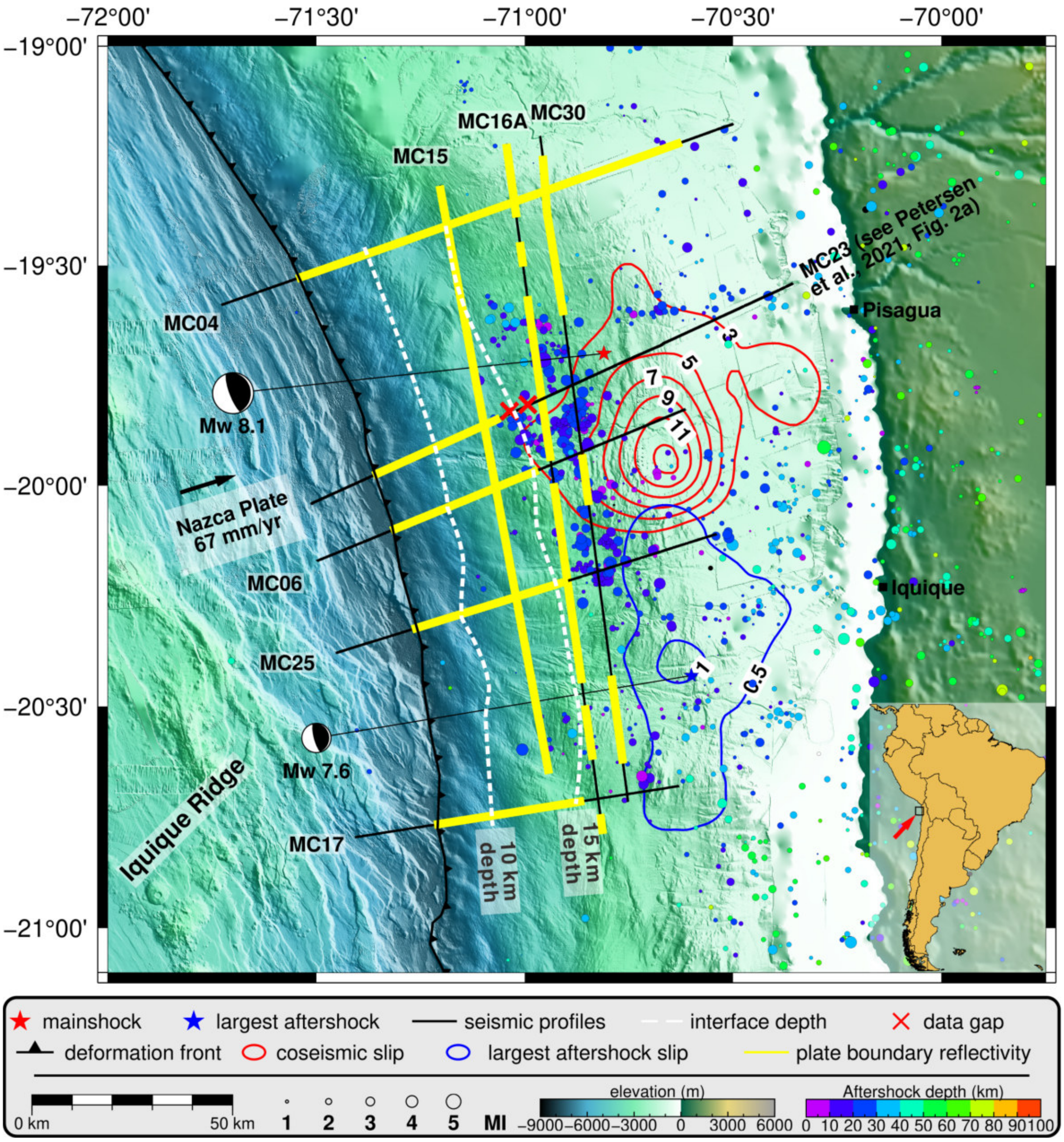

Figure 4.1: Overview map of the erosional margin of Northern Chile in the region affected by the 2014 Iquique earthquake. The hypocenter (star) and slip contour lines (in meters) of the 2014 Iquique M_w 8.1 mainshock (red) and M_w 7.7 aftershock (blue) are from Duputel et al. (2015). Black lines indicate the locations of the seismic lines used in this study with yellow regions indicating a coherent plate boundary reflection. Compare Petersen et al. (2021) for a detailed image of line MC23. The white dashed lines show the depth of the plate interface estimated from the seismic reflection data. Blue circles are aftershocks (December 2014 until October 2016) from the 2014 Iquique earthquake recorded by ocean bottom seismometers indicated as green and orange triangles (Petersen et al., 2021). Seafloor bathymetry from Geersen et al. (2018) combined with GEBCO_2019 bathymetry (`https://www.gebco.net`), SRTM topography from Farr et al. (2007). The convergence of the Nazca and South America plate indicated by a black arrow (Angermann et al., 1999)

For the subduction erosion dominated Central American margin, Ranero et al. (2008) suggested a high fluid content along the shallow aseismic section of the plate boundary (also compare to Bangs et al., 2015; Edwards et al., 2018) in a temperature regime where compaction dewatering and clay-mineral diagenetic reactions are expected to release most of the water in the subducting sediments (Saffer and Tobin, 2011). The authors further described a rapid decrease in fluid content where temperatures exceed ~150 °C, which corresponds to the transition from aseismic sliding at shallow depth to stick-slip sliding in the seismogenic zone.

On 1 April 2014, the M_w 8.1 Iquique earthquake ruptured the plate boundary between 19.5 °S - 21 °S along the erosive continental margin of Northern Chile (Hayes et al., 2014; Schurr et al., 2014; Ruiz et al., 2014; Schurr et al., 2020). Seismic rupture did not break updip to the trench but terminated under the mid-continental slope (Figure 4.1). Aftershocks of the 2014 Iquique earthquake concentrated around the updip limit of seismic rupture with little activity towards the trench (Petersen et al., 2021; Sippl et al., 2018). We use high-resolution multichannel seismic reflection profiles in a grid layout covering the 2014 Iquique mainshock and aftershock region as well as the surrounding forearc not affected by seismic rupture (Figure 4.1). The seismic reflectivity variations along the plate boundary elucidate the spatial variation in megathrust fluid pressure.

4.2 Data and Methods

Multichannel seismic reflection data. Seismic multichannel reflection data used in this study were acquired in 2016 during the MGL1610 cruise of *R/V Marcus G. Langseth* offshore Northern Chile (Tréhu et al., 2017). Seismic signals were generated with a source of 6600 cubic inches (108.15 liters), provided by four strings of 10 air-guns each. Data were recorded with an 8 km long streamer towed by *R/V Marcus G. Langseth.* The source was towed at 12 m depth below the water surface, and the record length was 16 s. The shots were acquired using a shot interval of 125 m to avoid interference from previous shots. Surface-related multiple prediction, anomalous amplitude noise attenuation and adaptive filter are effective methods to attenuate multiples in our 2D seismic data. The plate boundary could be observed as a low frequency response of the seismic record. After that, pre-stack depth migration is applied to the sections with the aim to reveal more structural details. See Supplementary Methods for more information.

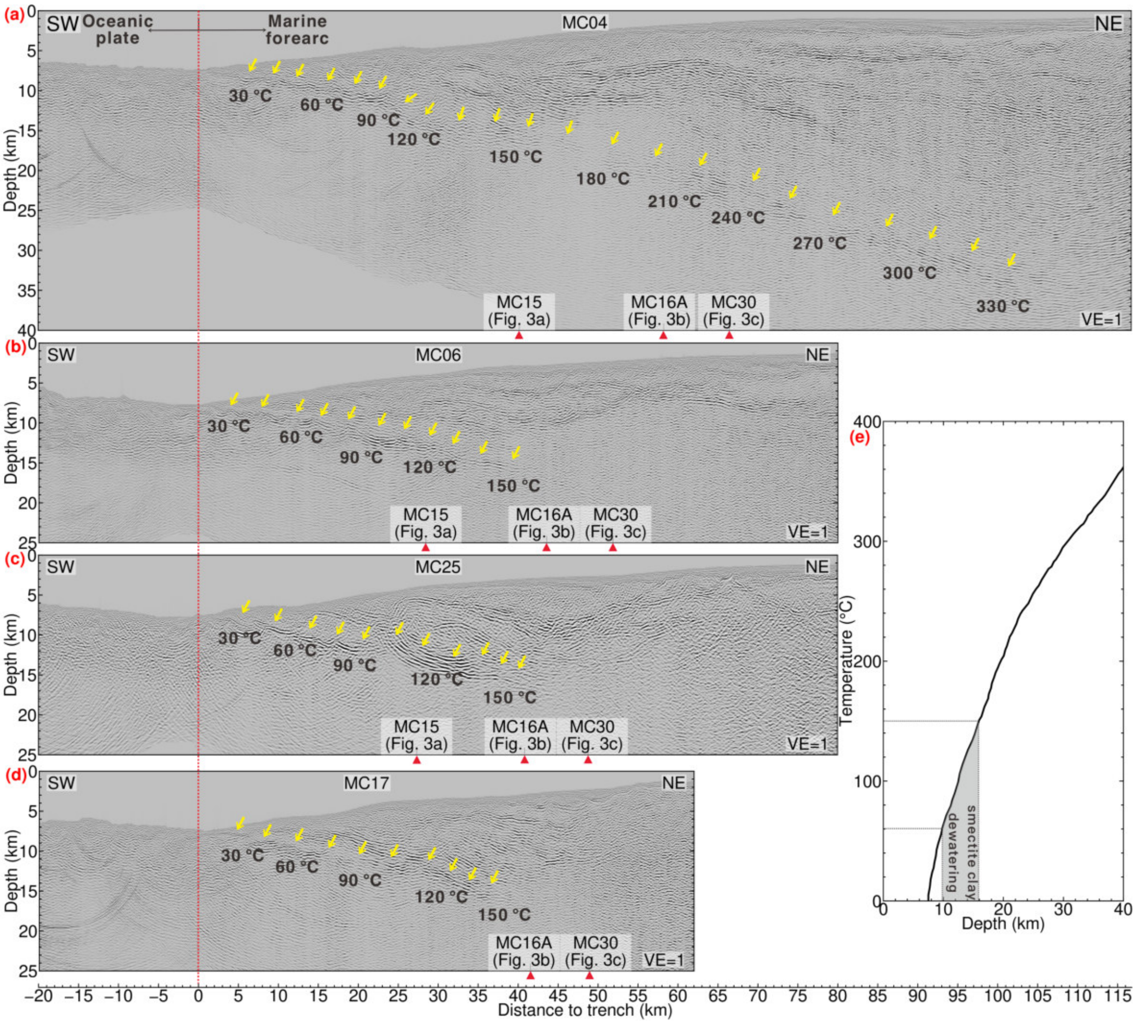

Figure 4.2: Pre-stack depth migrated section of seismic dip-lines. Yellow arrows indicate a coherent plate boundary reflection. The vertical red dashed line denotes the location of the deformation front. The red arrows specify the intersections with the strike lines. Temperatures at the plate boundary are from Kellner (2007). (a): seismic line MC04. (b): seismic line MC06. (c): seismic line MC25. (d): seismic line MC17. (e): Temperature distribution along the plate boundary from the trench downwards (Kellner, 2007). The approximate depth range of smectite clay dehydration is based on Kastner et al. (1991); Bekins et al. (1994); Spinelli (2004); Underwood (2007); Saffer and Tobin (2011).

4.3 Correspondance between plate boundary reflectivity and rupture surface of the 2014 Iquique earthquake

Pre-stack depth migrated seismic reflection profiles with a total length of 912 km cover the Northern Chilean marine forearc in the region that ruptured during the 2014 Iquique earthquake as well as in the adjacent un-ruptured forearc (Figure 4.1). The shallow plate boundary underneath the lower continental slope is visible as a prominent seismic reflection on all profiles. At greater depth, the reflectivity shows a high degree of variation in the dip direction and along strike. Along the northernmost line MC04, located to the north of the 2014 Iquique rupture where only sparse aftershocks occur (Figure 4.1; Petersen et al., 2021), the plate boundary is imaged as a band of strong, albeit discontinuous, reflectivity from the trench to at least 103 km landward of the deformation front (Figures 4.1 and 4.2a, yellow lines and arrows), where the plate boundary is at a depth of about 35 km. Between profile kilometers 0 - 35 km, the plate boundary is imaged with a high degree of lateral coherency from the deformation front adjacent to the trench axis to a depth of around 15 km on all profiles (Figures 4.1 and 4.2b - d, yellow lines and arrows). South of MC04, however, plate boundary reflectivity drops suddenly and is below the background noise level more than 30 - 35 km east of the trench.

The down-dip variations in plate boundary reflectivity are also seen on lines parallel to the trench (MC15, MC16A and MC30; Figure 4.3) which image the lower continental slope with increasing distance from the deformation front (Figure 4.1). The intersections of the trench-parallel lines with the dip lines provide an independent verification of the reflection character of the plate boundary at the crossing points. Along strike line MC15 which is located closest to the trench, a highly coherent plate boundary reflection is observed along the entire line at a depth of 11.5 - 16 km (Figure 4.1, yellow line; Figure 4.3a, yellow arrows). Strike line MC16A, located ~16 km farther downdip, shows intermittent high reflectivity on the plate boundary between profile kilometers 0 - 6, 20 - 33, 38 - 88, 94 - 137,145 - 150 and 157 - 175 km (Figure 4.3b). Elsewhere, the reflectivity is moderate or even absent. Again, the reflectivity pattern matches the reflectivity of the dip lines, as evidenced at the cross points and intersections with MC25 and MC04 (coherent plate boundary reflection) as well as MC06 and MC17 (weak or absent plate boundary reflection). Only ~8 km farther landward, strike line MC30 shows a completely different pattern of plate boundary reflectivity. Here the plate boundary is located at depths between 17 - 21 km (Figure 4.3c). Along line MC30, the plate boundary reflection is absent or very weak, except around the intersection with MC04, which is consistent with the reflection signal on MC04 at the corresponding depth.

Thermal constraints from numerical modelling (Kellner, 2007, Figure 4.2e) reveal the temperature structure along the plate boundary from the trench downwards. The lower limit of the coherent and highly reflective plate boundary around 15 km depths corresponds to a temperature of 120 - 150 °C (Figure 4.2). Further down-dip, plate boundary reflectivity decreases remarkably rapid in the rupture area of the 2014 Iquique earthquake and its main aftershock. Most noticeable, it stands also in sharp contrast to the region immediately north of the rupture zone (MC04), where a moderate plate boundary reflection is observed to a depth of 35 km, corresponding to a temperature well above 300 °C.

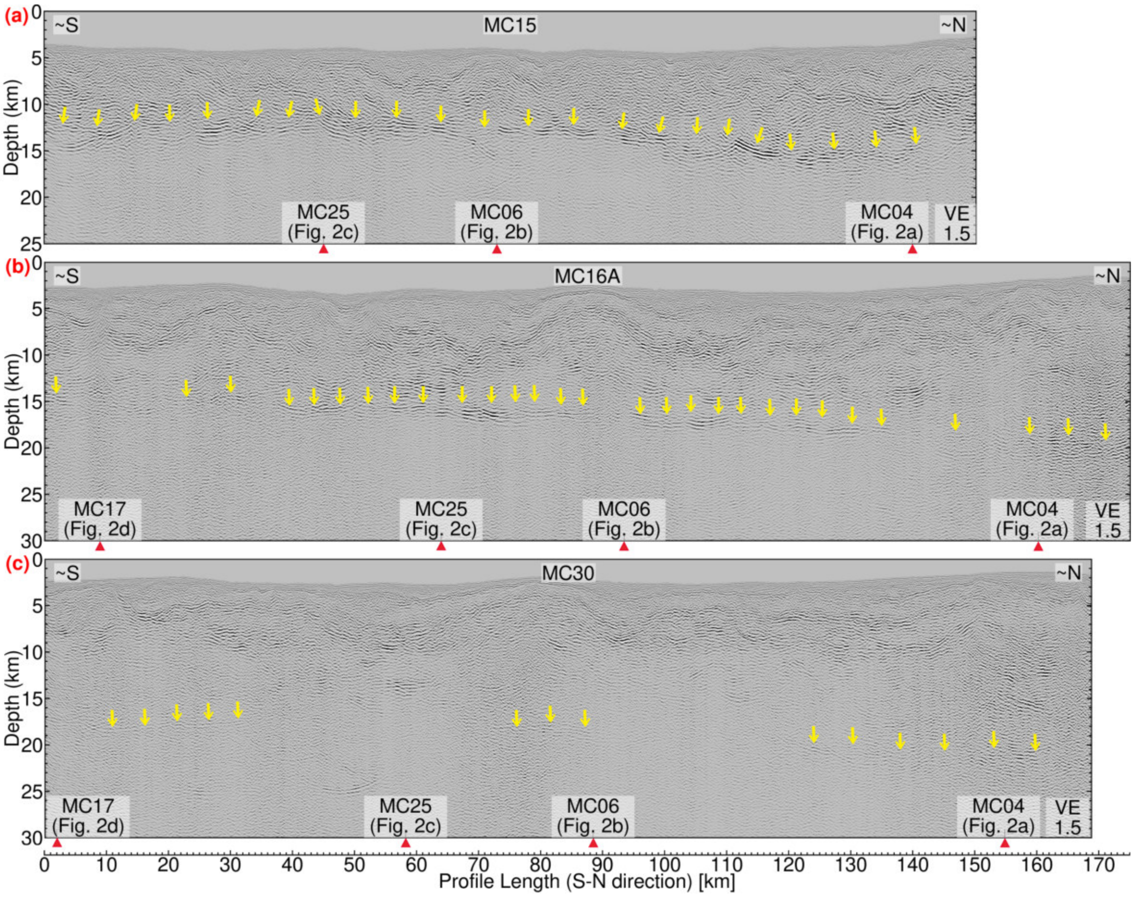

Figure 4.3: Pre-stack depth migrated sections of seismic strike-lines. Yellow arrows indicate a coherent plate boundary reflection. The red arrows specify the intersections with the dip lines. (a): seismic line MC15. (b): seismic line MC16A. (c): seismic line MC30. All symbols as in Figure 4.2.

Storch et al. (2021) observed down-dip variations in plate boundary reflectivity over short (5 - 10 km scale) distances. The maximum depth extent of reflectivity in their data is consistent with our observations. The seismic data used by Storch et al. (2021) were recorded in 1995 with a significantly shorter streamer and thus lack resolution at larger depths (> 16 km) compared to data from our seismic campaign and did not resolve the dramatic decrease in reflectivity in the region of the 2014 rupture.

4.4 Impact of fluid pressure on the 2014 Iquique earthquake rupture

A striking observation is the spatial correlation between the reflection character of the plate boundary and the rupture areas of the 2014 Iquique M_w 8.1 earthquake and the M_w 7.7

aftershock, and the aftershock distribution (Figure 4.1). Updip of both rupture areas, a highly reflective plate boundary coherently imaged on all seismic lines. Subduction zone plate boundaries that are imaged as coherent high reflections in seismic data are usually interpreted as high porosity and fluid rich fault zones. In many subduction zones, some of which have been targeted by scientific ocean drilling (Northern Barbados, Costa Rica, Nankai Trough, Hikurangi), such coherent, high reflectivity thoroughly outlines the shallow aseismic region of the plate boundary (Shipley et al., 1994; Casey Moore et al., 1998; Bangs et al., 1999; Ranero et al., 2008; Spinelli and Wang, 2008; Rampone et al., 2009; Bell et al., 2010; Bangs et al., 2015).

Along the erosive Central American margin, Ranero et al. (2008) observed a highly reflective shallow plate boundary (also compare to Bangs et al., 2015; Edwards et al., 2018). In their conceptual model, the high reflectivity is mainly caused by dehydration of sedimentary smectite clays at temperatures below 150 °C. The released fluids reduce the strength of the shallow plate boundary to an aseismic state and migrate upwards through an upper plate dissected by large normal faults. Off Northern Chile, the shallow plate boundary is also highly reflective and the outermost part of the marine forearc is similarly fractured by long-term subduction erosion (Petersen et al., 2021) and the subduction of excess lower plate topography in relation to the Iquique Ridge (Geersen et al., 2015). The small volume of trench fill along the Northern Chilean margin (Figure 4.2, also compare to Geersen et al., 2018), however, excludes subducting sediments as a significant fluid source for plate boundary reflectivity. Recent deep-ocean drilling campaigns targeting the oceanic plates offshore Costa Rica and Nankai recovered oceanic basalts with smectite concentrations (Kameda et al., 2011; Harris et al., 2013). In both cases, the smectite clay was formed as an alteration product during the basalt interaction with sea water. Dehydration of weathered clay-bearing basalt within the uppermost oceanic basement is generally less well studied and understood compared to dehydration reactions within the subducting sediments (Kastner et al., 1991; Bekins et al., 1994; Spinelli, 2004; Underwood, 2007; Saffer and Tobin, 2011), or metamorphic reactions that release fluids from the deeper sections of the oceanic crust and the upper mantle at temperatures $\dot{>}$ 300 °C Schmidt and Poli (1998); Peacock and Wang (1999); Jarrard (2003). However, similar to what is happening in the subducting sediments, dehydration of the subducting weathered basalt may initiate between the 60 °C and 150 °C isotherms (Bethke, 1986; Jarrard, 2003; Underwood, 2007; Saffer and Tobin, 2011; Kameda et al., 2011). For the fossil margin complex of the Shimanto Belt (southwest Japan), the smectite to chlorite conversion within the uppermost oceanic basement is discussed as a major source of water (Kameda et al., 2011; Hashimoto et al., 2012). Furthermore, the high *vp/vs* ratio derived from a recent local earthquake tomography using ocean bottom seismometers (Petersen et al., 2021) is indicative of hydration of the oceanic crust underneath the lower forearc. Therefore, we conclude that the coherent highly reflective aseismic shallow plate boundary off Northern Chile is fluid-rich, which is predominantly facilitated by pore water contained in intergranular and fracture porosity in layer 2a (Anderson et al., 1976; Jarrard, 2003; Kameda et al., 2011) of the oceanic crust and mineral bound water which is released through dehydration of the weathered clay-bearing oceanic basalt.

Farther downdip, into the seismogenic portion of the 2014 Iquique earthquake, the coherent reflectivity of the plate boundary diminishes rapidly where the plate boundary slipped in 2014 but not immediately to the north of the 2014 rupture zone (Figure 4.1). For the Central American margin and elsewhere, similar observations are usually explained by a reduction in fluid pressure and/or thinning of the fault zone to a thickness that lies below the resolution of seismic reflection data (Tobin and Saffer, 2009; Bangs et al., 2015). From our seismic reflection observation and the comparison to other ground-truthed subduction zones, we conclude that a high fluid content and high pore pressures at the shallow plate boundary updip of the 2014 Iquique rupture prevent the accumulation of elastic strain and therefore promote reduced coupling as suggested by Moreno et al. (2014) for the southern boundary of the 2010 Maule earthquake. In contrast, the well-drained region farther downdip promotes the build-up of elastic strain that was released during the 2014 Iquique earthquake. In particular, the three strike lines that sample the region seaward of the updip limit, the updip limit itself, and the region just below the updip limit, demonstrate the turnover from the coherent, strong reflective shallow plate boundary that did not rupture to the non-reflective plate boundary within the 2014 Iquique earthquake rupture area. While seismic resolution is a function of energy penetration with depth, profile MC04 (Figure 4.2a) documents sufficient resolution of our data set to image the plate boundary to a depth of ~35 km. While in general the reflection intensity decreases with increasing depth due to intrinsic attenuation and the viscoelastic material behavior of the subsurface (Bormann et al., 2012), the very rapid and rigorous disappearance of the plate boundary reflection over a very short depth range along-strike, in conjunction with the temperature isotherms increasing to beyond 150 °C precludes a seismic imaging problem. The ultimate reason for the higher plate boundary fluid content at depths beyond 15 km to the north of the 2014 Iquique earthquake remains enigmatic, however, our seismic reflection data clearly suggest a hydrogeological control on the updip and likely also the along-strike extent of seismic rupture along the erosive Northern Chilean continental margin.

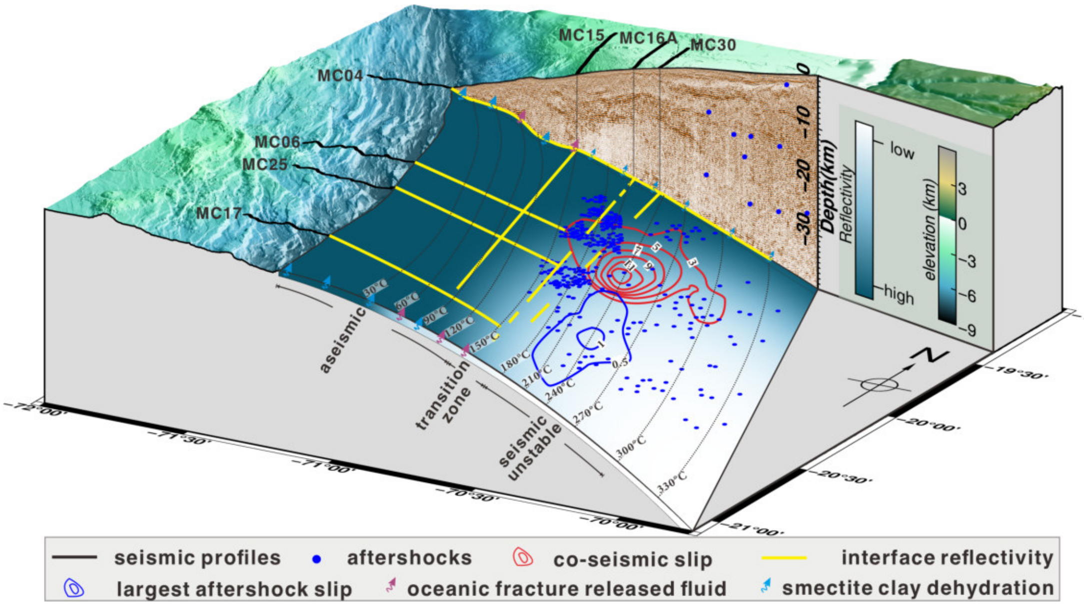

Figure 4.4: Conceptual model of the seismotectonic and hydrogeological setting in the region of the 2014 Iquique earthquake.

4.5 Implications for assessing the hazard of shallow earthquake rupture

he updip extent of seismic rupture during a plate boundary earthquake exerts a major influence on the magnitude of the associated tsunami. Models using only land geodetic measurements, however, cannot resolve whether the shallowest part of a plate boundary is locked and therefore accumulates elastic energy or if it creeps aseismically (Métois et al., 2016; Almeida et al., 2018; Kosari et al., 2020; Mallick et al., 2021). For the 2014 Iquique earthquake, we show that seismic reflectivity of the plate boundary is spatially related to the rupture area, with coherent, high reflectivity in the shallow aseismic regions that did not rupture and weak to absent reflectivity farther downdip within the rupture area (Figure 4.4). Seismic reflection data, which are sensitive to fluid-pressure variations along the shallow most part of the plate boundary, may provide crucial, but often missing, information towards a comprehensive evaluation of seismic and tsunami hazard along active margins. This is especially relevant close to the trench where land-based geodetic and seismological studies lack resolution and offshore geodetic data are sparse or missing, but where the hazard of tsunami and tsunamigenic earthquakes is greatest.

Acknowledgments and Data Availability Statement

B. Ma acknowledges funding from the China Scholarship Council (grant 201706400073). The authors gratefully acknowledge the acquisition of the MCS data and bathymetric data during cruise MGL1610 of the *R/V Marcus G. Langseth* in 2016 (United States National Science Foundation grant OCE-1459368 to Oregon State University). We thank K. Davenport for providing a preliminary version of an unpublished 3D *vp* model. Figures were generated using GMT43. EC-R thanks for the support of the ANID/FONDECYT grant 1210101.

Author Contributions

BM processed the seismic data with support of DK. BM, JG, DL and HK wrote the initial draft of the paper, which was critically revised by all co-authors. IG contributed to the discussion of the thermal models and implications of the findings. FP, MR, AT, ECR participated in cruise MGL1610 of *RV Marcus G. Langseth*. ECR, AT, MR, and YX contributed to the discussion of the seismic data. IG, DL, FP contributed to seismological topics.

Competing interests

The authors declare no competing interests.

References

Almeida, R., Lindsey, E. O., Bradley, K., Hubbard, J., Mallick, R., & Hill, E. M. (2018). Can the updip limit of frictional locking on megathrusts be detected geodetically? quantifying the effect of stress shadows on near-trench coupling. *Geophysical Research Letters*, *45*(10), 4754–4763, `https://doi.org/10.1029/2018gl077785`.

Anderson, R. N., Uyeda, S., & Miyashiro, A. (1976). Geophysical and geochemical constraints at converging plate boundaries–part i: Dehydration in the downgoing slab. *Geophysical Journal International*, *44*(2), 333–357, `https://doi.org/10.1111/j.1365-246X.1976.tb03660.x`.

Angermann, D., Klotz, J., & Reigber, C. (1999). Space-geodetic estimation of the nazca-south america euler vector. *Earth and Planetary Science Letters*, *171*(3), 329–334, `https://doi.org/10.1016/s0012-821x(99)00173-9`.

Bangs, N. L., McIntosh, K. D., Silver, E. A., Kluesner, J. W., & Ranero, C. R. (2015). Fluid accumulation along the costa rica subduction thrust and development of the seismogenic zone. *Journal of Geophysical Research: Solid Earth*, *120*(1), 67–86, `https://doi.org/10.1002/2014jb011265`.

Bangs, N. L. B., Shipley, T. H., Moore, J. C., & Moore, G. F. (1999). Fluid accumulation and channeling along the northern barbados ridge decollement thrust. *Journal of Geophysical Research: Solid Earth*, *104*(B9), 20399–20414, `https://doi.org/10.1029/1999jb900133`.

Bekins, B., McCaffrey, A. M., & Dreiss, S. J. (1994). Influence of kinetics on the smectite to illite transition in the barbados accretionary prism. *Journal of Geophysical Research: Solid Earth*, *99*(B9), 18147–18158, `https://doi.org/10.1029/94jb01187`.

Bell, R., Sutherland, R., Barker, D. H. N., Henrys, S., Bannister, S., Wallace, L., & Beavan, J. (2010). Seismic reflection character of the hikurangi subduction interface, new zealand, in the region of repeated gisborne slow slip events. *Geophysical Journal International*, *180*(1), 34–48, `https://doi.org/10.1111/j.1365-246X.2009.04401.x`.

Bethke, C. M. (1986). Inverse hydrologic analysis of the distribution and origin of gulf coast-type geopressured zones. *Journal of Geophysical Research*, *91*(B6), `https://doi.org/10.1029/JB091iB06p06535`.

Bormann, P., Engdahl, E. R., & Kind, R. (2012). *Seismic Wave Propagation and Earth models*, volume 1-105 of *New Manual of Seismological Observatory Practice 2 (NMSOP2)*.

Casey Moore, J., Klaus, A., Bangs, N. L., Bekins, B., Bücker, C. J., Brückmann, W., Erickson, S. N., Hansen, O., Horton, T., Ireland, P., Major, C. O., Moore, G. F., Peacock, S., Saito, S., Screaton, E. J., Shimeld, J. W., Henry Stauffer, P., Taymaz, T., Teas, P. A., & Tokunaga, T. (1998). Consolidation patterns during initiation and evolution of a plate-boundary decollement zone: Northern barbados accretionary prism. *Geology*, *26*(9), `https://doi.org/10.1130/0091-7613(1998)026<0811:Cpdiae>2.3.Co;2`.

Duputel, Z., Jiang, J., Jolivet, R., Simons, M., Rivera, L., Ampuero, J. P., Riel, B., Owen, S. E., Moore, A. W., Samsonov, S. V., Ortega Culaciati, F., & Minson, S. E. (2015). The iquique earthquake sequence of april 2014: Bayesian modeling accounting for prediction uncertainty. *Geophysical Research Letters*, *42*(19), 7949–7957, `https://doi.org/10.1002/2015gl065402`.

Edwards, J. H., Kluesner, J. W., Silver, E. A., Brodsky, E. E., Brothers, D. S., Bangs, N. L., Kirkpatrick, J. D., Wood, R., & Okamoto, K. (2018). Corrugated megathrust revealed offshore from costa rica. *Nature Geoscience*, *11*(3), 197–202, `https://doi.org/10.1038/s41561-018-0061-4`.

Farr, T. G., Rosen, P. A., Caro, E., Crippen, R., Duren, R., Hensley, S., Kobrick, M., Paller, M., Rodriguez, E., Roth, L., Seal, D., Shaffer, S., Shimada, J., Umland, J., Werner, M., Oskin, M., Burbank, D., & Alsdorf, D. (2007). The shuttle radar topography mission. *Reviews of Geophysics*, *45*(2), `https://doi.org/10.1029/2005rg000183`.

Geersen, J., Ranero, C. R., Barckhausen, U., & Reichert, C. (2015). Subducting seamounts control interplate coupling and seismic rupture in the 2014 iquique earthquake area. *Nat Commun*, *6*, 8267, `https://doi.org/10.1038/ncomms9267`.

Geersen, J., Ranero, C. R., Klaucke, I., Behrmann, J. H., Kopp, H., Tréhu, A. M., Contreras-Reyes, E., Barckhausen, U., & Reichert, C. (2018). Active tectonics of the north chilean marine forearc and adjacent oceanic nazca plate. *Tectonics*, *37*(11), 4194–4211, `https://doi.org/10.1029/2018tc005087`.

Harris, R., Sakaguchi, A., Petronotis, K., Baxter, A., Berg, R., Burkett, A., Charpentier, D., & Choi, J., e. a. (2013). *Input site U1414. Proc. IODP|*. Report.

Hashimoto, Y., Eida, M. I. O., Kirikawa, T., Iida, R., Takagi, M. I. E., Furuya, N., Nikaizo, A., Kikuchi, T., & Yoshimitsu, T. (2012). Large amount of fluid migration around shallow seismogenic depth preserved in tectonic mélange: Yokonami mélange, the cretaceous shimanto belt, kochi, southwest japan. *Island Arc*, *21*(1), 53–64, `https://doi.org/10.1111/j.1440-1738.2011.00806.x`.

Hayes, G. P., Herman, M. W., Barnhart, W. D., Furlong, K. P., Riquelme, S., Benz, H. M., Bergman, E., Barrientos, S., Earle, P. S., & Samsonov, S. (2014). Continuing megathrust earthquake potential in chile after the 2014 iquique earthquake. *Nature*, *512*(7514), 295–8, `https://doi.org/10.1038/nature13677`.

Hubbert, M. K. & Rubey, W. W. (1959). Role of fluid pressure in mechanics of overthrust faulting. *Geological Society of America Bulletin*, *70*(2), `https://doi.org/10.1130/0016-7606(1959)70[115:Rofpim]2.0.Co;2`.

Hurowitz, J. A. & McLennan, S. M. (2007). A 3.5 ga record of water-limited, acidic weathering conditions on mars. *Earth and Planetary Science Letters*, *260*(3-4), 432–443, `https://doi.org/10.1016/j.epsl.2007.05.043`.

Jarrard, R. D. (2003). Subduction fluxes of water, carbon dioxide, chlorine, and potassium. *Geochemistry, Geophysics, Geosystems*, *4*(5), `https://doi.org/10.1029/2002gc000392`.

Kameda, J., Ujiie, K., Yamaguchi, A., & Kimura, G. (2011). Smectite to chlorite conversion by frictional heating along a subduction thrust. *Earth and Planetary Science Letters*, *305*(1-2), 161–170, `https://doi.org/10.1016/j.epsl.2011.02.051`.

Kastner, M., Elderfield, H., & Martin, J. B. (1991). Fluids in convergent margins: what do we know about their composition, origin, role in diagenesis and importance for oceanic chemical fluxes? *Philosophical Transactions of the Royal Society of London. Series A: Physical and Engineering Sciences*, *335*(1638), 243–259, `https://doi.org/10.1098/rsta.1991.0045`.

Kellner, A. (2007). *Different styles of deformation of the fore-arc wedge along the Chilean convergent margin: insights from 3D numerical experiments.* Thesis.

Kosari, E., Rosenau, M., Bedford, J., Rudolf, M., & Oncken, O. (2020). On the relationship between offshore geodetic coverage and slip model uncertainty: Analog megathrust earthquake case studies. *Geophysical Research Letters*, *47*(15), `https://doi.org/10.1029/2020gl088266`.

Mallick, R., Meltzner, A. J., Tsang, L. L. H., Lindsey, E. O., Feng, L., & Hill, E. M. (2021). Long-lived shallow slow-slip events on the sunda megathrust. *Nature Geoscience*, `https://doi.org/10.1038/s41561-021-00727-y`.

Moore, J. C. & Saffer, D. (2001). Updip limit of the seismogenic zone beneath the accretionary prism of southwest japan: An effect of diagenetic to low-grade metamorphic processes and increasing effective stress. *Geology*, *29*(2), `https://doi.org/10.1130/0091-7613(2001)029<0183:Ulotsz>2.0.Co;2`.

Moreno, M., Haberland, C., Oncken, O., Rietbrock, A., Angiboust, S., & Heidbach, O. (2014). Locking of the chile subduction zone controlled by fluid pressure before the 2010 earthquake. *Nature Geoscience*, *7*(4), 292–296, `https://doi.org/10.1038/ngeo2102`.

Métois, M., Vigny, C., & Socquet, A. (2016). Interseismic coupling, megathrust earthquakes and seismic swarms along the chilean subduction zone (38°–18°s). *Pure and Applied Geophysics*, *173*(5), 1431–1449, `https://doi.org/10.1007/s00024-016-1280-5`.

Peacock, S. M. & Wang, K. (1999). Seismic consequences of warm versus cool subduction metamorphism: examples from southwest and northeast japan. *Science*, *286*(5441), 937–9, `https://doi.org/10.1126/science.286.5441.937`.

Petersen, F., Lange, D., Ma, B., Grevemeyer, I., Geersen, J., Klaeschen, D., Contreras-Reyes, E., Barrientos, S., Tréhu, A. M., Vera, E., & Kopp, H. (2021). Relationship between subduction erosion and the up-dip limit of the 2014 mw 8.1 iquique earthquake. *Geophysical Research Letters*, *48, e2020GL092207*(9), `https://doi.org/10.1029/2020GL092207`.

Rampone, E., Hofmann, A. W., & Raczek, I. (2009). Isotopic equilibrium between mantle peridotite and melt: Evidence from the corsica ophiolite. *Earth and Planetary Science Letters*, *288*(3-4), 601–610, `https://doi.org/10.1016/j.epsl.2009.10.024`.

Ranero, C. R., Grevemeyer, I., Sahling, H., Barckhausen, U., Hensen, C., Wallmann, K., Weinrebe, W., Vannucchi, P., von Huene, R., & McIntosh, K. (2008). Hydrogeological system of erosional convergent margins and its influence on tectonics and interplate seismogenesis. *Geochemistry, Geophysics, Geosystems*, *9*(3), `https://doi.org/10.1029/2007gc001679`.

Ruiz, S., Metois, M., Fuenzalida, A., Ruiz, J., Leyton, F., Grandin, R., Vigny, C., Madariaga, R., & Campos, J. (2014). Intense foreshocks and a slow slip event preceded the 2014 iquique mw 8.1 earthquake. *Science*, *345*(6201), 1165–9, `https://doi.org/10.1126/science.1256074`.

Saffer, D. M. & Tobin, H. J. (2011). Hydrogeology and mechanics of subduction zone forearcs: Fluid flow and pore pressure. *Annual Review of Earth and Planetary Sciences*, *39*(1), 157–186, `https://doi.org/10.1146/annurev-earth-040610-133408`.

Schmidt, M. W. & Poli, S. (1998). Experimentally based water budgets for dehydrating slabs and consequences for arc magma generation. *Earth and Planetary Science Letters*, *163*(1-4), 361–379, `https://doi.org/10.1016/s0012-821x(98)00142-3`.

Schurr, B., Asch, G., Hainzl, S., Bedford, J., Hoechner, A., Palo, M., Wang, R., Moreno, M., Bartsch, M., Zhang, Y., Oncken, O., Tilmann, F., Dahm, T., Victor, P., Barrientos, S., & Vilotte, J. P. (2014). Gradual unlocking of plate boundary controlled initiation of the 2014 iquique earthquake. *Nature*, *512*(7514), 299–302, `https://doi.org/10.1038/nature13681`.

Schurr, B., Moreno, M., Tréhu, A. M., Bedford, J., Kummerow, J., Li, S., & Oncken, O. (2020). Forming a mogi doughnut in the years prior to and immediately before the 2014 mw8.1 iquique, northern chile, earthquake. *Geophysical Research Letters*, *47*(16), `https://doi.org/10.1029/2020gl088351`.

Shipley, T. H., Moore, G. F., Bangs, N. L., Moore, J. C., & Stoffa, P. L. (1994). Seismically inferred dilatancy distribution, northern barbados ridge decollement: Implications for fluid migration and fault strength. *Geology*, *22*(5), `https://doi.org/10.1130/0091-7613(1994)022<0411:Siddnb>2.3.Co;2`.

Sippl, C., Schurr, B., Asch, G., & Kummerow, J. (2018). Seismicity structure of the northern chile forearc from >100,000 double-difference relocated hypocenters. *Journal of Geophysical Research: Solid Earth*, *123*(5), 4063–4087, `https://doi.org/10.1002/2017jb015384`.

Spinelli, G. A. (2004). Along-strike variations in underthrust sediment dewatering on the nicoya margin, costa rica related to the updip limit of seismicity. *Geophysical Research Letters*, *31*(4), `https://doi.org/10.1029/2003gl018863`.

Spinelli, G. A. & Wang, K. (2008). Effects of fluid circulation in subducting crust on nankai margin seismogenic zone temperatures. *Geology*, *36*(11), `https://doi.org/10.1130/g25145a.1`.

Storch, I., Buske, S., Victor, P., & Oncken, O. (2021). Seismic images of the northern chilean subduction zone at 19°40s, prior to the 2014 iquique earthquake. *Geophysical Journal International*, *225*(2), 1048–1061, `https://doi.org/10.1093/gji/ggab035`.

Tobin, H. J. & Saffer, D. M. (2009). Elevated fluid pressure and extreme mechanical weakness of a plate boundary thrust, nankai trough subduction zone. *Geology*, *37*(8), 679–682, `https://doi.org/10.1130/g25752a.1`.

Tréhu, A. M., Vera, E., & Riedel, M. (2017). *PICTURES: Pisagua/Iquique crustal tomography to understand the region of the earthquake source.* Report.

Underwood, M. B. (2007). *Sediment Inputs to Subduction Zones: Why Lithostratigraphy and Clay Mineralogy Matter.* The seismogenic zone of subduction thrust faults. Columbia University Press, 2007.

Supporting Information

Seismic Processing

Seismic data processing was conducted with the Schlumberger OMEGA2 software. Here we present the processing sequences and the corresponding results in terms of seismic line MC04. The same processing strategy is used for all profiles to eliminate possible discrepancies of the plate boundary interface during processing. An overview of the processing scheme is shown below (Suppl. Figure 4.5). The main seismic processing included four steps:

A. Step1: Processing Geometry Implementation

In this step, the seismic data are exposed to a series of pre-processing modules, including sail extract module, geometry crooked module, geometry update module and grid define module, aiming to implement the processing geometry. In particular, the sail extract module is used to merge the geometry survey file information with the seismic traces. The geometry crooked module analyses the location of detectors, sources, and midpoints and projects them onto a smooth 2D crooked common-mid-point (CMP) profile. Subsequently, the geometry update module and the grid define module were used to update the seismic trace header literals to the new processing grid. These pre-processing steps prepare the seismic data set for further analysis. Seismic shooting was conducted at an interval of 125 m to avoid interference from the previous shot. Due to the large shot interval, the original CMP gathers are imaged with prominent spatial aliasing. The aliasing has serious effects on the performance of multichannel data analysis processes such as *f-k* filtering. Because of spatial aliasing, these processes can perceive events with steep dips at high frequencies as different from what they are and, hence, do not treat them properly.

B. Step2: Increase Vertical Resolution and General Noise Cleaning

In this step, four modules were used to increase the vertical resolution and clean the general noise. In particular, the deconvolution module is applied to compress the basic wavelet, thus increasing temporal resolution. The direct wave cleaning module was employed in shallow seafloor areas to enhance near-surface wide-angle reflections. Attenuation of random noise (RNA) was applied by a predictive deconvolution in the fx-domain. The anomalous amplitude attenuation (AAA) removed high amplitude events such as marine swell, rig and ship noise by transforming the seismic data into frequency bands and applying a spatial median filter. These pre-processing steps yield CMP gathers (Suppl. Figure 4.6a) which will be interpolated in the next step.

C. Step3: Shot Interpolation

To avoid prominent spatial aliasing between neighboring shots resulting from the large shot interval, shot-ordered seismic data were interpolated three times from 125 m to 15.625 m by *f-k* trace interpolation. As the result is not a multiple of the receiver interval, an irregular interpolator module was used to interpolate it to 12.5 m, where aliased components have been eliminated (Suppl. Figure 4.6b).

D. Step 4: Multiple attenuation

Prior to multiple attenuation, the plate boundary reflection is severely obscured by multiples (Suppl. Figure 4.7a). The multiples were predicted by surface related multiple elimination (SRME) using wavefield inversion based on the Kirchhoff integral and subtracted from the raw data after shot interpolations. After the multiple attenuation, we applied the *f-k* filtering to remove the high frequencies to enhance the image (Suppl. Figure 4.7b). The plate boundary reflection is clearly observed in the travel time range where the first multiple occurs and we can now trace the plate boundary interface further landward on the time section of seismic line MC04 (Suppl. Figure 4.8). The extensive data volume generated by the shot interpolations led to long calculation times in the pre-stack time domain and the pre-stack depth domain, so we reconstructed the offsets of CMP gathers with an increment of 100 m. After the reconstruction of offset distances, a preliminary *vp* model based on an unpublished 3D *vp* model from ocean bottom seismometers (OBS) during cruise MGL1610 of the *R/V Marcus G. Langseth* in 2016 was applied for the pre-stack depth migration. Referring to the OBS velocity field, we calculated the velocity gradient starting from the seafloor to yield an initial velocity model (Suppl. Figure 4.9) for application to the multichannel seismic profiles. Although this initial velocity model is not sufficiently confining the shallow depth (< 15 km) and may produce an inaccuracy of 1 - 2 km in the depth of the plate boundary compared to an accurate velocity model, it does not affect the spatial distribution of the reflectivity. In the meanwhile, this initial velocity does not enable to carry out amplitude analysis. However, our main focus is on the reflectivity pattern and the lateral coherence and continuity of the plate boundary reflectivity. The pre-stack depth migrated seismic images are not significantly affected by seafloor multiples anymore and resolve sub-seafloor structures in the upper plate and subducting lower plate at high resolution (Suppl. Figure 4.10).

Supplementary Discussion

Reflection energy absorption, seismic processing parameters, differences of gun energy during seismic acquisition and shooting direction may all potentially cause a variation of reflectivity along the plate boundary. To allow a spatial comparison of the reflectivity and avoid issues caused by seismic processing, the same processing strategy is used for all profiles. In addition, we discuss the following issues:

A. Is the plate interface on seismic line MC04 visible to greater depth because of stronger gun energy during data acquisition? The plate interface is traced to a depth of approximately 35 km on the northern dip line MC04 but disappears at shallower depth on the dip lines that run through the rupture area of the 2014 Iquique earthquake. The acquisition geometry and gun array remained unchanged during the survey, which covered seismic lines parallel to the trench as well as profiles in the dip direction. Strike line MC30, which crosses the middle continental slope and is located furthest from the trench axis, documents that the plate interface along the northern part of the line can be traced to greater depth than along the southern part. This observation is augmented by all seismic dip lines and seismic strike lines of our survey.

B. Is the difference of the plate interface reflection caused by shooting direction?

The shooting direction did not cause the observed differences of the plate interface reflection as seismic dip lines MC04, MC 06, and MC25 were shot from west to east, while seismic dip lines MC17 and MC231 were shot from east to west. There are at least two seismic lines in the same direction, documenting that the shooting direction does not exert a major influence.

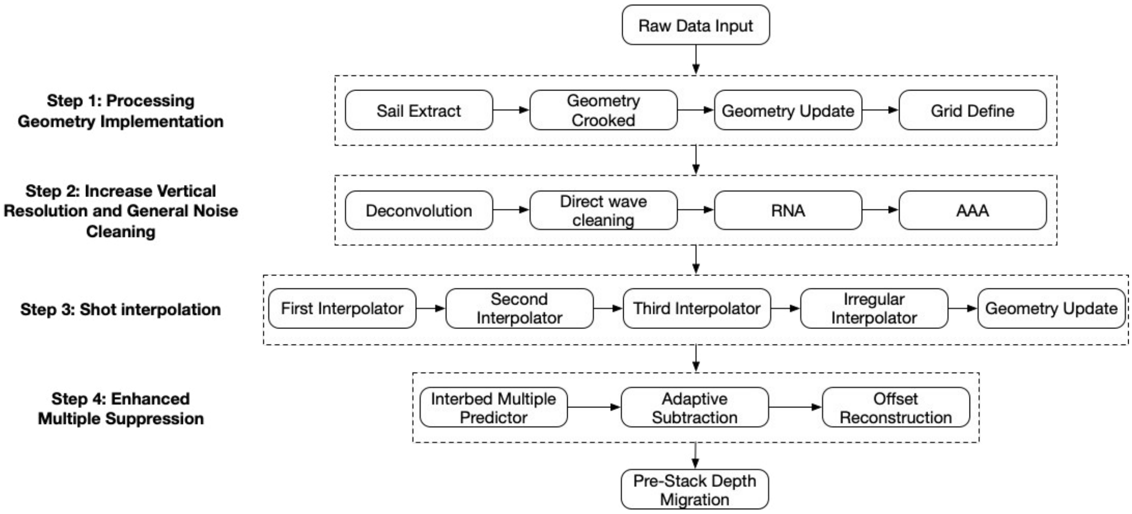

Figure 4.5: Overview of the processing sequence.

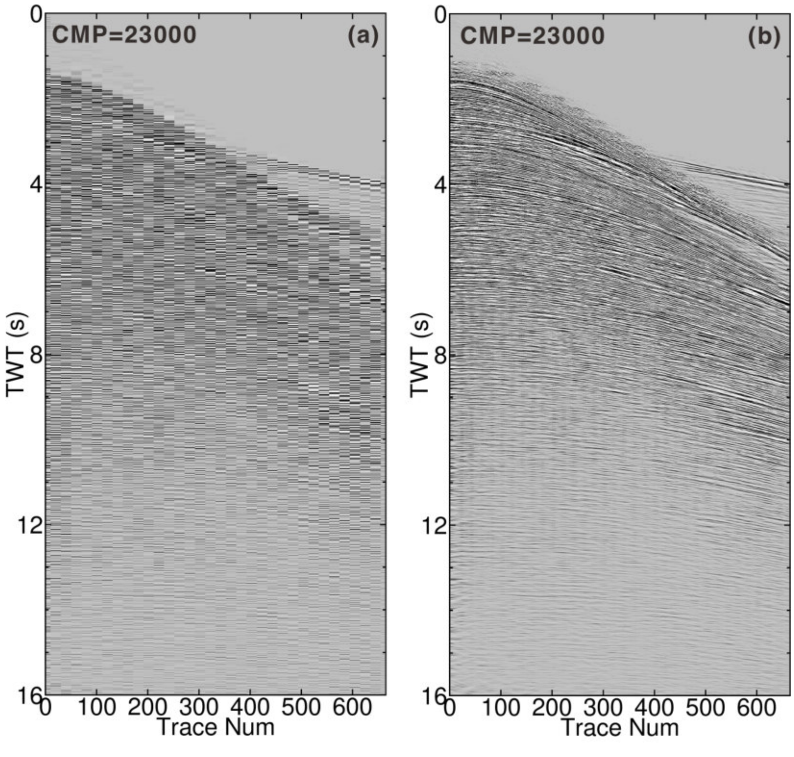

Figure 4.6: The CMP gathers before and after interpolation of seismic line MC04. Before the interpolation processing, the trace spacing is 250 m, which is shown in (a). After the interpolation processing the trace spacing is 25 m in (b).

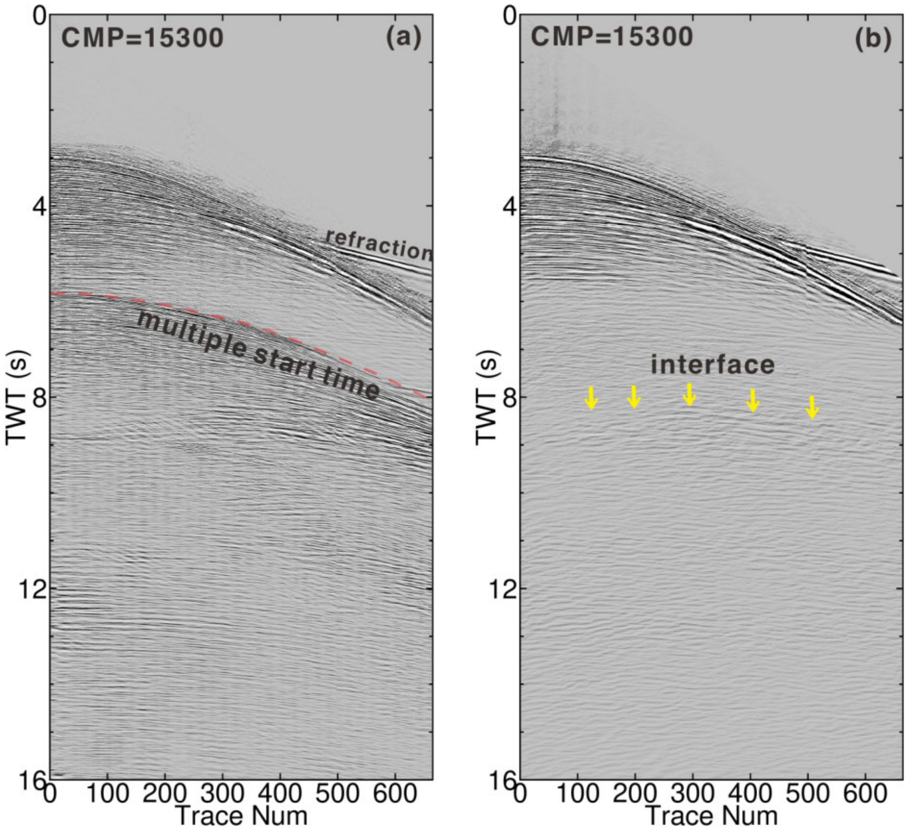

Figure 4.7: The CMP gathers before and after the de-multiple step of MC04. Before the demultiple processing, seismic signals are obscured by several multiple orders below the seafloor multiple start time indicated by the transparent red dashed line in (a). After the demultiple processing and high frequencies elimination, the multiples are mostly eliminated and we can see the interface traced by yellow arrows around 8 - 9 s TWT in (b).

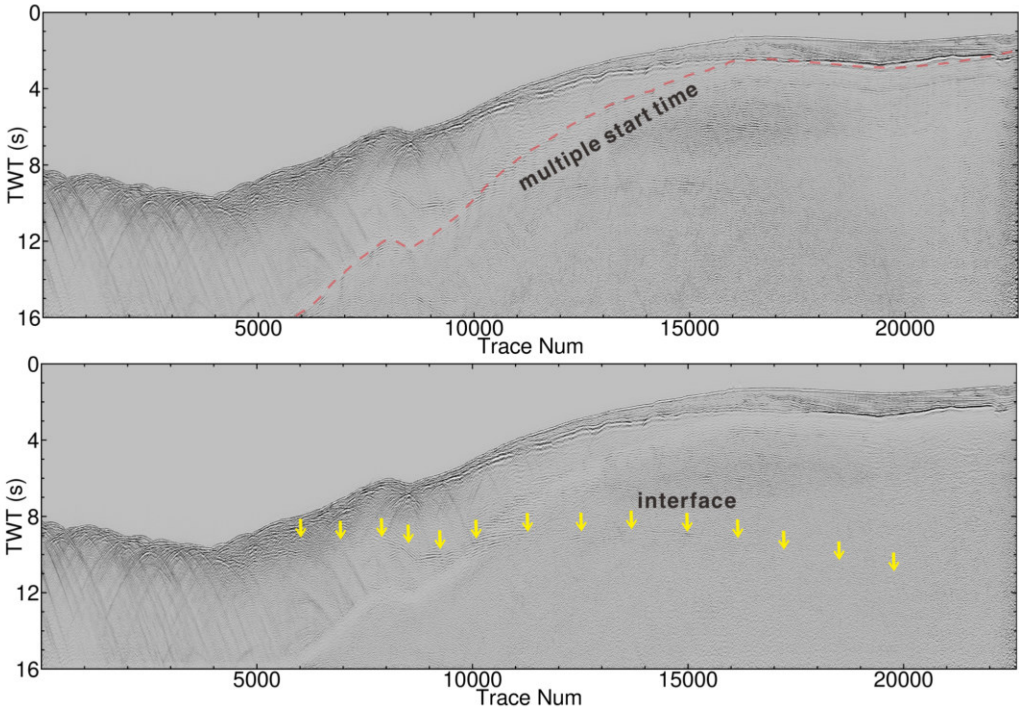

Figure 4.8: Stack section in the time domain of seismic line MC04 before and after the demultiple processing. Before the demultiple processing, the interface reflection is obscured by the multiples below the seafloor multiple start time indicated by the transparent red dashed line in (a). After the demultiple processing, the interface reflection can be traced around trace number 20000, as indicated by the yellow arrows in (b). Sections are shown after application of a depth customized gain of amplitudes.

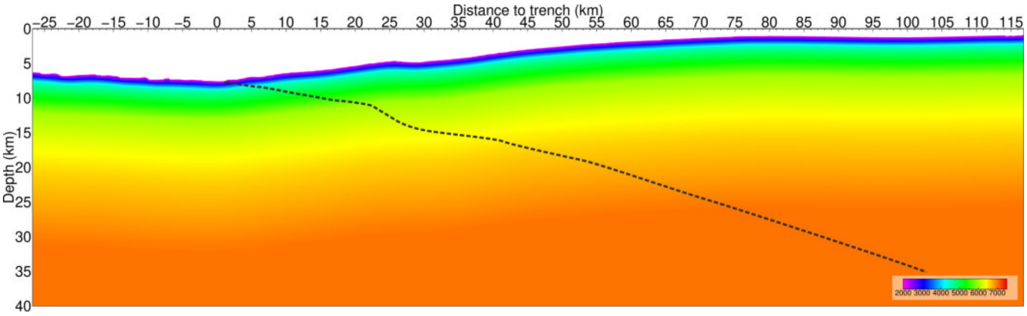

Figure 4.9: An initial variation velocity model based on an unpublished 3D OBS velocity model was applied for the pre-stack depth migration. The black dashed line indicates the plate boundary of profile MC04.

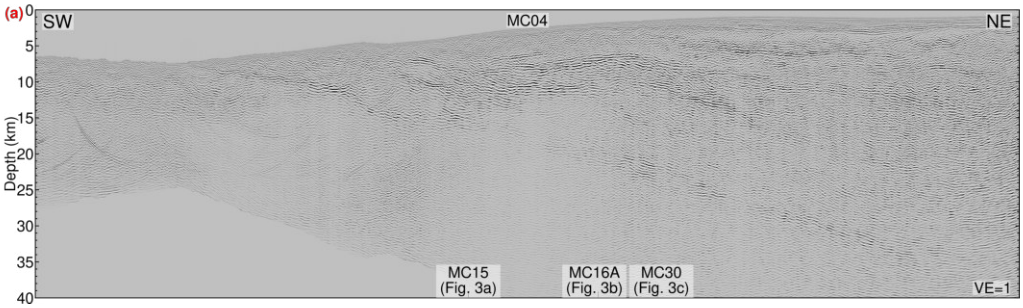

Figure 4.10: The pre-stack depth migrated seismic image of seismic line MC04.

5 Repeating earthquakes reveal pre-seismic upper plate weakening by the 2014 Iquique foreshock sequence

Florian Petersen[1], Dietrich Lange[1], Ingo Grevemeyer[1], Eduardo Contreras-Reyes[3] and Heidrun Kopp[1,2]

1) GEOMAR Helmholtz Centre for Ocean Research Kiel, Kiel, Germany
2) Institute of Geosciences, Kiel University, Kiel, Germany
3) Departamento de Geofísica, Facultad de Ciencias Físicas y Matemáticas, Universidad de Chile, Santiago, Chile

Submitted to **Journal of Geophysical Research: Solid Earth**, August 2021.

Key Points

- Repeating earthquakes are used to study the depth-dependent variation of slip in the marine forearc.
- The OBS data allow to discriminate between repeaters in the upper plate and plate interface during the seismic cycle.
- The gradual unlocking of the plate interface forces the reverse reactivation of upper plate extensional faults causing subduction erosion.

Abstract

Repeating earthquakes are considered to be a proxy for the surrounding aseismic slip. Here, we analyze offshore hypocenters several years before and after the 2014 M_w 8.1 Iquique earthquake. High-resolution ocean-bottom seismometer recordings of repeating earthquakes during the inter-, pre- and postseismic phase document the depth-dependent slip in the overriding South American plate. We find upper plate repeating earthquakes aligned parallel to the trench and coast, suggesting a large trench parallel striking fault structure in the upper plate as the origin of those events. The analysis of repeater sequences focal mechanisms reveals a reverse reactivation of the large-scale extensional faults induced by the 2014 Iquique foreshock sequences at the seismogenic up-dip limit. The cumulative slip in the frontal overriding plate accelerates ten days before the mainshock, suggesting a shortening of the frontal wedge. We propose that the pre-seismic gradual unlocking of the plate interface forced upper plate extensional faults to slip in thrust mode in response to the basal erosion of the upper plate.

Plain Language Summary

The north Chilean subduction zone consists of the down-going, subducting Nazca plate and the overriding South American plate. The contact zone between the two tectonic plates produces the largest earthquakes on the planet. Before and after such large earthquakes, like the M_w 8.1 2014 event, smaller earthquakes are generated, known as fore- and aftershocks. Some of these earthquakes are repeated earthquakes. These repeating earthquakes are ruptures at the same location at different times with very similar rupture behavior repeatedly breaking the same small patch. Our study searches for repeating

earthquakes before and after the mainshock. We use ocean-bottom seismometers to estimate the accurate location of the repeating earthquakes throughout several years before and after the main earthquake. We find that deformation has occurred on large fractures in the overriding plate before the 2014 earthquake and increased during the last ten days. Estimates of the faulting mechanisms of the repeating earthquakes have shown that the overriding plate is under compression, which means that the tectonic erosion of the plate has been reactivated. We propose that the overriding plate enters a long phase of relaxation and extension of the fractures sets in while stress builds up at the plate boundary.

5.1 Introduction

Megathrust earthquakes are one of the main drivers of subduction erosion, empowering the removal of material from the base of the overriding plate in the course of subduction. The temporal fluctuation of deformation along the megathrust and within the frontal upper plate are the key factors to understand the process of margin subsidence extending over several seismic cycles (Wang and Hu, 2006; Wang et al., 2010). Seismic reflection techniques and forearc seismicity observations reveal the tectonic structure and state of stress of shallow erosional margins (e.g., Ranero and von Huene, 2000; von Huene and Ranero, 2003; Sallarès and Ranero, 2005; Obana et al., 2013; Reginato et al., 2020; Ma et al., submitted; Läderach et al., 2012). Sediment-starved margins are often characterized by crystalline basement or older sedimentary rocks that are fractured by large extensional faulting as the result of long-term permanent subsidence of the forearc (von Huene and Lallemand, 1990; von Huene et al., 2004). In principle, the presence of upper plate extensional faults above a coseismic rate-strengthening interplate fault is contradictory to the high basal friction that is required to erode the upper plate base (Wang et al., 2010).

Repeating earthquakes (repeaters) are characterized by nearly identical waveforms and are inferred to recur at the same location by repeated rupturing of small asperities that catch up with the surrounding aseismic slip (Nadeau and McEvilly, 1999; Uchida and Bürgmann, 2019). Since their recognition two decades ago, repeaters have been found along all types of plate boundaries worldwide, including transform faults (Nadeau and Johnson, 1998; Bohnhoff et al., 2017), extensional faults (Valoroso et al., 2017; Vuan et al., 2017; Duverger et al., 2018) and convergent megathrust faults (Chen et al., 2007; Uchida and Matsuzawa, 2013; Kato and Nakagawa, 2014). Repeater studies allow the estimate of cumulative slip from moment magnitudes (M_w) and improved our understanding of aseismic/slow-slip earthquakes and earthquake triggering and our knowledge of the earthquake cycle (e.g., Uchida and Bürgmann, 2019).

The north Chilean subduction zone is an excellent area to study stress varying processes and mechanisms leading to shallow subduction erosion. The M_w 8.1 2014 Iquique earthquake demonstrated the impact of subduction erosion on postseismic stress changes on the marine forearc by the occurrence of abundant aftershock seismicity at the seismogenic up-dip limit (León-Ríos et al., 2016; Petersen et al., 2021). The megathrust event on April 1, 2014, was preceded by an intensive and long foreshock sequence in the up-dip area of the main rupture starting in July 2013 (Schurr et al., 2014). Similar to the 2011 M_w 9.0 Tohoku foreshock period earthquake, the last two weeks of the Iquique precursory sequence were characterized by seismicity migration towards the nucleation center (Brodsky and Lay, 2014). However, the mechanisms that generate foreshocks are often unknown, and their duration indicates no direct relation to the mainshock magnitude (e.g., Abercrombie and Mori, 1996). On March 16, a M_w 6.7 earthquake struck in the upper plate and initiated the final phase of foreshock activity, leading to a gradual unlocking of the plate interface until April 1 (Brodsky and Lay, 2014; Kato and Nakagawa, 2014; Schurr et al., 2014; Meng et al., 2015; Herman et al., 2016; Kato et al., 2016; Schurr et al., 2020).

Interaction between upper-plate faults and the plate interface was modeled and discussed previously (e.g., Delouis et al., 1998; Kato et al., 2011; Hardebeck, 2012; Aron et al., 2013; Li et al., 2014; Contreras-Reyes et al., 2015). Activation of upper plate faults depends on the orientation of the crustal fault and its location relative to the slip on the interface (Li et al., 2014). Although some earthquakes showed this behavior [Maule 2010 earthquake: Farías et al. (2011), Lange et al. (2012); Tohoku 2011 earthquake: Kato et al. (2011)], repeating earthquakes allow observation of the interaction down to smaller slip and for longer periods.

In expectation of a great earthquake to rupture the long-standing seismic gap, which last ruptured in 1877, the north Chilean subduction zone is densely monitored onshore by the Integrated Plate Boundary Observatory Chile since 2006 (GFZ and CNRS-INSU, 2006) with permanent broadband seismic stations complemented by other permanent geophysical instruments. In response to the 2014 Iquique earthquake, additional temporary seismic stations were deployed (Soto et al. (2019). Offshore and directly above the aftershock sequence two successive long-term networks of amphibious seismic stations were deployed to augment the land network (Petersen et al., 2021). Without OBS observations, events beneath the marine forearc have poor hypocentral depth estimates because they occur outside the onshore network. As a result, slip from repeaters is mostly assumed to occur on the plate interface in subduction zones (e.g., Kato and Nakagawa, 2014; Meng et al., 2015; Kato et al., 2016). The OBS networks installed after the M_w 8.1 2014 Iquique earthquake allow to discriminate between the megathrust and upper plate faulting. The comprehensive long-term monitoring of earthquakes along the north Chilean subduction zone allows the investigation of seismic slip-related processes during the interseismic and postseismic phase during the end of one seismic cycle.

This study examines recent seismicity catalogs for the northern Chilean subduction zone to detect repeating earthquakes. To study the depth-dependent behavior of repeating earthquakes, we estimate the sequence hypocenter using high-resolution offshore hypocenter locations from an amphibious seismometer deployment conducted over 23 months after the Iquique earthquake. Since repeaters rupture repeatedly the identical fault patch, high-resolution hypocentral depths can be obtained for all events in case the location is accurately known for at least one event. We suggest that the gradual unlocking of the plate interface at the seismogenic up-dip limit drives the frontal upper plate into a compressive state of stress. This progressively weakens the upper plate, resulting in the reverse reactivation of the large-scale extensional faults and in active subduction erosion of the overriding South American plate.

5.2 Data and methods

5.2.1 Earthquake catalogs

In northern Chile, several seismological studies investigated the seismicity at the plate interface between the overriding South American plate and the subducting Nazca plate (e.g., Ruiz et al., 2014; Sippl et al., 2018; Soto et al., 2019), including a two-year amphibious deployment (Petersen et al., 2021). To identify the maximum number of repeating earthquakes, we use earthquakes from published catalogs covering the interseismic phase and six years of the postseismic phase (2007 until December 2020). The catalogs of Sippl et al. (2018) and Centro Seismológico Nacional (CSN; Barrientos, 2018) start in 2007 and cover the entire north Chilean region. During the 2014 Iquique foreshock series and after the mainshock, the permanent land stations were complemented by over 80 additional temporary seismic stations (Soto et al., 2019). The resulting catalog from Soto et al. (2019) starts in March 2014 and focuses on the rupture area of the 2014 Iquique earthquake and its greatest aftershock. The catalog ends shortly after the deployment of OBS in December 2014, which encompasses 1,778 events during 23 months of offshore seismological recordings of the marine forearc until the end of October 2016 (Petersen et al., 2021). The catalog from CSN (Barrientos, 2018) covers the period from November 2016 until December 2020, following the OBS deployment. We focus on the region of the 2014 Iquique rupture (19 °S - 21 °S and 70.0 °W - 72 °W, Figure 5.1).

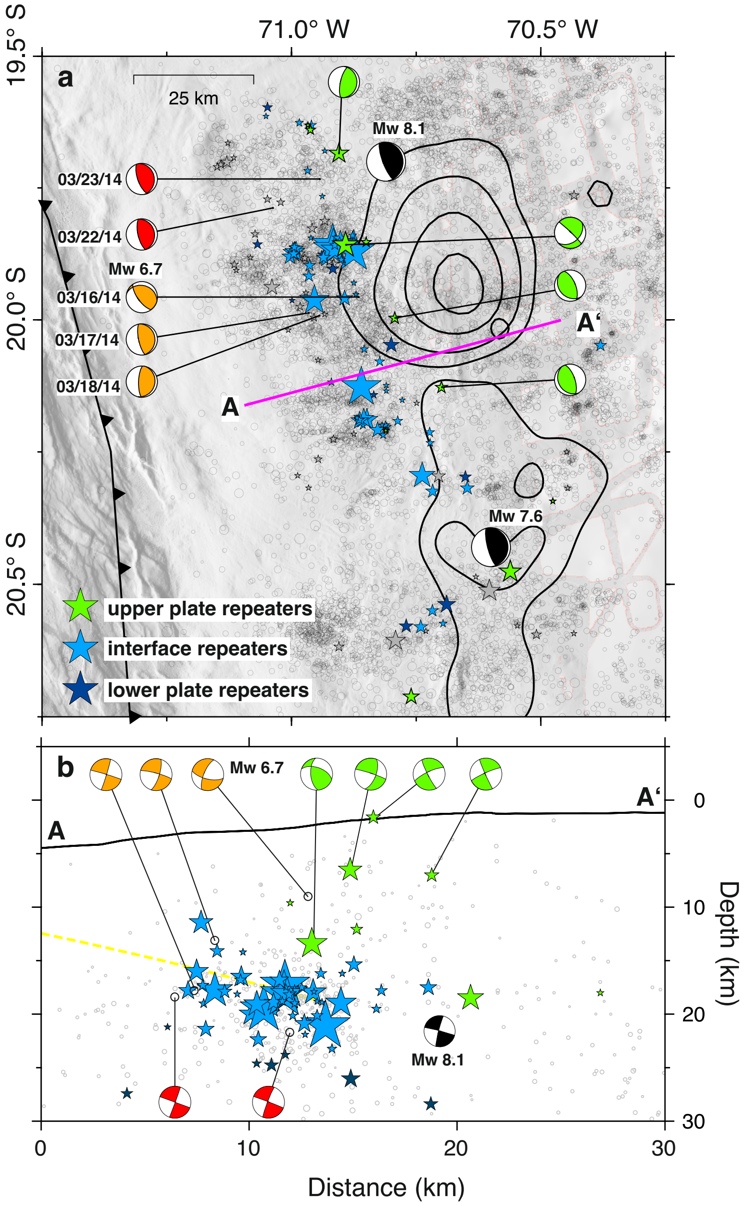

Figure 5.1: Repeating earthquake analysis offshore northern Chile. (a) Map view of the 2014 Iquique rupture area. The stars mark relocated (blue and green) and non-relocated (gray) repeating earthquake sequences. Upper plater repeater clusters are indicated in green und repeater clusters along the plate interface in light blue. Symbol size is scaled by the number of repeaters per sequence (4 − 30). Black lines indicate the coseismic slip model (Duputel et al., 2015, 3, 6, 9, and 12 m contour lines) and aftershock slip model (Duputel et al., 2015, 0.85 and 0.6 m contour lines). Bathymetry from (Geersen et al., 2018) combined with GEBCO, SRTM Topography from Farr et al. (2007). Focal mechanisms mark the location of the two foreshocks with the first three $M_w \geq 6$ between March 16 and March 18 (orange) and the second $M_w > 6$ from March 22 until March 23 (red), including the April 1 mainshock (M_w 8.1) and greatest aftershock (M_w 7.6) in black. The seismicity from the searched catalog is shown as gray circles. (b) Cross-profile through the marine forearc up-dip offshore northern Chile. Stars mark the location of relocated repeating earthquake sequences within the upper plate, plate interface and lower plate. The plate boundary derived from multi-channel seismic data (Petersen et al., 2021) is indicated as a blue dashed line.

5.2.2 Identifying repeating earthquakes

Our combined seismological catalog encompasses 15,429 earthquakes from January 2007 until December 2020. We performed cross-calculations on the vertical components between all earthquakes with a horizontal inter-event distance of less than 20 km, taking the highest location uncertainties into account. To find as many repeaters as possible, we use waveforms of 18 broadband land-stations (seismic networks CX and C1) and 5 OBS deployed in the vicinity of the 2014 Iquique earthquake rupture area for cross-correlation. In addition, we estimated theoretical P-phase onsets on unpicked stations (TauP, Crotwell et al., 1999) using a local minimum 1D velocity model (Petersen et al., 2021).

The identification of repeating earthquakes depends on the moment magnitudes, and hence the corner frequency. In general, two earthquakes located within a quarter of a wavelength cannot be separated based on waveform similarity (Geller and Mueller, 1980). Therefore, the search for repeating earthquakes requires high-frequency waveform data with quarter wavelengths smaller than the event rupture size from scaling relations to identify repeating earthquakes. The waveforms are filtered using a band-pass with four different overlapping frequency bands ($0.1-1$ Hz; $0.5-2$ Hz; $1-4$ Hz, and $3-15$ Hz). We consider the recommended minimum frequency for certain earthquake moment magnitudes from Uchida (2019) to reduce the number of potentially different earthquakes. Next, we cross-correlate the vertical components starting 5 s before and 30 s after the P-phase onset to make sure the S-phase is included.

We classify event pairs if the cross-correlation coefficient (CC) is above 0.95, following the Igarashi et al. (2003) repeater criterion. A histogram of the cross-correlation coefficient from broadband station PB11 is shown in Figure 5.6. An event pair whose cross-correlation coefficient is larger than 0.95 at a cross-correlation waveform length of 35 s and identified at two or more stations is further considered as a repeater event pair. In total, we identified 2,608 repeater event pairs. The last step to combine repeating earthquake sequences is to group repeater event pairs that have events in common into a cluster of repeating earthquakes until all clusters are mutually exclusive.

5.2.3 Seismic fault slip estimation

Earthquake pairs with high CC at the same station can be considered as recurrent earthquakes, representing repeated ruptures of the same fault patch. In general, repeating earthquakes are defined as small asperities catching up with the surrounding aseismic slip (Uchida and Bürgmann, 2019). To quantitate the seismic slip driven by the aseismic surrounding, we converted the seismic moment M_0 (dyn cm) to fault slip d (cm), employing the widely used empirical relationship (Nadeau and Johnson, 1998; Igarashi et al., 2003):

$$log(d) = 2.36 + 0.17\ log(M_0) \tag{5.1}$$

The seismic moment M_0 can be estimated using the relationship between moment magnitude M_w and scalar seismic moment (Hanks and Kanamori, 1979):

$$log(M_0) = 1.5M_w + 16.1 \tag{5.2}$$

Not all used catalogs included moment magnitudes (M_w) for all events. Therefore, we converted local magnitudes (M_l) to M_w to estimate the M_0 using a relationship between local magnitudes and moment magnitudes for the Iquique area (Figure 5.2; Petersen et al., 2021). The $M_l - M_w$ empirical relationship is comparable to the 2010 MauleM_w 8.8 earthquake aftershock sequence (Lange et al., 2012) up to a local magnitude of 4.1. For higher local magnitudes, we use the $M_l - M_w$ relationship to convert the magnitudes determined for northern Chile (Meng et al., 2015).

$$\begin{array}{ll} M_w = 0.74\ M_l + 1.56 & M_l \leq 4.1 \\ M_w = M_l + 0.09 & 4.1 < M_l < 5.71 \end{array} \tag{5.3}$$

Prior to the Iquique earthquake (from 2007 until the end of March 2014) the magnitude of completeness (M_c) for the catalogs from Sippl et al. (2018) and Soto et al. (2019) is between M_c 2.7 and 2.9, respectively. Owing to the increase in numbers of the aftershock station deployment, the M_c decreases to 1.7 shortly after the mainshock on April 1, 2014 until December 2014. During the OBS deployment, the M_c is 1.8 during 2015 and 2.5 in 2016 (Petersen et al., 2021). After the final recovery of OBS in November 2014, the M_c increases to 3.5, as a result of the decrease in station density along the north Chilean coast (Barrientos, 2018). Due to the M_c variations in time, it is possible that the cumulative slip based on found repeating earthquakes in our estimates is overestimated for the given time periods with high M_c. Since the missing events are mostly small in magnitude, their contribution to the cumulative slip will be small and hence likely not significantly increase the cumulative slip.

Finally, in order to study the fault mechanism of the repeating earthquakes, we combine first polarities from repeaters in one sequence (Barrientos, 2018; Petersen et al., 2021) and calculate the focal mechanism for the entire repeater sequence using FPFIT (Reasenberg et al., 1985).

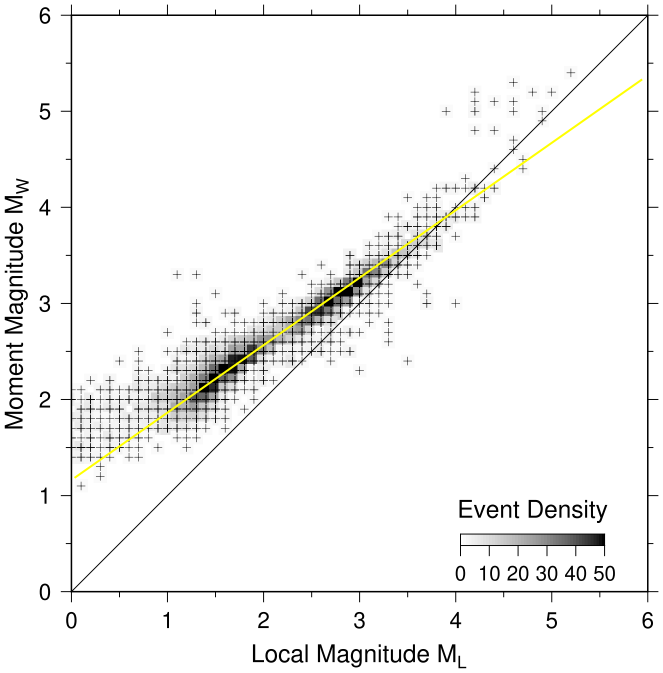

Figure 5.2: Moment magnitudes M_w versus local magnitudes M_l from the local earthquake catalog based on OBS data for the 2014 Iquique earthquake rupture area (Petersen et al., 2021). The grey color scale indicates the number of magnitude pairs. The blue line has a slope of 0.74.

5.3 Results

The repeating earthquake distribution that has been found by analyzing thirteen years of seismicity data of the north Chilean subduction zone is displayed in Figure 5.1. In our study area, we found that 1,939 events (~15 %) are repeating earthquakes and that 65 % of these repeaters are considered as event doublets/triplets or outside of our study area (Figure 5.7). To distinguish between closely triggered, on neighboring faults, and co-located earthquakes, we only take into account all 143 repeater sequences which contain at least three events or sequences with more than four events that span more than 20 days. The resulting 681 repeating earthquakes, which we will further analyze, are in the moment magnitude range between 1.4 and 4.3 (Figure 5.8). Therefore, we detected more repeating earthquakes than previous studies of the 2014 Iquique earthquake (Kato and Nakagawa, 2014; Meng et al., 2015; Kato et al., 2016; Schurr et al., 2020). The study from Kato et al. (2016) uses a similar search procedure and identified 408 repeating earthquakes between 2008 and 31 May 2014 using a constructed catalog by template matching waveforms. Thus, we identified 1,159 repeating earthquakes in the same time period (including doublets). This difference is mainly caused by the disparity in the seismic catalogs used for the repeater analysis. Here, we use a compilation of earthquake catalogs that were acquired using temporary seismic land-stations and OBS (Sippl et al., 2018;

Soto et al., 2019; Petersen et al., 2021) in addition to the permanent broadband stations onshore(Barrientos, 2018) used by Kato et al. (2016).

In addition to the enhanced detection of offshore earthquakes, the OBS deployment after the Iquique mainshock (Petersen et al., 2021) allowed a more accurate hypocenter estimation in the marine forearc (Husen et al., 1999). Since events of a repeater sequence rupture on co-located locations (Uchida and Bürgmann, 2019; Uchida, 2019), it allows the complete repeater cluster to be “relocated” to the event with the most accurately known hypocentral coordinates. In our case, the hypocenters during the OBS deployment (Figure 5.1) effectively expanded the high resolution of hypocentral coordinates for events of the whole time series (e.g., obtaining high-resolution hypocenters for the interseismic, although this was before the OBS deployment). The relocation enables us to study the depth-dependent occurrence of repeater clusters and accompanied surrounding aseismic slip not only on the subduction interface, but also deformation of upper plate faults that have been imaged with multi-channel seismic (MCS) data (Sallarès and Ranero, 2005; Reginato et al., 2020; Petersen et al., 2021; Ma et al., submitted).

The time span of the complete repeater sequence (2007 - 2020) is larger than the time span of the OBS deployments. In total, we find 143 repeater sequences, of which 83 (58 %) repeaters containing events registered on the OBS. We assign the location and hypocenter from the event located with the OBS data to the whole repeater sequence. Then, we classify the events as plate interface repeaters in case, their depth is within ± 4 km of the plate interface derived from the MCS data (Petersen et al., 2021; Ma et al., submitted). For the remaining 60 repeater sequences, we average the individual event locations.

Repeaters above the plate interface are classified as upper plate repeaters, and all repeaters below the plate interface as intraplate repeaters (Figure 5.1b). Since we focus on repeating earthquakes in the upper plate, the misclassification of plate interface repeaters as upper plate repeaters or the disregard of non-relocated repeaters might also have an impact on our analysis. Due to the OBS deployment eight months after the Iquique 2014 mainshock, we might have missed upper plate repeater sequences that have not been active during the 23 months of the OBS deployment. However, repeater recurrence times are lower than 23 months and it is therefore unlikely that we have missed a significant number of repeaters.

5.3.1 Spatial distribution of upper plate repeating earthquakes

The spatial distribution of repeating earthquake sequences in the marine forearc is shown in Figure 5.1, with the color code separating the sequences relocated with OBS-derived depths (blue and green stars, Figure 5.1) and non-relocated sequences (gray stars, Figure 5.1). The relocated and non-relocated repeater sequences occur in similar regions as the Iquique foreshocks and aftershocks. Previous repeater studies investigated the foreshock aseismic slip or slow-slip (Kato and Nakagawa, 2014; Kato et al., 2016; Schurr et al., 2020) and discussed the accompanying aseismic slip in the context of bifold plate interface slip behavior before and after the mainshock (Meng et al., 2015). However, the spatial distribution of repeaters changes significantly after the OBS-derived hypocenters are used to relocate the repeater sequences. We are now able to differentiate repeating earthquake activity within the overriding plate, at the plate interface, and in the lower plate, respectively. The highest density of repeater sequences appears to cluster at the seismogenic up-dip limit of the 2014 Iquique earthquake. This area between the rupture zone and the trench was affected by the largest foreshocks ($M \geq 6$) since March 16, 2014 (Figure 5.1a, orange, and red focal mechanisms), which migrated north towards the mainshock nucleation hypocenter (e.g., Kato and Nakagawa, 2014). Non-relocated repeater sequences occur closer to the trench then relocated repeaters, suggesting an East to West bias of earthquake locations. Petersen et al. (2021) showed that accurately located aftershocks using OBS stations reduce the East-West bias significantly, especially far offshore, and mapped a distinct seismogenic up-dip limit at ~35 km distance from the trench. Therefore, it can be expected that 41 % of the non-relocated repeater sequences that are far offshore are located farther east. Down-dip and north of the coseismic slip area, small isolated repeater sequences occur, surrounding a circular-shaped main rupture asperity of the 2014 Iquique earthquake (Schurr et al., 2020). The region between the greatest aftershock and the mainshock (between 20.15 °S and 20.25 °S; Figure 5.1) shows one large interface repeater sequence and several intermediate repeater sequences farther south that cluster in two areas. These repeaters were associated with the occurrence of aseismic slip induced by incoming interplate corrugations (Soto et al., 2019), but the previous East-West streak-like pattern from Soto et al. (2019) disappears after the relocation using OBS data. Besides the mainshock rupture area, we find repeaters in the vicinity of the greatest aftershock, south of the mainshock, but the lateral repeater distribution is significantly different from the mainshock area. Intermediate plate interface repeater and non-relocated sequences are distributed in the slip area of the greatest aftershock.

Repeating earthquakes in the upper plate are distributed in a near trench-parallel pattern with a location mainly east of the plate interface repeaters. In cross-profiles, the upper plate repeaters indicate an east-to-west depth increase (Figure 5.1a-c) and correlate to large-scale seaward dipping faults in the upper plate that are derived from multi-channel seismic data acquired after the 2014 Iquique earthquake (Petersen et al., 2021; Ma et al., submitted). The existence of the identified large-scale faults is also supported by large seaward dipping outcrops on the forearc (Geersen et al., 2018). Below the plate boundary in the oceanic crust, we find a lower repeater activity with small clusters containing six or fewer repeating earthquakes. Focal mechanisms of upper plate repeater sequences indicate a thrust fault movement (Figure 5.1).

5.3.2 Repeater cumulative pre-seismic and coseismic slip

Some plate interface repeaters are active since the deployment of broadband seismic stations of the IPOC network development in 2007. In contrast to the area of the greatest aftershock south of 20.25 °S, the up-dip region of the main rupture area indicates a frequent repeater activity since the end of 2009 with a nearly constant increase of cumulative seismic slip until July 2013 (Figure 5.3a-b). Considering only the relocated plate interface repeaters, the best linear fit of the cumulative seismic slip rate during the interseismic phase is 0.96 cm/yr (Figure 5.9). Non-relocated repeaters (Figure 5.3a, gray line) indicate a similar slip rate in the same period, but most of these repeaters occured south of 20.25 °S (Figure 5.3b). The estimated average cumulative slip rate is 0.29 cm/yr greater than the value of 0.67 cm/yr calculated by Kato et al. (2016) in their repeater analysis. The discrepancy in slip rate may result from the different earthquake catalogs with lower magnitudes of completeness in our study. The increase of plate interface repeater activity in July 2013 coincides with the proposed initiation of the Iquique foreshock sequence (Schurr et al., 2014; Kato et al., 2016)).

Repeater activity in the upper plate first emerged in January 2013, about 430 days before the mainshock up-dip of the later rupture area and again in January 2014 at the northern edge of the rupture area (Figure 5.3a). The foreshock burst in July 2013, which marks the initiation of the foreshock period (Schurr et al., 2014; Kato et al., 2016) and the largest foreshock earthquake on March 16 with a moment magnitude of 6.7, which indicated a major impact on foreshock seismicity, did not affect upper plate repeaters (Figure 5.5). After the subsequent northward migration of seismicity at a rate of 2 - 10 km per day (Kato and Nakagawa, 2014; Meng et al., 2015; Herman et al., 2016), the last larger foreshock burst occurred on March 22 and 23, which ruptured a compact asperity with two $M_w >$,6 events, causing significant repeater activity on upper plate sequences located northeast of the two $M_w > 6$ events (Figure 5.5, green stars). Comparing the average cumulative seismic slip between upper plate and interface, the upper plate slip significantly dominates from March 22 until March 26 (Figure 5.4a). After the coseismic rupture of the Iquique earthquake on April 1, 2014, repeaters reactivated ~5 days after the mainshock, and the locations are concentrated at the up-dip limit of the main rupture with ~10 cm averaged cumulative slip in nine days (Figure 5.3c and d). The nearly constant increase of cumulative upper plate slip is equal to the simultaneous increase of interface and non-relocated repeater cumulative slip (Figure 5.3d).

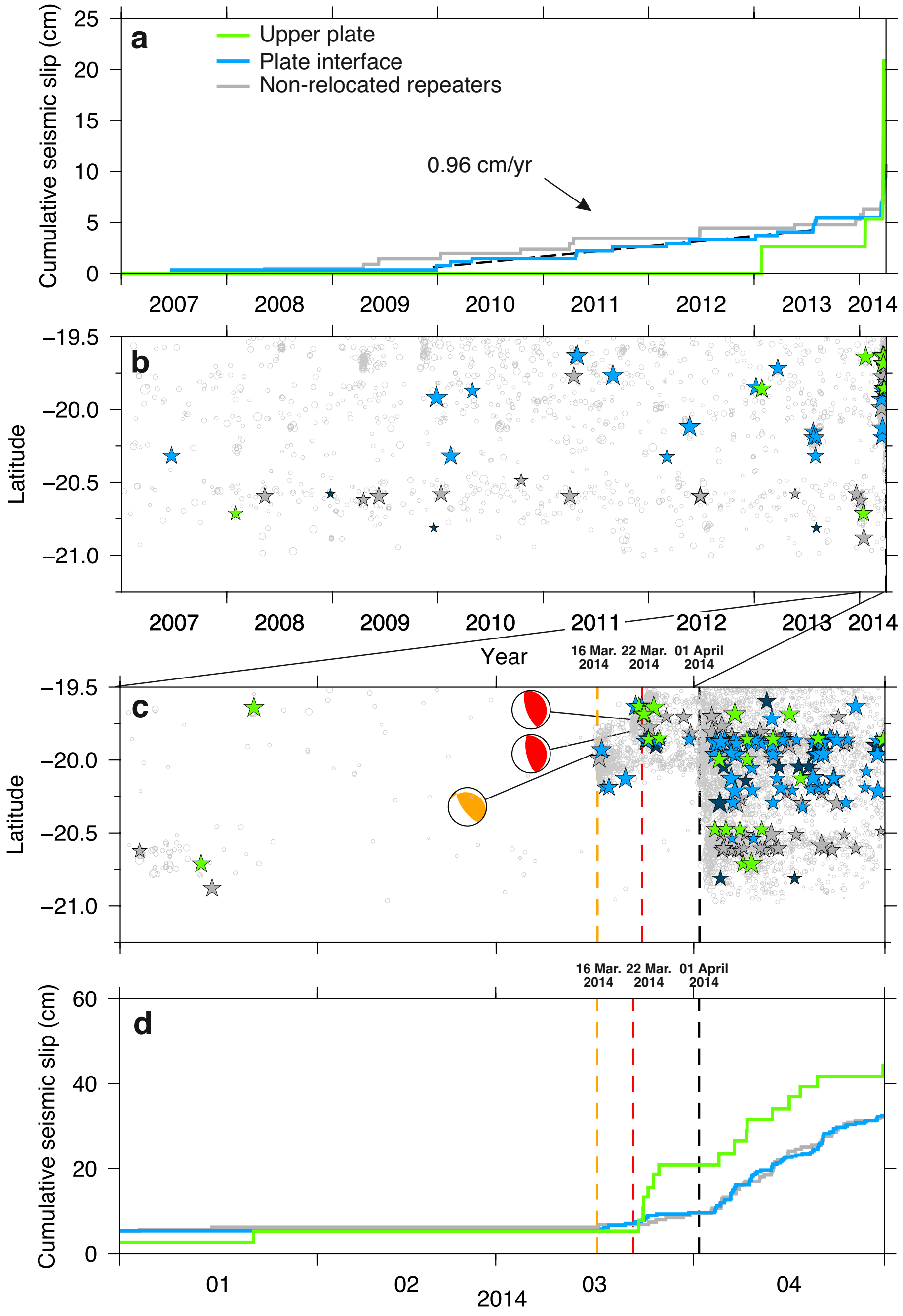

Figure 5.3: Repeating earthquake activity and cumulative seismic slip before and one month after the Iquique mainshock. (a) Cumulative seismic slip from 2007 until May 1, separated into repeaters within the upper plate (light blue line), plate interface (blue line), and non-relocated repeater sequences (gray line). (b) Repeater activity in space. Stars mark the repeating earthquakes and symbol size is scaled by seismic slip. The color scale is similar to panel a. (c) closeup of the pre-seismic and coseismic phases. The time of the greatest foreshock with M_w 6.7, on March 16, is marked by the orange dashed line and orange focal mechanism. The time of the last foreshock burst, on March 22, is marked by the red dashed line and red focal mechanism. (d) Same as panel a, but from January 2014 to April 1.

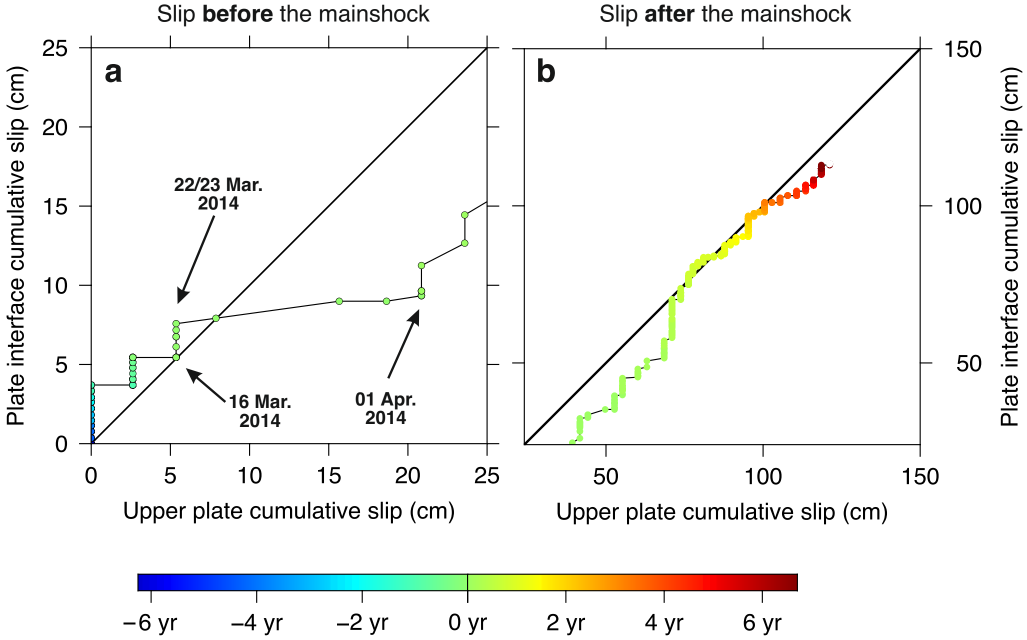

Figure 5.4: Comparison of the cumulative upper plate versus interface cumulative slip. Color scale indicates the time in years before and after the 2014 Iquique earthquake on April 1. (a) The arrows mark the time of upper plate and plate interface slip during the final foreshock sequences starting on March 16 and March 22, respectively. (b) Upper plate aseismic fault slip versus interface slip after the 2014 Iquique earthquake. The cumulative daily slip was averaged for the upper plate and the plate interface.

5.4 Discussion

The study of repeating earthquakes in the north Chilean marine forearc, using OBS derived high-resolution offshore hypocenters, reveals the slip partitioning from repeating earthquakes over 13 years, from the pre-seismic to the postseismic phase of the 2014 Iquique earthquake. Repeating earthquakes are assumed to represent small asperities on fault patches triggered to slip seismically by surrounded aseismic fault slip (Nadeau and McEvilly, 1999; Uchida and Bürgmann, 2019). We are able to assign repeater sequences to the plate boundary and overriding plate above the up-dip limit of the 2014 Iquique earthquake by using the highest quality hypocenter from the whole period. To our knowledge, this is the first observation of seismic slip of repeating earthquakes in a marine forearc where hypocenters can be assigned to the overriding plate and the interface allowing to observe the transient behavior of faulting for the different depth levels during the seismic cycle.

Previous studies reported that the upper plate presents low seismic activity during the foreshock sequence of the 2014 Iquique earthquake (e.g., Meng et al., 2015; Herman et al., 2016). Here we show that slip not only occured along the plate boundary but that in the upper plate averaged slip has accelerated since January 2013 significantly ten days before the main rupture (Figures 5.3a and 5.4a). Furthermore, the March 16 foreshock event with a moment magnitude M_w 6.7 at 12 km depth (global centroid moment tensor project gCMT) triggered a significant change in seismicity rate at the plate interface, whereas upper plate repeaters remained largely unaffected (Figure 5.3c and d; Schurr et al., 2014).

In contrast, the last foreshock burst ten days before the mainshock activated several repeater clusters in the upper plate up-dip of the main rupture (Figure 5.5, green stars). We note that between March 22 and the mainshock on April 1, slip significantly occurs on the upper plate faults compared to events belonging to the plate interface (Figure 5.4a). Slip on the upper plate exceeded slip on the interface approximately eightfold (upper plate ~16 mm, lower plate ~2 mm slip, Figure 5.4a). This is clearly different from the previous foreshock period before March 22 (Figure 5.4a) or postseismic phase (Figure 5.4b) where partitioning of slip appears more balanced. Since the thrust events of March 22 and 23, 2014, are related to the plate interface (Figure 5.1b), we interpret this as a triggering mechanism of upper plate faults above the seismogenic up-dip limit by stress changes at the plate interface during the latest stage of the foreshock period. A similar interaction of repeating events for Parkfield along the San Andreas Fault has been observed by Chen et al. (2013) and interpreted as triggering by stress changes induced from larger events.

The near linear alignment of upper plate repeaters parallel to the trench and coast suggests the presence of a large margin parallel trending structure in the upper plate as the origin (Figure 5.1). The spatial distribution of repeaters suggests that they occurred along large seaward-dipping normal faults which were previously identified in multi-channel seismic reflection lines (Petersen et al., 2021; Ma et al., submitted) and multibeam bathymetric data (Geersen et al., 2018). Upper plate seismicity above the up-dip limit of the 2014 Iquique mainshock likely occurred along these large normal faults, supporting subduction erosion at the base of the upper plate during the coseismic and early postseismic phase (von Huene and Ranero, 2003; von Huene et al., 2004; Petersen et al., 2021). Wang et al. (2010) discussed the contradiction between the widely observed extensional faults at erosional margins and the compressional forces needed to induce high basal friction to erode the upper plate. In their model, coseismic stress transfer from the seismogenic zone to the outermost aseismic wedge leads to a strengthening of the shallow megathrust and compression of the overlying upper plate (Hu and Wang, 2008; Wang et al., 2010).

Focal mechanisms of the repeater sequences (Figure 5.1) reveal compressional faulting along large upper plate normal faults. We interpret this as inverse reactivation of the normal faults, resulting from a stress transfer as described by the model of Wang et al. (2010). During the progressing foreshock sequence of the 2014 Iquique earthquake, accompanied by plate interface aseismic slip/transients and slow-slip events (Kato and Nakagawa, 2014; Bedford et al., 2015; Herman et al., 2016), the upper plate entered a compressional state

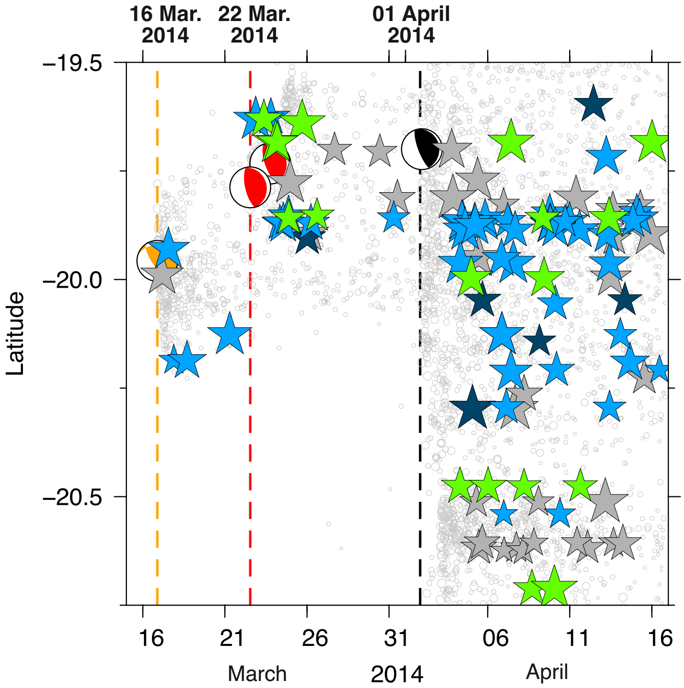

Figure 5.5: Repeater distribution in time in the latest foreshock and early postseismic periods. The stars mark individual events of repeater sequences. The symbol color indicates the corresponding occurrence depth with the same color code as figure 5.1. The gray circles show non-repeating earthquakes. The focal mechanisms mark the rupture latitude and time of the two latest foreshock bursts on March 16 and March 22. The black dashed line indicates the Iquique rupture on April 1.

in response to the strengthening of the shallow plate interface (Wang et al., 2010) . This forced the upper plate faults hosting the repeaters up-dip of the main rupture to start slipping in thrust mode. After re-locking of the megathrust, the outermost wedge undergoes continuous deformation driven by afterslip. Simultaneously at the shallow plate interface, small rate-weakening patches emerge in the surrounding rate-strengthening interface thereby generating the observed aftershocks (Soto et al., 2019; Petersen et al., 2021).

Further, at the same time, repeaters occurred at the plate boundary, suggesting that the resolution was high enough to detect offshore repeaters. In contrast to the coseismic compression of upper plate faults, the interseismic forearc relaxation evokes tensional forces on the upper plate, resulting in a normal slip motion along the extensional faults (Wang et al., 2010). Fault slip inversion (e.g. “back-slip” of repeating events) will appear as negative correlation coefficients in the cross-correlation, but we did not detect cross-correlations coefficients below -0.85 (Figure 5.6). The process of interseismic relaxation through normal faulting of the upper plate fault is assumed to occur over geological timescales with low slip rates (Ranero and von Huene, 2000) and may require observations over the length of a complete seismic cycle.

Upper plate relaxation and associated vertical subsidence during the interseismic phase have been observed and estimated by comparing historical megathrust events in central Chile with the 2010 M_w 8.8 Maule earthquake (Melnick et al., 2012; Wesson et al., 2015). The Isla Santa María, located on the forearc, has subsided almost one and a half meters between two large megathrust events in 1835 and 2010. Fault inversion caused by upper plate repeaters following the 2014 Iquique earthquake produced an average cumulative slip of about 1.21 m in total until the end of 2020 (Figure 5.10b). Interseismic relaxation in the overriding plate therefore needs to accommodate these 1.21 m plus an additional normal component that generates the observed permanent deformation pattern of long-term margin subsidence evidenced through prominent upper plate normal faults. By considering the recurrence time of large earthquakes in the Iquique area since 1877, the required extensional fault displacement rate of upper plate faults must be larger than 8.8 mm/yr to accommodate the fault deformation by upper plate weakening.

Interseismic tension of the frontal upper plate requires a creeping or slow slipping interface underneath. Using repeating earthquakes, we can quantify the percentage of plate interface slip during the interseismic phase five years prior to the Iquique earthquake. We assume a constant increase in cumulative slip during the interseismic phase to estimate the annual deformation at the interface where the repeating earthquakes occur. The analysis of relocated repeater locations shows a nearly constant cumulative slip rate of 0.96 cm/yr from the end of 2009 until July 2013 (Figure 5.3a). This estimated cumulative slip rate represents approx. 14 % of the 6.7 cm/yr convergence rate of the Nazca plate underneath the South American plate (Angermann et al., 1999). This fraction of seismic slip of the convergence rate is consistent with the observed plate interface locking (~80 %) derived from geodetic measurements (Schurr et al., 2014; Métois et al., 2016). The rate of 0.96 cm/yr represents a first-order estimation of the aseismic fault slip, which supports the absence of upper plate repeaters during the interseismic phase. However, the inhomogeneous distribution of plate interface repeaters, especially in the region south of the 2014 Iquique mainshock (Figure 5.1a), suggests another process that controls the occurrence of repeaters up-dip of the mainshock. GPS measurements revealed a significant along-strike decrease in interseismic locking from the Iquique rupture area to the shallow plate interface (Schurr et al., 2014), where most repeaters are located. This observation supports the concept that the repeating earthquakes are controlled by a nearby large asperity rather than representing the overall aseismic slip (Sammis and Rice, 2001).

The presence of repeating earthquakes in the upper plate raises the question about the impact on tsunami hazards in the north Chilean region. Generally, it is suggested that repeaters act as indicators for creeping faults, which in turn, lower the degree of coupling and lower the accumulation of strain. The probability of these large-scale upper plate faults slipping suddenly during a megathrust event would consequently be reduced. However, the plate interface up-dip of the rupture area has not experienced coseismic slip and either may have resisted the rupture (Lay et al., 2014), or the shallow plate boundary behaves aseismically (Ma et al., submitted). Nevertheless, in the case of a nascent megathrust rupture, filling the southern remaining seismic gap, the upper plate faults still pose a significant potential for sudden thrust slip and tsunami triggering (Wendt et al., 2009). The potential hazard underlines the necessity of seafloor geodesy techniques to monitor seafloor outcrops of such large-scale faults or to monitor the stress relaxation process after a great subduction earthquake (Petersen et al., 2019).

5.5 Conclusion

We analyze repeating earthquakes recorded over 13 years during and before the 2014 Iquique earthquake using high-resolution offshore hypocenter locations and OBS. The OBS data result in accurate hypocenter depths to distinguish deformation between the upper plate and plate boundary. Although the OBS network was deployed 23 months on the marine forearc starting eight months after the 2014 Iquique earthquake, accurate locations using the OBS data can be assigned to the other repeater sequences, even if the events occurred before or after the OBS deployment. Upper plate repeating earthquakes are spatially correlated to large extensional faults in the upper plate imaged by MCS data and multibeam bathymetry. The along-strike aligned upper plate repeater sequences indicate accelerating cumulative slip in the overriding plate following two strong plate interface events ten days before the mainshock. For other times the partitioning of slip in the upper crust and interface is more balanced. The gradual unlocking of the plate interface forces the reverse reactivation of upper plate extensional faults causing subduction erosion.

Acknowledgments and Data

This publication is funded by the German Research Foundation (DFG) under grant LA2970/4-1. We thank Sippl et al. (2018), Soto et al. (2019) and CSN for providing the event catalogs, and Duputel et al. (2015) for providing slip models. Figures were created using the Generic Mapping Tools (Wessel et al., 2013). We thank Felix Gross for providing the computing power to calculate the large number of waveform cross-correlations. EC-R acknowledges the support of the Chilean National Research Agency (ANID, grant FONDECYT 1210101).

The seismic waveform data from the networks CX and C1 are available from GFZ and CNRS-INSU (2006). OBS seismic catalog and waveform data are available from

PANGAEA `https://doi.pangaea.de/10.1594/PANGAEA.929899`. Earthquake catalog from the Chilean land network was provided by the CSN (Barrientos, 2018). Earthquake focal mechanisms were obtained from the Global Centroid-Moment-Tensor catalog (`www.globalcmt.org`).

References

Abercrombie, R. E. & Mori, J. (1996). Occurrence patterns of foreshocks to large earthquakes in the western united states. *Nature*, *381*(6580), 303–307, `https://doi.org/10.1038/381303a0`.

Angermann, D., Klotz, J., & Reigber, C. (1999). Space-geodetic estimation of the nazca-south america euler vector. *Earth and Planetary Science Letters*, *171*(3), 329–334, `https://doi.org/10.1016/s0012-821x(99)00173-9`.

Aron, F., Allmendinger, R. W., Cembrano, J., González, G., & Yáñez, G. (2013). Permanent fore-arc extension and seismic segmentation: Insights from the 2010 maule earthquake, chile. *Journal of Geophysical Research: Solid Earth*, *118*(2), 724–739, `https://doi.org/10.1029/2012jb009339`.

Barrientos, S. (2018). The seismic network of chile. *Seismological Research Letters*, *89*(2A), 467–474, `https://doi.org/10.1785/0220160195`.

Bedford, J., Moreno, M., Schurr, B., Bartsch, M., & Oncken, O. (2015). Investigating the final seismic swarm before the iquique-pisagua 2014 mw 8.1 by comparison of continuous gps and seismic foreshock data. *Geophysical Research Letters*, *42*(10), 3820–3828, `https://doi.org/10.1002/2015gl063953`.

Bohnhoff, M., Wollin, C., Domigall, D., Küperkoch, L., Martínez-Garzón, P., Kwiatek, G., Dresen, G., & Malin, P. E. (2017). Repeating marmara sea earthquakes: indication for fault creep. *Geophysical Journal International*, *210*(1), 332–339, `https://doi.org/10.1093/gji/ggx169`.

Brodsky, E. E. & Lay, T. (2014). Recognizing foreshocks from the 1 april 2014 chile earthquake. *Science*, *344*(6185), 700–2, `https://doi.org/10.1126/science.1255202`.

Chen, K. H., Bürgmann, R., & Nadeau, R. M. (2013). Do earthquakes talk to each other? triggering and interaction of repeating sequences at parkfield. *Journal of Geophysical Research: Solid Earth*, *118*(1), 165–182, `https://doi.org/10.1029/2012jb009486`.

Chen, K. H., Nadeau, R. M., & Rau, R.-J. (2007). Towards a universal rule on the recurrence interval scaling of repeating earthquakes? *Geophysical Research Letters*, *34*(16), `https://doi.org/10.1029/2007gl030554`.

Contreras-Reyes, E., Ruiz, J. A., Becerra, J., Kopp, H., Reichert, C., Maksymowicz, A., & Arriagada, C. (2015). Structure and tectonics of the central chilean margin (31°–33°s): implications for subduction erosion and shallow crustal seismicity. *Geophysical Journal International*, *203*(2), 776–791, `https://doi.org/10.1093/gji/ggv309`.

Crotwell, H. P., Owens, T. J., & Ritsema, J. (1999). The taup toolkit: Flexible seismic travel-time and ray-path utilities. *Seismological Research Letters*, *70*(2), 154–160, `https://doi.org/10.1785/gssrl.70.2.154`.

Delouis, B., Philip, H., Dorbath, L., & Cisternas, A. (1998). Recent crustal deformation in the antofagasta region(northern chile) and the subduction process. *Geophysical Journal International*, *132*(2), 302–338, `https://doi.org/10.1046/j.1365-246x.1998.00439.x`.

Duputel, Z., Jiang, J., Jolivet, R., Simons, M., Rivera, L., Ampuero, J. P., Riel, B., Owen, S. E., Moore, A. W., Samsonov, S. V., Ortega Culaciati, F., & Minson, S. E. (2015). The iquique earthquake sequence of april 2014: Bayesian modeling accounting for prediction uncertainty. *Geophysical Research Letters*, *42*(19), 7949–7957, `https://doi.org/10.1002/2015gl065402`.

Duverger, C., Lambotte, S., Bernard, P., Lyon-Caen, H., Deschamps, A., & Nercessian, A. (2018). Dynamics of microseismicity and its relationship with the active structures in the western corinth rift (greece). *Geophysical Journal International*, *215*(1), 196–221, `https://doi.org/10.1093/gji/ggy264`.

Farr, T. G., Rosen, P. A., Caro, E., Crippen, R., Duren, R., Hensley, S., Kobrick, M., Paller, M., Rodriguez, E., Roth, L., Seal, D., Shaffer, S., Shimada, J., Umland, J., Werner, M., Oskin, M., Burbank, D., & Alsdorf, D. (2007). The shuttle radar topography mission. *Reviews of Geophysics*, *45*(2), `https://doi.org/10.1029/2005rg000183`.

Farías, M., Comte, D., Roecker, S., Carrizo, D., & Pardo, M. (2011). Crustal extensional faulting triggered by the 2010 chilean earthquake: The pichilemu seismic sequence. *Tectonics*, *30*(6), `https://doi.org/10.1029/2011tc002888`.

Geersen, J., Ranero, C. R., Klaucke, I., Behrmann, J. H., Kopp, H., Tréhu, A. M., Contreras-Reyes, E., Barckhausen, U., & Reichert, C. (2018). Active tectonics of the north chilean marine forearc and adjacent oceanic nazca plate. *Tectonics*, *37*(11), 4194–4211, `https://doi.org/10.1029/2018tc005087`.

Geller, R. J. & Mueller, C. S. (1980). Four similar earthquakes in central california. *Geophysical Research Letters*, *7*(10), 821–824, `https://doi.org/10.1029/GL007i010p00821`.

GFZ & CNRS-INSU (2006). Ipoc seismic network. integrated plate boundary observatory chile - ipoc. *Other/Seismic Network*, `https://doi.org/10.14470/ PK615318`.

Hanks, T. C. & Kanamori, H. (1979). A moment magnitude scale. *Journal of Geophysical Research*, *84*(B5), `https://doi.org/10.1029/JB084iB05p02348`.

Hardebeck, J. L. (2012). Coseismic and postseismic stress rotations due to great subduction zone earthquakes. *Geophysical Research Letters*, *39*(21), `https://doi.org/10.1029/2012gl053438`.

Herman, M. W., Furlong, K. P., Hayes, G. P., & Benz, H. M. (2016). Foreshock triggering of the 1 april 2014 mw 8.2 iquique, chile, earthquake. *Earth and Planetary Science Letters*, *447*, 119–129, `https://doi.org/10.1016/j.epsl.2016.04.020`.

Hu, Y. & Wang, K. (2008). Coseismic strengthening of the shallow portion of the subduction fault and its effects on wedge taper. *Journal of Geophysical Research*, *113*(B12), `https://doi.org/10.1029/2008jb005724`.

Husen, S., Kissling, E., Flueh, E. R., & Asch, G. (1999). Accurate hypocentre determination in the seismogenic zone of the subducting nazca plate in northern chile using a combined on-/offshore network. *Geophysical Journal International*, *138*(3), 687–701, `https://doi.org/10.1046/j.1365-246x.1999.00893.x`.

Igarashi, T., Matsuzawa, T., & Hasegawa, A. (2003). Repeating earthquakes and interplate aseismic slip in the northeastern japan subduction zone. *Journal of Geophysical Research: Solid Earth*, *108*(B5), `https://doi.org/10.1029/2002jb001920`.

Kato, A., Fukuda, J., Kumazawa, T., & Nakagawa, S. (2016). Accelerated nucleation of the 2014 iquique, chile mw 8.2 earthquake. *Sci Rep*, *6*, 24792, `https://doi.org/10.1038/srep24792`.

Kato, A. & Nakagawa, S. (2014). Multiple slow-slip events during a foreshock sequence of the 2014 iquique, chile mw 8.1 earthquake. *Geophysical Research Letters*, *41*(15), 5420–5427, `https://doi.org/10.1002/2014gl061138`.

Kato, A., Sakai, S., & Obara, K. (2011). A normal-faulting seismic sequence triggered by the 2011 off the pacific coast of tohoku earthquake: Wholesale stress regime changes in the upper plate. *Earth, Planets and Space*, *63*(7), 745–748, `https://doi.org/10.5047/eps.2011.06.014`.

Lange, D., Tilmann, F., Barrientos, S. E., Contreras-Reyes, E., Methe, P., Moreno, M., Heit, B., Agurto, H., Bernard, P., Vilotte, J.-P., & Beck, S. (2012). Aftershock seismicity of the 27 february 2010 mw 8.8 maule earthquake rupture zone. *Earth and Planetary Science Letters*, *317-318*, 413–425, `https://doi.org/10.1016/j.epsl.2011.11.034`.

Lay, T., Yue, H., Brodsky, E. E., & An, C. (2014). The 1 april 2014 iquique, chile, mw 8.1 earthquake rupture sequence. *Geophysical Research Letters*, *41*(11), 3818–3825, `https://doi.org/10.1002/2014gl060238`.

León-Ríos, S., Ruiz, S., Maksymowicz, A., Leyton, F., Fuenzalida, A., & Madariaga, R. (2016). Diversity of the 2014 iquique's foreshocks and aftershocks: clues about the complex rupture process of a mw 8.1 earthquake. *Journal of Seismology*, *20*(4), 1059–1073, `https://doi.org/10.1007/s10950-016-9568-6`.

Li, S., Moreno, M., Rosenau, M., Melnick, D., & Oncken, O. (2014). Splay fault triggering by great subduction earthquakes inferred from finite element models. *Geophysical Research Letters*, *41*(2), 385–391, `https://doi.org/10.1002/2013gl058598`.

Läderach, C., Korger, E. I. M., Schlindwein, V., Müller, C., & Eckstaller, A. (2012). Characteristics of tectonomagmatic earthquake swarms at the southwest indian ridge between 16°e and 25°e. *Geophysical Journal International*, *190*(1), 429–441, `https://doi.org/10.1111/j.1365-246X.2012.05480.x`.

Ma, B., Geersen, J., Lange, D., Klaeschen, D., Grevemeyer, I., Petersen, F., Riedel, M., Xia, Y., Tréhu, A. M., Contreras-Reyes, E., & Kopp, H. (submitted). Megathrust reflectivity reveals the updip limit of the 2014 iquique earthquake rupture. *Nature Geoscience*.

Melnick, D., Cisternas, M., Moreno, M., & Norambuena, R. (2012). Estimating coseismic coastal uplift with an intertidal mussel: calibration for the 2010 maule chile earthquake (mw = 8.8). *Quaternary Science Reviews*, *42*, 29–42, `https://doi.org/10.1016/j.quascirev.2012.03.012`.

Meng, L., Huang, H., Bürgmann, R., Ampuero, J. P., & Strader, A. (2015). Dual megathrust slip behaviors of the 2014 iquique earthquake sequence. *Earth and Planetary Science Letters*, *411*, 177–187, `https://doi.org/10.1016/j.epsl.2014.11.041`.

Métois, M., Vigny, C., & Socquet, A. (2016). Interseismic coupling, megathrust earthquakes and seismic swarms along the chilean subduction zone (38°–18°s). *Pure and Applied Geophysics*, *173*(5), 1431–1449, `https://doi.org/10.1007/s00024-016-1280-5`.

Nadeau, R. M. & Johnson, L. R. (1998). Seismological studies at parkfield vi: Moment release rates and estimates of source parameters for small repeating earthquakes. *Bulletin of the Seismological Society of America*, *88*(3), 790–814.

Nadeau, R. M. & McEvilly, T. V. (1999). Fault slip rates at depth from recurrence intervals of repeating microearthquakes. *Science*, *285*(5428), 718–21, `https://doi.org/10.1126/science.285.5428.718`.

Obana, K., Kodaira, S., Shinohara, M., Hino, R., Uehira, K., Shiobara, H., Nakahigashi, K., Yamada, T., Sugioka, H., Ito, A., Nakamura, Y., Miura, S., No, T., & Takahashi, N. (2013). Aftershocks near the updip end of the 2011 tohoku-oki earthquake. *Earth and Planetary Science Letters*, *382*, 111–116, `https://doi.org/10.1016/j.epsl.2013.09.007`.

Petersen, F., Kopp, H., Lange, D., Hannemann, K., & Urlaub, M. (2019). Measuring tectonic seafloor deformation and strain-build up with acoustic direct-path ranging. *Journal of Geodynamics*, *124*, 14–24, `https://doi.org/10.1016/j.jog.2019.01.002`.

Petersen, F., Lange, D., Ma, B., Grevemeyer, I., Geersen, J., Klaeschen, D., Contreras-Reyes, E., Barrientos, S., Tréhu, A. M., Vera, E., & Kopp, H. (2021). Relationship between subduction erosion and the up-dip limit of the 2014 mw 8.1 iquique earthquake. *Geophysical Research Letters*, *48, e2020GL092207*(9), `https://doi.org/10.1029/2020GL092207`.

Ranero, C. R. & von Huene, R. (2000). Subduction erosion along the middle america convergent margin. *Nature*, *404*(6779), 748–52, `https://doi.org/10.1038/35008046`.

Reasenberg, P., Oppenheimer, D., & USGS (1985). *FPFIT, FPPLOT and FPPAGE Fortran computer programs for calculating and displaying earthquake fault-plane solutions*. Report.

Reginato, G., Vera, E., Contreras-Reyes, E., Tréhu, A. M., Maksymowicz, A., Bello-González, J. P., & González, F. (2020). Seismic structure and tectonics of the continental wedge overlying the source region of the iquique mw8.1 2014 earthquake. *Tectonophysics*, *796*, `https://doi.org/10.1016/j.tecto.2020.228629`.

Ruiz, S., Metois, M., Fuenzalida, A., Ruiz, J., Leyton, F., Grandin, R., Vigny, C., Madariaga, R., & Campos, J. (2014). Intense foreshocks and a slow slip event preceded the 2014 iquique mw 8.1 earthquake. *Science*, *345*(6201), 1165–9, `https://doi.org/10.1126/science.1256074`.

Sallarès, V. & Ranero, C. (2005). Structure and tectonics of the erosional convergent margin off antofagasta, north chile (23°30ś). *Journal of Geophysical Research*, *110*(B6), `https://doi.org/10.1029/2004jb003418`.

Sammis, C. G. & Rice, J. R. (2001). Repeating earthquakes as low-stress-drop events at a border between locked and creeping fault patches. *Bulletin of the Seismological Society of America*, *91*(3), 532–537, `https://doi.org/10.1785/0120000075`.

Schurr, B., Asch, G., Hainzl, S., Bedford, J., Hoechner, A., Palo, M., Wang, R., Moreno, M., Bartsch, M., Zhang, Y., Oncken, O., Tilmann, F., Dahm, T., Victor, P., Barrientos, S., & Vilotte, J. P. (2014). Gradual unlocking of plate boundary controlled initiation of the 2014 iquique earthquake. *Nature*, *512*(7514), 299–302, `https://doi.org/10.1038/nature13681`.

Schurr, B., Moreno, M., Tréhu, A. M., Bedford, J., Kummerow, J., Li, S., & Oncken, O. (2020). Forming a mogi doughnut in the years prior to and immediately before the 2014 mw8.1 iquique, northern chile, earthquake. *Geophysical Research Letters*, *47*(16), `https://doi.org/10.1029/2020gl088351`.

Sippl, C., Schurr, B., Asch, G., & Kummerow, J. (2018). Seismicity structure of the northern chile forearc from >100,000 double-difference relocated hypocenters. *Journal of Geophysical Research: Solid Earth*, *123*(5), 4063–4087, `https://doi.org/10.1002/2017jb015384`.

Soto, H., Sippl, C., Schurr, B., Kummerow, J., Asch, G., Tilmann, F., Comte, D., Ruiz, S., & Oncken, O. (2019). Probing the northern chile megathrust with seismicity: The 2014 m8.1 iquique earthquake sequence. *Journal of Geophysical Research: Solid Earth*, *124*(12), 12935–12954, `https://doi.org/10.1029/2019jb017794`.

Uchida, N. (2019). Detection of repeating earthquakes and their application in characterizing slow fault slip. *Progress in Earth and Planetary Science*, *6*(1), `https://doi.org/10.1186/s40645-019-0284-z`.

Uchida, N. & Bürgmann, R. (2019). Repeating earthquakes. *Annual Review of Earth and Planetary Sciences*, *47*(1), 305–332, `https://doi.org/10.1146/annurev-earth-053018-060119`.

Uchida, N. & Matsuzawa, T. (2013). Pre- and postseismic slow slip surrounding the 2011 tohoku-oki earthquake rupture. *Earth and Planetary Science Letters*, *374*, 81–91, `https://doi.org/10.1016/j.epsl.2013.05.021`.

Valoroso, L., Chiaraluce, L., Di Stefano, R., & Monachesi, G. (2017). Mixed-mode slip behavior of the altotiberina low-angle normal fault system (northern apennines, italy) through high-resolution earthquake locations and repeating events. *Journal of Geophysical Research: Solid Earth*, *122*(12), 10,220–10,240, `https://doi.org/10.1002/2017jb014607`.

von Huene, R. & Lallemand, S. (1990). Tectonic erosion along the japan and peru convergent margins. *Geological Society of America Bulletin*, *102*(6), 704–720, `https://doi.org/10.1130/0016-7606(1990)102<0704:TEATJA>2.3.CO;2`.

von Huene, R. & Ranero, C. R. (2003). Subduction erosion and basal friction along the sediment-starved convergent margin off antofagasta, chile. *Journal of Geophysical Research: Solid Earth*, *108*(B2), `https://doi.org/10.1029/2001jb001569`.

von Huene, R., Ranero, C. R., & Vannucchi, P. (2004). Generic model of subduction erosion. *Geology*, *32*(10), `https://doi.org/10.1130/g20563.1`.

Vuan, A., Sugan, M., Chiaraluce, L., & Di Stefano, R. (2017). Loading rate variations along a midcrustal shear zone preceding the mw 6.0 earthquake of 24 august 2016 in central italy. *Geophysical Research Letters*, *44*(24), `https://doi.org/10.1002/2017gl076223`.

Wang, K. & Hu, Y. (2006). Accretionary prisms in subduction earthquake cycles: The theory of dynamic coulomb wedge. *Journal of Geophysical Research: Solid Earth*, *111*(B6), `https://doi.org/10.1029/2005jb004094`.

Wang, K., Hu, Y., von Huene, R., & Kukowski, N. (2010). Interplate earthquakes as a driver of shallow subduction erosion. *Geology*, *38*(5), 431–434, `https://doi.org/10.1130/g30597.1`.

Wendt, J., Oglesby, D. D., & Geist, E. L. (2009). Tsunamis and splay fault dynamics. *Geophysical Research Letters*, *36*(L15303), `https://doi.org/10.1029/2009gl038295`.

Wessel, P., Smith, W. H. F., Scharroo, R., Luis, J., & Wobbe, F. (2013). Generic mapping tools: Improved version released. *Eos, Transactions American Geophysical Union*, *94*(45), 409–410, `https://doi.org/10.1002/2013eo450001`.

Wesson, R. L., Melnick, D., Cisternas, M., Moreno, M., & Ely, L. L. (2015). Vertical deformation through a complete seismic cycle at isla santa maría, chile. *Nature Geoscience*, *8*(7), 547–551, `https://doi.org/10.1038/ngeo2468`.

Supporting Information

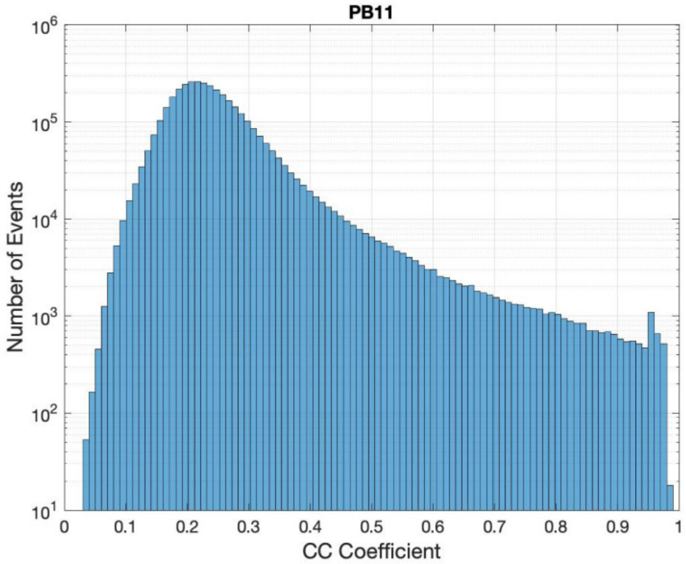

Figure 5.6: Frequency distribution of cross-correlation coefficients of the permanent broadband stations PB11 from the IPOC network.

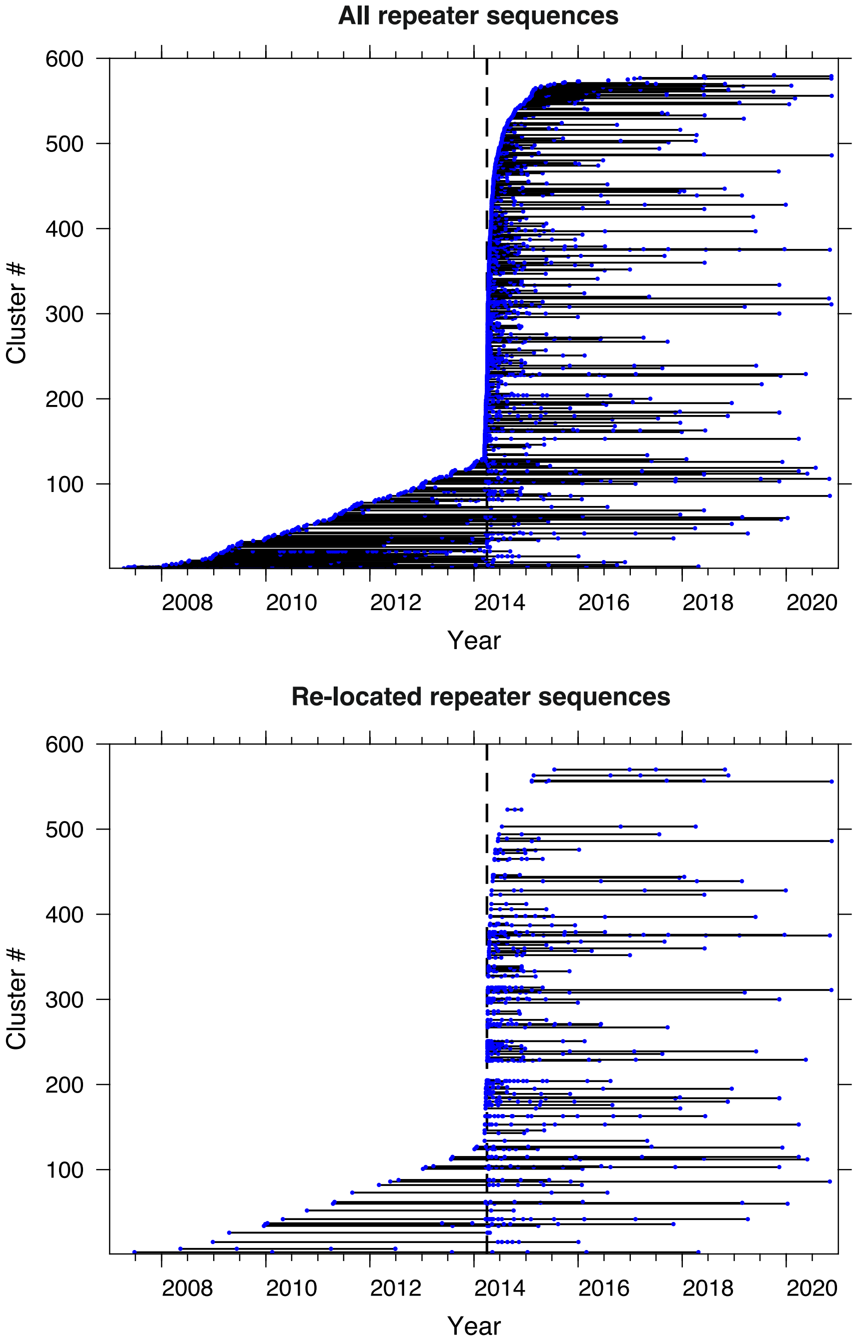

Figure 5.7: Results of the repeater clustering from 2007 until the end of 2020. (Upper panel) The time span repeater sequences, which contain at least three events with or sequences with more than four events that span more than 20 days, is plotted with black lines, including the individual events belonging to each cluster (blues dots). (Lower panel) All re-located repeating earthquake sequences.

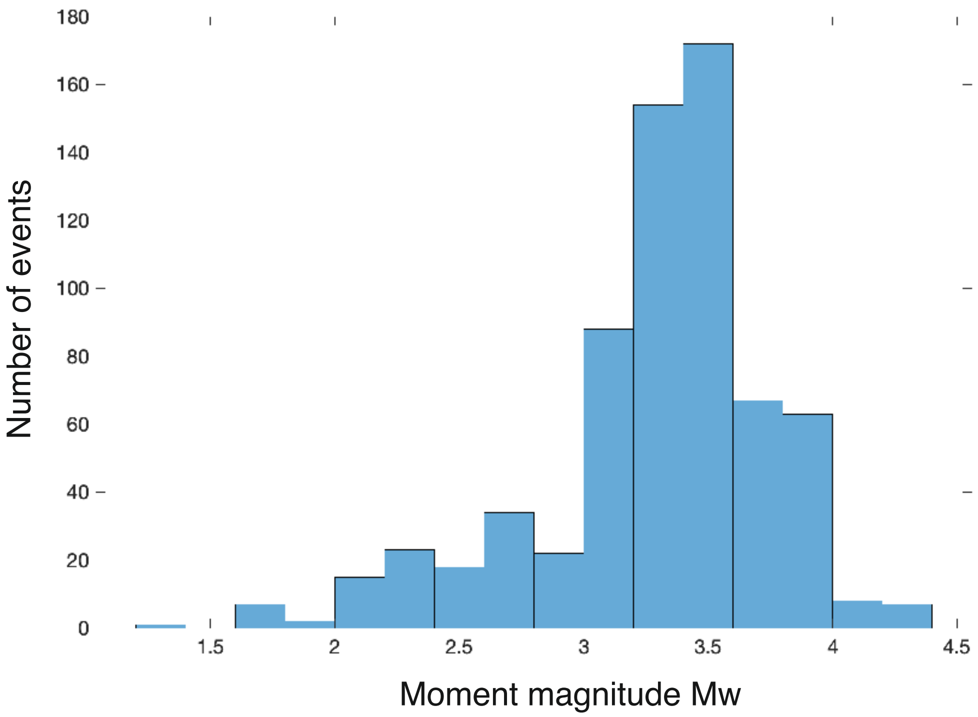

Figure 5.8: Frequency distribution of moment magnitudes M_w for all considered repeating earthquakes.

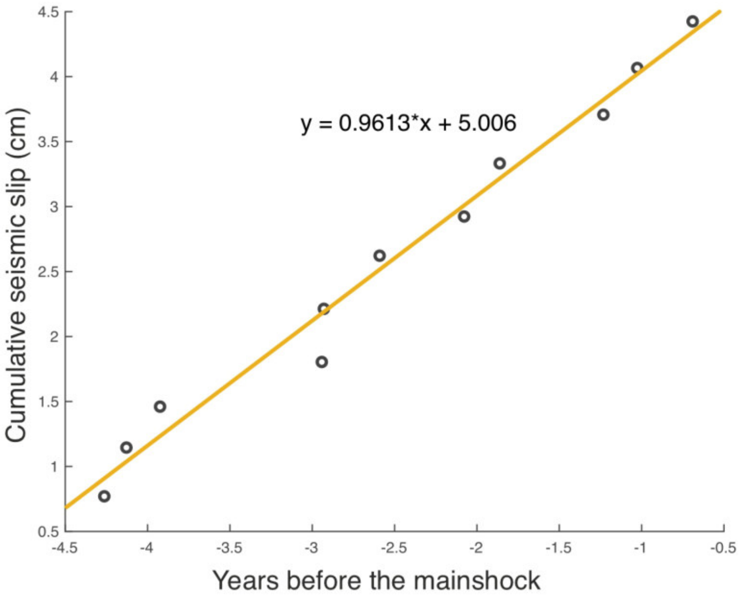

Figure 5.9: Averaged interseismic cumulative slip from plate interface repeaters from the end of 2009 until July 2013.

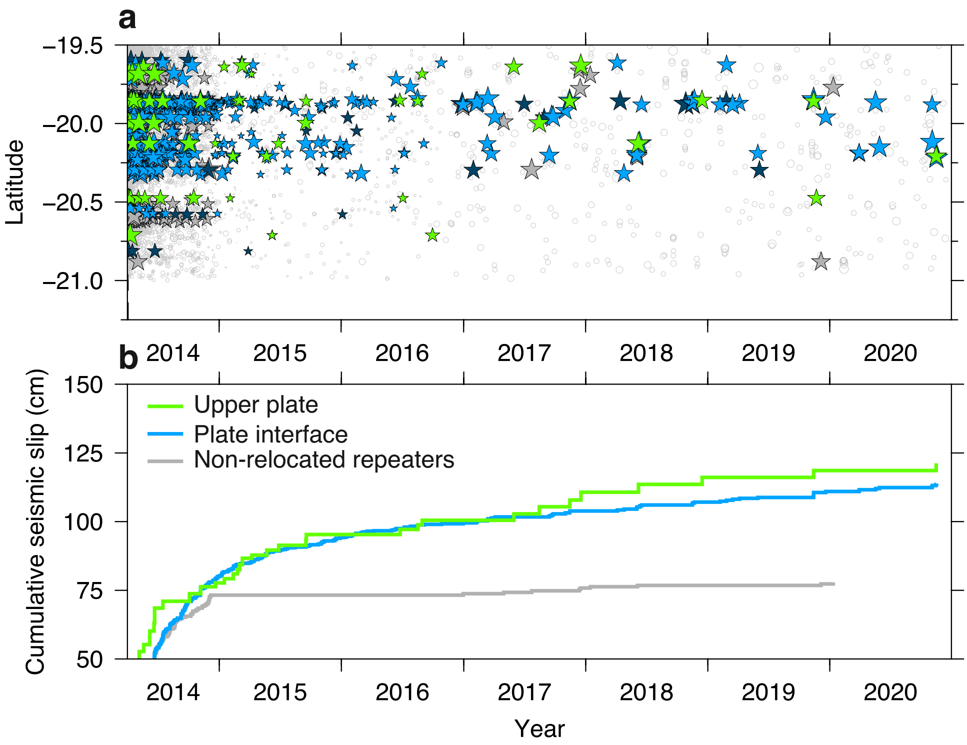

Figure 5.10: Repeating earthquake activity after the 2014 Iquique earthquake. (a) Repeater activity in time versus latitude. Stars mark the repeating earthquakes and symbol size is scaled by seismic slip. (b) Cumulative slip of upper plate, plate interface and non-relocated repeaters. The color scale is similar to panel a.

6 Measuring tectonic seafloor deformation and strain-build up with acoustic direct-path ranging

Invited review article

Florian Petersen[1], Heidrun Kopp[1,2], Dietrich Lange[1], Katrin Hannemann[1,3] and Morelia Urlaub[1]

1) GEOMAR Helmholtz Centre for Ocean Research Kiel, Germany
2) Institute of Geosciences, Kiel University, Kiel, Germany
3) Now at Institute of Geophysics and Geology, University Leipzig, Germany

Published in **Journal of Geodynamics**, February 2019.

DOI: 10.1016/j.jog.2019.01.002

Abstract

The Earth 'ocean floor deforms continuously under the influence of plate tectonic processes. In recent years, the development of deep-sea instruments using acoustic direct-path ranging allows observations of ocean floor deformation with unprecedented spatial and temporal resolution. Due to rapid technological progress, acoustic ranging emerged as a central research field to monitor seafloor deformation. Here we review recent developments and the progress of direct-path ranging applications. We discuss the methodology and examine the effects of the oceanographic environment on the measurement precision. Comparing the resolution of previous deployments, we find that the baseline uncertainty increases linearly with baseline length, at least for distances up to 3 km, but with different linear relations for each deployment. Measurements of displacement at millimeter-level precision across normal, thrust or strike-slip faults are discussed to evaluate the influence of dedicated network designs appropriate for the discrete fault geometries. Furthermore, tectonically quiet areas, such as flanks of coastal or ocean island volcanoes and passive continental margins pose substantial hazards that often lack in-situ monitoring and are therefore a significant target for the application of seafloor geodetic techniques.

6.1 Introduction

Our comprehension of Earth's crustal dynamics has fundamentally advanced through satellite geodesy, but the frequency-dependent attenuation of electromagnetic waves in seawater limits satellite geodesy to the onshore domain, whereas it is not applicable offshore. The satellite-based geodetic techniques in Earth Sciences comprise the Global Positioning System (GPS) and Interferometric Synthetic Aperture Radar (InSAR). These techniques have been applied routinely for more than three decades to monitor active motion of tectonic plates, the movement of fault zones and plate boundaries as well as volcanic activity (e.g., Owen et al., 2000; Reilinger et al., 2006; Tong et al., 2010). Furthermore, gravity models reveal large scale tectonic structures of the seafloor but are not capable to resolve tectonic deformation with high temporal and spatial resolution (Sandwell et al., 2014). Therefore, the global coverage with standard geodetic and surveying methods is only 30 %, even when considering all ocean islands. However, most tectonic plate boundaries are located offshore and most earthquakes occur along plate boundaries. Away from active plate boundaries, non-tectonic seafloor displacement arises where volcanic activity builds steep edifices that are prone to gravitational sliding and catastrophic flank failures with subsequent tsunami generation. This also applies to passive continental margins, where the largest slope failures have been detected to date (Masson et al., 2006).

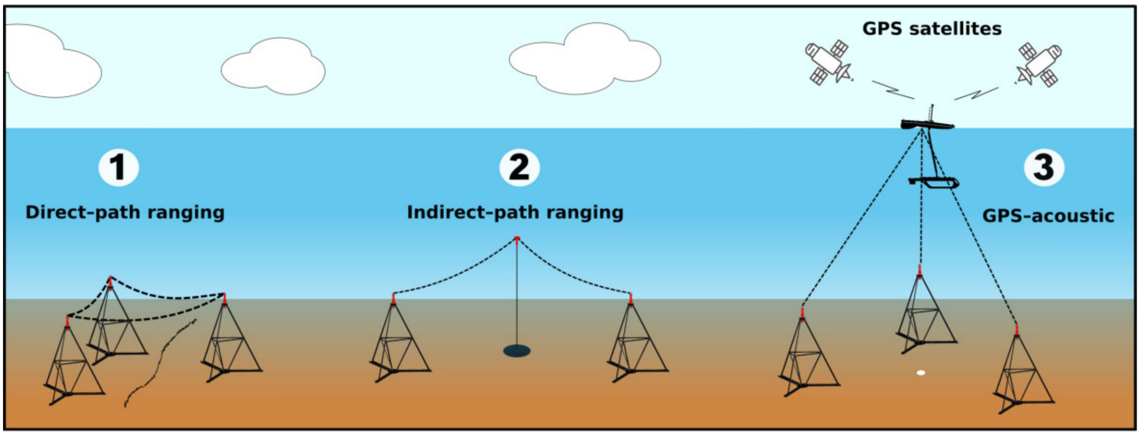

Figure 6.1: Illustration of acoustic geodesy methods to monitor seafloor displacement. (1) Acoustic direct-path ranging between several transponders to monitor relative displacement, for example across tectonic faults, (2) Indirect-path ranging between transponders and a water column floating transponder to extend measuring distances to several kilometers, (3) GPS-acoustic measurement with combination of satellite GPS positioning and a seafloor transponder network to determine the centered seafloor position (white dot) in the global reference frame (modified after Spiess, 1985).

The first steps towards seafloor geodesy were initiated by the development of underwater vehicle positioning at meter scale (Yamamoto et al., 2018; Bürgmann and Chadwell, 2014). Technological achievements in the 1980s facilitated the development of first acoustic geodesy studies capable of centimeter-scale monitoring of seafloor displacement (Spiess, 1980, 1985). Today, technical advances, together with enhanced battery capacity allows the operational extension of seafloor geodetic applications of up to ten years. Besides some free-fall deployments (e.g., Phillips et al., 2008; McGuire and Collins, 2013), accuracy seafloor geodetic installations at narrow fault zones or in regions of significant seafloor topography often require difficult and cost-intensive Remotely Operated Vehicle (ROV) and Autonomous Underwater Vehicle (AUV) operations.

6.2 Acoustic ranging

Displacement at the seafloor occurs in vertical and horizontal directions. The vertical component can be estimated by pressure variations of the water column at the seafloor after the correction of the tidal constituents (Polster et al., 2009). The relative horizontal displacement is calculated from travel time and water sound speed. Spiess (1985) proposed three basic set-ups for acoustic seafloor geodesy measurements (Figure 6.1):

1) Direct-path ranging allows distance measurements between two or more transponders in an array configuration across a geologic feature. This direct-path ranging

method provides relative deformation measurement since the absolute transponder positions are not determined (e.g., Sakic et al., 2016).

1) Indirect-path ranging provides up to several kilometer-long ranges between transponders and an interrogator transponder in-between, which can be a floating or vessel operated device. The enlargement of measured distances using an interrogator can be combined with a direct-path ranging network (e.g., Yamamoto et al., 2018).

1) GPS-acoustic or GPS-A determines the absolute position of a transponder network relative to the global reference. This is done by acoustically measuring the relative position of the seafloor transponders to a sea surface vehicle with known position (using GPS satellites). The precise determination of the seafloor transponders location is achieved through a high number of acoustic measurements (e.g., Gagnon et al., 2005).

Ocean bottom pressure sensors are commonly linked to all acoustic geodesy installations.

6.2.1 Direct-path and indirect-path ranging

The objective of direct-path and indirect-path ranging is the detection of relative seafloor deformation at millimeter precision and high temporal resolution. Travel time information between transponders is used to derive the relative acoustic distance, which is represented by a baseline between two seafloor transponders. Travel times are dependent on the sound speed in water. The sound speed information, however, requires the correction for temporal variations in temperature, pressure, and salinity, which are all *in situ* measurable parameters. However, the in-situ measurement of these parameters is commonly only conducted at the transponder sites and is therefore not available along the entire acoustic ray path between the geodetic stations. Consequently, the sound speed is approximated by averaging the measurements from both endpoints of the baseline. The seafloor deformation is subsequently inferred using multiple baselines. The combination of direct-path and indirect-path approaches allows the expansion of the survey area by installing moored interrogation transponders. The centered floating transponder is triangulated by at least three surrounded stations and position changes over time reveals seafloor deformation (Chadwell and Sweeney, 2010). The use of acoustic signals for the detection of seafloor deformation was first discussed by Spiess (1980, 1985). In the early 1990s, the U.S. Geological Survey installed one of the first acoustic ranging networks to measure horizontal deformation associated with seafloor spreading across the southern Juan de Fuca Ridge (Figure 6.2), a divergent plate boundary offshore Oregon State (Chadwick et al., 1995; Morton et al., 1994). Three transponders were installed in an L-shape configuration across the Cleft segment comprising one crossing-ridge baseline and one along-ridge baseline. No active spreading of the ridge was observed during the two years of direct-path ranging (Chadwell et al., 1999). A second ridge-crossing deployment also yielded no extensional motion within the uncertainty of 10 mm at the Cleft segment (Chadwick and Stapp, 2002; Chadwell and Spiess, 2008). Further to the north, Chadwick et al. (1999) deployed five acoustic transponders across the active rift zone of Axial Seamount on the Juan de Fuca Ridge, offshore Cascadia (Figure 6.2), with a precision of ≥ 1 cm over a distance of 100 m − 400 m and measured up to 9 cm horizontal extension during an eruption of Axial Seamount. In 2007, (McGuire and Collins, 2013) deployed seven acoustic ranging transponders across the Discovery Transform Fault on the East Pacific Rise (Figure 6.2) to enhance our understanding of plate motion partitioning of aseismic and seismic slip and achieved millimeter baseline precision for a 1 km long baseline. Furthermore, acoustic direct-path ranging has been employed in monitoring an unstable slope to determine deformation across the headwall of a prospective submarine landslide in the Santa Barbara Basin offshore California (Figure 6.2 Blum et al., 2010).

6.2.2 GPS-acoustic (GPS-A)

While the direct-path or indirect-path acoustic ranging techniques reveal the relative displacements between transponders on the seafloor, they do not provide information about the absolute position in the global reference frame. Direct satellite-based positioning (i.e. ‘underwater GPS’) is not possible at the seafloor. Therefore, a complementary acoustic ranging method (relative measurement) to transfer the absolute coordinates from GPS from the sea surface (e.g. from a ship or autonomous surface vehicle) onto the transponder array on the seafloor is required. This system is called GPS-acoustic or GPS-A because it combines GPS and acoustic methods (e.g., Figure 6.1 and Spiess (1985); Gagnon et al. (2005); Fujimoto (2006); Matsumoto et al. (2008)). A GPS-acoustic system measures the two-way travel time between the mounted transducer on board of a ship or surface vehicle and the seafloor transponder (e.g., Fujita et al., 2006). Simultaneously, the system determines the ship’s coordinates via GPS and the ship’s movement with a motion sensor. One difficulty of the GPS-A method is the precise and accurate positioning of the GPS antennas relative to the transponder mounted on the ship, which communicates with the beacons on the seafloor (Chadwell, 2003). Data acquisition campaigns are conducted in regular intervals from once to a few times per year and are mainly realized by vessels. First tests of autonomous surface vehicle operations are initiated at the Cascadia subduction zone (Chadwell, 2016) and at the Mexican subduction zone (Cruz-Atienza et al., 2018).

The GPS-A method was developed at Scripps Institution of Oceanography in the 1980s. The first GPS-acoustic campaign was conducted offshore Vancouver Island to measure the

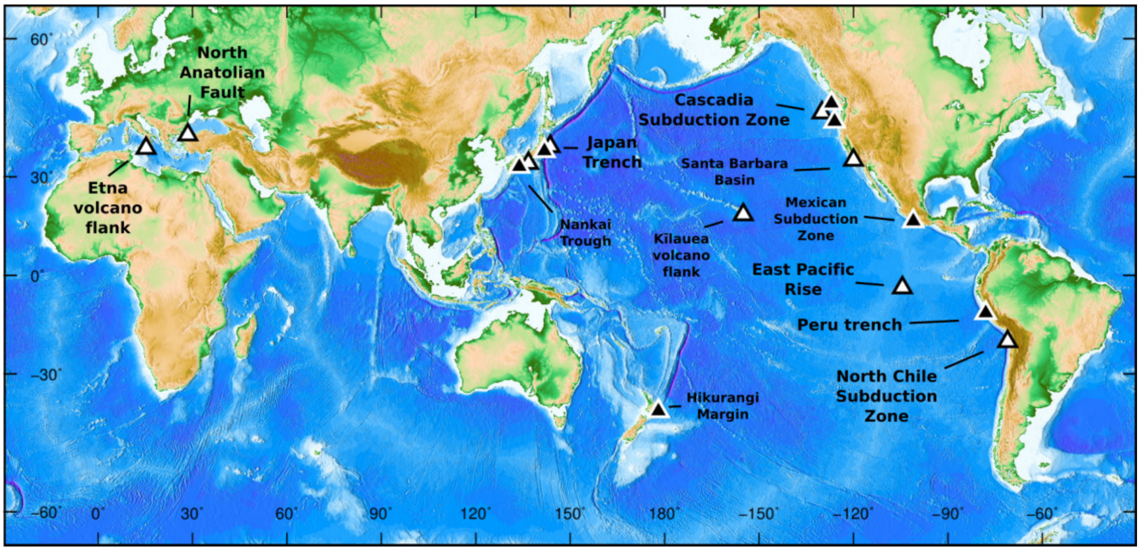

Figure 6.2: Global map summarizing acoustic seafloor geodesy networks. Black triangles indicate GPS-acoustic experiments and white triangles show direct-path ranging deployments. From West to East: Etna volcanic flank: Urlaub et al. (2018); North Anatolian Fault: Sakic et al. (2016); Kido et al. (2017); Nankai Trough: Osada et al. (2008); Yokota et al. (2016); Japan Trench: Sun et al. (2014)); Yamamoto et al. (2017a,b); Hikurangi Margin: Henrys et al. (2016); Kilauea volcanic flank: Brooks et al. (2011); Cascadia subduction zone: Chadwick et al. (1995), Chadwell et al. (1999); Spiess et al. (1998); Chadwick and Stapp (2002); Santa Barbara Basin: Blum et al. (2010); East Pacific Rise: McGuire and Collins (2013); Mexican subduction zone: Cruz-Atienza et al. (2018); Peru shallow forearc: Gagnon et al. (2005); North Chilean subduction zone: Hannemann et al. (2017) and J. McGuire, pers. comm. Figure modified from Weatherall et al. (2015).

convergence of the Cascadia subduction zone offshore Vancouver Island at centimeter-scale resolution (Spiess, 1985; Spiess et al., 1998)(Figure 6.2). In 2001, Gagnon et al. (2005) targeted the subduction zone offshore Peru (Figure 6.2) with a seafloor GPS-acoustic array and installed two transponder networks spaced 30 km apart from each other. The networks were arranged perpendicular to the trench to obtain the absolute horizontal deformation and to determine the up-dip limit of the locked subduction interface. After two years the five days-long data acquisition survey revealed no slip along the thrust fault with 1 cm precision. This observation, as well as the shallow M_w 7.5 earthquake in 1996 offshore Peru with the subsequent tsunami (Satake and Tanioka, 1999) supports shallow locking of the Peruvian subduction zone from 40 km to 2 km depth.

Pioneering seafloor monitoring in a convergence setting is located off Japan, where the first co-seismic displacement was recorded using acoustic seafloor geodesy during the M_w 7.3 Kii Peninsula earthquake in 2004 at the Nankai Trough Kumano Basin (Kido et al., 2006) (Figure 6.2). The observed horizontal trench-perpendicular displacement is three times larger than predicted by global navigation satellite system (GNSS) models derived on land. On the marine forearc of the Nankai Trough, 15 GPS-acoustic stations were deployed by the Hydrographic and Oceanographic Department of the Japan Coast Guard and six stations were installed offshore Honshu prior to the 2011 Tohoku-Oki event by Tohoku University and the Japan Coast Guard (Sato et al., 2013). The Nankai Trough located between the Philippine Sea and Amur plate is interpreted as a locked plate interface with an expected megathrust event in the near future (Yokota et al., 2016). Yokota et al. (2016) showed that offshore plate coupling heterogeneities cannot be precisely resolved using only the GNSS observations. Hence the set-up of GPS- acoustic sites provides a crucial extension to the onshore GNSS sites. A network of seven GPS-acoustic stations recorded the M_w 9 Tohoku-Oki earthquake. This great event generated up to $\sim$31m of co-seismic displacement measured in-situ near the trench (Kido et al., 2011; Sato et al., 2011) and provided surprising results about the deformation of the marine forearc during the postseismic period. In subduction zones, onshore observations previously suggested that the overriding plate is moving during the postseismic period in the same direction as the coseismic slip, which is directed towards the trench. However, offshore GPS-A data from Sun et al. (2014) revealed the contrary motion of the marine forearc during the postseismic period which can be explained with viscoelastic relaxation processes.

6.3 Ocean bottom pressure

Atmospheric pressure sensors are commonly used in navigation applications to determine topographic elevation, whereas the relatively low density of air limits the application for geodesy. However, seawater has a higher density and the pressure increases with approximately 100 kPa every 10m in depth change. Ocean bottom pressure sensors commonly use Bourdon tube mechanical gauges (Paros, 1976; Wearn and Larson, 1982). The coiled tube is open on one side to ensure a constant balance with the surrounding pressure at the seafloor. An oscillating quartz element is attached at the closed end. Increasing ambient pressure induces uncoiling of the tube and changes the tensile stress and following resonant frequency changes of the oscillating quartz element (Watts and Kontoyiannis, 1990). The initial exponential drift and vertical short-term deformation can be well measured. However, long-term changes are difficult to distinguish from unpredictable linear sensor drift (Polster et al., 2009). Pressure sensors have been used widely at the seafloor (e.g., Ballu et al., 2010; Ohta et al., 2012; Sasagawa et al., 2016; Wallace et al., 2016), in boreholes (e.g., Davis et al., 2011), and in the water column to detect approaching tsunamis and to calculate their magnitude (e.g., Baba, 2004). Uplift and subsidence of the seafloor are monitored in many cases with continuous seafloor pressure measurements. Vertical seafloor deformation has been monitored since the late 1980s during eruptions of the Axial Seamount located on the Juan de Fuca Ridge (Fox, 1999; Chadwick et al., 2006).

Recent applications of absolute pressure gauges focus on slow slip events at subduction zones, e.g. Hikurangi subduction zone in New Zealand (Wallace et al., 2016) and the Boso Peninsula, Japan (Sato et al., 2017) Their usage has also added additional constraints on precursory slip (Ito et al., 2013) and afterslip processes (Ohta et al., 2012) of the 2011 Tohoku-Oki event.

6.4 Methodology of acoustic direct-path ranging

Acoustic direct-path ranging transponders are commonly equipped with high-precision hydrophone transducers to transmit and receive acoustic signals. A piezoelectric element converts an electronic signal to a pressure signal emitted with omnidirectional pattern and vice versa converts incoming pressure to an electronic signal. These signals consist of a phase-coded pulse in a kHz range bandwidth and are transmitted between transponders in a network to yield distances derived from the two-way travel times and consequently deformation over time (e.g., Seitz et al., 2007; Osada et al., 2008; Sakic et al., 2016). The transmitted acoustic rays are also reflected at the seafloor, sea surface and water column interfaces, however, the reflected signals have increased or shortened travel times and random phases and amplitudes. Two major procedures are used: One master transponder transmits a common interrogation signal to all slave acoustic repeater stations and measures the travel time periodically (Chadwick and Stapp, 2002; Osada et al., 2008; McGuire and Collins, 2013). This method involves a risk in terms of data loss in the case of failure at the master transponder and results in one-way baseline measurements. Alternatively, one transponder acts as master and transmits an interrogation signal to all other (slave) transponders in the same network using a phase-encoded acoustic signal. Afterwards, another transponder sends an interrogation signal as master to all other transponders. The slave transponders individually reply after a specific delay time. The resulting travel time is calculated by cross-correlation of transmitted and received signals at the first transponder. Additionally, advanced signal processing techniques are used to improve the precision of the direct arrival selection in the cross-correlation (i.e. pseudo peak subtraction or cluster analysis of resulting correlograms, for details see Azuma et al. (2016)). Thereafter, the whole procedure is repeated using another transponder to transmit a common interrogation signal (Chadwick et al., 1999; Dunn et al., 2016; Sakic et al., 2016). As a result, the baselines are measured in both directions and the data are stored on all transponders to minimize possible data loss.

The frequency range of 5 kHz to 100 kHz is widely used for subsea navigation and results in wavelengths of $1.5-30$ cm (Urick, 1983), which is similar to electromagnetic wavelengths of the L-Band used for GPS navigation systems (Bajaj et al., 2002). The optimum frequency band for acoustic signals is dependent on the measuring distance and becomes lower as the distance increases. At lower frequencies, the noise level increases, and for higher frequencies, the acoustic signal is more affected by attenuation (Stewart et al., 1981). While precise travel time measurements are essential for millimeter resolution in underwater geodetic implementations, variations in sound speed are the major obstacle for precise travel time and hence distance measurements (e.g., Sakic et al., 2016). In isothermal waters of the deep-sea, the vertical sound velocity gradient is mainly controlled by the increase of pressure with depth, which allows high baseline resolution. However, the direct ranging is limited by geometric spreading and absorption loss of acoustic signals. Besides this, bending (e.g. bending upward away from seafloor) of sound rays in the deep-sea (Spiess, 1985) requires in occasion up to 5 m high structures, frames or floating units, which, however, are more prone to tilt and hence influence baseline lengths. Subsea deployments oblige a recovery procedure at the end of operation. The most common method is a release mechanism with anchor and buoys, which is also prone to a higher degree of tilt. Tilting of instruments can be minimized by installing frames on monuments (e.g., Phillips et al., 2008; McGuire and Collins, 2013) or without attached buoyancy bodies on the seafloor. Data correction for inclination is feasible if tiltmeter data with known orientation are available.

6.4.1 Time of flight

The time of flight can be measured with microsecond resolution, equivalent to millimeters of range. The two-way travel-time is defined as the time of flight from one transponder to another and the time required by the reply (Figure 6.3a). Two-way time of flight travel time measurements do not require a most accurate time synchronization on both endpoints, however, long-term monitoring must take the transponder clock drift into account. Drifts greater than 3.8 ppm (120 s/yr) affect the two-way travel time with a baseline error of more than 5 mm, hence the determination of the sound wave propagation velocity on both endpoints or ideally along the acoustic path is crucial to detect millimeter-level distance changes. This is achieved by monitoring the ambient parameters of temperature, pressure, and conductivity (salinity) or by direct measurements with high-frequency sound velocity meters (Osada et al., 2012). In addition, the measurement of seafloor displacement by acoustic ranging between two fixed transponders or between a transponder and a ship depends on the quality of the received sound signals. In conclusion, the combination of travel time and sound velocity yields the geometrical distance between two transponders. Additionally repeating interrogations over months and years provide the baseline changes.

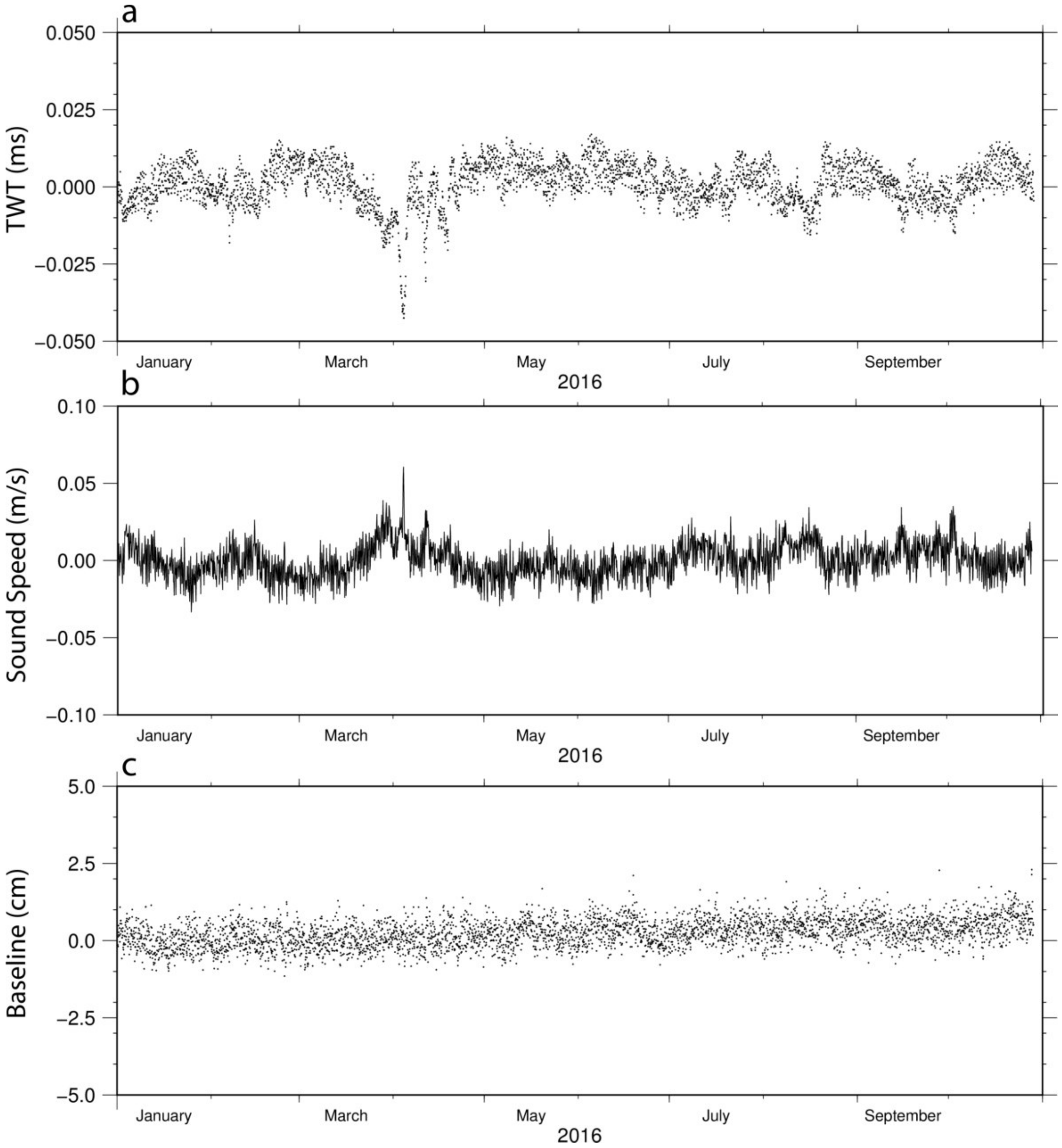

Figure 6.3: Time series examples from a direct-path installation at the Northern Chilean subduction zone in more than 5000 m water depth from January to November 2016. (a) Two-way travel-time between two acoustic transponders. The measurement occurs nine times per day in both directions. The travel-times are obtained by cross-correlating the transmitted and received signal. (b) Sound speed between two acoustic transponders. Temperature, pressure and a constant salinity were used to calculate the sound speed by using the Leroy et al. (2008) formula. Changes in sound speed are less than 0.05 m/s in deep oceans. (c) A baseline example between two stable transponders inferred from the conversion (Eq. 6.1) from two-way travel-time (a) and sound speed (b).

6.4.2 Speed of sound in oceans

The speed of sound in oceans is approximately five times faster than in the atmosphere and its spatial and temporal behavior has important effects on propagating acoustic waves. It is predominantly controlled by temperature and less dependent on salinity and pressure (Wilson, 1960). Shallow water mixing largely affects temperature and salinity, whereas below 1000 m water depth temperature and salinity stabilize and the linearly increasing pressure dominates Urick (1983). The depth varying temperature, salinity, and pressure create a horizontal layer of minimum sound speed in the water column of the oceans. Sound waves are trapped in this low-velocity zone termed SOFAR (Sound Fixing and Ranging) channel and can propagate for thousands of kilometers (e.g., Metz et al., 2016). This unique characteristic of the SOFAR channel is used for large-scale monitoring of oceanographic properties with acoustic tomography Munk et al. (1995).

Nevertheless, ocean bottom water mass variations and turbulence imposed by currents significantly decrease the signal-to-noise ratio of sound speed measurements. Sound speed formulas are polynomial fits to empirically determined values from laboratory measurements of seawater temperature, pressure, and conductivity. Different equations were developed: Chen and Millero (1976) published a solution that is known as the UNESCO equation and has developed into the international standard algorithm. On the contrary, Grosso (1974) estimated sound speed from absolute measurements with seawater and offer an alternative to the standard algorithm, however, this approach is limited to a smaller range of environmental parameters. The Leroy et al. (2008) formula uses latitude and depth instead of pressure. However, direct-path ranging monitors relative changes of transponder locations and the sensor precision of the measurement is less dependent on the absolute values of temperature, pressure and salinity, as most uncertainty in baseline precision is imposed from the temporal changes of the physical properties of the water mass along the ray paths (Figure 6.3b).

6.4.3 Baselines

The acoustic distance between two acoustic geodetic stations or beacons, which is derived from the conversion of time of flight and sound speed in water, is called a baseline (Figure 6.3c). Time of flight is measured as two-way travel-time (twt) from one transponder to another. Simultaneous incoming reply signals at the interrogator transponder result in signal time clashes and hence cross-correlation failure. Therefore, a delay time ($delta_i$) for each transponder i is set to avoid signal time clashes. The delay times are chosen based on the expected travel times between the stations. The baseline is then calculated with:

$$s = v \cdot \frac{(twt - delta_i)}{2} \tag{6.1}$$

The sound speed v can be measured directly by SV (sound velocity) probes with less accuracy (Sakic et al., 2016), thus v is commonly calculated from temperature, pressure and salinity (Chen and Millero, 1976, Section 6.4.2). The aforementioned uncertainty propagation from the averaged sound speeds to the estimated acoustic distances is also visible in the baseline estimates presented in Figure 6.3c. Moreover, the baseline data often show apparent drifts originating from sensor drifts (in addition to the potential tectonic deformation signal), therefore the separation of deformation from the sensor drift signal is crucial. For instance, Sakic et al. (2016) utilized a least squares inversion approach using a strike-slip deformation model to linearly detrend the baselines. The method assumes that no deformation between two reference transponders (e.g. on one side of a strike-slip fault, where the crustal block is assumed stable) occurs.

6.4.4 Resolution

The estimated baseline changes are strongly related to transient changes of the water column conditions that can exceed the expected deformation signal, especially for long direct-path baselines. The standard deviations of baselines reveal a linear increase in relation to the ranging distance within one network (Figure 6.4). This is related to the aforementioned mapping of the sound speed uncertainties into the acoustic distance, due to the incompletely known sound speed distribution along the ray path.

The resulting uncertainty of sound speed by averaging the in-situ measurements at the ranging transponders affects the acoustic distance determination. Therefore, the measurements require a certain accuracy to achieve mm precision. These values are dependent on pressure (and hence water depth), temperature and salinity. For instance, if a 1 mm baseline precision is to be achieved for a 1000 m baseline, considering an ideal time measurement, in 5000 m water depth, salinity of 32 PSU and temperature of 5 °C, the following sensor accuracy should be met. Pressure sensors of oceanographic moorings can achieve an accuracy of 0.01 kPa (approx. 0.1 cm absolute depth), which is lower than the required sensor accuracy of 1 kPa (approx. 10 cm absolute depth). Salinity can be determined by electrical conductivity measurements, but long-term measurement of conductivity is a major challenge in acoustic direct-path ranging. Custom conductivity sensors achieve salinity accuracy less than 0.001 PSU and are biased by sensor fouling induced drift. To circumnavigate this problem, sound speed calculations with assumed constant salinity values are commonly used to convert travel times to baselines (e.g., Osada et al., 2012; Sakic et al., 2016; Urlaub et al., 2018). The temperature measurements require a high accuracy

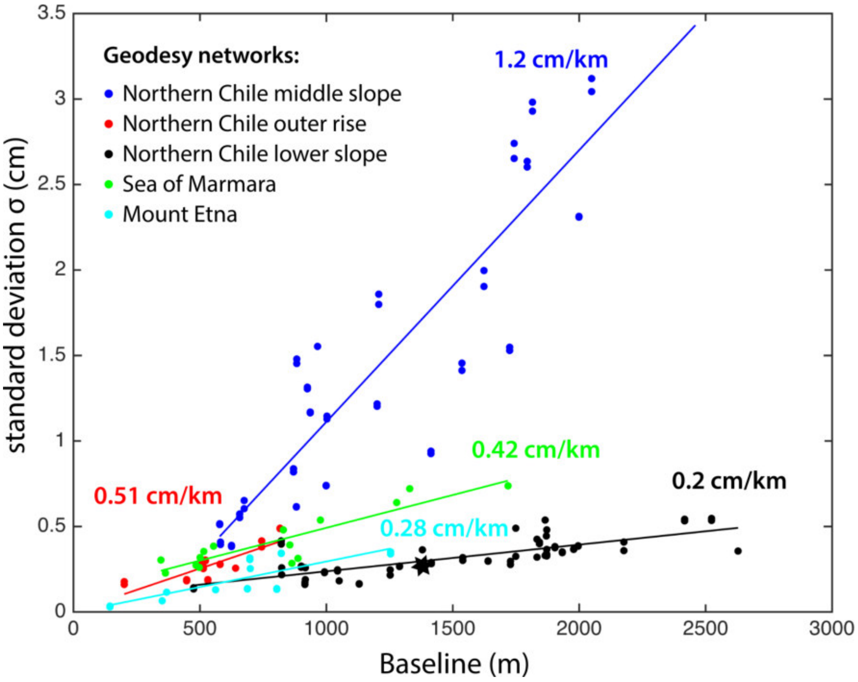

Figure 6.4: Baseline length plotted against standard deviation (SD) of baseline scatter as proxy for baseline precision. Five direct-path ranging GeoSEA networks run by GEOMAR are color-coded: (blue) North Chilean subduction zone in 2300 m water depth located on the middle continental slope, (red) North Chilean subduction zone in 5000 m water depth located seaward of the deep- sea trench on the oceanic plate, (black) North Chilean subduction zone in 5300 m water depth located east of the deep-sea trench on the lower slope of the marine forearc (Baseline of Figure 6.3 is marked as black star), (green) North Anatolian Fault in 800 m water depth in the Kumburgaz Basin of the Marmara Sea, (cyan) on Mount Etna's eastern flank in 1000 m water depth.

of 0.0005 the following sensor accuracy should be met. Pressure sensors of oceanographic moorings can achieve an accuracy of 0.01 kPa (approx. 0.1 cm absolute depth), which is lower than for a 1 mm long baseline precision. However, millimeter precision can be achieved with a stable temperature and salinity field (e.g., McGuire and Collins, 2013; Sakic et al., 2016).

Analysis of seafloor geodetic networks in distinct ocean environments and water depths indicates a linear increase of uncertainty with distance for each deployment. We assign this behavior to sound speed heterogeneities along the ray path (e.g., Chadwell and Sweeney, 2010) This is supported by comparing the standard deviation of baselines in the geodetic networks deployed in different oceanographic conditions. A network located on the middle continental slope of the north Chilean forearc shows a moderate resolution compared to other geodetic networks, which used the identical instrumentation (Figure 6.4, compare blue curve and data points to all others). This region is well known as an area of upwelling and of being highly influenced by the northward flowing Humboldt current (e.g., Montecino and Lange, 2009). This is an example of how the mixing of water masses due to ocean currents presumably influence the ray path uncertainties of the baselines. Although Figure 6.4 shows that short ranges result in smaller scatter, long baseline measurements are often favored in regions of distributed deformation since strain resolution increases linearly with increasing distances. Geodolite distance measurements indicate a similar precision decrease with line length (Savage and Prescott, 1973). In their study, standard deviation shows a non-linear increase with line length above 5 km, however, aircraft obtained temperature profiles improved the measurements in the past. For acoustic ranging, it remains unclear if the linear relation between baseline lengths and baseline uncertainties holds for distances exceeding ~3 km or if a similar behavior to geodolite measurements appears since nonlinear effects in the ray propagation increase.

6.5 Application of direct-path ranging to different fault scenarios

The primary target of acoustic seafloor geodesy so far is to monitor crustal displacement or slope stability. Often acoustic ranging networks are employed at fault systems repeatedly struck by devastating earthquakes. Currently, the precise distribution of coseismic and postseismic slip or interseismic strain accumulation is unknown along submarine fault segments (Lange et al., 2014), so that partitioning of seismic and aseismic slip along these segments is not resolved. Different targets and tectonic displacement patterns require dedicated network designs of the direct-path ranging geodetic array. In this section, we discuss how networks are best designed for different fault geometries. The distribution between horizontal and vertical displacement is mainly governed by the fault's dipping angle. Considering a shallow dipping fault, most of the displacement at the fault will be horizontal. For a steeply dipping fault, the largest displacement component at the fault will be vertical. In general, baselines will shorten when crossing a thrust fault (compressional fault) and lengthen when crossing a normal fault (extensional fault), while both, shortening and lengthening of baselines will be observed across a strike-slip fault, depending on the baseline geometry relative to the fault.

6.5.1 Strike-slip fault

Strike-slip faults are nearly-vertical fault zones characterized by horizontal shear deformation. During the interseismic phase of the seismic cycle, steady motion occurs distant from the fault, while the fault is accumulating stress (e.g., Reid, 1910; Savage and Burford, 1970). The amount of accumulated stress is reflected by the locking degree of the fault. The network design for a strike-slip fault should consider the end members of a fully locked and a fully creeping fault (e.g., Savage and Burford, 1970, 1973). The measured displacement is dependent on the distance to the fault since the strain occurs not only on razor-sharp lineament and hence, strain decays rapidly with distance to the fault. Furthermore, the baselines are measured at different angles to the fault. We modified the one-dimensional simple elastic rebound model of an infinite strike-slip fault for a creeping (coseismic phase) fault and a locked (interseismic phase) fault (Savage and Burford, 1970, 1973). In the interseismic phase one side moves in one direction in the far field. In this phase the fault is locked to the depth W, below which it is freely slipping. In the coseismic phase, the fault moves with displacement $D = v \cdot t$ in one direction, but the slip $s(x)$ decreases with perpendicular distance x to the fault, because motion occurred in the far field during the interseismic phase. The direct-path ranging approach monitors only the very near field of the fault. Considering a transponder pair crossing the fault to monitor the baseline length l and length change u during the seismic cycle, one transponder is located on one side close to the fault and the second transponder across the fault in a distance $x = l \cdot \sin(\alpha)$. The observed baseline change $u(l, \alpha)$ is hence a function of the angle α between the baseline and the fault at the seafloor, and length of the baseline l:

$$\text{(a) Coseismic phase: } u(l, \alpha) = \left(D - \left(\frac{D}{\pi} \cdot tan^{-1} \right) \left(\frac{x}{W} \right) \right) \cdot cos(\alpha) \tag{6.2}$$

$$\text{(b) Interseismic phase: } u(l, \alpha) = \left(\frac{D}{2} - \left(\frac{D}{\pi} \right) \cdot tan^{-1} \right) \left(\frac{x}{W} \right) \cdot cos(\alpha) \tag{6.3}$$

In both phases (coseismic and interseismic), the maximum measurement of change in baseline length is observed for nearly fault parallel baselines (Figure 6.5). Short baselines, during the coseismic phase, experience higher relative baseline changes than longer baselines (Equation 6.2, Figure 6.5a), whereas the inverse behavior is observed for a locked fault (Equation 6.3, Figure 6.5b), for which longer baselines have higher relative changes in baseline length. However, the maximum baseline change in the interseismic phase is approx. 40 % less than a measured coseismic fault motion. These considerations show the relevance of specific network designs at strike-slip faults.

The North Anatolian Fault is a continental strike-slip fault that forms the boundary between the Eurasian and the Anatolian plates. The right lateral strike-slip fault system creates the marine pull-apart basin of the Sea of Marmara. The North Anatolian Fault experienced a westward propagating sequence of events in the 20th century with the last large destructive earthquake (M_w 7.4) in 1999 near the city of Izmit causing more than 17,000 casualties (Hubert-Ferrari et al., 2000). The Izmit event marked the end of the 20^{th} century sequence, which terminated at the eastern boundary of the Sea of Marmara. The east-to-west migration of major events along the North Anatolian Fault

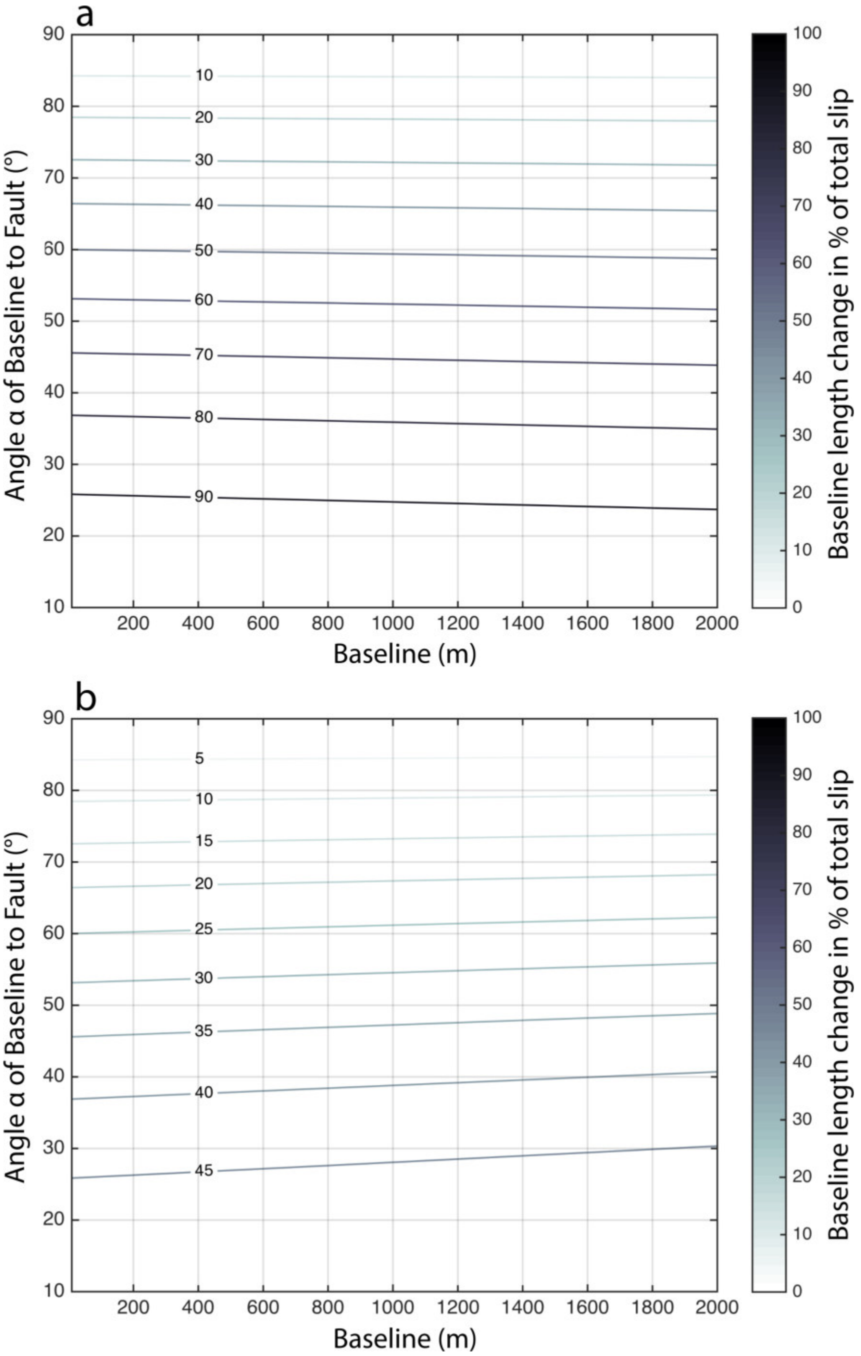

Figure 6.5: (a) Coseismic or creeping baseline-length change in percent of the fault slip as a function (Eq. 6.2) of the intersect angle of the direct-path ranging baseline and a strike-slip fault and the baseline length (modified after Savage and Burford, 1970), (b) Interseismic deformation (Eq. 6.3) of a locked fault zone for a simple elastic rebound model of a strike-slip fault with 15 km locking depth (beneath which the fault is freely creeping). In both plots, the contour lines show the deformation of a baseline in percentage of the total slip.

left a seismic gap in the central main Marmara fault segment (Ambraseys, 2002; Şengör et al., 2005). The offshore location of the fault in the Sea of Marmara impedes studies to gain a detailed knowledge of the fault geometry and depth of the seismogenic zone in the western region. Networks of Ocean Bottom Seismometers (OBS) and onshore seismometers identified distinct areas of active seismicity and areas of absent seismicity (Schmittbuhl et al., 2015; Yamamoto et al., 2017b). The heterogeneous local distribution of seismicity lead to the deployment of acoustic ranging networks to monitor potential strain accumulation or surface fault creep across the western and the central Marmara Sea segments. Onshore GPS surveys in the vicinity of Marmara derive slip partitioning in the Sea of Marmara with a predicted right-lateral slip rate of 18 - 20 mm/yr and extension of 8 mm/yr across the Sea of Marmara Basins (Le Pichon et al., 2001). Ergintav et al. (2014) considered a minimum aseismic creep rate of 2 mm/a and additional geo-mechanical models suggest a strain accumulation rate of 10 - 16 mm/a (Hergert et al., 2011).

Two networks were installed in 2014 under Turkish-Japanese and Turkish-French-German collaboration. KOERI, Turkey, and IRIDeS from Tohoku University in Sendai, Japan, deployed a network of five transponders in September 2014. After 20 months of operation, changes in baseline length consistent with right-lateral strike-slip motion indicate a creeping fault segment with 9 - 14 mm/yr (Kido et al., 2017). The joint IUEM (Institute University Institute European De La Mer), GEOMAR (Helmholtz Centre for Ocean Research Kiel) and ITU (Istanbul Teknik Üniversitesi) cruise simultaneously installed a seafloor geodesy array in 2014 (Sakic et al., 2016). Ten acoustic monitoring transponders in two independent networks were deployed on the Central High across the North Anatolian Fault to measure horizontal deformation and strain build-up (Figure 6.6). This segment is considered to be locked or aseismically creeping (e.g., Ergintav et al., 2014; Sakic et al., 2016). The first six months of direct-path ranging data were processed with a least square inversion and revealed no significant deformation within the acoustic network (Sakic et al., 2016) in-line with a locked fault segment.

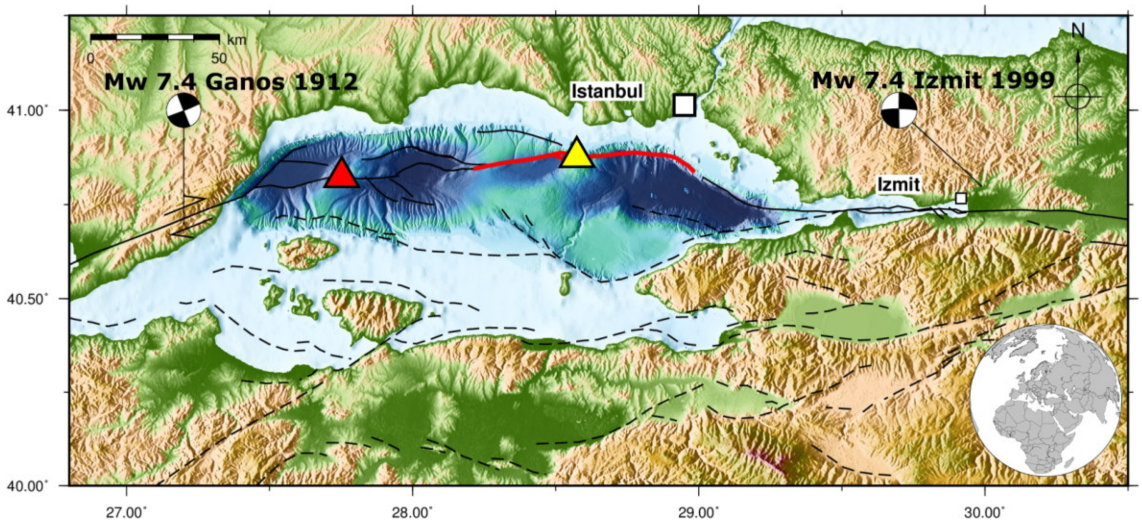

Figure 6.6: Location map of seafloor geodetic direct-path ranging networks in the Sea of Marmara to monitor the locked segment (red line) of the North Anatolian Fault. Direct-path ranging networks are installed by the Tohoku University (Kido et al., 2017, red triangle) at the Tekirdag Basin and western Kumburgaz Basin and by GEOMAR in the eastern Kumburgaz Basin (Sakic et al., 2016, yellow triangle). Fault traces (grey lines) from Armijo et al. (2002). The recent major earthquakes near the Sea of Marmara occurred in 1912 (Ganos, M_w 7.4) and 1999 (Izmit, M_w 7.4) (e.g., Barka, 2002; Aksoy et al., 2010). The cities of Istanbul and Izmit (white squares) are indicated for reference.

6.5.2 Normal and thrust fault

Dip-slip faults involve vertical and horizontal shifting of rocks. Mid oceanic ridges, subduction zones and passive margins are deformed by such active normal, reverse and thrust faults. Acoustic ranging networks at dip-slip faults require a different set-up compared to strike-slip fault systems. Network designs need to consider the baseline length in relation to the fault step height and the obliquity of the baseline to the fault. In contrast to strike-slip faults, baseline orientation across normal and reverse faults needs to be optimally conducted perpendicular to the surface expression of the fault and in line with the expected maximum deformation direction for oblique behavior.

Generally, steep faults result in mostly vertical displacement and slip is mostly inferred by hydrostatic pressure changes. In turn, horizontal changes for shallow dipping faults are large and the vertical displacement small. Overall, the dislocation modeling of normal and thrust faults is based on elastic modeling (Savage, 1983), yet the elastic case is more complex than the strike-slip modeling (section 6.5.1).

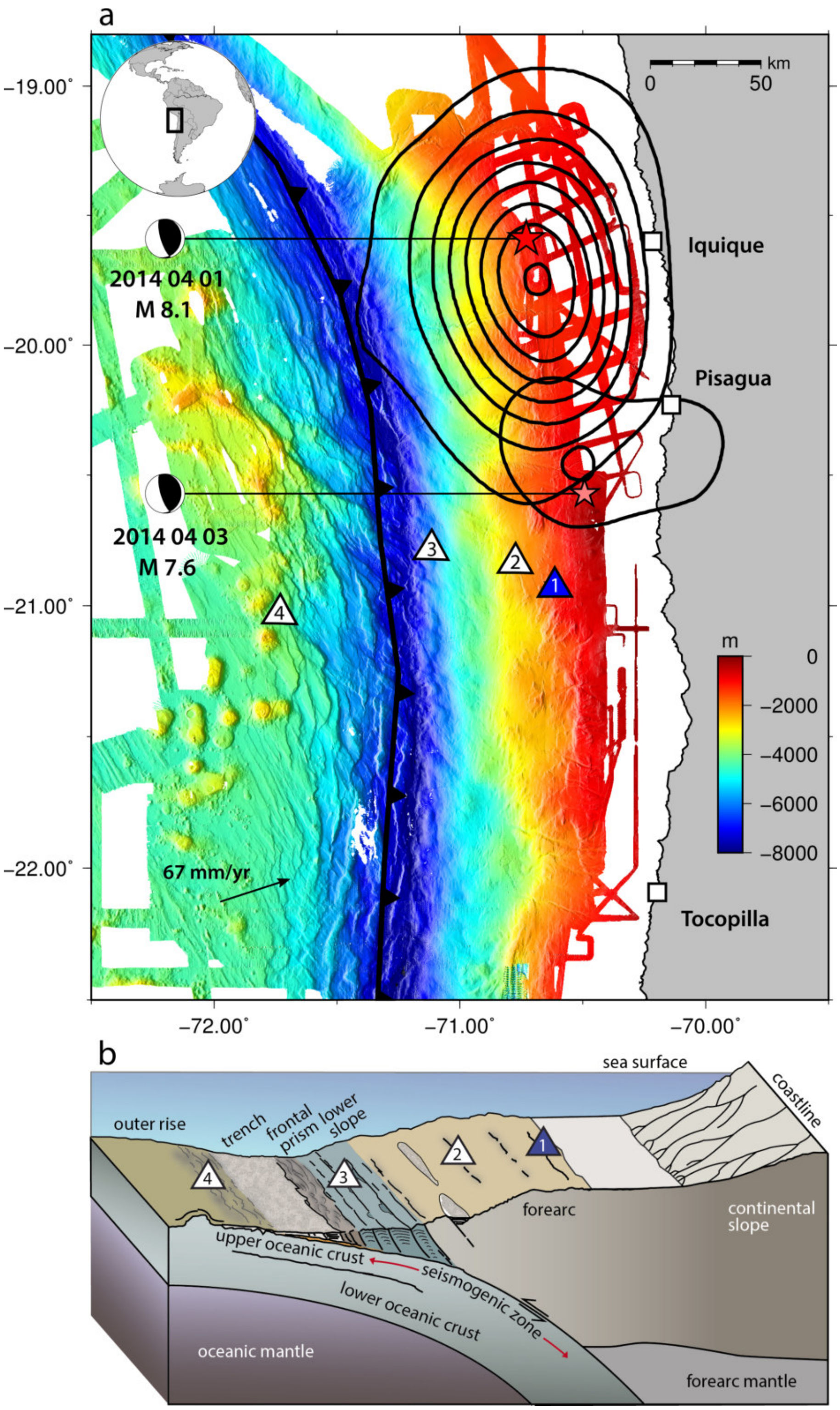
a
−19.00˚
−20.00˚
−21.00˚
−22.00˚
−72.00˚
−71.00˚
−70.00˚
km
0
50
Iquique
Pisagua
Tocopilla
2014 04 01
M 8.1
2014 04 03
M 7.6
67 mm/yr
1
2
3
4
m
0
−2000
−4000
−6000
−8000
b
sea surface
coastline
outer rise
trench
frontal prism
lower slope
forearc
continental slope
upper oceanic crust
seismogenic zone
lower oceanic crust
oceanic mantle
forearc mantle

Figure 6.7 ***(previous page)*****:** Location of current direct-path ranging networks monitoring the marine forearc of the north Chilean subduction zone. (a) White triangles indicate the locations of the GEOMAR direct-path ranging networks, located on the forearc middle slope (2), lower slope (3) and outer rise (4) (Hannemann et al., 2017) and blue triangle indicates the location on the forearc (1) of the WHOI direct- path ranging network (J. McGuire, pers. comm.). Contour lines indicate the co-seismic rupture areas of the 1 April 2014 Iquique M_w 8.2 and 3 April 2014 Tocopilla M_w 7.6 earthquakes in 0.5 m slip intervals with 5 m maximum slip for the Iquique event (Schurr et al., 2014). The swath bathymetric data collected during R/V SONNE cruise SO244, R/V Marcus G. Langseth cruise MGL1610 complemented with data from other cruises with R/V SONNE and R/V METEOR (Geersen et al., 2018). Plate boundary data between Nazca and South America from Bird (2003) and black arrow indicates the annual movement of the Nazca Plate with respect to the South American Plate (Angermann et al., 1999). The cities of Iquique, Pisagua and Tocopilla (white squares) are in-dicated for reference. (b) Schematic cross-section of the Chilean subduction zone to illustrate the target structures of the different networks (modified from Kopp, 2013).

Subduction zones host the greatest thrust earthquakes in the offshore domain, commonly far out of the reach of onshore geodetic observations. In northern Chile, the oceanic Nazca plate is subducting underneath the South American continent with a rate of 67 mm/yr (Angermann et al., 1999) (Figure 6.7). This segment of the megathrust has been identified as a seismic gap prior to the 2014 Iquique M_w 8.1 earthquake (e.g., Comte and Pardo, 1991; Schurr et al., 2014). In December 2015, 23 acoustic transponders were installed in three networks across the subduction zone to monitor submarine faults (Hannemann et al., 2017). Two networks are located on the continental slope, to observe fault motion of the topographic ridges and the complex deformation induced by the incoming Nazca Plate. A third network monitors normal faults caused by oceanic plate bending in the upper crust of the outer rise. In addition, Woods Hole Oceanographic Institution (WHOI) deployed a network in shallower depth on the upper continental slope (J. McGuire, pers. comm.; Figure 6.7). The four network locations are aligned in a trench perpendicular orientation to fully capture the strain build up across the North Chilean subduction zone. The monitoring is still ongoing.

The M_w 9.0 Tohoku-Oki earthquake in 2011 caused a co-seismic surface displacement up to 31 m (Kido et al., 2011; Iinuma et al., 2012) towards the Japan Trench first observed with seafloor geodetic methods. Deformation during the post-seismic phase was monitored by offshore GPS-acoustic measurements and shows evidence for viscoelastic relaxation after the main event (Sun et al., 2014). The relative motion of the incoming plate and the frontal prism represents the motion of the shallow plate boundary fault, therefore Yamamoto et al. (2017a, 2018) installed in 2013 three continuous direct-path ranging networks across the Japan Trench in addition to the already existing GPS-acoustic networks. The results indicate no significant shortening or deformation of the trench-crossing baseline and indicate absence of afterslip at the shallow portion within the resolution.

Hitherto, slow earthquakes or slow-slip events have been observed at several convergent plate boundaries (e.g., Ito et al., 2013; Graindorge, 2004; Wallace et al., 2016) by absolute pressure gauges at the seafloor or in boreholes, though solely the vertical deformation component was measured and an acoustic direct-path ranging observation of slow earthquakes is still lacking.

6.5.3 Unstable slopes

In addition to active tectonic faults, submarine slopes prone to mass wasting and slope failure are a target of seafloor geodetic investigations. At submerged slopes, in particular at passive continental margins or ocean island volcanic edifices, sudden mass movements may generate devastating tsunamis that potentially cause the loss of human lives and destruction of infrastructure. Direct-path ranging provides information on the spatial and temporal dynamics of areas with a tendency of failure and are thus crucial to hazard assessment (Urlaub and Villinger, 2018). The first assessment of an area prone to slope failure was conducted at the northern flank of the Santa Barbara Basin (Blum et al., 2010). A connecting seafloor crack between two slides is suspected to evolve into the headwall of a future slide. The two years of monitoring of the crack revealed no active seafloor movement. Absolute pressure gauges have been used to monitor the offshore décollement of the landslide associated to Kilauea's unstable flank (Phillips et al., 2008; Brooks et al., 2011). During a four-year period, the data revealed an uplift of 9.0 ± 2.4 cm/a. However, only the acoustic ranging technique is capable of determining slip along the décollement fault plane or relative to the stable surrounding. Active volcanoes grow in mass and are prone to gravitational or magma induced instabilities leading to flank movements and, potentially, collapses (McGuire, 1996). In the geologic record catastrophic failures of volcanic flank edifices were identified for example at the Canary Islands (Krastel et al., 2001), Cape Verde Islands (Ramalho et al., 2015), Fiji archipelago (Cronin et al., 2004), Mount Kilauea (Moore et al., 1994; Phillips et al., 2008), Ritter Island (Johnson, 1987), and Mount Etna (Calvari, 1996). Currently, numerous volcanoes with submerged flanks show evidence of flank movement (Poland et al., 2017).

One example for the application of acoustic ranging in such settings is the unstable submerged volcanic flank of Mount Etna, Italy (Figure 6.8). Mount Etna on the east coast of Sicily is the largest and most active volcano in Europe. Over the last decades, extensive satellite geodetic surveys focusing on the onshore flanks of Mount Etna have revealed the instability of its eastern flank, which continuously moves seawards with displacement rates of up to 50 mm/yr (Borgia et al., 1992; Palano, 2016).

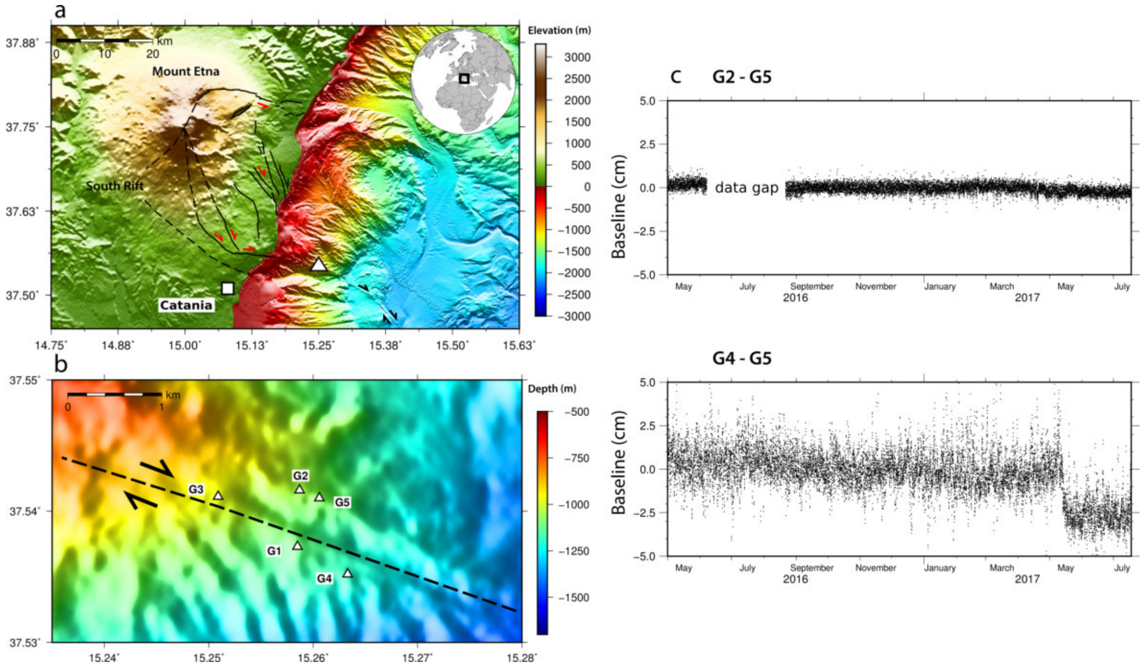

Figure 6.8: Seafloor geodetic monitoring of the unstable south-eastern Flank of Mount Etna. (a) Map of Etna volcano with the city of Catania in Sicily with onshore faults after Barreca et al. (2013) Topography and bathymetry after Ryan et al. (2009) and Gutscher et al. (2017). The direct-path ranging network (white triangle) is located at the southern boundary of the presumably sliding flank. (b) Close-up of the direct path-ranging network with five monitoring transponders (white triangles). (c) Baseline time series of G2 - G5 and G4 - G5 (b). Right-lateral slow-slip deformation occurred within 8 days in May 2017 (modified after Urlaub et al., 2018).

Offshore measurements to complement these surveys were lacking to date, but necessary to capture the full spectrum of flank movement and to understand the causes and mechanisms responsible for volcanic flank instability and, ultimately, to improve the regional hazard assessment. In 2016, five direct-path monitoring transponders were installed across the right-lateral strike-slip fault that defines the southern boundary of the sliding sector (Figure 6.8) (Gross et al., 2016). Since then the seafloor geodetic network revealed up to 4 cm of right-lateral fault slip released in a slow-slip event lasting eight days (Urlaub et al., 2018). These unique data show the importance of so far unconsidered offshore deformation at unstable slopes for an improved assessment of the mass volumes affected by slope instability.

6.6 Summary

The field of seafloor geodesy is a rapidly emerging research field driven by fast technological developments and increasing number of deployments worldwide. GPS-acoustic observations of the Tohoku-Oki event revealed the importance of seafloor geodesy to understand the co-seismic and post-seismic deformation of the overriding plate at convergent margins during megathrust events. The acoustic ranging method is divided into two major implementations. Combination of satellite-based GPS and acoustic ranging to the seafloor and direct-path ranging between two or more transponders are the preferred methods. The corresponding reference systems are global or local, respectively, and the choice of method and hence reference system depends on the addressed geological question. The propagation of sound waves in water and environmental conditions of oceans constrain the extent and resolution of acoustic seafloor networks. Furthermore, the analysis of error sources is required to identify sensor drift induced baseline changes. The precision of deformation measurements is not only determined by the oceanographic environment but also by the implemented network design and fault geometry as discussed above. Besides major tectonic fault scenarios such as strike-slip, normal and thrust faults, submarine slopes prone to failure are targets of seafloor geodesy using direct- or indirect-path ranging methods.

Acoustic ranging networks are currently monitoring subduction zones as the Northern Chilean subduction zone (Hannemann et al., 2017) and in the region of the Tohoku-Oki megathrust event of the Japan trench (Yamamoto et al., 2017b). Strike-slip faults are monitored along the submerged western part of the North Anatolian Fault (Sakic et al., 2016; Kido et al., 2017) and the unstable eastern flank of Mount Etna in Sicily (Urlaub et al., 2018). Numerous new seafloor geodetic networks are currently in the planning stage and will be installed in the coming years.

In this article, we reviewed the recent technological and data processing strategies as well as applications of direct path acoustic ranging for different geological settings. Baseline resolution with mm precision can be measured nowadays, even for large numbers of baselines and time spans of years. We show that the baseline uncertainty increases linearly with baseline length with different relations for each deployment. This finding holds at least for baselines up to 3 km. Acoustic direct-path ranging as a part of acoustic seafloor geodetic approaches is a promising method to understand the processes of fault deformation and strain build-up of tectonic and non-tectonic structures

6.7 Outlook

The recent progress and increasing number of scientific applications of acoustic seafloor geodetic surveys demonstrate the significant potential of the method. Decreasing energy consumption and increasing energy storage in batteries will allow operation of ten years and beyond, and the ability to integrate additional sensors. Technological developments will allow a more feasible deployment without the requirement of remote operating vehicles

(ROV) and autonomous surface vehicles (ASV). For instance, autonomous data collection campaigns or alternative sea surface platforms, such as moored buoys or towed buoys or rafts, small-unmanned engine boats or wave gliders can dramatically reduce survey costs and lay the foundation for monitoring in near real-time. Additionally gathered oceanographic parameters of long-term acoustic monitoring stations which periodically measure the ambient parameters of the water column provide the opportunity to monitor water mass movements at the seafloor at small scales as well as seasonal or annual oceanographic changes (e.g., Thomson and Davis, 2017). Therefore, global geodetic data can be used to infer properties to provide new insight into ocean bottom currents at very high spatial resolution. A recent example observed frequent transient and subtle cold water pulses of -0.02 °C at intervals of several days flowing through a direct-path ranging network in the Sea of Marmara (Sakic et al., 2016; Timmermann, 2016). Seafloor geodesy such as acoustic direct-path ranging and GPS-acoustic surveys will be crucial in fully revealing plate tectonic processes and mitigation of marine hazards, including tsunamis.

Acknowledgments

The successful development and enforcement of seafloor geodetic techniques are the common effort of many institutes and individuals in the past and present. We gratefully acknowledge the Editorial team of Journal of Geodynamics for the invitation to write this review article. We thank Roland Bürgmann and an anonymous reviewer for their comments and suggestions which helped us to improve the manuscript.

References

Aksoy, M. E., Meghraoui, M., Vallée, M., & Çakır, Z. (2010). Rupture characteristics of the a.d. 1912 mürefte (ganos) earthquake segment of the north anatolian fault (western turkey). *Geology*, *38*(11), 991–994, `https://doi.org/10.1130/g31447.1`.

Ambraseys, N. N. (2002). The seismic activity of the marmara sea region over the last 2000 years. *Bulletin of the Seismological Society of America*, *92*(1), 1–18, `https://doi.org/10.1785/0120000843`.

Angermann, D., Klotz, J., & Reigber, C. (1999). Space-geodetic estimation of the nazca-south america euler vector. *Earth and Planetary Science Letters*, *171*(3), 329–334, `https://doi.org/10.1016/s0012-821x(99)00173-9`.

Armijo, R., Meyer, B., Navarro, S., King, G., & Barka, A. (2002). Asymmetric slip partitioning in the sea of marmara pull-apart: a clue to propagation processes of the north anatolian fault? *Terra Nova*, *14*(2), 80–86, `https://doi.org/10.1046/j.1365-3121.2002.00397.x`.

Azuma, R., Tomita, F., Iinuma, T., Kido, M., & Hino, R. (2016). Development and examination of new algorithms of traveltime detection in gps/acoustic geodetic data for precise and automated analysis. *Earth, Planets and Space*, *68*(1), `https://doi.org/10.1186/s40623-016-0521-2`.

Baba, T. (2004). Tsunami magnitudes determined from ocean-bottom pressure gauge data around japan. *Geophysical Research Letters*, *31*(8), `https://doi.org/10.1029/2003gl019397`.

Bajaj, R., Ranaweera, S. L., & Agrawal, D. P. (2002). Gps location-tracking technology. *Computer*, *35*(4), `https://doi.org/10.1109/MC.2002.993780`.

Ballu, V., Bouin, M.-N., Calmant, S., Folcher, E., Bore, J.-M., Ammann, J., Pot, O., Diament, M., & Pelletier, B. (2010). Absolute seafloor vertical positioning using combined pressure gauge and kinematic gps data. *Journal of Geodesy*, *84*(1), 65–77, `https://doi.org/10.1007/s00190-009-0345-y`.

Barka, A. (2002). The surface rupture and slip distribution of the 17 august 1999 izmit earthquake (m 7.4), north anatolian fault. *Bulletin of the Seismological Society of America*, *92*(1), 43–60, `https://doi.org/10.1785/0120000841`.

Barreca, G., Bonforte, A., & Neri, M. (2013). A pilot gis database of active faults of mt. etna (sicily): A tool for integrated hazard evaluation. *Journal of Volcanology and Geothermal Research*, *251*, 170–186, `https://doi.org/10.1016/j.jvolgeores.2012.08.013`.

Bird, P. (2003). An updated digital model of plate boundaries. *Geochemistry, Geophysics, Geosystems*, *4*(3), `https://doi.org/10.1029/2001gc000252`.

Blum, J. A., Chadwell, C. D., Driscoll, N., & Zumberge, M. A. (2010). Assessing slope stability in the santa barbara basin, california, using seafloor geodesy and chirp seismic data. *Geophysical Research Letters*, *37*(13), `https://doi.org/10.1029/2010gl043293`.

Borgia, A., Ferrari, L., & Pasquarè, G. (1992). Importance of gravitational spreading in the tectonic and volcanic evolution of mount etna. *Nature*, *357*(6375), 231–235, `https://doi.org/10.1038/357231a0`.

Brooks, B. A., Foster, J. H., McGuire, J. J., & Behn, M. (2011). *Submarine Landslides and Slow Earthquakes: Monitoring Motion with GPS and Seafloor Geodesy*, book section Chapter 48, (pp. 889–907).

Bürgmann, R. & Chadwell, D. (2014). Seafloor geodesy. *Annual Review of Earth and Planetary Sciences*, *42*(1), 509–534, `https://doi.org/10.1146/annurev-earth-060313-054953`.

Calvari, Sonia Groppelli, G. (1996). Relevance of the chiancone volcaniclastic deposit in the recent history of etna volcano (italy). *Journal of Volcanology and Geothermal Research*, *72*.

Chadwell, C. D. (2003). Shipboard towers for global positioning system antennas. *Ocean Engineering*, *30*(12), 1467–1487, `https://doi.org/10.1016/s0029-8018(02)00141-5`.

Chadwell, C. D. (2016). Initiation of gps-acoustics measurements on the continental slope of the cascadia subduction zone. *AGU Fall Meeting 2016*, *T31C-2907*.

Chadwell, C. D., Hildebrand, J. A., Spiess, F. N., Morton, J. L., Normark, W. R., & Reiss, C. A. (1999). No spreading across the southern juan de fuca ridge axial cleft during 1994-1996. *Geophysical Research Letters*, *26*(16), 2525–2528, `https://doi.org/10.1029/1999gl900570`.

Chadwell, C. D. & Spiess, F. N. (2008). Plate motion at the ridge-transform boundary of the south cleft segment of the juan de fuca ridge from gps-acoustic data. *Journal of Geophysical Research*, *113*(B4), `https://doi.org/10.1029/2007jb004936`.

Chadwell, C. D. & Sweeney, A. D. (2010). Acoustic ray-trace equations for seafloor geodesy. *Marine Geodesy*, *33*(2-3), 164–186, `https://doi.org/10.1080/01490419.2010.492283`.

Chadwick, W. W., Embley, R. W., Milburn, H. B., Meinig, C., & Stapp, M. (1999). Evidence for deformation associated with the 1998 eruption of axial volcano, juan de fuca ridge, from acoustic extensometer measurements. *Geophysical Research Letters*, *26*(23), 3441–3444, `https://doi.org/10.1029/1999gl900498`.

Chadwick, W. W., Milburn, H. B., & Embley, R. W. (1995). Acoustic extensometer: measuring mid-ocean spreading. *Oceanographic Literature Review*, *42*(11), 961.

Chadwick, W. W., Nooner, S. L., Zumberge, M. A., Embley, R. W., & Fox, C. G. (2006). Vertical deformation monitoring at axial seamount since its 1998 eruption using deep-sea pressure sensors. *Journal of Volcanology and Geothermal Research*, *150*(1-3), 313–327, `https://doi.org/10.1016/j.jvolgeores.2005.07.006`.

Chadwick, W. W. & Stapp, M. (2002). A deep-sea observatory experiment using acoustic extensometers: precise horizontal distance measurements across a mid-ocean ridge. *IEEE Journal of Oceanic Engineering*, *27*(2), 193–201, `https://doi.org/10.1109/joe.2002.1002473`.

Chen, C.-T. & Millero, F. J. (1976). The specific volume of seawater at high pressures. *Deep Sea Research and Oceanographic Abstracts*, *23*(7), 595–612, `https://doi.org/10.1016/0011-7471(76)90003-6`.

Comte, D. & Pardo, M. (1991). Reappraisal of great historical earthquakes in the northern chile and southern peru seismic gaps. *Natural Hazards*, *4*(1), 23–44, `https://doi.org/10.1007/bf00126557`.

Cronin, S. J., Ferland, M. A., & Terry, J. P. (2004). Nabukelevu volcano (mt. washington), kadavu – a source of hitherto unknown volcanic hazard in fiji. *Journal of Volcanology and Geothermal Research*, *131*(3-4), 371–396, `https://doi.org/10.1016/s0377-0273(03)00414-1`.

Cruz-Atienza, V. M., Ito, Y., Kostoglodov, V., Hjörleifsdóttir, V., Iglesias, A., Tago, J., Calò, M., Real, J., Husker, A., Ide, S., Nishimura, T., Shinohara, M., Mortera-Gutierrez, C., García, S., & Kido, M. (2018). A seismogeodetic amphibious network in the guerrero seismic gap, mexico. *Seismological Research Letters*, *89*(4), 1435–1449, `https://doi.org/10.1785/0220170173`.

Davis, E., Heesemann, M., & Wang, K. (2011). Evidence for episodic aseismic slip across the subduction seismogenic zone off costa rica: Cork borehole pressure observations at the subduction prism toe. *Earth and Planetary Science Letters*, *306*(3-4), 299–305, `https://doi.org/10.1016/j.epsl.2011.04.017`.

Dunn, S., Hatchell, P., van den Beukel, A., de Vries, R., & Frafjord, T. (2016). A long-term seafloor deformation monitoring campaign at ormen lange gas field. *First Break*, *34*, 55–64.

Ergintav, S., Reilinger, R. E., Çakmak, R., Floyd, M., Cakir, Z., Doğan, U., King, R. W., McClusky, S., & Özener, H. (2014). Istanbul's earthquake hot spots: Geodetic constraints on strain accumulation along faults in the marmara seismic gap. *Geophysical Research Letters*, *41*(16), 5783–5788, `https://doi.org/10.1002/2014gl060985`.

Fox, C. G. (1999). In situ ground deformation measurements from the summit of axial volcano during the 1998 volcanic episode. *Geophysical Research Letters*, *26*(23), 3437–3440, `https://doi.org/10.1029/1999gl900491`.

Fujimoto, H. (2006). Ocean bottom crustal movement observation using gps/acoustic system by universities in japan. *Journal of the Geodetic Society of Japan*, *52*(4), 265–272, `https://doi.org/10.11366/sokuchi1954.52.265`.

Fujita, M., Ishikawa, T., Mochizuki, M., Sato, M., Toyama, S.-i., Katayama, M., Kawai, K., Matsumoto, Y., Yabuki, T., Asada, A., & Colombo, O. L. (2006). Gps/acoustic seafloor geodetic observation: method of data analysis and its application. *Earth, Planets and Space*, *58*(3), 265–275, `https://doi.org/10.1186/bf03351923`.

Gagnon, K., Chadwell, C. D., & Norabuena, E. (2005). Measuring the onset of locking in the peru-chile trench with gps and acoustic measurements. *Nature*, *434*(7030), 205–8, `https://doi.org/10.1038/nature03412`.

Geersen, J., Ranero, C. R., Klaucke, I., Behrmann, J. H., Kopp, H., Tréhu, A. M., Contreras-Reyes, E., Barckhausen, U., & Reichert, C. (2018). Active tectonics of the north chilean marine forearc and adjacent oceanic nazca plate. *Tectonics*, *37*(11), 4194–4211, `https://doi.org/10.1029/2018tc005087`.

Graindorge, D. (2004). Deep structures of the ecuador convergent margin and the carnegie ridge, possible consequence on great earthquakes recurrence interval. *Geophysical Research Letters*, *31*(4), `https://doi.org/10.1029/2003gl018803`.

Gross, F., Krastel, S., Geersen, J., Behrmann, J. H., Ridente, D., Chiocci, F. L., Bialas, J., Papenberg, C., Cukur, D., Urlaub, M., & Micallef, A. (2016). The limits of seaward spreading and slope instability at the continental margin offshore mt etna, imaged by high-resolution 2d seismic data. *Tectonophysics*, *667*, 63–76, `https://doi.org/10.1016/j.tecto.2015.11.011`.

Grosso, V. A. D. (1974). New equation for the speed of sound in natural waters (with comparisons to other equations). *The Journal of the Acoustical Society of America*, *56*(4), 1084–1091, `https://doi.org/10.1121/1.1903388`.

Gutscher, M.-A., Kopp, H., Krastel, S., Bohrmann, G., Garlan, T., Zaragosi, S., Klaucke, I., Wintersteller, P., Loubrieu, B., Le Faou, Y., San Pedro, L., Dominguez, S., Rovere, M., Mercier de Lepinay, B., Ranero, C., & Sallares, V. (2017). Active tectonics of the calabrian subduction revealed by new multi-beam bathymetric data and high-resolution seismic profiles in the ionian sea (central mediterranean). *Earth and Planetary Science Letters*, *461*, 61–72, `https://doi.org/10.1016/j.epsl.2016.12.020`.

Hannemann, K., Lange, D., Kopp, H., Petersen, F., & Contreras-Reyes, E. (2017). Deformation offshore northern chile monitored by a seafloor geodetic network (geosea). *EGU General Assembly 2017, 7833*.

Henrys, S., Harris, R., Ito, Y., Kido, M., Kinoshita, C., Muramoto, T., Ohta, K., Quinn, W., Suzuki, S., Tomita, F., & Zal, H. (2016). *Hikurangi Ocean Bottom Investigation of Tremor and Slow Slip (HOBITSS III)*. Report.

Hergert, T., Heidbach, O., Bécel, A., & Laigle, M. (2011). Geomechanical model of the marmara sea region-i. 3-d contemporary kinematics. *Geophysical Journal International*, *185*(3), 1073–1089, `https://doi.org/10.1111/j.1365-246X.2011.04991.x`.

Hubert-Ferrari, A., Barka, A., Jacques, E., Nalbant, S. S., Meyer, B., Armijo, R., Tapponnier, P., & King, G. C. (2000). Seismic hazard in the marmara sea region following the 17 august 1999 izmit earthquake. *Nature*, *404*(6775), 269–73, `https://doi.org/10.1038/35005054`.

Iinuma, T., Hino, R., Kido, M., Inazu, D., Osada, Y., Ito, Y., Ohzono, M., Tsushima, H., Suzuki, S., Fujimoto, H., & Miura, S. (2012). Coseismic slip distribution of the 2011 off the pacific coast of tohoku earthquake (m9.0) refined by means of seafloor geodetic data. *Journal of Geophysical Research: Solid Earth*, *117*(B7), `https://doi.org/10.1029/2012jb009186`.

Ito, Y., Hino, R., Kido, M., Fujimoto, H., Osada, Y., Inazu, D., Ohta, Y., Iinuma, T., Ohzono, M., Miura, S., Mishina, M., Suzuki, K., Tsuji, T., & Ashi, J. (2013). Episodic slow slip events in the japan subduction zone before the 2011 tohoku-oki earthquake. *Tectonophysics*, *600*, 14–26, `https://doi.org/10.1016/j.tecto.2012.08.022`.

Johnson, R. W. (1987). Large-scale volcanic cone collapse the 1888 slope failure of ritter volcano, and other examples from papua new guinea. *Bulletin of Volcanology*, *49*, 669–679.

Kido, M., Fujimoto, H., Miura, S., Osada, Y., Tsuka, K., & Tabei, T. (2006). Seafloor displacement at kumano-nada caused by the 2004 off kii peninsula earthquakes, detected through repeated gps/acoustic surveys. *Earth, Planets and Space*, *58*(7), 911–915, `https://doi.org/10.1186/bf03351996`.

Kido, M., Osada, Y., Fujimoto, H., Hino, R., & Ito, Y. (2011). Trench-normal variation in observed seafloor displacements associated with the 2011 tohoku-oki earthquake. *Geophysical Research Letters*, *38*(24), `https://doi.org/10.1029/2011gl050057`.

Kido, M., Yamamoto, R., Ohta, Y., Takahashi, N., Yamamoto, Y., Kalafat, D., Pinar, A., Ozener, H., Ozeren, S., & Kaneda, Y. (2017). Seafloor geodetic survey revealed partial creep of north anatolian fault at the western part of the sea of marmara, turkey. *EGU General Assembly 2017*, (pp. 17657).

Kopp, H. (2013). Invited review paper: The control of subduction zone structural complexity and geometry on margin segmentation and seismicity. *Tectonophysics*, *589*, 1–16, `https://doi.org/10.1016/j.tecto.2012.12.037`.

Krastel, S., Schmincke, H.-U., Jacobs, C. L., Rihm, R., Le Bas, T. P., & Alibés, B. (2001). Submarine landslides around the canary islands. *Journal of Geophysical Research: Solid Earth*, *106*(B3), 3977–3997, `https://doi.org/10.1029/2000jb900413`.

Lange, D., Bedford, J. R., Moreno, M., Tilmann, F., Baez, J. C., Bevis, M., & Kruger, F. (2014). Comparison of postseismic afterslip models with aftershock seismicity for three subduction-zone earthquakes: Nias 2005, maule 2010 and tohoku 2011. *Geophysical Journal International*, *199*(2), 784–799, `https://doi.org/10.1093/gji/ggu292`.

Le Pichon, X., Şengör, A. M. C., Demirbağ, E., Rangin, C., İmren, C., Armijo, R., Görür, N., Çağatay, N., Mercier de Lepinay, B., Meyer, B., Saatçılar, R., & Tok, B. (2001). The active main marmara fault. *Earth and Planetary Science Letters*, *192*(4), 595–616, `https://doi.org/10.1016/s0012-821x(01)00449-6`.

Leroy, C. C., Robinson, S. P., & Goldsmith, M. J. (2008). A new equation for the accurate calculation of sound speed in all oceans. *J Acoust Soc Am*, *124*(5), 2774–82, `https://doi.org/10.1121/1.2988296`.

Masson, D. G., Harbitz, C. B., Wynn, R. B., Pedersen, G., & Lovholt, F. (2006). Submarine landslides: processes, triggers and hazard prediction. *Philos Trans A Math Phys Eng Sci*, *364*(1845), 2009–39, `https://doi.org/10.1098/rsta.2006.1810`.

Matsumoto, Y., Ishikawa, T., Fujita, M., Sato, M., Saito, H., Mochizuki, M., Yabuki, T., & Asada, A. (2008). Weak interplate coupling beneath the subduction zone off fukushima, ne japan, inferred from gps/acoustic seafloor geodetic observation. *Earth, Planets and Space*, *60*(6), e9–e12, `https://doi.org/10.1186/bf03353114`.

McGuire, J. J. & Collins, J. A. (2013). Millimeter-level precision in a seafloor geodesy experiment at the discovery transform fault, east pacific rise. *Geochemistry, Geophysics, Geosystems*, *14*(10), 4392–4402, `https://doi.org/10.1002/ggge.20225`.

McGuire, W. J. (1996). Volcano instability a review of contemporary themes. *Geological Society Special Publication*, *110*.

Metz, D., Watts, A. B., Grevemeyer, I., Rodgers, M., & Paulatto, M. (2016). Ultra-long-range hydroacoustic observations of submarine volcanic activity at monowai, kermadec arc. *Geophysical Research Letters*, *43*(4), 1529–1536, `https://doi.org/10.1002/2015gl067259`.

Montecino, V. & Lange, C. B. (2009). The humboldt current system: Ecosystem components and processes, fisheries, and sediment studies. *Progress in Oceanography*, *83*(1-4), 65–79, `https://doi.org/10.1016/j.pocean.2009.07.041`.

Moore, J. G., Normark, W. R., & Holcomb, R. T. (1994). Giant hawaiian landslides. *Annual Review of Earth and Planetary Sciences*, *22*(1), 119–144, `https://doi.org/10.1146/annurev.ea.22.050194.001003`.

Morton, J. L., Normark, W. R., Reiss, C. A., & Tucker, S. P. (1994). Seafloor horizontal deformation measurements using dual-frequency intelligent transponders. *Proc. Int. Symp. on Marine Positioning*, (pp. 81–86).

Munk, W., Worcester, P., & Wunsch, C. (1995). *Ocean acoustic tomography.* Cambridge, University Press, Cambridge.

Ohta, Y., Hino, R., Inazu, D., Ohzono, M., Ito, Y., Mishina, M., Iinuma, T., Nakajima, J., Osada, Y., Suzuki, K., Fujimoto, H., Tachibana, K., Demachi, T., & Miura, S. (2012). Geodetic constraints on afterslip characteristics following the march 9, 2011, sanriku-oki earthquake, japan. *Geophysical Research Letters*, *39*(16), `https://doi.org/10.1029/2012gl052430`.

Osada, Y., Kido, M., & Fujimoto, H. (2012). A long-term seafloor experiment using an acoustic ranging system: Precise horizontal distance measurements for detection of seafloor crustal deformation. *Ocean Engineering*, *51*, 28–33, `https://doi.org/10.1016/j.oceaneng.2012.05.006`.

Osada, Y., Kido, M., Fujimoto, H., & Kaneda, Y. (2008). Development of a seafloor acoustic ranging system toward the seafloor cable network system. *Ocean Engineering*, *35*(14-15), 1401–1405, `https://doi.org/10.1016/j.oceaneng.2008.07.007`.

Owen, S., Segall, P., Lisowski, M., Miklius, A., Denlinger, R., & Sako, M. (2000). Rapid deformation of kilauea volcano: Global positioning system measurements between 1990 and 1996. *Journal of Geophysical Research: Solid Earth*, *105*(B8), 18983–18998, `https://doi.org/10.1029/2000jb900109`.

Palano, M. (2016). Episodic slow slip events and seaward flank motion at mt. etna volcano (italy). *Journal of Volcanology and Geothermal Research*, *324*, 8–14, `https://doi.org/10.1016/j.jvolgeores.2016.05.010`.

Paros, J. M. (1976). Digital pressure transducers. *Meas. Data*, *10*(2), 74–79.

Phillips, K. A., Chadwell, C. D., & Hildebrand, J. A. (2008). Vertical deformation measurements on the submerged south flank of kīlauea volcano, hawai'i reveal seafloor motion associated with volcanic collapse. *Journal of Geophysical Research*, *113*(B5), `https://doi.org/10.1029/2007jb005124`.

Poland, M. P., Peltier, A., Bonforte, A., & Puglisi, G. (2017). The spectrum of persistent volcanic flank instability: A review and proposed framework based on kīlauea, piton de la fournaise, and etna. *Journal of Volcanology and Geothermal Research*, *339*, 63–80, `https://doi.org/10.1016/j.jvolgeores.2017.05.004`.

Polster, A., Fabian, M., & Villinger, H. (2009). Effective resolution and drift of paroscientific pressure sensors derived from long-term seafloor measurements. *Geochemistry, Geophysics, Geosystems*, *10*(8), `https://doi.org/10.1029/2009gc002532`.

Ramalho, R. S., Winckler, G., Madeira, J., Helffrich, G. R., Hipolito, A., Quartau, R., Adena, K., & Schaefer, J. M. (2015). Hazard potential of volcanic flank collapses raised by new megatsunami evidence. *Sci Adv*, *1*(9), e1500456, `https://doi.org/10.1126/sciadv.1500456`.

Reid, H. F. (1910). *The mechanics of the earthquake: the California earthquake of 18 April, 1906.* Report, Carnegie Institute, Washington D.C.

Reilinger, R., et al. (2006). Gps constraints on continental deformation in the africa-arabia-eurasia continental collision zone and implications for the dynamics of plate interactions. *Journal of Geophysical Research: Solid Earth*, *111*(B5), `https://doi.org/10.1029/2005jb004051`.

Ryan, W. B. F., Carbotte, S. M., Coplan, J. O., O'Hara, S., Melkonian, A., Arko, R., Weissel, R. A., Ferrini, V., Goodwillie, A., Nitsche, F., Bonczkowski, J., & Zemsky, R. (2009). Global multi-resolution topography synthesis. *Geochemistry, Geophysics, Geosystems*, *10*(3), `https://doi.org/10.1029/2008gc002332`.

Sakic, P., Piété, H., Ballu, V., Royer, J. Y., Kopp, H., Lange, D., Petersen, F., Özeren, M. S., Ergintav, S., Geli, L., Henry, P., & Deschamps, A. (2016). No significant steady state surface creep along the north anatolian fault offshore istanbul: Results of 6 months of seafloor acoustic ranging. *Geophysical Research Letters*, *43*(13), 6817–6825, `https://doi.org/10.1002/2016gl069600`.

Sandwell, D. T., Muller, R. D., Smith, W. H., Garcia, E., & Francis, R. (2014). Marine geophysics. new global marine gravity model from cryosat-2 and jason-1 reveals buried tectonic structure. *Science*, *346*(6205), 65–7, `https://doi.org/10.1126/science.1258213`.

Sasagawa, G., Cook, M. J., & Zumberge, M. A. (2016). Drift-corrected seafloor pressure observations of vertical deformation at axial seamount 2013-2014. *Earth and Space Science*, *3*(9), 381–385, `https://doi.org/10.1002/2016ea000190`.

Satake, K. & Tanioka, Y. (1999). Sources of tsunami and tsunamigenic earthquakes in subduction zones. *Pure and Applied Geophysics*, *154*(3-4), 467–483, `https://doi.org/10.1007/s000240050240`.

Sato, M., Fujita, M., Matsumoto, Y., Ishikawa, T., Saito, H., Mochizuki, M., & Asada, A. (2013). Interplate coupling off northeastern japan before the 2011 tohoku-oki earthquake, inferred from seafloor geodetic data. *Journal of Geophysical Research: Solid Earth*, *118*(7), 3860–3869, `https://doi.org/10.1002/jgrb.50275`.

Sato, M., Ishikawa, T., Ujihara, N., Yoshida, S., Fujita, M., Mochizuki, M., & Asada, A. (2011). Displacement above the hypocenter of the 2011 tohoku-oki earthquake. *Science*, *332*(6036), 1395, `https://doi.org/10.1126/science.1207401`.

Sato, T., Hasegawa, S., Kono, A., Shiobara, H., Yagi, T., Yamada, T., Shinohara, M., & Usui, N. (2017). Detection of vertical motion during a slow-slip event off the boso peninsula, japan, by ocean bottom pressure gauges. *Geophysical Research Letters*, *44*(6), 2710–2715, `https://doi.org/10.1002/2017gl072838`.

Savage, J. C. (1983). A dislocation model of strain accumulation and release at a subduction zone. *Journal of Geophysical Research: Solid Earth*, *88*(B6), 4984–4996, `https://doi.org/10.1029/JB088iB06p04984`.

Savage, J. C. & Burford, R. O. (1970). Accumulation of tectonic strain in california. *Bulletin of the Seismological Society of America*, *60*(6), 1877–1896.

Savage, J. C. & Burford, R. O. (1973). Geodetic determination of relative plate motion in central california. *Journal of Geophysical Research*, *78*(5), 832–845, `https://doi.org/10.1029/JB078i005p00832`.

Savage, J. C. & Prescott, W. H. (1973). Precision of geodolite distance measurements for determining fault movements. *Journal of Geophysical Research*, *78*(26), 6001–6008, `https://doi.org/10.1029/JB078i026p06001`.

Schmittbuhl, J., Karabulut, H., Lengliné, O., & Bouchon, M. (2015). Seismicity distribution and locking depth along the main marmara fault, turkey. *Geochemistry, Geophysics, Geosystems*, *17*(3), 954–965, `https://doi.org/10.1002/2015gc006120`.

Schurr, B., Asch, G., Hainzl, S., Bedford, J., Hoechner, A., Palo, M., Wang, R., Moreno, M., Bartsch, M., Zhang, Y., Oncken, O., Tilmann, F., Dahm, T., Victor, P., Barrientos, S., & Vilotte, J. P. (2014). Gradual unlocking of plate boundary controlled initiation of the 2014 iquique earthquake. *Nature*, *512*(7514), 299–302, `https://doi.org/10.1038/nature13681`.

Seitz, H.-M., Brey, G. P., Zipfel, J., Ott, U., Weyer, S., Durali, S., & Weinbruch, S. (2007). Lithium isotope composition of ordinary and carbonaceous chondrites, and differentiated planetary bodies: Bulk solar system and solar reservoirs. *Earth and Planetary Science Letters*, *260*(3-4), 582–596, `https://doi.org/10.1016/j.epsl.2007.06.019`.

Spiess, F. (1985). Suboceanic geodetic measurements. *IEEE Transactions on Geoscience and Remote Sensing*, *GE-23*(4), 502–510, `https://doi.org/10.1109/tgrs.1985.289441`.

Spiess, F. N. (1980). Acoustic techniques for marine geodesy. *Marine Geodesy*, *4*(1), 13–27, `https://doi.org/10.1080/15210608009379369`.

Spiess, F. N., Chadwell, C. D., Hildebrand, J. A., Young, L. E., Purcell, G. H., & Dragert, H. (1998). Precise gps/acoustic positioning of seafloor reference points for tectonic studies. *Physics of the Earth and Planetary Interiors*, *108*(2), 101–112, `https://doi.org/10.1016/s0031-9201(98)00089-2`.

Stewart, J. L., Westerfield, E. C., & Brandon, M. K. (1981). Optimum frequencies for noise-limited active sonar detection. *The Journal of the Acoustical Society of America*, *70*(5), 1336–1338, `https://doi.org/10.1121/1.387148`.

Sun, T., Wang, K., Iinuma, T., Hino, R., He, J., Fujimoto, H., Kido, M., Osada, Y., Miura, S., Ohta, Y., & Hu, Y. (2014). Prevalence of viscoelastic relaxation after the 2011 tohoku-oki earthquake. *Nature*, *514*(7520), 84–7, `https://doi.org/10.1038/nature13778`.

Thomson, R. E. & Davis, E. E. (2017). Equatorial k elvin waves generated in the western tropical p acific o cean trigger mass and heat transport within the m iddle a merica t rench off c osta r ica. *Journal of Geophysical Research: Oceans*, *122*(7), 5850–5869, `https://doi.org/10.1002/2017jc012848`.

Timmermann, A. (2016). Investigation of cold water events at the bottom of the sea of marmara from november 2014 to april 2016. *Bachelor Thesis. Kiel University.*

Tong, X., Sandwell, D., Luttrell, K., Brooks, B., Bevis, M., Shimada, M., Foster, J., Smalley, R., Parra, H., Báez Soto, J. C., Blanco, M., Kendrick, E., Genrich, J., & Caccamise, D. J. (2010). The 2010 maule, chile earthquake: Downdip rupture limit revealed by space geodesy. *Geophysical Research Letters*, *37*(24), `https://doi.org/10.1029/2010gl045805`.

Urick (1983). *Principles of underwater sound*, volume 3rd ed. McGraw-Hill Book Company.

Urlaub, M., Petersen, F., Gross, F., Bonforte, A., Puglisi, G., Guglielmino, F., Krastel, S., Lange, D., & Kopp, H. (2018). Gravitational collapse of mount etna's southeastern flank. *Sci Adv*, *4*(10), eaat9700, `https://doi.org/10.1126/sciadv.aat9700`.

Urlaub, M. & Villinger, H. (2018). Combining in situ monitoring using seabed instruments and numerical modelling to assess the transient stability of underwater slopes. *Geological Society, London, Special Publications*, *477*(1), 511–521, `https://doi.org/10.1144/sp477.8`.

Wallace, L. M., Webb, S. C., Ito, Y., Mochizuki, K., Hino, R., Henrys, S., Schwartz, S. Y., & Sheehan, A. F. (2016). Slow slip near the trench at the hikurangi subduction zone, new zealand. *Science*, *352*(6286), 701–4, `https://doi.org/10.1126/science.aaf2349`.

Watts, D. R. & Kontoyiannis, H. (1990). Deep-ocean bottom pressure measurement: Drift removal and performance. *Journal of Atmospheric and Oceanic Technology*, *7*(2), 296–306, `https://doi.org/10.1175/1520-0426(1990)007<0296:Dobpmd>2.0.Co;2`.

Wearn, R. B. & Larson, N. G. (1982). Measurements of the sensitivities and drift of digiquartz pressure sensors. *Deep Sea Research Part A. Oceanographic Research Papers*, *29*(1), 111–134, `https://doi.org/10.1016/0198-0149(82)90064-4`.

Weatherall, P., Marks, K. M., Jakobsson, M., Schmitt, T., Tani, S., Arndt, J. E., Rovere, M., Chayes, D., Ferrini, V., & Wigley, R. (2015). A new digital bathymetric model of the world's oceans. *Earth and Space Science*, *2*(8), 331–345, `https://doi.org/10.1002/2015ea000107`.

Wilson, W. D. (1960). Speed of sound in sea water as a function of temperature, pressure, and salinity. *The Journal of the Acoustical Society of America*, *32*(6), 641–644, `https://doi.org/10.1121/1.1908167`.

Yamamoto, R., Hino, R., Kido, M., & Honsho, C. (2017a). Monitoring postseismic motion of the frontal wedge after 2011 tohoku earthquake by across-trench acoustic ranging. *EGU General Assembly 2017*, *5395*.

Yamamoto, R., Hino, R., Kido, M., Osada, Y., & Honsho, C. (2018). Direct measurement of postseismic motion of incoming pacific plate after the 2011 tohoku earthquake using acoustic ranging system. *EGU General Assembly 2018*, (pp. 11566).

Yamamoto, Y., Takahashi, N., Pinar, A., Kalafat, D., Citak, S., Comoglu, M., Polat, R., & Kaneda, Y. (2017b). Geometry and segmentation of the north anatolian fault beneath the marmara sea, turkey, deduced from long-term ocean bottom seismographic observations. *Journal of Geophysical Research: Solid Earth*, *122*(3), 2069–2084, `https://doi.org/10.1002/2016jb013608`.

Yokota, Y., Ishikawa, T., Watanabe, S., Tashiro, T., & Asada, A. (2016). Seafloor geodetic constraints on interplate coupling of the nankai trough megathrust zone. *Nature*, *534*(7607), 374–7, `https://doi.org/10.1038/nature17632`.

Şengör, A. M. C., Tüysüz, O., İmren, C., Sakınç, M., Eyidoğan, H., Görür, N., Le Pichon, X., & Rangin, C. (2005). The north anatolian fault: A new look. *Annual Review of Earth and Planetary Sciences*, *33*(1), 37–112, `https://doi.org/10.1146/annurev.earth.32.101802.120415`.

7 Interseismic strain build-up on the submarine North Anatolian Fault offshore Istanbul

Dietrich Lange[1], Heidrun Kopp[1,2], Jean-Yves Royer[3], Pierre Henry[4], Ziyadin Çakir[5], **Florian Petersen**[1], Pierre Sakic[6,7], Valerie Ballu[6], Jörg Bialas[1], Sinan Ozeren[5], Semih Ergintav[8] and Louis Géli[9]

1) GEOMAR Helmholtz Centre for Ocean Research Kiel, Germany
2) Institute of Geosciences, Kiel University, Kiel, Germany
3) Laboratoire Géosciences Océan, Université de Brest and CNRS, Plouzané, France
4) Aix Marseille Univ, CNRS, IRD, INRA, Coll France, CEREGE, Aix-en-Provence, France
5) Eurasian Institute of Earth Sciences, Istanbul Teknik Üniversitesi, Istanbul, Turkey
6) Laboratoire LIENSs, Université de la Rochelle and CNRS, La Rochelle, France
7) GFZ Helmholtz-Zentrum Potsdam, Germany
8) Kandilli Observatory and Earthquake Research Institute, Department of Geodesy, Bogazici University, Istanbul, Turkey
9) Institut Français de Recherche pour l'Exploitation de la Mer (IFREMER), Deéparte-ment Ressources Physiques et Ecosystèmes de Fond 87 de Mer, Unité des Géosciences Marines, Plouzané, France

Published in **Nature Communication**, July 2019

DOI: 10.1038/s41467-019-11016-z

Abstract

Using offshore geodetic observations, we show that a segment of the North Anatolian Fault in the central Sea of Marmara is locked and therefore accumulating strain. The strain accumulation along this fault segment was previously extrapolated from onshore observations or inferred from the absence of seismicity, but both methods could not distinguish between fully locked or fully creeping fault behavior. A network of acoustic transponders measured crustal deformation with mm-precision on the seafloor for 2.5 years and did not detect any significant fault displacement. Absence of deformation together with sparse seismicity monitored by ocean bottom seismometers indicates complete fault locking to at least 3 km depth and presumably into the crystalline basement. The slip-deficit of at least 4 m since the last known rupture in 1766 is equivalent to an earthquake of magnitude 7.1 to 7.4 in the Sea of Marmara offshore metropolitan Istanbul.

7.1 Introduction

It is well known that Istanbul city and populations along the coasts of the Sea of Marmara were previously severely affected by earthquakes related to the submerged North Anatolian Fault (NAF) in the Sea of Marmara (Ambraseys, 2002a). Some of the earthquakes were associated with seismically driven sea-waves and six destructive run-ups are known from historical reports for the last 20 centuries (Ambraseys, 2002b). For example, the 1766 earthquake, suggested to have nucleated beneath the western Sea of Marmara (Parsons et al., 2000), resulted in very strong shaking in Istanbul (Mercalli Intensity VII, very strong shaking) and seismically driven sea-waves submerged the quays in Istanbul (Ambraseys, 2002b).

The Sea of Marmara, crossed by the NAF, is one of the regions on the globe where the fragmentary knowledge on the degree of fault locking poses a significant impediment for assessing the seismic hazard in one of Europe's most populated regions, the Istanbul metropolitan area. Since 1939, destructive seismic events on the onshore portion of the NAF have propagated westwards towards Istanbul (Figure 7.1c) (Karabulut et al., 2011). The most recent events were the M_w 7.2 Düzce and M_w 7.4 Izmit earthquakes in 1999 (Figure 7.1a) that caused 854 and 18,000 casualties, respectively. Towards the Dardanelles in the west, the M_w 7.4 Ganos earthquake ruptured the NAF in 1912 (Aksoy et al., 2010). In the Sea of Marmara, the NAF forms a well-known seismic gap along a 150 km-long segment (Bohnhoff et al., 2013), inferred to have last ruptured in 1766, whereas all the onshore segments of the NAF from the province Erzincan in Eastern Anatolia to the Sea of Marmara ruptured in the last 100 years (Stein et al., 1997). The degree of aseismic deformation and hence the locking state of the marine fault segments of the NAF cannot be well resolved using onshore GPS stations alone (Klein et al., 2017). Owing to the lack of offshore observations, the uncertainty on fault slip rates on the order of 10 mm a^{-1} in the central part of the Sea of Marmara prevails.

While onshore deformation of faults is monitored using geodetic techniques such as GPS and InSAR, movement of offshore faults remains mostly unknown due to the opacity of water to electromagnetic waves. As a result, we rely on extrapolated observations of GPS land measurements to the marine domain (Hergert and Heidbach, 2010; Ergintav et al., 2014). However, extrapolating onshore observations requires assumptions about crustal properties and fault geometry to determine the locking state of a fault or fault segment (Ergintav et al., 2014). Inferring the slip rate of faults from seismicity (Schmittbuhl et al., 2015; Bohnhoff et al., 2017; Yamamoto et al., 2017) includes assumptions about the frictional behaviour of the fault because deformation is known to be partitioned into seismic moment release (e.g. through micro-seismicity) and aseismic creep (Lange et al., 2014). Other studies use the relationship between the frequency and magnitude of earthquakes, known as the Gutenberg–Richter law, to infer the state of differential stresses on faults (Tormann et al., 2015). Our blindness to offshore deformation leads to pivotal debates in science. For instance, the kinematic state of a fault can vary between the two end members from fully locked to continuously creeping, resulting in a slip accumulation between zero and full displacement along the fault. The fault kinematics is thus determinative of hazard estimates and we are far from the level of knowledge we have on deformation onshore (Bürgmann and Chadwell, 2014). Seafloor uplift and subsidence can be resolved by pressure measurements (Wallace et al., 2016) and absolute horizontal displacement by combining GPS and acoustic measurements (Gagnon et al., 2005). Direct and continuous acoustic path-ranging between two sites on the seafloor becomes increasingly used in oil exploration (Dunn et al., 2016) and research (McGuire and Collins, 2013; Urlaub et al., 2018; Petersen et al., 2019; Yamamoto et al., 2019). Recent works used submarine fibre optic telecommunication cables to detect subtle strain changes induced by distant earthquakes (Marra et al., 2018). Here, we use acoustic ranging techniques to measure horizontal crustal strain on the seafloor with mm-precision over periods of years and dozens of baselines to resolve tectonic deformation. The geodetic monitoring together with the OBS observation indicate that the NAF segment in the Kumburgaz Basin is fully locked.

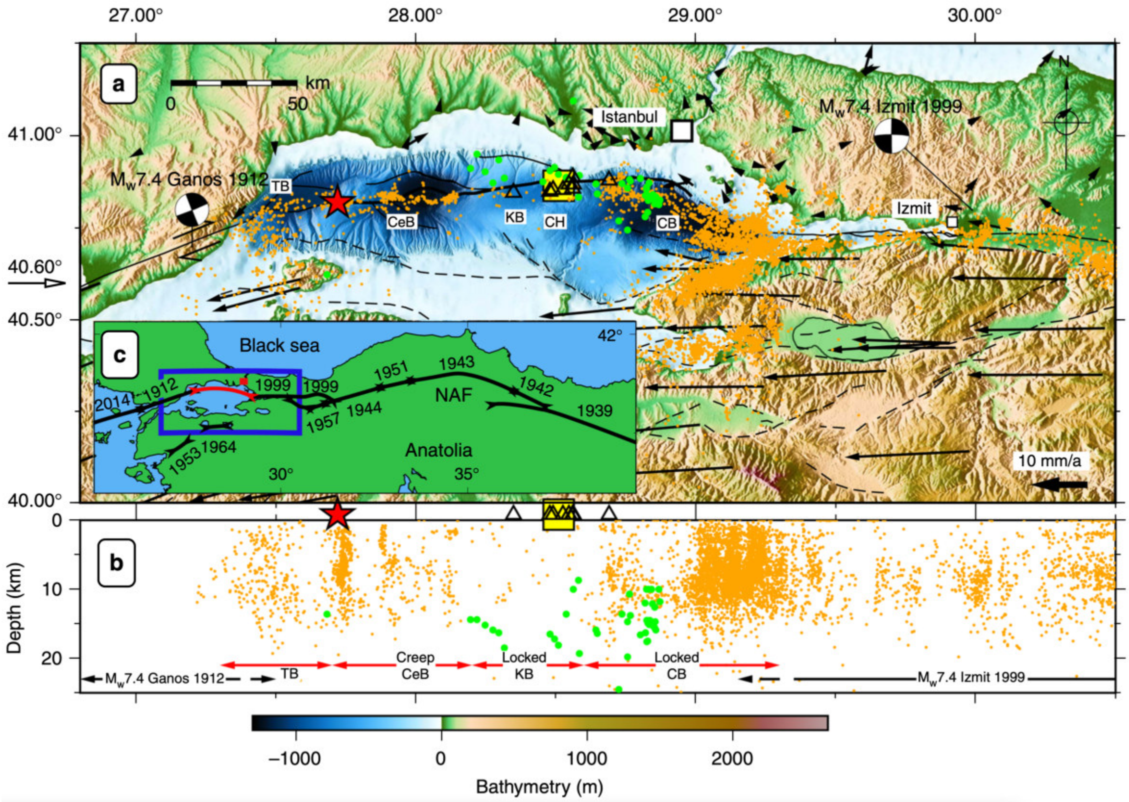

Figure 7.1: Overview and tectonic setting of the Sea of Marmara. (a) Tectonic setting of the NAF (solid line) in the Marmara region with local seismicity (orange dots) between 1999 – 2009 (Karabulut et al., 2011) and 2010 – 2012 (Hergert and Heidbach, 2010). The geodetic acoustic network is located in the yellow box (top center) and the local ocean bottom seismometer (OBS) stations (29/10/2014 – 25/04/2015 and 26/04/2015 - 13/04/2016) are indicated with triangles. Microseismicity based on the OBS (this study) in the area of the geodetic network is shown with green circles. The red star indicates the location of a recent Turkish-Japanese direct path-ranging network in the western Sea of Marmara (Yamamoto et al., 2019). Fault traces of the NAF (Armijo et al., 2005) and GPS displacements relative to stable Eurasia (Ergintav et al., 2014) are shown with black arrows and lines. Bathymetry from (Le Pichon et al., 2001) and topography from (Ryan et al., 2009). Tekirdağ basin (TB), Central Basin (CeB), Kumburgaz Basin (KB), Central High (CH) and Çınarcık Basin (CB) (Schmittbuhl et al., 2015). (b) Profile view of seismicity north of 40.6 °N, same symbols as in panel a. Sedimentary basins are indicated with red arrows and the extent of the Ganos 1912 and Izmit 1999 earthquakes (Bohnhoff et al., 2017) are indicated with black arrows. Creeping (Schmittbuhl et al., 2015; Bohnhoff et al., 2017; Yamamoto et al., 2019) and locked (Bohnhoff et al., 2013) segments of the NAF are labelled. See text for discussion about locked fault beneath the KB and the CB. (c) Large-scale tectonic setting of north-western Turkey with rupture zones of major earthquakes (Armijo et al., 2005; Bohnhoff et al., 2013) along the North Anatolian Fault (NAF)

7.2 Methods

7.2.1 Direct path ranging method

We measure the acoustic distance between two transponders by the two-way travel time of acoustic signals between the transponders and from the sound velocity, measured independently (Yamamoto et al., 2019; Petersen et al., 2019):

$$s = v \cdot \frac{(TWT - delta_i)}{2} \tag{7.1}$$

where s is the acoustic distance (i.e. baseline length), v the sound velocity in water, and TWT the two-way travel time of the signal between the transponders and deltai the response delay time of the responding station i to the incoming signal. Due to the two-way travel time measurement, the acoustic signals travel in forward and backward direction and directional effects imposed by water fluxes cancel out. This is only possible since the temporal changes of water currents are clearly slower than our two-way travel times, which are mostly below 3 s. Overall little is known on the accurate water parameters on the seafloor of the Sea of Marmara because most stations measuring oceanic parameters are located at shallow water depths (Aydoğdu et al., 2018). The temperature and pressure are measured at the active transponder during the TWT measurement; the velocity along the acoustic path is approximated by the harmonic mean of the sound velocities of water at the stations (i.e. the endpoints of ray-paths).

7.2.2 Acoustic transponders

Ten acoustic distance metres, four from the Ocean Geosciences Laboratory in Brest (station names start with F) and six from Geomar's GeoSEA array in Kiel, Germany (station names start with G), were installed late October 2014 (Sakic et al., 2016) and fully operable until 5 May 2017. During the last visit with *R/V Yunus* on 29 January 2018 only three F-stations were running, all others stopped due to empty batteries. During the 2.5 years of complete operation of the network, each transponder measured temperature, pressure, inclination (Figure 7.3 and Supplementary Figures 7.7 − 7.9) and two-way travel times to the neighbouring stations (Supplementary Figure 7.12).

7.2.3 Sound velocity

Each transponder had an integrated sound-velocity sensor but they showed unexpected offsets and long-term drift of up to 0.5 m s^{-1} water speed in the time-series, which would map into apparent baseline changes of ~0.5 m. Although the sound speed measurement turned out useless for estimating the baseline lengths, they could be used to estimate salinity at the transponders in the order of 38.6 PSU, in-line with published data (Boyer et al., 2013). The sound speed (Figure 7.3d, Supplementary Figure 7.13) was calculated from temperature, pressure and the derived salinity value (Leroy et al., 2008) assumed to have remained constant throughout the experiment.

7.2.4 Salinity

The sound speed v can be calculated from pressure, temperature, and salinity (Leroy et al., 2008). We use the empirical relations, assuming a constant salinity, as in similar acoustic experiments (Chadwell et al., 1999; Osada et al., 2012).

7.2.5 Temperature

For the time after 5th May 2017 until January 2018 the F-stations were still operable, but the temperature sensors of the F-stations do not allow estimating a high-resolution baseline since artefacts of their temperature sensor cannot be isolated from a baseline change. Both networks operated independently but measured some common baselines (Figure 7.2). We use the temperature data from the G-transponders for the close-by F transponders (distances less than 100 m each) since they have a high-resolution temperature sensor. The temperature timeseries from the G-stations (sample interval of 90 min) were spline interpolated onto the measurement times of the close by F-stations (six measurements during the first 10 min of each hour).

Station F4 stopped sending out active baselines requests on 25 April 2015 but still responded to incoming baselines requests allowing to estimate the baselines for one-direction during the deployment (using pressure and temperature for F4 of close-by stations). The pressure sensor of transponder G2 was only working until 10 April 2016, later on, we used the pressure of G5 instead. Stations F2 (faulty temperature sensor) and G4 (temperature sensor broken after 19 November 2015) had both artefacts with the temperature sensors. Although close by to G1 the temperatures of G1 could not be used for G4 nor F1 since both stations are likely located in a slightly different temperature field as suggested by the travel times measurements from G4 to all other transponders (Supplementary Figure 7.12). Since the acoustic distance changes are dependent on sound speed variations (Eq. 7.1), which in turn are mostly influenced by temperature (Leroy et al., 2008), the lack of accurate temperature measurements of G4 and F1 does not allow isolating a geologic movement using these stations. We extensively tried to use temperatures of G1 and G5 for

G4 and F1, but this cannot compensate the different behaviour of travel time and due to the small heterogeneities of the temperature field and due to the trade-off between distance and water speed (Eq. 7.1) we did not use baselines from and to G4 and F1. Adopting the temperatures from other G-stations to G5 resulted in apparent baseline lengthening of ~1 cm to all other stations.

The temperature measurements (Figure 7.9a and Supplementary Figure 7.7) indicate a long-term increase of temperature with an approximate rate of 0.028 °C per year (~0.07 °C during the 2.5 years of deployment). Together with the temperature increase in the western part of the Sea of Marmara (Yamamoto et al., 2019) (annual rate of 0.02 °C at the location indicated with a red star, Figure 7.1), these observations might suggest general warming of sea bottom water in the Sea of Marmara. Furthermore, we observe repeated influx of cold water with an average temperature drop of 0.016 °C and average durations of two days. The temperature change can be tracked as the temperature successively drops within mostly ~10 h from east to west suggesting water mass movement of ~5 cm s^{-1} and shows a seasonal effect with a higher rate of temperature drops in winter time (November - February).

7.2.6 Pressure

The pressure time series (Figure 7.3b and Supplementary Figure 7.8) for all sensors are very similar with variations similar to tide-gauge observation at the north coast of the Sea of Marmara (tide gauge station Marmara Ereğlisi, `https:// tudes.hgk.msb.gov.tr/tudesportal/`, downloaded 2 September 2018). The pressure does not show a clear geological long-term trend as expected for a tectonic uplift or subsidence and we interpret the signal as long-term water changes above the transponders such as river-runoff, water in-flow from the Black Sea and the Dardanelles. For the baselines, pressure changes of 1 kPa would result in a baseline change of 11 mm for a 1000 m long baseline in case pressure change would not be compensated by travel times.

7.2.7 Installation of geodetic frames on the seafloor

First, potential sites along the NAF were mapped using high-resolution Autonomous Underwater Vehicle (AUV) bathymetry (Grall et al., 2018a,b). Then, 4 m high frames (Supplementary Figure 7.14) with the transponder on top were lowered to the seafloor using a deep-sea cable. For accurate positioning on a target position, two transponders attached to the cable above the frame were used. Furthermore, buoyancy and weight were attached to the cable and above the frame, which allowed detecting the touch-down of the frames on the seafloor by observing the cable slack (Kopp et al., 2017). After their installation, all stations were inspected using a Remotely Operated Vehicle (Supplementary Figures 7.14 and 7.15).

7.2.8 Seismicity

The OBSs were first deployed in a very small aperture array (29 October 2014 until 25 April 2015, upright green triangles) and then re-deployed along the NAF (26 April 2015 until 13 April 2016; inverted green triangles) (Figure 7.1). The OBS network was installed in the shipping lane of the access to the Bosphorus in order to avoid station loss due to fishing activities. As a result, the elongated installation prevents very accurate estimates of the event depths using OBS only. Therefore, all events shown with red circles were located with land and OBS observations. Only events with RMS values smaller then 1 s and recorded on more than five stations are used. Events were located using the 1D velocity model from Cros and Geli (2013) and the seismological analysis software SEISAN (Havskov and Ottemoller, 1999). The OBS stations did not sig- nificantly increase the number of events detected close to the geodetic network. Few additional events were detected compared to Koeri's catalogue, but P-S times (always larger than 2 s) and P polarisation indicate that these events did occur outside the OBS network and hence the geodetic network.

7.3 Results

7.3.1 Direct path ranging experiment

Our inability to resolve sub-horizontal tectonic displacement on the seafloor is addressed by a path-ranging method based on acoustic travel-time measurements (McGuire and Collins, 2013; Bürgmann and Chadwell, 2014; Sakic et al., 2016; Urlaub et al., 2018; Yamamoto et al., 2019). Distance changes between seafloor instruments are estimated from two-way travel times and sound speed of water. Sound speed along the entire ray-path is approximated by the geometric mean of the sound velocities measured at both endpoints. In October 2014, an offshore geodetic network of intercommunicating transponders was installed in 800 m water depth where the NAF trace is identified in high-resolution multibeam seafloor bathymetry maps (Grall et al., 2018a,b) acquired by autonomous underwater vehicles (Figure 7.2) and in 3.5 kHz seismic profiles (Geli and Henry, 2009). The deployment site was selected based on the existence of a linear scarp of the NAF clearly visible in the bathymetry as a proxy for maximised strain release along the NAF

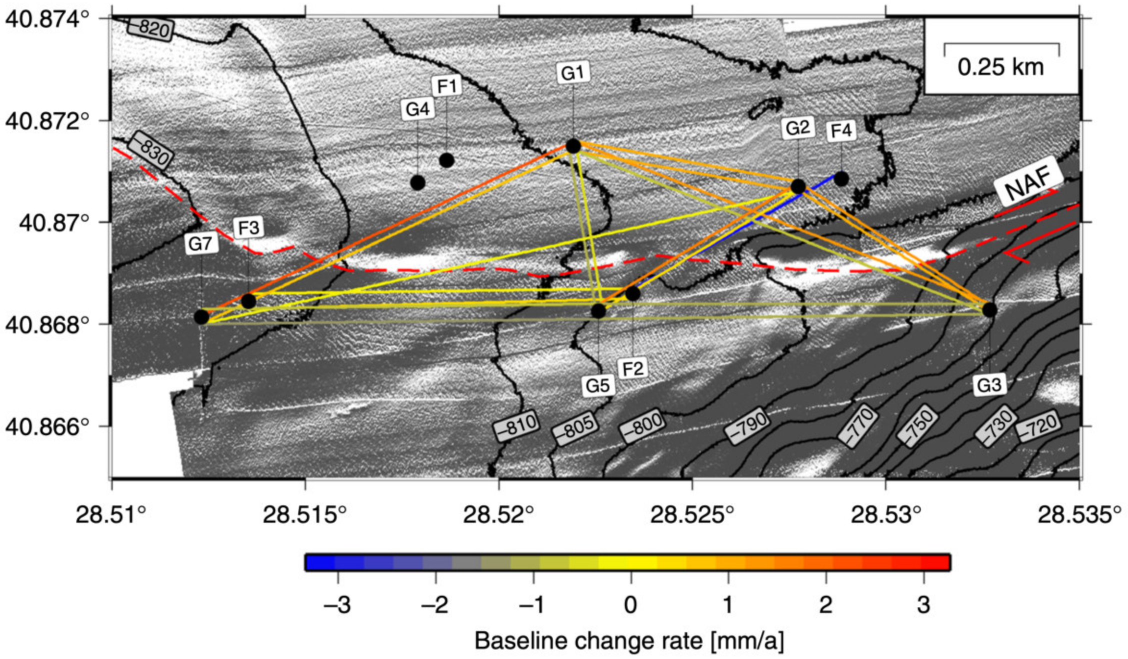

Figure 7.2: Baseline shortening or lengthening rates, based on the total deformation measured at the end of the deployment, are colour coded. A constant strain of $4.5 \cdot 10^{-6}$ was subtracted to each baseline in order to correct for the inferred constant salinity decrease of 0.002 PSU yr^{-1}. Transponder locations are shown as black circles. F- and G- stations only communicate within their respective network. High-resolution shaded bathymetry map (Grall et al., 2018a,b) is shown with a light source from the South

(Le Pichon et al., 2001; Armijo et al., 2005). Ten acoustic transponders, four from the Ocean Geosciences Laboratory in Brest, France (station names starting with F) and 6 from GEOMAR's GeoSEA array in Kiel, Germany (station names starting with G), were installed (Sakic et al., 2016) in October 2014 and remained fully operational until May 5, 2017. Each set of stations, manufactured by Sonardyne Ltd (UK), used a different center-frequency (F: 22.5 kHz, G: 17 kHz), so the F- and G-stations communicated only with F- and G-stations, respectively. Pairs of stations, <100 m apart, shared common baselines and all stations monitored the temperature, pressure, and tilt (Figure 7.3a, b, Supplementary Figures 7.7 – 7.9) at the transponder site along with the two-way travel time between them (Figure 7.3c).

7.3.2 Baseline estimation

We use 650.000 two-way travel time measurements based on two soundings, respectively. Each station either interrogates the other stations of its kind or acts as a replying instrument, thus the experiment forms an autonomous intercommunicating network on the seafloor, rather than observations at individual positions. The acoustic distance is then calculated from the average sound-speed in water multiplied by the one-way travel time.

We estimate the sound-speed in water from temperature and pressure measurements (Leroy et al., 2008), assuming a constant salinity, similar to other path-ranging experiments (Chadwell et al., 1999; Osada et al., 2012; McGuire and Collins, 2013). Figure 7.3 shows the time series of the measured parameters together with the calculated sound speed and baselines for the southwest-northeast fault crossing baseline G2 - G5.

For the final strain estimates (Figure 7.4), we subtracted a mean strain of $4.5 \cdot 10^{-6}$ estimated from all baselines not crossing the fault (corresponding to a baseline decrease of 4.5 mm for a 1000 m long baseline during 2.5 years). Subtracting a constant strain value, instead of a constant increase or decrease in the baseline lengths, accounts for the fact that linear trends in sensor drift or water parameters are linearly related to strain. In addition, considering strain makes the observation independent from the baseline lengths. The baselines show a consistent behaviour (Figure 7.2, Supplementary Figures 7.10, 7.11 and Supplementary Table 7.1), with a long-term resolution better than 8 mm for all baselines (Figure 7.3), and strain is smaller than $1 \cdot 10^{-5}$ for all baselines (e.g. less than 1 cm deformation on a 1 km-long measurement distance). For instantaneous baseline changes, the resolution capability is ~2 mm, in particular, if an event would influence different baselines. We interpret the nominal lengthening of all baselines as a result of subtle changes in the physical properties of water, such as a salinity decrease of 0.005 practical salinity units (PSU) during the 2.5 years of deployment (0.002 PSU a^{-1}). Alternatively, one could consider a total drift in all pressure sensors of -0.242 kPa or a total drift in all temperature sensors of -0.00126 °C. In particular, a pressure drift of -0.242 kPa during the deployment cannot be distinguished from a local uplift of 2.4 cm. Because the Sea of Marmara is an extensional step-over or pull-apart structure system including substantial subsidence (Armijo et al., 2002) with the basement imaged at a depth of ~4.5 km below the Central High and therefore close to the geodetic network, uplift is unlikely (Bécel et al., 2010). The data suggest an absence of vertical movement and the remaining small baseline changes originate from measurement uncertainties of the pressure and temperature sensors. The subtle changes of water parameters such as the temperature increase of 0.002 °C on March 2016 (Figure 7.3a) might be a sensor artefact since they are not compensated by pressure or travel time resulting in an apparent ~3 mm baseline length change (Figure 7.3e). However, since baseline estimates are based on the equation distance = time × velocity, travel times and water sound-speeds must be jointly accurately known. This problem is similar to the hypocenter-depth-velocity dependency in earthquake location techniques. This is the reason why the network was designed to measure a high number of baselines across the fault to allow isolating effects of sensor drift from baseline changes.

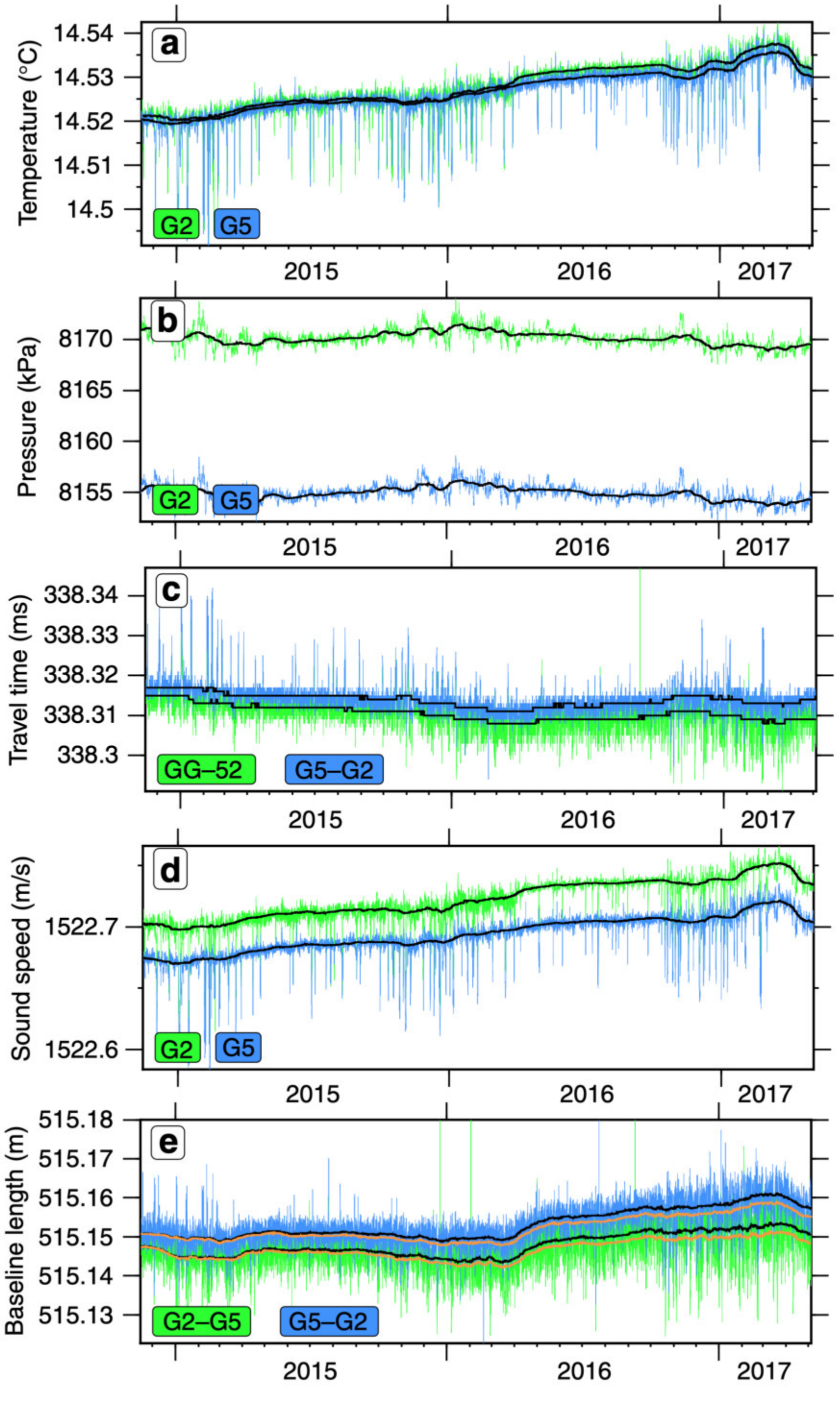

Figure 7.3: Measured parameters and estimated baseline for station pair G2-G5. Black lines indicate monthly medians. (a) Temperature. (b) Pressure. (c) Acoustic one-way travel times between the transponders for the forward- and backward measurement. (d) Estimated sound speed from temperature and pressure (using a constant salinity). (e) Resulting baselines for both measurement directions. Orange lines indicate the monthly mean baseline lengths with the inferred linear salinity decrease rate of 0.002 PSU yr^{-1}

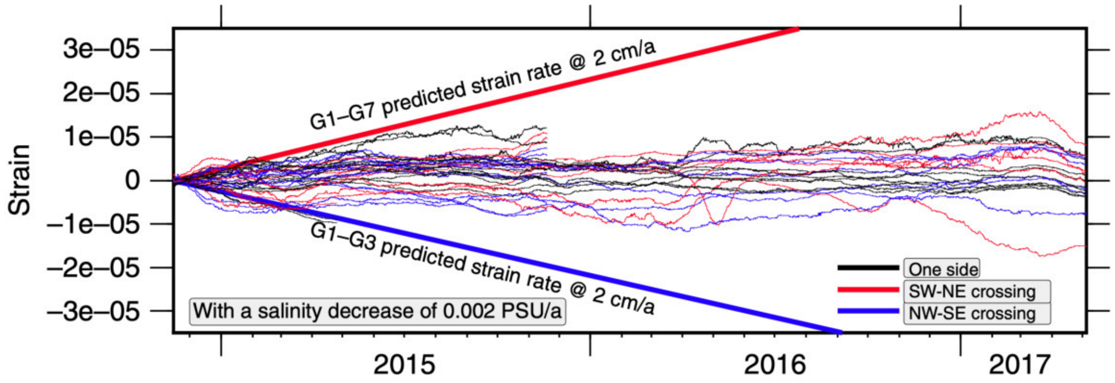

Figure 7.4: Strain of all baselines. Strain (monthly medians) estimated from the measured travel times and calculated sound speeds based on pressure, temperature and a linear salinity decrease of 0.002 PSU yr^{-1}. Baselines not crossing the fault (e.g. sub-parallel to the NAF) are shown in black; for a simple, east-west oriented, right-lateral strike-slip fault, baselines oriented southwest-northeast (red lines) should lengthen and those oriented northwest- southeast (blue lines) should shorten. Predicted strain rates correspond to a strike-slip movement reaching the seafloor.

7.3.3 Estimation of slip on the fault from baseline data

We compared the observed baseline changes with a vertical west-east trending strike-slip model crossing the network. We used a least square inversion to determine the slip rate of the fault which minimizes the differences between the observations and the strike-slip fault model (Sakic et al., 2016). This approach implicitly includes the assumption that baselines located on one side of the fault (i.e. not crossing the fault) are not changing. From baselines crossing the fault we found an optimal rate for strike-slip movement of 0.80 ± 1.25 mm yr^{-1}. This suggests that the surface fault slip rate across the network is close to zero and consistent with the results from the first six months of deployment (Sakic et al., 2016). Analysis of the geodetic data during the first six months of the deployment resulted in an upper bound on the slip rate of 6 mm yr^{-1} only (Sakic et al., 2016). The seven-fold increase of fault slip resolution clearly demonstrates the need for long-term deployments in order to resolve tectonic processes.

7.3.4 Modelling of strain and locking depth

Next, we model strain for vertical strike-slip faulting. We use an analytical half-space solution, based on the elastic dislocation theory for an infinitely long vertical strike-slip fault (Rybicki, 1971). Since the geodetic network is located on low rigidity sediments, we model the dependency of strain in the presence of a low rigidity layer (= weak layer). We use a simple model consisting of two horizontal layers with a rigidity contrast (Rybicki,

1971) to investigate the dependency of strain on creep below given depths, rigidity and varying thickness of the overlying sedimentary layer. The slip rates estimated for the NAF from onshore observations range between 15 and 27 mm yr^{-1} (Meade, 2002; Reilinger et al., 2006; Hergert and Heidbach, 2010) from GPS observations and between 15 and 19.7 mm yr^{-1} from mass deposit considerations (Kurt et al., 2013; Grall et al., 2013). We model fault creep with a rate of 20 mm yr^{-1} (in-between the GPS and geological estimates) for different faulting depths, above which the fault is locked and below which it creeps. The modelled strain is linearly depen- dent on the inferred slip rate of 20 mm yr^{-1} (Rybicki, 1971). We model scenarios for creep below 3 km (corresponding to the thickness of the basin sediments (Bécel et al., 2010) and hence strain in the pre-kinematic basement rocks (Figure 7.5a) and for creep below 4.5 km depth (corresponding to the depth of the crystalline basement) (Figure 7.5b). The depths of the geological units are known from a seismic profile passing in ~5 km distance south-east of the geodetic network (Bécel et al., 2010). The results show that the overlaying low rigidity sedimentary layers focus the strain close to the fault (Figure 7.5a,b). Fault creep below 3 km (Figure 7.5a), corresponding to slip in the pre-kinematic basement rocks (Bécel et al., 2010), is clearly above the strain rate sensitivity of the geodetic network. The strain rate sensitivity of the geodetic network is $1.6 \cdot 10^{-6}$ yr^{-1} corresponding to the inverted strike-slip movement of 0.8 mm yr^{-1} considering the 500 m coverage of the geodetic network per- pendicular to the fault (Figure 7.5). Modeling the minimal fault slip inferred from onshore geodetic observations (16 mm yr^{-1}) results in 20 % less strain and would still have been above to the sensitivity of the offshore geodetic network, in particular, due to the existence of weak shallow layers (Figure 7.5a). From the modelling we find the locking depth of 3 km as the most conservative estimate. The strain rate induced from 20 mm yr^{-1} creep in the crystalline basement (Figure 7.5b), located below 4.5 km (Bécel et al., 2010) depth, results in a signal exceeding the strain rate sensitivity for sedimentary layers thicker than 1 km.

Slip at depths below 16 km (Figure 7.5c), corresponding to the interseismic deformation, results in a small strain signal and is still in line with the measurement uncertainty of strike-slip faulting of 0.80 ± 1.25 mm yr^{-1}. In the last step, we modelled the dependency of strain on rigidity contrasts between the upper and lower layer (Figure 7.5d). We estimated the rigidity from empirical relations from a seismic P-velocity profile (Bécel et al., 2010) (Supplementary Table 7.2). Despite the uncertainties of the empirical relations we find rigidity ratios clearly exceeding 10 for the material above and below the basement, so the calculated strain rate of strike-slip faulting on the seafloor is little dependent on these large values (Figure 7.5d). From the strain rate estimates, we conclude that the strain rate sensitivity of the geodetic network is likely sufficient to resolve fault movement above the basement (Figure 7.5a,b) and the model shows that the maximal resolution is reached for slip occurring at depths below 5.5 km (Figure 7.5d).

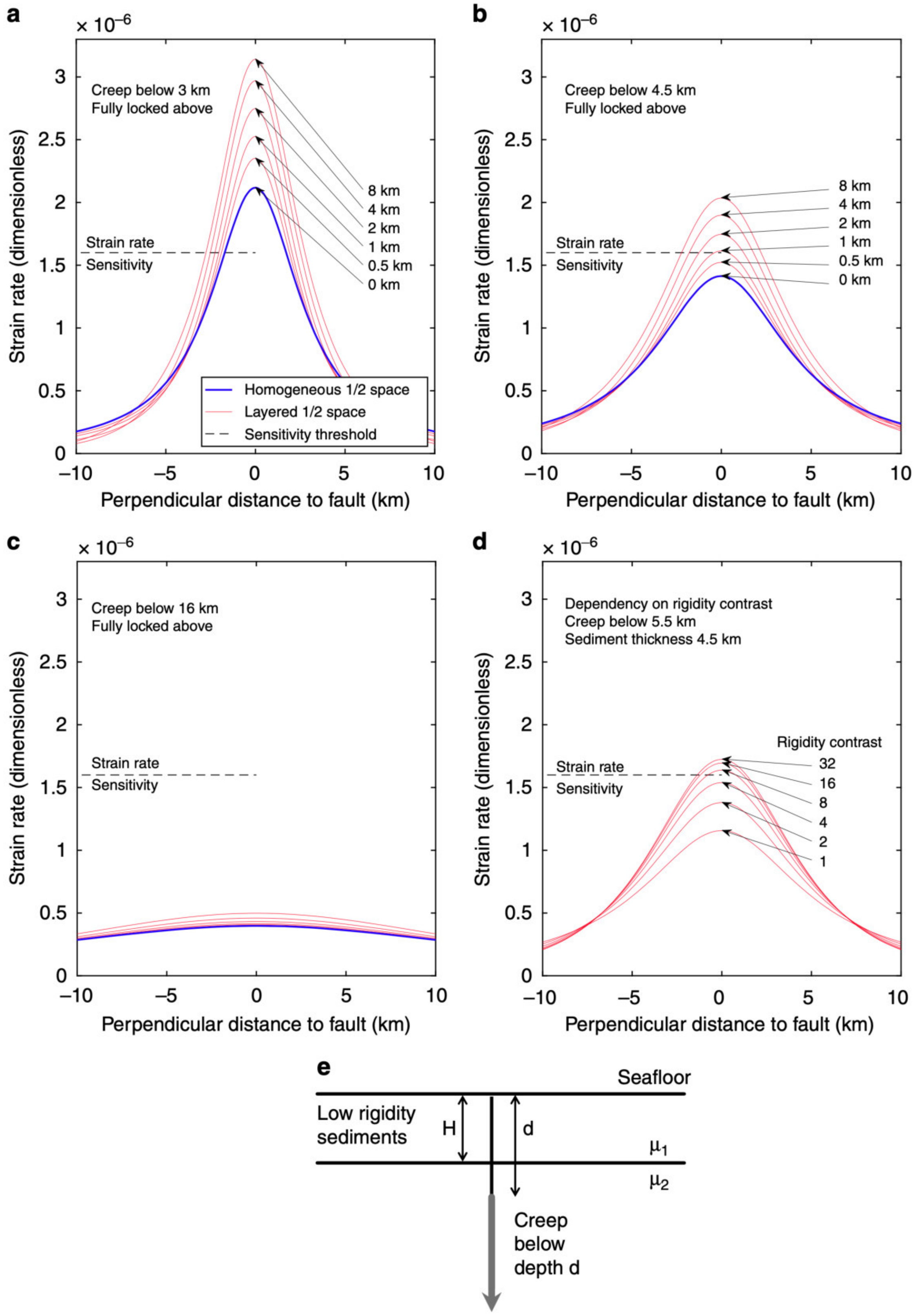
a
× 10⁻⁶
Creep below 3 km
Fully locked above
8 km
4 km
2 km
1 km
0.5 km
0 km
Strain rate
Sensitivity
Homogeneous 1/2 space
Layered 1/2 space
Sensitivity threshold
Strain rate (dimensionless)
Perpendicular distance to fault (km)
b
Creep below 4.5 km
Fully locked above
c
Creep below 16 km
Fully locked above
d
Dependency on rigidity contrast
Creep below 5.5 km
Sediment thickness 4.5 km
Rigidity contrast
32
16
8
4
2
1
0
0.5
1
1.5
2
2.5
3
–10
–5
0
5
10
e
Seafloor
Low rigidity sediments
H
d
μ1
μ2
Creep below depth d

Figure 7.5 ***(previous page)*****:** Modelled strain rates for a vertical strike-slip fault. The strain for homogenous and layered half space, based on elastic dislocation theory, was estimated using the analytical solution for a horizontally layered half-space and a vertical strike-slip fault (Rybicki, 1971). (a) Model for creeping below 3 km depth corresponding to slip in the pre-kinematic basement rocks (Bécel et al., 2010) and below. Above the locking depth, the fault is fully locked. Below the locking depth, the fault creeps at 20 mm yr^{-1}. The ratio of rigidity between the lower and upper layer is 4. The strain rate sensitivity of the geodetic network is $1.6 \cdot 10^{-6}$ yr^{-1}, corresponding to strike-slip movement of 0.8 mm yr^{-1} considering a 500 m extension of the geodetic network perpendicular to the fault. (b) Model for slip below 4.5 km in the basement rocks (Bécel et al., 2010). (c) Creep below 16 km depth corresponding to interseismic deformation. d Dependency of rigidity contrast on the strain rate for a 4.5 km weak layer and creep below 5.5 km. Rigidity contrast from empirical relations is in the range between 8 and 16 (Supplementary Table 7.2). (e) Sketch showing the modelling setup and parameters. μ_1 and μ_2 are the rigidities of the shallow layer and below.

With the possibility of distributed strike-slip across a few kilometre-wide zone of faults at the seafloor (Le Pichon et al., 2001; Grall et al., 2018a; Henry et al., 2018; Wollin et al., 2018), we might not have captured the complete possible slip. However, deformation is clearly focussed beneath the geodetic network since the fault trace can be unambiguously identified in the bathymetry (Le Pichon et al., 2001; Grall et al., 2018a). In particular, there is a clear 3.5 km right-lateral offset of a ridge between the baselines, indicating the location of the geodetic network above the main zone of surface deformation of the NAF (Armijo et al., 2005).

7.3.5 Local seismicity

To better detect small-magnitude events indicative of a creeping behaviour, two small aperture OBS arrays were deployed in the vicinity of the geodetic stations and close to the NAF: a 5 km wide array during five months and a 12 km wide array for the next 12 months (Figures 7.1 and 7.6). Such small aperture OBS arrays are significantly more sensitive to low-magnitude (from 0 and up) and shallow seismicity than larger aperture OBS arrays (e.g., 10 km station spacing) which have typically a magnitude of completeness of 1 (Yamamoto et al., 2017). The OBS detections were complemented with phase picks from the land stations of the Kandilli Observatory and Earthquake Research Institute (KOERI). In 17 months, only 45 events with local magnitudes between 1.4 and 4.2 were detected and none are located near the geodetic experiment (Figure 7.6). These events are 9 to 25 km deep and slightly offset (~2 km) from the NAF surface trace. The offset can be explained with the increased strain and hence stress accumulation in the vicinity of the locked fault (Rybicki, 1971) (Figure 7.5c) and gas migrations at depth (Henry et al., 2018; Geli et al., 2018). The local observation is in-line with the sparse seis- micity recorded by onshore stations during the last decade along this segment of the NAF (Figure 7.1) and, as the geodetic observation, also concurs with its quasi-locked status.

7.4 Discussion

Seismicity below the Kumburgaz Basin is sparse (Figures 7.1b and 7.6). This observation precludes a model where the fault would be locked at shallow depths but creeping at deeper levels (as modelled in Figure 7.5), since seismicity would focus along the locking/ creeping transition, as observed on the Prince Island segment (Bohnhoff et al., 2013) southeast of Istanbul (29.1 °E). The seismic gap beneath the Kumburgaz Basin, together with the high level of seismicity on either side rather suggests that this section of the NAF is either completely locked or fully creeping. The observation of sparse seismicity, together with the absence of observable deformation from the geodetic network (Figures 7.4 and 7.5) indicates a completely locked fault below the geodetic network down to larger depths.

Our results contrast with that of the Turkish-Japanese path-ranging (Yamamoto et al., 2019) in the western part of the Sea of Marmara (red star in Figure 7.1). Their data evidence a continuous dextral strike-slip deformation of 10.7 ± 4.7 mm yr^{-1} in an area characterized by pronounced seismicity and where active creeping was previously inferred from repeating seismic events (Schmittbuhl et al., 2015; Bohnhoff et al., 2017). The seismicity patterns beneath both geodetic networks significantly differ but are consistent with the respective geodetic observations, where the fault segment with no seismicity seems locked, whereas the fault segment with a high level of seismicity is interpreted as being partially creeping. Although this observation is common for onshore faults, submarine faults may have a different behaviour due to the possible high amount of gas migrating upwards (Henry et al., 2018; Geli et al., 2018; Batsi et al., 2018) and the large water content of the shallow sediments. The fault segment east of our geodetic network related to the çınarcık Basin (CB) segment is characterized by seismicity which significantly increased (Bohnhoff et al., 2013) after the M_w 7.4 1999 Izmit earthquake and was suggested to be related to stress increase imposed from the 1999 Izmit rupture zone to the eastern Sea of Marmara (Bohnhoff et al., 2013). Although this segment is characterized by small magnitude seismicity, high-resolution hypocenter locations revealed that seismicity occurs almost exclusively below 10 km depth with very sparse seismicity at shallow depths (Bohnhoff et al., 2013), interpreted as being locked. Furthermore, seismicity in the eastern Sea of Marmara is characterized by the absence of repeating events suggested to be related to a locked fault (Bohnhoff et al., 2017).

Assuming a quasi-locked status of the NAF in the Sea of Marmara since its last known rupture in 1766, the accumulated slip deficit would be in the order of 4 m. We estimate

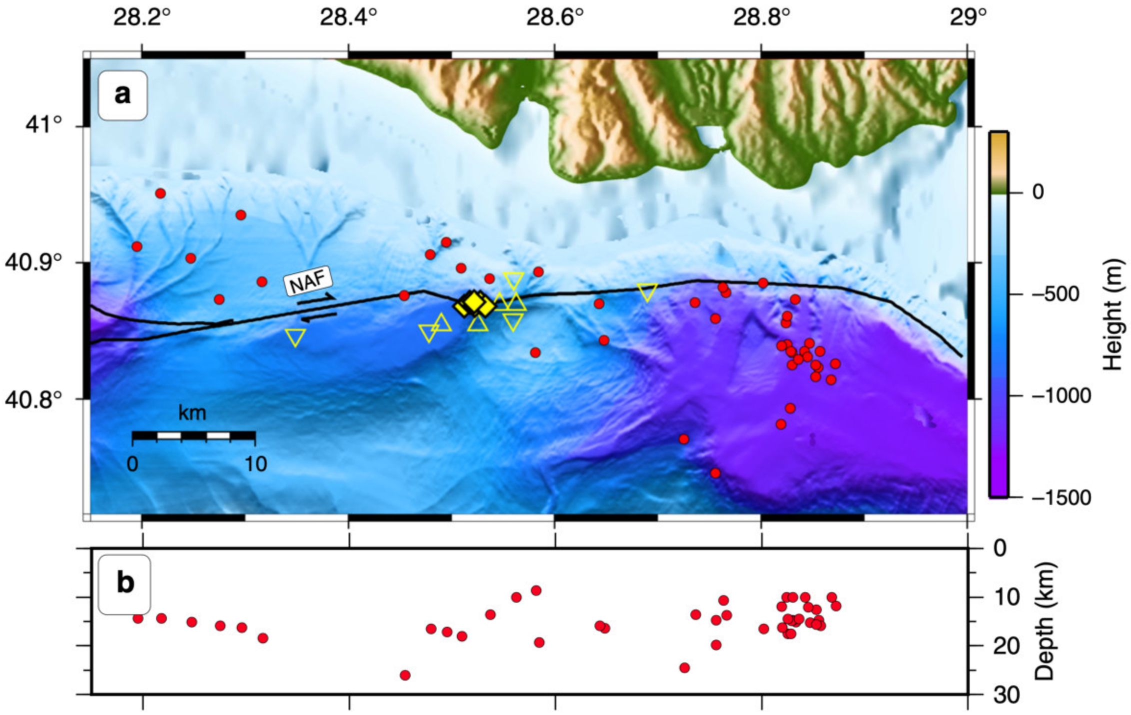

Figure 7.6: Seismicity located with the ocean bottom seismometer data. Microseismicity locations in map view (a) and projected along a vertical west-east trending profile (b). The OBSs were first deployed in a very small aperture array (29 October 2014 until 25 April 2015, upright triangles) and then re-deployed along the NAF (26 April 2015 until 13 April 2016; inverted triangles). Red circles show the events located with phases from OBS data combined with arrival times from land stations (KOERI). Yellow diamonds clustered near the OBSs show the geodetic stations. Bathymetry from Le Pichon et al. (2001), topography from Ryan et al. (2009) and fault traces from Armijo et al. (2005)

(Supplementary Table 7.3) the equivalent moment magnitude with 7.1 magnitude units for an earthquake rupturing a 34 km-long fault segment of the NAF beneath the Kumburgaz Basin (Figure 7.1). The slip deficit for a larger rupture involving all unbroken and locked segments in the Sea of Marmara Istanbul (e.g. rupture of the NAF in the Kumburgaz Basin and CB, Figure 7.1) equals a moment magnitude 7.4 earthquake passing 25 km South of the city center of Istanbul. The magnitudes are in-line with previous studies (Armijo et al., 2005; Bohnhoff et al., 2016) and with the magnitudes of historical events along the NAF (Ambraseys, 2002a; Parsons et al., 2000) and can be considered as a major hazard for the close-by Istanbul metropolitan area and its 15 million inhabitants.

Previous studies assumed a complete locking of the NAF in the eastern Sea of Marmara based on onshore observations since in situ seafloor data were not available. Using observations from an intercommunicating network of acoustic transponders located on the seafloor and measuring across the NAF we show that the fault is locked down to at least 3 km and presumably down to 5.5 km depth, into the crystalline basement. Long-term

OBS deployments designed to detect very small microseismicity reveal very sparse seismicity and absence of events directly beneath the OBS network. The geodetic monitoring together with the OBS observation indicate that the fault in the Kumburgaz Basin is fully locked. Together with recent results from a geodetic network (Yamamoto et al., 2019) in the western Sea of Marmara, which revealed partial creep, our results indicate a complex fault locking pattern of the submerged NAF. Two unbroken and locked segments in the Sea of Marmara with accumulated strain equivalent to an earthquake between magnitude 7.1 and 7.4 remain and need to be considered in hazard assessments and risk estimates for the contiguous Istanbul metropolitan area. This study clearly demonstrates that *in situ* seafloor geodetic measurements along with OBS monitoring can fill observational gaps at sea and advocates the urgent need to conduct similar studies in regions with a high hazard potential from active faults offshore.

Acknowledgements

The acoustic seafloor monitoring in the Sea of Marmara is a joint project of the Istanbul Technical University (Turkey) together with the University of Brest (France) and GEOMAR Helmholtz Centre for Ocean Research Kiel (Germany). We thank C. Hammersley and T. Bennetts from Sonardyne for their technical support with the geodetic instruments over the years. We thank the crews and Captains of *R/V Pourquoi Pas?*, *R/V Poseidon*, *R/V Yunus* and *Oktay 8* for their support during installation and maintenance of the network. The GeoSEA Array is funded through grant 03F0658I of the BMBF (German Federal Ministry of Education and Research). Support was provided by the bilateral ANR/TÜBITAK collaborative research project MAREGAMI (ANR-16-CE03-0010-02 and Tübitak Project 116Y371). The French geodetic array was funded by the European Union, the Brittany Region and the French government (CPER ODO); support for the cruises was provided by CNRS-INSU through the European Monitoring Seafloor Observatory programme (EMSO).

Author contributions

J.Y.R., V.B. and H.K. funded and designed the experiment. D.L. and H.K. drafted the manuscript, which was revised and edited by all authors. P.H. implemented the analytical solution for the strain calculations, the modelling of strain was done by D.L. The GPS land-stations and calculation of the water column parameters were done by S.O., S.E. and F.P. The offshore geodetic dataset was independently processed witch different software written by D.L., F.P. who reached the same results. P.S. inverted the strike-slip rate from baseline data. The OBS data was processed by D.L. with input from L.G., J.B. and Z.C. All authors were involved in the configuration of the transponder network, network design, site selection, ship cruises, customs clearance, and logistics since the start of marine operations in 2014.

Competing interests

H.K., D.L. and F.P. are inventors of a patent to install stations on the seafloor using a deep-sea cable (Kopp et al., 2017). This method is not necessarily required for the installation of the stations which can also be done conventionally with a remotely operated vehicle or using a free-fall procedure. All other authors declare no competing interests.

Data Availability Statement

The geodetic data that support the findings of this study can be downloaded through the data repository PANGEA (G-stations, data `https://doi.org/10.1594/PANGAEA.900275`) 52 and through SEANOE (F-stations, data `https://doi.org/10.17882/59750`) (Royer et al., 2019). The phase picks from the onshore seismological data is from KOERI (downloaded 15 June 2018). OBS data can be requested from the corresponding author.

Code availability

The custom code used for the processing of the offshore geodetic data can be downloaded from `https://github.com/flp-geo/geosea`.

References

Aki, K. (1966). Generation and propagation of g waves from the niigata earthquake of june 16, 1964. : Part 2. estimation of earthquake moment, released energy, and stress-strain drop from the g wave spectrum. *Engineering*.

Aksoy, M. E., Meghraoui, M., Vallée, M., & Çakır, Z. (2010). Rupture characteristics of the a.d. 1912 mürefte (ganos) earthquake segment of the north anatolian fault (western turkey). *Geology*, *38*(11), 991–994, `https://doi.org/10.1130/g31447.1`.

Ambraseys, N. N. (2002a). The seismic activity of the marmara sea region over the last 2000 years. *Bulletin of the Seismological Society of America*, *92*(1), 1–18, `https://doi.org/10.1785/0120000843`.

Ambraseys, N. N. (2002b). Seismic sea-waves in the marmara sea region during the last 20 centuries. *Journal of Seismology*, *6*(4), 571–578, `https://doi.org/10.1023/a:1021158610252`.

Armijo, R., Meyer, B., Navarro, S., King, G., & Barka, A. (2002). Asymmetric slip partitioning in the sea of marmara pull-apart: a clue to propagation processes of the north anatolian fault? *Terra Nova*, *14*(2), 80–86, `https://doi.org/10.1046/j.1365-3121.2002.00397.x`.

Armijo, R., et al. (2005). Submarine fault scarps in the sea of marmara pull-apart (north anatolian fault): Implications for seismic hazard in istanbul. *Geochemistry, Geophysics, Geosystems*, *6*(6), `https://doi.org/10.1029/2004gc000896`.

Aydoğdu, A., Hoar, T. J., Vukicevic, T., Anderson, J. L., Pinardi, N., Karspeck, A., Hendricks, J., Collins, N., Macchia, F., & Özsoy, E. (2018). Osse for a sustainable marine observing network in the sea of marmara. *Nonlinear Processes in Geophysics*, *25*(3), 537–551, `https://doi.org/10.5194/npg-25-537-2018`.

Batsi, E., Lomax, A., Tary, J., Klingelhoefer, F., Riboulot, V., Murphy, S., Monna, S., Özel, N. M., Kalafat, D., Saritas, H., Cifçi, G., Çagatay, N., Gasperini, L., & Géli, L. (2018). An alternative view of the microseismicity along the western main marmara fault. *Bulletin of the Seismological Society of America*, *108*(5A), 2650–2674, `https://doi.org/10.1785/0120170258`.

Bohnhoff, M., Bulut, F., Dresen, G., Malin, P. E., Eken, T., & Aktar, M. (2013). An earthquake gap south of istanbul. *Nat Commun*, *4*, 1999, `https://doi.org/10.1038/ncomms2999`.

Bohnhoff, M., Martínez-Garzón, P., Bulut, F., Stierle, E., & Ben-Zion, Y. (2016). Maximum earthquake magnitudes along different sections of the north anatolian fault zone. *Tectonophysics*, *674*, 147–165, `https://doi.org/10.1016/j.tecto.2016.02.028`.

Bohnhoff, M., Wollin, C., Domigall, D., Küperkoch, L., Martínez-Garzón, P., Kwiatek, G., Dresen, G., & Malin, P. E. (2017). Repeating marmara sea earthquakes: indication for fault creep. *Geophysical Journal International*, *210*(1), 332–339, `https://doi.org/10.1093/gji/ggx169`.

Boyer, T. P., Antonov, J. I., Baranova, O. K., Garcia, H. E., Johnson, D. R., Mishonov, A. V., O'Brien, T. D., Seidov, D., Smolyar, I., Zweng, M. M., Paver, C. R., Locarnini, R. A., Reagan, J. R., Forgy, C., Grodsky, A., & Levitus, S. (2013). World ocean database 2013. `https://doi.org/http://doi.org/10.7289/V5NZ85MT`.

Bécel, A., Laigle, M., de Voogd, B., Hirn, A., Taymaz, T., Yolsal-Cevikbilen, S., & Shimamura, H. (2010). North marmara trough architecture of basin infill, basement and faults, from psdm reflection and obs refraction seismics. *Tectonophysics*, *490*(1-2), 1–14, `https://doi.org/10.1016/j.tecto.2010.04.004`.

Bürgmann, R. & Chadwell, D. (2014). Seafloor geodesy. *Annual Review of Earth and Planetary Sciences*, *42*(1), 509–534, `https://doi.org/10.1146/annurev-earth-060313-054953`.

Castagna, J. P., Batzle, M. L., & Eastwood, R. L. (1985). Relationships between compressional-wave and shear-wave velocities in clastic silicate rocks. *GEOPHYSICS*, *50*(4), 571–581, `https://doi.org/10.1190/1.1441933`.

Chadwell, C. D., Hildebrand, J. A., Spiess, F. N., Morton, J. L., Normark, W. R., & Reiss, C. A. (1999). No spreading across the southern juan de fuca ridge axial cleft during 1994-1996. *Geophysical Research Letters*, *26*(16), 2525–2528, `https://doi.org/10.1029/1999gl900570`.

Cros, E. & Geli, L. (2013). Caracterisation of microseimicity in the western sea of marmara: implications in terms of seismic monitoring. *Archimer, Irfemer Rep.*, `https://doi.org/10.13155/38916`.

Dunn, S., Hatchell, P., van den Beukel, A., de Vries, R., & Frafjord, T. (2016). A long-term seafloor deformation monitoring campaign at ormen lange gas field. *First Break*, *34*, 55–64.

Ergintav, S., Reilinger, R. E., Çakmak, R., Floyd, M., Cakir, Z., Doğan, U., King, R. W., McClusky, S., & Özener, H. (2014). Istanbul's earthquake hot spots: Geodetic constraints on strain accumulation along faults in the marmara seismic gap. *Geophysical Research Letters*, *41*(16), 5783–5788, `https://doi.org/10.1002/2014gl060985`.

Gagnon, K., Chadwell, C. D., & Norabuena, E. (2005). Measuring the onset of locking in the peru-chile trench with gps and acoustic measurements. *Nature*, *434*(7030), 205–8, `https://doi.org/10.1038/nature03412`.

Gardner, G. H. F., Gardner, L. W., & Gregory, A. R. (1974). Formation velocity and density—the diagnostic basics for stratigraphic traps. *GEOPHYSICS*, *39*(6), 770–780, `https://doi.org/10.1190/1.1440465`.

Geli, L. & Henry, P. (2009). *MARMESONET cruise, RV Le Suroît,*. Report.

Geli, L., et al. (2018). Gas and seismicity within the istanbul seismic gap. *Sci Rep*, *8*(1), 6819, `https://doi.org/10.1038/s41598-018-23536-7`.

Grall, C., Dupre, S., Guerin, C., Normand, A., Gaillot, A., Fleury, J., & Henry, P. (2018a). Processed asterx auv data from the sea of marmara: high-resolution bathymetry and seafloor backscatter images. *SEANOE*, `https://doi.org/10.17882/55744`.

Grall, C., Henry, P., Dupré, S., Géli, L., Scalabrin, C., Zitter, T. A. C., Sengor, A. M. C., Namik Cagatay, M., & Cifci, G. (2018b). Upward migration of gas in an active tectonic basin: An example from the sea of marmara. *Deep Sea Research Part II: Topical Studies in Oceanography*, *153*, 17–35, `https://doi.org/10.1016/j.dsr2.2018.06.007`.

Grall, C., Henry, P., Thomas, Y., Westbrook, G. K., Çağatay, M. N., Marsset, B., Saritas, H., Çifçi, G., & Géli, L. (2013). Slip rate estimation along the western segment of the main marmara fault over the last 405-490 ka by correlating mass transport deposits. *Tectonics*, *32*(6), 1587–1601, `https://doi.org/10.1002/2012tc003255`.

Hanks, T. C. & Kanamori, H. (1979). A moment magnitude scale. *Journal of Geophysical Research*, *84*(B5), `https://doi.org/10.1029/JB084iB05p02348`.

Havskov, J. & Ottemoller, L. (1999). Seisan earthquake analysis software. *Seismological Research Letters*, *70*(5), 532–534, `https://doi.org/10.1785/gssrl.70.5.532`.

Henry, P., Grall, C., Kende, J., Viseur, S., Özeren, M. S., Şengör, A. M. C., Dupré, S., Scalabrin, C., & Géli, L. (2018). A statistical approach to relationships between fluid emissions and faults: The sea of marmara case. *Deep Sea Research Part II: Topical Studies in Oceanography*, *153*, 131–143, `https://doi.org/10.1016/j.dsr2.2018.05.010`.

Hergert, T. & Heidbach, O. (2010). Slip-rate variability and distributed deformation in the marmara sea fault system. *Nature Geoscience*, *3*(2), 132–135, `https://doi.org/10.1038/ngeo739`.

Karabulut, H., Schmittbuhl, J., Özalaybey, S., Lengliné, O., Kömeç-Mutlu, A., Durand, V., Bouchon, M., Daniel, G., & Bouin, M. P. (2011). Evolution of the seismicity in the eastern marmara sea a decade before and after the 17 august 1999 izmit earthquake. *Tectonophysics*, *510*(1-2), 17–27, `https://doi.org/10.1016/j.tecto.2011.07.009`.

Klein, E., Duputel, Z., Masson, F., Yavasoglu, H., & Agram, P. (2017). Aseismic slip and seismogenic coupling in the marmara sea: What can we learn from onland geodesy? *Geophysical Research Letters*, *44*(7), 3100–3108, `https://doi.org/10.1002/2017gl072777`.

Kopp, H., Lange, D., Steffen, K. P., & Petersen, F. (2017). Vorrichtung zur lösbaren verbindung eines drahtes und verfahren zum ausbringen des gerätes in ein gewässer mit der vorrichtung. *no. DE 10 2016 107 558.2*, `https://doi.org/https://oceanrep.geomar.de/40152/`.

Kurt, H., Sorlien, C. C., Seeber, L., Steckler, M. S., Shillington, D. J., Cifci, G., Cormier, M. H., Dessa, J. X., Atgin, O., Dondurur, D., Demirbag, E., Okay, S., Imren, C., Gurcay, S., & Carton, H. (2013). Steady late quaternary slip rate on the cinarcik section of the north anatolian fault near istanbul, turkey. *Geophysical Research Letters*, *40*(17), 4555–4559, `https://doi.org/10.1002/grl.50882`.

Lange, D., Bedford, J. R., Moreno, M., Tilmann, F., Baez, J. C., Bevis, M., & Kruger, F. (2014). Comparison of postseismic afterslip models with aftershock seismicity for three subduction-zone earthquakes: Nias 2005, maule 2010 and tohoku 2011. *Geophysical Journal International*, *199*(2), 784–799, `https://doi.org/10.1093/gji/ggu292`.

Le Pichon, X., Şengör, A. M. C., Demirbağ, E., Rangin, C., İmren, C., Armijo, R., Görür, N., Çağatay, N., Mercier de Lepinay, B., Meyer, B., Saatçılar, R., & Tok, B. (2001). The active main marmara fault. *Earth and Planetary Science Letters*, *192*(4), 595–616, `https://doi.org/10.1016/s0012-821x(01)00449-6`.

Leroy, C. C., Robinson, S. P., & Goldsmith, M. J. (2008). A new equation for the accurate calculation of sound speed in all oceans. *J Acoust Soc Am*, *124*(5), 2774–82, `https://doi.org/10.1121/1.2988296`.

Marra, G., Clivati, C., Luckett, R., Tampellini, A., Kronjager, J., Wright, L., Mura, A., Levi, F., Robinson, S., Xuereb, A., Baptie, B., & Calonico, D. (2018). Ultrastable laser interferometry for earthquake detection with terrestrial and submarine cables. *Science*, *361*(6401), 486–490, `https://doi.org/10.1126/science.aat4458`.

McGuire, J. J. & Collins, J. A. (2013). Millimeter-level precision in a seafloor geodesy experiment at the discovery transform fault, east pacific rise. *Geochemistry, Geophysics, Geosystems*, *14*(10), 4392–4402, `https://doi.org/10.1002/ggge.20225`.

Meade, B. J. (2002). Estimates of seismic potential in the marmara sea region from block models of secular deformation constrained by global positioning system measurements. *Bulletin of the Seismological Society of America*, *92*(1), 208–215, `https://doi.org/10.1785/0120000837`.

Osada, Y., Kido, M., & Fujimoto, H. (2012). A long-term seafloor experiment using an acoustic ranging system: Precise horizontal distance measurements for detection of seafloor crustal deformation. *Ocean Engineering*, *51*, 28–33, `https://doi.org/10.1016/j.oceaneng.2012.05.006`.

Parsons, T., Toda, S., Stein, R. S., Barka, A., & Dieterich, J. H. (2000). Heightened odds of large earthquakes near istanbul: An interaction-based probability calculation. *Science*, *288*(5466), 661–5, `https://doi.org/10.1126/science.288.5466.661`.

Petersen, F., Kopp, H., Lange, D., Hannemann, K., & Urlaub, M. (2019). Measuring tectonic seafloor deformation and strain-build up with acoustic direct-path ranging. *Journal of Geodynamics*, *124*, 14–24, `https://doi.org/10.1016/j.jog.2019.01.002`.

Reilinger, R., et al. (2006). Gps constraints on continental deformation in the africa-arabia-eurasia continental collision zone and implications for the dynamics of plate interactions. *Journal of Geophysical Research: Solid Earth*, *111*(B5), `https://doi.org/10.1029/2005jb004051`.

Royer, J.-Y., Piété, H., Ballu, V., & Sakic, P. (2019). Seafloor acoustic ranging data across the north-anatolian fault, marmara sea, turkey. *SEANOE*, `https://doi.org/10.17882/59750`.

Ryan, W. B. F., Carbotte, S. M., Coplan, J. O., O'Hara, S., Melkonian, A., Arko, R., Weissel, R. A., Ferrini, V., Goodwillie, A., Nitsche, F., Bonczkowski, J., & Zemsky, R. (2009). Global multi-resolution topography synthesis. *Geochemistry, Geophysics, Geosystems*, *10*(3), `https://doi.org/10.1029/2008gc002332`.

Rybicki, K. (1971). The elastic residual field of a very long strike-slip fault in the presence of a discontinuity. *Bulletin of the Seismological Society of America*, *61*(1), 79–92.

Sakic, P., Piété, H., Ballu, V., Royer, J. Y., Kopp, H., Lange, D., Petersen, F., Özeren, M. S., Ergintav, S., Geli, L., Henry, P., & Deschamps, A. (2016). No significant steady state surface creep along the north anatolian fault offshore istanbul: Results of 6 months of seafloor acoustic ranging. *Geophysical Research Letters*, *43*(13), 6817–6825, `https://doi.org/10.1002/2016gl069600`.

Schmittbuhl, J., Karabulut, H., Lengliné, O., & Bouchon, M. (2015). Seismicity distribution and locking depth along the main marmara fault, turkey. *Geochemistry, Geophysics, Geosystems*, *17*(3), 954–965, `https://doi.org/10.1002/2015gc006120`.

Stein, R. S., Barka, A. A., & Dieterich, J. H. (1997). Progressive failure on the north anatolian fault since 1939 by earthquake stress triggering. *Geophysical Journal International*, *128*(3), 594–604, `https://doi.org/10.1111/j.1365-246X.1997.tb05321.x`.

Tormann, T., Enescu, B., Woessner, J., & Wiemer, S. (2015). Randomness of megathrust earthquakes implied by rapid stress recovery after the japan earthquake. *Nature Geoscience*, *8*(2), 152–158, `https://doi.org/10.1038/ngeo2343`.

Urlaub, M., Petersen, F., Gross, F., Bonforte, A., Puglisi, G., Guglielmino, F., Krastel, S., Lange, D., & Kopp, H. (2018). Gravitational collapse of mount etna's southeastern flank. *Sci Adv*, *4*(10), eaat9700, `https://doi.org/10.1126/sciadv.aat9700`.

Wallace, L. M., Webb, S. C., Ito, Y., Mochizuki, K., Hino, R., Henrys, S., Schwartz, S. Y., & Sheehan, A. F. (2016). Slow slip near the trench at the hikurangi subduction zone, new zealand. *Science*, *352*(6286), 701–4, `https://doi.org/10.1126/science.aaf2349`.

Wollin, C., Bohnhoff, M., Martínez-Garzón, P., Küperkoch, L., & Raub, C. (2018). A unified earthquake catalogue for the sea of marmara region, turkey, based on automatized phase picking and travel-time inversion: Seismotectonic implications. *Tectonophysics*, *747-748*, 416–444, `https://doi.org/10.1016/j.tecto.2018.05.020`.

Yamamoto, R., Kido, M., Ohta, Y., Takahashi, N., Yamamoto, Y., Pinar, A., Kalafat, D., Özener, H., & Kaneda, Y. (2019). Seafloor geodesy revealed partial creep of the north anatolian fault submerged in the sea of marmara. *Geophysical Research Letters*, *46*(3), 1268–1275, `https://doi.org/10.1029/2018gl080984`.

Yamamoto, Y., Takahashi, N., Pinar, A., Kalafat, D., Citak, S., Comoglu, M., Polat, R., & Kaneda, Y. (2017). Geometry and segmentation of the north anatolian fault beneath the marmara sea, turkey, deduced from long-term ocean bottom seismographic observations. *Journal of Geophysical Research: Solid Earth*, *122*(3), 2069–2084, `https://doi.org/10.1002/2016jb013608`.

Supplementary Information

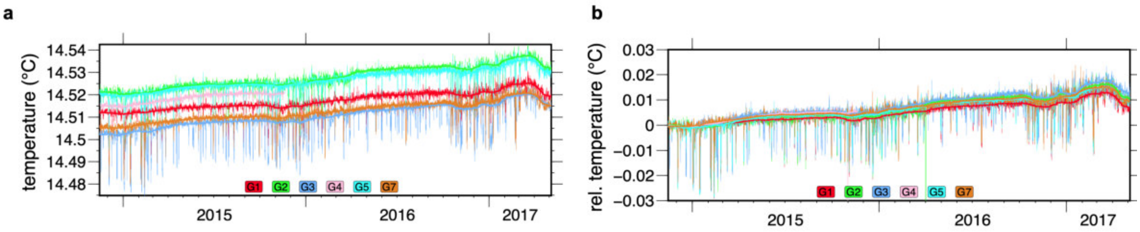

Figure 7.7: High-resolution temperature data used for the baseline calculation. (a) Absolute temperatures for all stations show an increase in temperature of approx. 0.007 °C yr^{-1}. Temperature sensors of the French network had a long time drift and were not used for the baseline calculation. Therefore, the time-series of the close-by G-station temperature sensors were interpolated onto the measurement times of the F-stations. F-station temperature values are not shown since they would overlay and obscure the G-data. Station G4 stopped logging temperature after 19 November 2015. (b) Relative temperature data used for the baseline calculation. For better visualization values were set to zero at the beginning of the experiment. Black lines indicate monthly means.

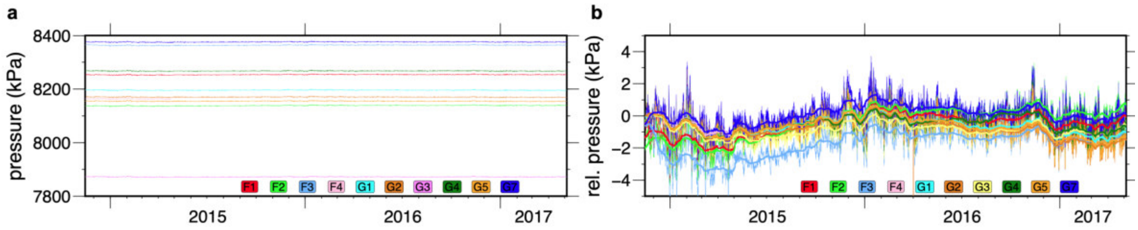

Figure 7.8: Pressure data. (a) Absolute pressure for all stations. (b) Relative pressure changes for all stations. For better visualization values were set to zero at the beginning of the experiment. Lines indicate monthly means. F2 measured a relative increase of approximately 1 kPa (equivalent to 10 cm water column change) relative to closeby station G5 which we interpret as most likely due to a systematic pressure drift of station F2. In general, the pressure sensors used are known to have a long term mean drift of 0.88 ± 0.73 kPa yr^{-1}. As a result, drift and the differences between the pressure measurements might all be explained with sensor drift. Resolution of pressure is around 10 Pa corresponding to an effective depth resolution of ~1 mm.

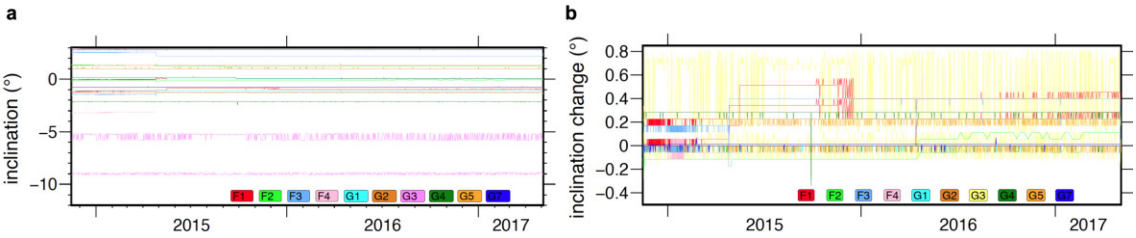

Figure 7.9: Inclinometer data. (a) Absolute inclinometer data of all stations documenting the stability of the transponders. Since the orientation of the sensors is not known, pitch and roll only relate to the instrument reference frame. (b) Relative inclination change. For better visualization values were set to zero at the beginning of the experiment. Station G3 is located on an inclined slope and has the largest forward- and backward tilt of maximal 0.8°. Most stations have tilt smaller than the amplitude resolution of the inclinometer of 0.057° which equals to a maximal 4 mm lateral movement of the top of a 4 m high structure. Station G3 (shown with yellow lines) is located on a slope and tilted by 8° shows variations of inclination of 0.23° which equals to a maximal 1.6 cm lateral movement of a vertical 4 m high structure.

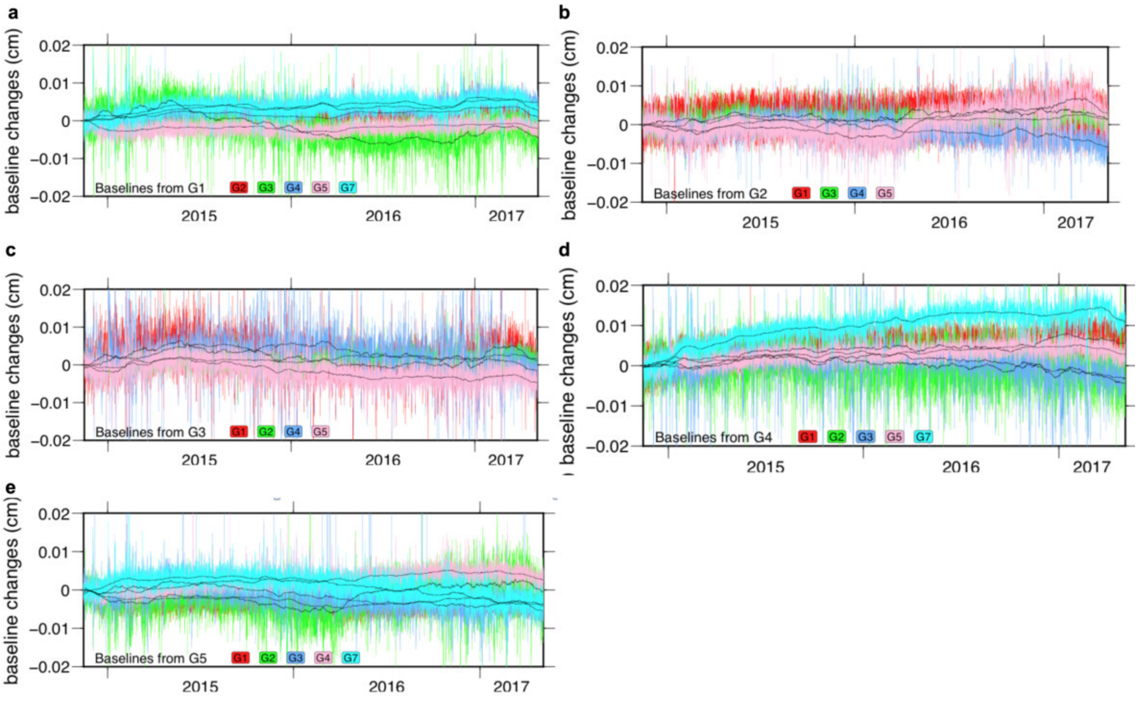

Figure 7.10: Baselines from one G-transponder to all others. Black lines indicate 14-days average (median). Due to different baseline lengths, absolute values are difficult to compare. Therefore, zero is set arbitrarily at the beginning of the experiment. As discussed in the text, the baselines were linearly de-trended using a strain rate of $1.8 \cdot 10^{-6}$ per year, corresponding to 1.8 mm baseline correction for a 1 km long baseline. Baselines of G4 after 19 November 2015 are based on the temperature measurements taken from F5 and are therefore not reliable (see discussion above).

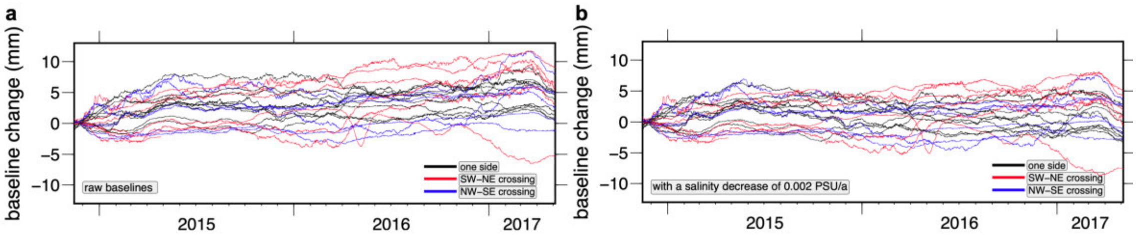

Figure 7.11: Baseline length changes. (a) Baselines for all stations calculated using the sound speed estimated from pressure, temperature and a constant salinity. The average baseline lengthening of 3.6 mm is likely originating from a linear salinity decrease at a rate of -0.002 PSU yr^{-1} resulting in apparent lengthening of baselines. See the main text for discussion about the linear correction. (b) Same as panel a, but after removing the mean strain of 4.5 - 6 (corresponding to a baseline decrease of 4.5 mm for a 1000 m long baseline during the deployment time) estimated from all baselines on one side of the fault. The baselines are measured in the direction of the curved acoustic ray traveling from one transponder to the other and therefore include the horizontal and vertical components of the length changes.

baseline	baseline length at end of deployment	baseline inclination	baseline drift from linear regression (raw data)	drift uncertainty from linear regression (raw data)	drift uncertainty (raw data)	strain (raw data)	baseline change at end of deployment (raw data)	Baseline change corrected for salinity change (Fig. 2)	Basline change rate corrected for salinity change (Fig. 2)
ID-ID	(m)	(°)	(mm)	(mm yr^{-1})	(mm yr^{-1})	(dimensionless)	(mm)	(mm)	(mm yr^{-1})
F2-F3	870.44	-1.20	3.225	0.006	0.008	5.62698E-06	4.9	1.00	0.415
F2-F4	499.18	0.50	-1.001	0.014	0.013	-1.05303E-05	-5.3	-7.49	-3.123
F3-F2	870.44	1.20	2.900	0.008	0.008	4.41075E-06	3.8	-0.06	-0.026
G1-G2	500.06	0.40	2.369	0.010	0.010	9.69793E-06	4.8	2.61	1.087
G1-G3	977.23	1.70	1.882	0.025	0.025	8.07988E-06	7.9	3.52	1.465
G1-G5	363.65	0.10	0.257	0.010	0.004	-3.33919E-06	-1.2	-2.84	-1.185
G1-G7	887.29	-1.20	3.038	0.012	0.012	6.63526E-06	5.9	1.91	0.796
G2-G1	500.06	-0.40	2.161	0.009	0.009	9.09449E-06	4.5	2.31	0.961
G2-G3	497.16	3.00	2.276	0.008	0.007	1.01783E-05	5.1	2.83	1.180
G2-G5	515.15	-0.30	3.359	0.024	0.028	6.05517E-06	3.1	0.81	0.338
G2-G7	1329.92	-0.90	3.113	0.024	0.024	4.01819E-06	5.3	-0.62	-0.257
G3-G1	977.24	-1.70	-0.670	0.028	0.025	2.19627E-06	2.1	-2.23	-0.931
G3-G2	497.16	-3.00	1.980	0.007	0.007	9.34042E-06	4.6	2.42	1.006
G3-G5	855.00	-1.90	-0.007	0.014	0.012	6.20012E-07	0.5	-3.30	-1.376
G3-G7	1717.88	-1.60	0.749	0.022	0.022	2.82349E-06	4.9	-2.85	-1.188
G5-G1	363.64	-0.10	1.400	0.008	0.013	1.09166E-06	0.4	-1.23	-0.514
G5-G2	515.16	0.30	4.590	0.025	0.020	1.25827E-05	6.5	4.17	1.739
G5-G3	855.00	1.90	0.464	0.014	0.012	1.56283E-06	1.3	-2.50	-1.040
G5-G7	863.08	-1.30	-0.503	0.017	0.014	9.48331E-07	0.8	-3.05	-1.271
G7-G1	887.29	1.20	3.886	0.012	0.012	1.02315E-05	9.1	5.10	2.125
G7-G5	863.09	1.30	0.158	0.019	0.017	2.2792E-06	2.0	-1.90	-0.792
mean	771.67	-0.10	1.697	0.015	0.014	4.45733E-06	3.4	-0.07	-0.028

Table 7.1: Details of estimated baselines, strains, and baseline drifts. Linear regression was done without the constant salinity decrease of 0.002 PSU/a.

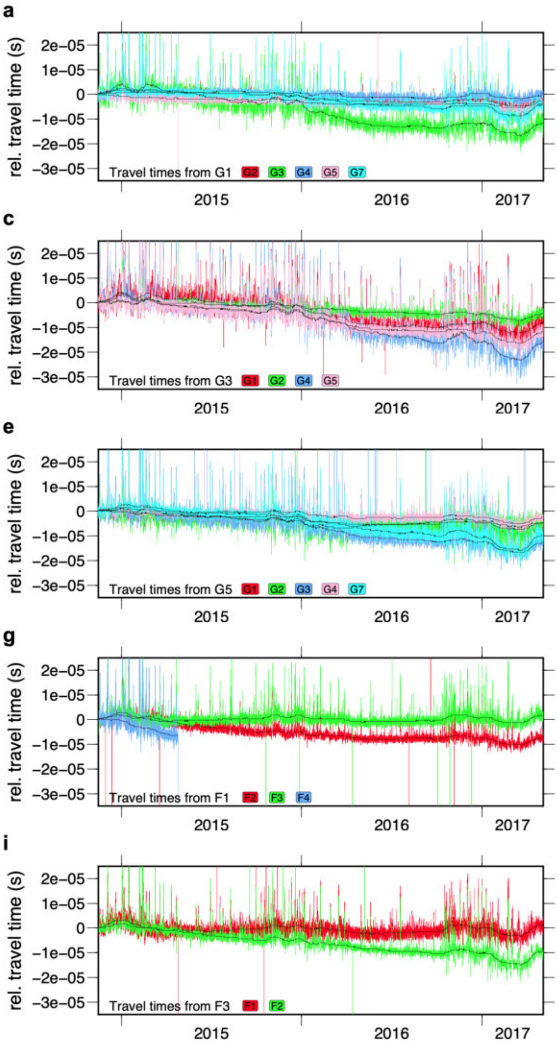

Figure 7.12: Measured travel times. Relative travel times for all baselines measured from one transponder to all others. Due to different baseline lengths, absolute values are difficult to compare. Therefore, zero is set arbitrarily at the beginning of the experiment. Transponder names are given in the bottom left.

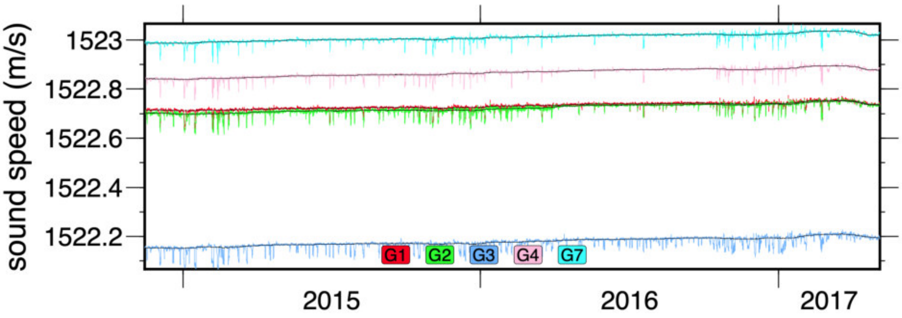

Figure 7.13: Estimated sound speed. Sound speed of water calculated from pressure, temperature and a constant salinity for all G-stations. Sound speed differs between stations due to different water depths.

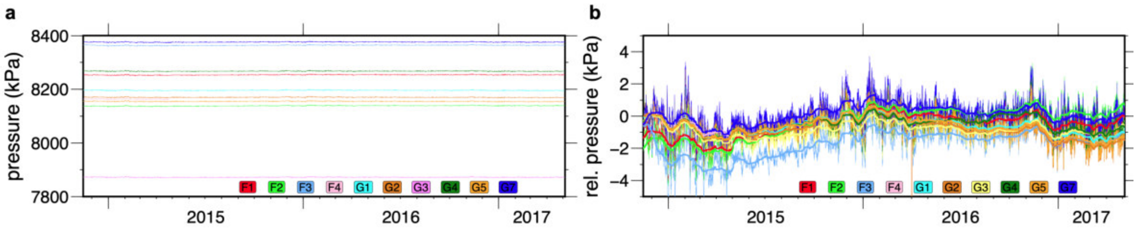

Figure 7.14: Station on the seafloor. Remotely Operated Vehicle (ROV) images showing transponder G3 (a) and F4 (b) on the seafloor. The photos were taken during the MARSITE cruise of research vessel Pourquois Pas? shortly after the installation on 2 November 2014. Frames are approximately 4 m high and the total weight under water of the G-transponders is 311 kg to support stability of the installation.

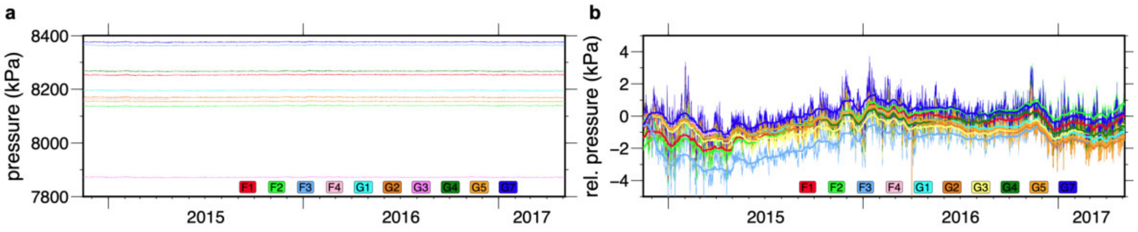

Figure 7.15: Seafloor image. ROV manipulator arm touching the seafloor. The seafloor in the area of the geodetic deployment consists of muddy sediments.

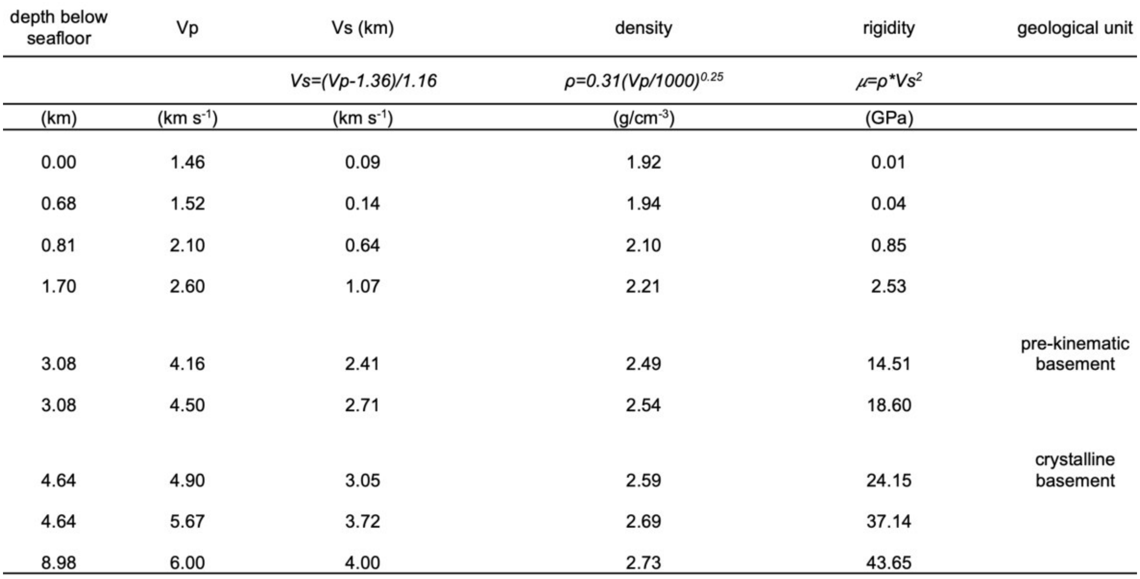

depth below seafloor	Vp	Vs (km)	density	rigidity	geological unit
		$Vs=(Vp-1.36)/1.16$	$\rho=0.31(Vp/1000)^{0.25}$	$\mu=\rho*Vs^2$	
(km)	(km s^{-1})	(km s^{-1})	(g/cm^{-3})	(GPa)	
0.00	1.46	0.09	1.92	0.01	
0.68	1.52	0.14	1.94	0.04	
0.81	2.10	0.64	2.10	0.85	
1.70	2.60	1.07	2.21	2.53	
3.08	4.16	2.41	2.49	14.51	pre-kinematic basement
3.08	4.50	2.71	2.54	18.60	
4.64	4.90	3.05	2.59	24.15	crystalline basement
4.64	5.67	3.72	2.69	37.14	
8.98	6.00	4.00	2.73	43.65	

Table 7.2: Rigidity estimate of sediment below the geodetic network. We used the seismic P-wave velocity (*vp*) profile and depth of geological units from seismic refraction observations located ~5 km south-west of the geodetic network (Bécel et al., 2010). Shear wave velocity (*vs*) was estimated using the empirical mudrock line line (Castagna et al., 1985) from vp velocities. Density was estimated using Gardner's empirical relation (Gardner et al., 1974) from vp and rigidity using the standard relation from density and *vs*. Because the empirical relations include significant uncertainties we used for the modelling rigidity ratio of 4 between the upper (weak) and lower (strong) layer and modelled the weak layer with 3 km and crystalline basement depth (Bécel et al., 2010).

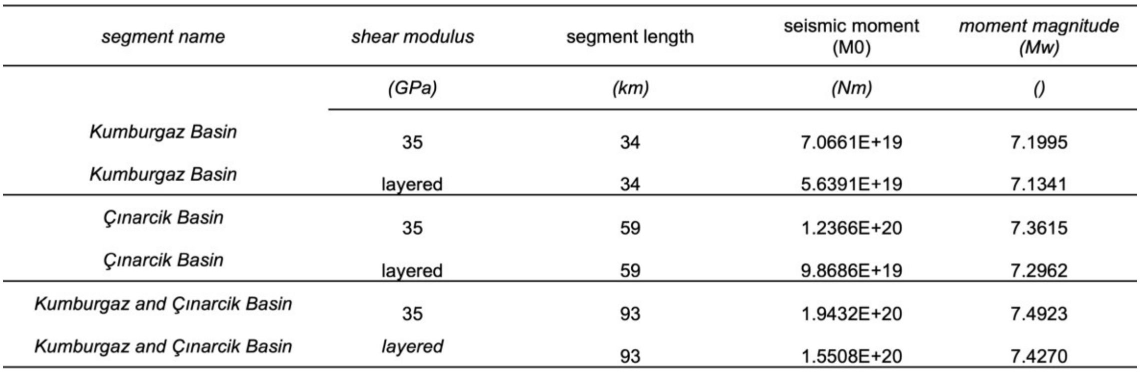

segment name	*shear modulus*	segment length	seismic moment (M0)	*moment magnitude (Mw)*
	(GPa)	*(km)*	*(Nm)*	*()*
Kumburgaz Basin	35	34	7.0661E+19	7.1995
Kumburgaz Basin	layered	34	5.6391E+19	7.1341
Çınarcik Basin	35	59	1.2366E+20	7.3615
Çınarcik Basin	layered	59	9.8686E+19	7.2962
Kumburgaz and Çınarcik Basin	35	93	1.9432E+20	7.4923
Kumburgaz and Çınarcik Basin	*layered*	93	1.5508E+20	7.4270

Table 7.3: Magnitude estimates for different scenarios. Accumulated seismic moment and moment magnitude estimates for the Kumburgaz and çınarcık Basin (Figure 7.1). We estimated the moment magnitude for constant shear modulus of 35 GPa and for rocks with increasing shear modulus with depth using the values from Supplementary Table 7.2. The seismic moment (Aki, 1966) was calculated for an accumulated slip of 4m and a fault locking depth of 15 km and converted to equivalent moment magnitude (Hanks and Kanamori, 1979). For the horizontally layered shear modulus scenario the seismic moment is 25 % smaller compared to a constant shear modulus of 35 GPa. The difference in moment magnitude is small (0.065 magnitude units) due to the logarithmic conversion from seismic moment to moment magnitude.

8 Gravitational Collapse of Mount Etna's south-eastern flank

Morelia Urlaub[1], **Florian Petersen**[1], Felix Gross[2], Alessandro Bonforte[3], Giuseppe Puglisi[3], Francesco Guglielmino[3], Sebastian Krastel[2], Dietrich Lange[1] and Heidrun Kopp[1,2]

1) GEOMAR Helmholtz Centre for Ocean Research Kiel, Kiel, Germany.
2) Institute of Geosciences, Kiel University, Kiel, Germany.
2) Istituto Nazionale di Geofisica e Vulcanologia, Sezione di Catania, Osservatorio Etneo, Catania, Italy

Published in **Science Advances**, October 2018.

DOI: 10.1126/sciadv.aat9700

Abstract

The southeastern flank of Etna volcano slides into the Ionian Sea at rates of centimeters per year. The prevailing understanding is that pressurization of the magmatic system, and not gravitational forces, controls flank movement, although this has also been proposed. So far, it has not been possible to separate between these processes, because no data on offshore deformation were available until we conducted the first long-term seafloor displacement monitoring campaign from April 2016 until July 2017. Unprecedented seafloor geodetic data reveal a > 4 cm slip along the offshore extension of a fault related to flank kinematics during one 8-day-long event in May 2017, while displacement on land peaked at ~4 cm at the coast. As deformation increases away from the magmatic system, the bulk of Mount Etna's present continuous deformation must be driven by gravity while being further destabilized by magma dynamics. We cannot exclude flank movement to evolve into catastrophic collapse, implying that Etna's flank movement poses a much greater hazard than previously thought. The hazard of flank collapse might be underestimated at other coastal and ocean island volcanoes, where the dynamics of submerged flanks are unknown.

8.1 Introduction

Volcanic flanks can slide in response to various internal and external forces. For example, the unbalanced weight distribution of a volcanic edifice and horizontal "pushing" due to magmatic intrusions can trigger flank spreading. Unstable flanks can fail catastrophically and result in giant landslides, such as those at the submarine slopes off Hawaii (Moore et al., 1989; Morgan et al., 2000; Denlinger and Morgan, 2014). Catastrophic collapses of ocean island volcanoes or those built at the shoreline pose the largest threat as the sudden dis placement of large amounts of material in water can trigger tsunamis with extreme effects (Keating and McGuire, 2000; Ramalho et al., 2015). Assessing the hazard potential of cata strophic collapse requires a profound understanding of the mecha nisms that cause flank movement, which is also crucial for the design of appropriate monitoring strategies.

Numerous hypotheses have been proposed to explain flank sliding at Mount Etna, including increases in magma pressure (Lundgren et al., 2004), eruptive activity (Acocella et al., 2003), repeated dyke intrusions (Bruno et al., 2017), basement uplift (Stewart et al., 1993), gravita tional spreading (Borgia et al., 1992), gravitational reorganization (Merle and Borgia, 1996), gravity driven instability accelerated by inflation and/or lateral intrusions (Bonforte et al., 2008), or combined magmatic inflation and continental margin in stability (Chiocci et al., 2011). All hypotheses are derivatives of two basic processes capable of triggering flank instability: horizontal pushing of ascending magmatic intrusions or gravitational pull. These endmember mechanisms have fundamentally different hazard implications: While magma dynamics can trigger slope failures near the magma path ways (Bonforte and Guglielmino, 2015), gradual deepseated gravitational deformation can induce catastrophic collapse as in the cases of Mombacho (van Wyk de Vries and Francis, 1997), Kilauea ((Morgan et al., 2000), other Hawaiian volcanoes (Denlinger and Morgan, 2014), and Ritter Island, Papua New Guinea (Karstens et al., 2019). The overall consensus for Etna has been that it is mainly the magnetic plumbing system that drives movement of the unstable southeastern flank, rather than gravitational or tectonic forces.

Uncertainties regarding the causes of flank sliding originate from the lack of information on the dynamics of the submarine part of Etna volcano. Onshore geodetic measurements have documented largescale continuous seaward motion at an average rate of 3 to 5 cm per year since the early 1980s (Hutton and Boore, 1987; Patanè et al., 2003; Bonforte et al., 2011; Bruno et al., 2017), immediately evidencing the highest rates at the coast (Houlié et al., 2006; Jokat et al., 2008). However, no information on the movement of the submarine part of the flank existed before this study. Here, we document rapid deformation of Etna's offshore flank and combine the offshore measurements with onshore ground deformation. Our combined onshoreoffshore data define the dynamics of the entire volcanic flank.

8.2 Seafloor displacement measurements at Etna's submerged flank

Established satellitebased geodetic tools are not adaptable for use in the marine environment due to the opacity of seawater to electro magnetic waves. Underwater, distances can be estimated with the sound speed of water and travel time measurements between tran sponders on the seafloor. Periodic backandforth acoustic interro gations between several transponders equipped with absolute pressure sensors and arranged in a network allow continuous determination of seafloor displacement in horizontal and vertical directions within the network (Brooks et al., 2011; McGuire and Collins, 2013; Bürgmann and Chadwell, 2014). A network of five such transponders was placed on both sides of the submerged southern boundary of Etna's unstable flank (Gross et al., 2016) at a water depth of ~1200 m. Changes in distance between transponders across the fault and increases in pressure at transponders to the north of the fault indicate movement of the presumed unstable flank relative to the stable surrounding. Our seafloor network is the first to monitor an offshore strikeslip event in subcentimeter reso lution, therewith proving the feasibility of the emerging acoustic direct path ranging method to monitor volcanic flank instability.

On land, the spatial outline of the unstable flank is well defined by geodetic, geophysical, and geological methods (Figure 8.1): Along the northern boundary of the unstable flank, deformation focuses along the leftlateral Pernicana fault (Bonforte et al., 2011). To the south, the rightlateral Tremestieri and Acitrezza (ATF) fault systems accommodate most of the flank movement (Bonforte et al., 2011; Wang et al., 2011). Off the coast, the Riposto Ridge forms the prolongation of the northern boundary. In distal direction, two anticlines observed in seismic reflection data mark the seaward termination of the unstable volcanic flank (Figure 8.1) (Gross et al., 2016). To the south, a rightlateral transpressive fault north of Catania Canyon, interpreted as the offshore prolongation of onshore fault systems, represents the southern boundary of the unstable flank (Chiocci et al., 2011; Gross et al., 2016).

This fault is a pronounced westeast striking feature in the bathymetry (Figures 8.1 and 8.2C). Seismic data indicate distinct reflection characteristics on either side of the fault (Figure 8.5) (Gross et al., 2016). On the basis of these observations, we deployed transponders 1 and 4 south of the fault and transponders 2, 3, and 5 north of the fault (Figure 8.2C). All transponders were in line of sight of each other, resulting in 10 base lines with distances between 144 and 1254 m. All transponders monitored distances to all other transponders and pressures every 90 min. Periodic data upload via an acoustic link provided a continuous time series from April 2016 to July 2017.

8.3 Material and Methods

8.3.1 Bathymetry

Bathymetric data were acquired during research vessel (RV) Meteor expedition M86/2 in 2012 with hullmounted Kongsberg Simrad EM122 and EM710 multibeam sounders. Standard data processing with MBSystem produced a grid with a cell size of 30 m by 30 m. Coastal bathymetry was acquired in the framework of the MaGIC (Marine Geohazards along the Italian Coast) project (Chiocci and Ridente, 2011).

8.3.2 Seafloor geodesy

The direct-path acoustic ranging method provides relative positioning by using high precision acoustic transponders (Sonardyne Autonomous Monitoring Transponders, AMT). Multiple transponders installed at the seafloor measure the time of flight of acoustic signals between them with a microsecond resolution and water sound speed, temperature, and absolute pressure. Travel time observations were converted into distances with millimetric precision. Pressure measurements provided information on vertical displacement. Dual axis inclinometers detected changes in instrument tilt. Repeated interrogations over

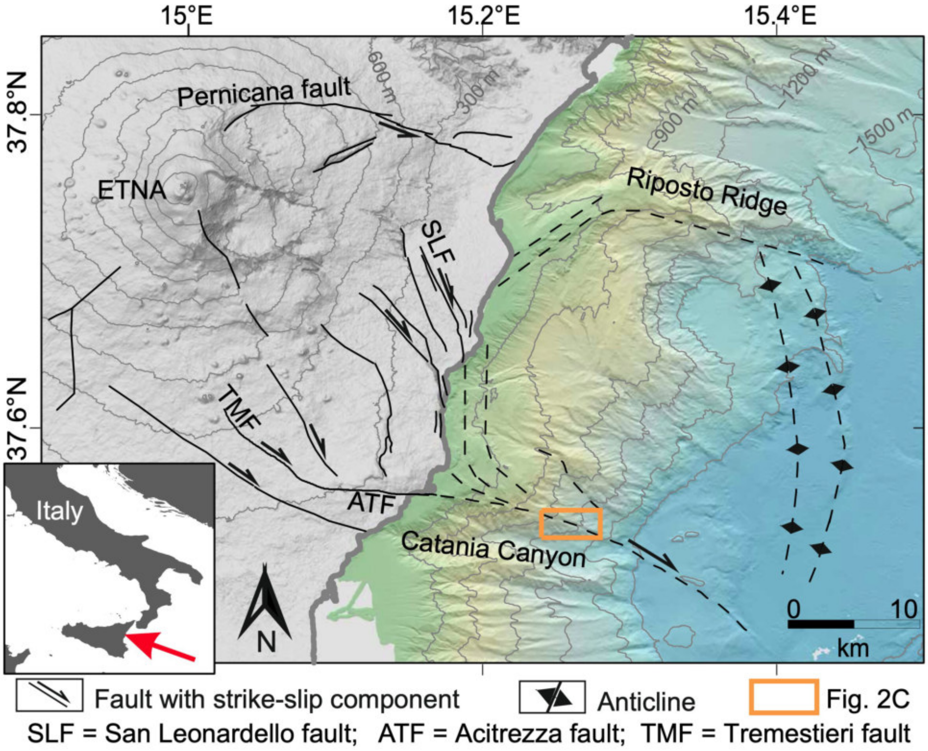

Figure 8.1: Morphologic map of Mount Etna including tectonic features of the southeastern flank. Onshore topography in gray and offshore bathymetry in green to blue colors. Contour line interval is 300 m. Main features are shown as dashed (Gross et al., 2016) and solid (Barreca et al., 2013) black lines. The thick gray line delineates the coastline. The orange rectangle marks the location of the seafloor geodetic network.

months to years allowed the determination of displacements and, hence, deformation of the seafloor inside the network for extended periods, depending on battery capacity.

Here, we used five transponders from GEOMAR's GeoSEA array. The transponders communicated with 8 ms phasecodes pulses and an 8 kHz bandwidth with a centered frequency of 18 kHz. The acoustic ranges were calculated by crosscorrelation of the interrogation and receiving signals. The AMTs logged pressure, temperature, tilt, and sound speed. The log period for each transponder was set to 90 min. We noted instability in the sound speed measurement and recalculated the sound speed using the highresolution tempera ture and pressure measurements at each transponder and assum ing a constant salinity of 34 practical salinity units (Leroy et al., 2008). We removed the tide signals from the pressure data using the data provided by the Istituto Superiore per la Protezione e la Ricerca Ambientale tide gauge in the port of Catania (`www.mareografico.it`). Pressure was converted to depth with the seawater density of 1024 kg/m (Denlinger and Morgan, 2014). For better com parison to the relative distance measurements obtained by acoustic telemetry, and because we are mostly interested in the relative move ment of the unstable sector compared to the stable sector, we only showed relative vertical displacement between transponder pairs. These were obtained by subtracting the time series recorded by one transponder from that of another transponder.

The autonomous monitoring transponders were located at the outcrop of a fault at the seafloor. Locations for individual transponders were chosen on the basis of a closely spaced highresolution two dimensional (2D) seismic survey and swath bathymetric data. The network design ensures that at least two AMTs sit at each side of the fault and are in acoustic sight of each other. The AMTs were mounted on anchored buoyancy bodies. The deployed trapezeshaped setup results in 10 monitored baselines. Besides transponder 1, all baselines were recorded in two directions (forward and backward measure ments), resulting in six bidirectional baselines and four unidirec tional baselines. Distances for forward (for example, measuring the travel time from AMT 1 to 2 and return) and backward measurements (measuring from AMT 2 to 1 and return) closely agree for all transponder pairs.

We deployed the transponders in April 2016 during *RV Poseidon* expedition POS496 at meter precision using ultrashort baseline acoustic positioning in water depths of 950 to 1180 m. Data stored in each sta tion were uploaded from the seafloor to the surface with an acoustic modem.

8.3.3 Onshore geodesy

We processed and integrated the onshore data covering the same period as the offshore data acquisitions to compare the results and extend the information about the deformation measured by the sea floor network. GPS data collected during the first week of April 2016 and the last week of July 2017 were processed separately by using the usual approach adopted for geodetic surveys (Barreca et al., 2013) to obtain the most precise coordinates of each station at the two periods. Thus, the 3D displacements at the GPS stations from April 2016 to July 2017 were obtained by comparing the two sets of coordinates.

The Sentinel-1A ascending (31 March 2016 and 30 July 2017) and descending (6 April 2016 and 30 July 2017) data were processed by GAMMA software, using the socalled twopass interferome try (Massonnet and Feigl, 1998) to generate the interferometric products. A spectral diversity method was used to coregister the Sentinel-1 pairs to obtain an extremely high precision (< 0.01 pixel). The result of this processing is the ground displacement along the Line Of Sight (LOS) across the entire area. To derive the 3D surface motion maps, we integrated GPS and DInSAR displacements by applying the SISTEM method (Guglielmino et al., 2011). A linear matrix equation accounts for both GPS and DInSAR data, the solution of which provides the strain tensor, the displacement field, and the rigid body rotation tensor throughout the entire investigated area.

8.4 Results

For most parts of the observation period, acoustic distances between transponders remained stable within approximately 0.5 cm (Figure 8.2 and Figure 8.6). However, a significant change in distances occurred be tween 12 and 20 May 2017.Only baselines across the fault recorded the 8daylong aseismic fault motion that stands out from the back ground noise (Figure 8.1 Figure 8.6). Relative distance changes during the May 2017 event ranged between 0.6 and −3.9 cm for different transponder pairs (Table 8.1, Figure 8.2, and Figure 8.6). As expected for a dextral strikeslip fault, length changes are dependent on the angle of the baseline to the fault (Figure 8.7). This angle can be used to deter mine true fault slip. The main uncertainty in slip results from the lack of knowledge of the exact fault trace on the seafloor. The ranging data confirm that the fault trace must run in the very narrow corridor between transponders 1 and 3 (Figure 8.2C) within a range of 5°. Taking into account all fault crossing baselines, the true slip is between 3.87 and 4.23 cm (Table 8.1). We also observe that transponders on the north side of the fault showed a downward vertical displacement of 1 cm relative to those on the south side during the May 2017 event (Figure 8.2 and Figure 8.8).

Overall, no significant changes in distances or depths occurred between transponders that were located on the same fault side (Figure 8.2 and Figures 8.6 to 8.8). We exclude the possibility of a local land slide coherently moving these transponders based on the lack of evidence for soft sediments in seismic and sediment echosounder data, as well as in seafloor samples. The observed distance changes are in all aspects consistent with right-lateral strikeslip movement sep arating transponders 2, 3, and 5 from transponders 1 and 4 (Figure 8.2C).

Notably, the observed length change in the network of ~4 cm provides a minimum estimate of the true slip along the fault during the May 2017 event. The gross motion of the unstable flank might not have been fully captured, leading to a potential underestimation of slip. The southern boundary fault splits into several branches to ward the seafloor, as imaged in seismic data (Figure 8.5) (Gross et al., 2016). The network of transponders, however, does not span over all fault branches. Branches out of the reach of our network may have also accommo dated flank movement during the investigated time period.

A slip of 4 cm corresponds to a moment magnitude release equivalent to a M_w of 4.3 to 5.3 earthquake (Hanks and Kanamori, 1979). Since the initiation of instrumental seismic recording at Etna in the 1980s, no earthquake with a magnitude larger than 4 has been observed in the area (Alparone et al., 2013). Hence, the main style of deformation of the offshore volcanic flank is episodic and aseismic sliding rather than seismic rupture.

8.5 Overall flank dynamics

Our offshore observations show that the submarine part of Mount Etna's southeastern flank moves in east and downward direction with a minimum aseismic fault slip of at least 4 and 1 cm relative subsidence, respectively (Figure 8.2). The total slip may be even larger as not all fault branches could be captured by the seafloor network (Figure 8.5). Onshore, the seaward flank motion at Etna in the observation period April 2016 to July 2017 manifested in continuous deformation (Figure 8.12) rather than in episodic slip, as observed offshore. Cumulative displacements were highest along the coast (Figure 8.3). SISTEM (simultaneous and integrated strain tensor estimation from geodetic and satellite deformation measurements) integration of GPS (Figure 8.9) and DInSAR (Differential Interferometry Synthetic Aperture Radar) (Figure 8.10) data (Guglielmino et al., 2011) shows that flank movement mainly occurred across the ATF and San Leonardello fault (Figure 8.3 and Figure 8.11) with a maximum slip of ~2 cm along each fault. The offshore flank movement was thus in the same order of magnitude as the sum of onshore fault slips for identical periods of time. Therefore, the offshore fault probably cumulated the slip of both the ATF and San Leonardello fault.

Gross onshore and offshore movements are kinematically consistent (Fig 8.4) and, therefore, are expressions of the same underlying process related to flank instability. The observed differences in fault slip mode during the observation period, i.e., continuous creep onshore and slow slip offshore, can result from variations in fault properties, such as temperature, fluid pressure, or fault gouge material (Scholz, 2018), while still representing the same overall dynamics. Nevertheless, onshore deformation at Etna's unstable flank also manifests in slow slip events along the coastline, as monitored by continuous GPS (Bruno et al., 2017).

8.6 Discussion

Reasons for instability of Mount Etna's southeastern flank have been related either to the volcano's magmatic plumbing system or to gravitational forces. Displacement induced by magma injection strongly decays with distance to the dyke (Elsworth and Voight, 1995). Inflation of the volcanic edifice caused by uprising magma is expected to cause the highest

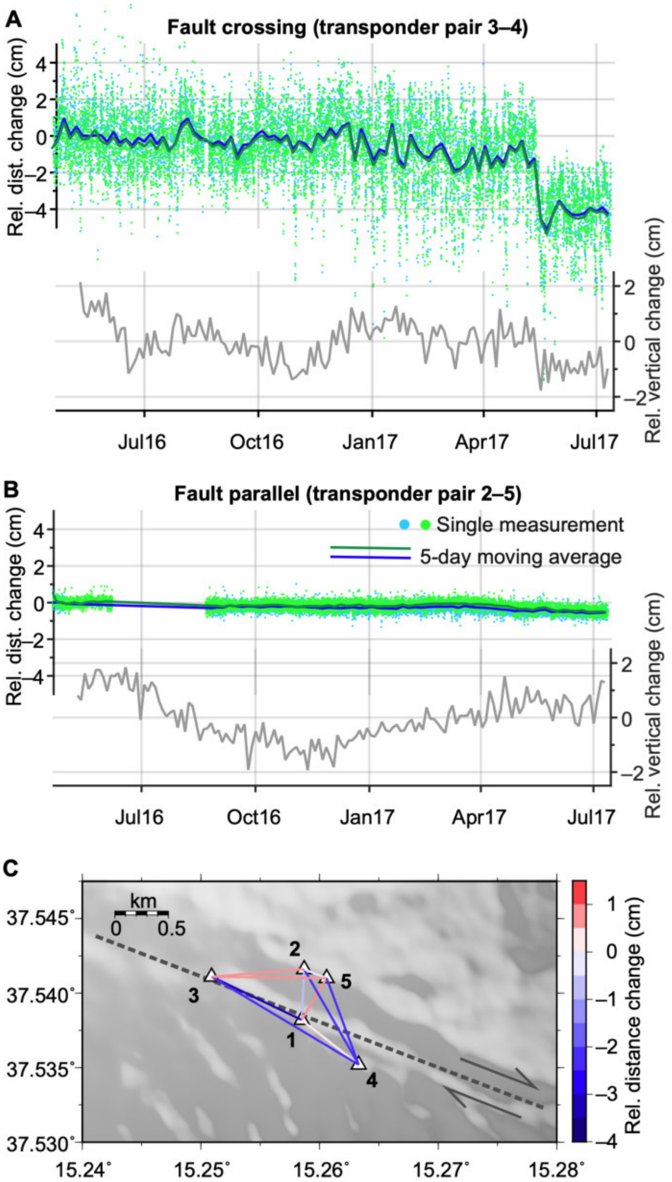

Figure 8.2: Seafloor deformation across the fault that marks the offshore southern boundary of Mount Etna's unstable flank, as recorded by the network of five autonomous monitoring transponders. (A and B) Relative changes in distances between transponder pairs (blue and green colors indicate active interrogation and passive response of acoustic signals, respectively) and relative vertical displacement between transponder pairs (gray line, 3-day moving average). Time series for all other transponder pairs are shown in Figures 8.6 and 8.7. (C) Map view of relative distance changes within the array during the observation period plotted on gray-shaded bathymetry (see Figure 8.1 for location). Black numbers indicate transponder numbers.

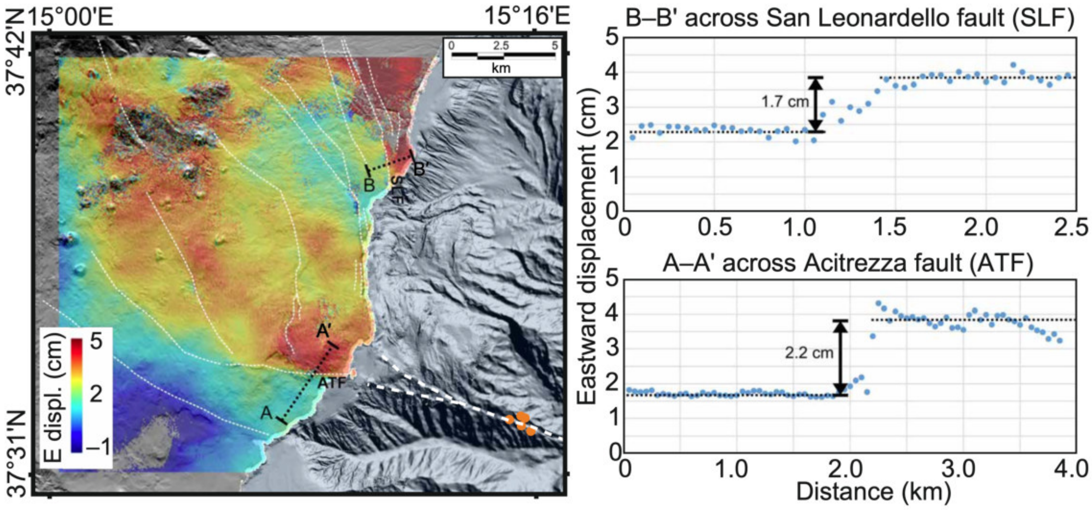

Figure 8.3: Eastward displacement of the southeastern flank of Mount Etna from April 2016 to July 2017. The map is obtained by integrating GPS and InSAR analysis using the SISTEM method (Guglielmino et al., 2011). White dashed lines show principal faults. Dots show locations of the seafloor geodetic transponders.

displacements near the volcanic center, which is inconsistent with our data. In contrast, our geodetic measurements demonstrated that flank movement increases away from the summit toward the coast and into the Ionian Sea, while no increase in magma activity was noticed simultaneous to the May 2017 offshore event, implying that magma dynamics cannot be solely responsible for the observed deformation pattern. The comparison of onshore and offshore fault slip further suggests that offshore deformation focuses along one fault north of Catania Canyon and that strain is partitioned near the coast into two fault systems (Figure 8.4). The observations of (i) largest deformation away from and (ii) strain partitioning toward the summit indicate that the basal shear zone accommodating flankmovement began offshore and has developed retrogressively landward. Therefore, the forcing mechanism that controls the bulk of Mount Etna's flank movement must have its origin seaward and is separated from the volcanic edifice. Gravitational pull of the subsiding continental margin is a potential tectonic trigger (Bonforte et al., 2011).

Yet, magmatic activity also influences flank movement as episodic accelerations of onshore flank movement have been related to dyke intrusions and magma ascent repeatedly (Bonforte et al., 2013; Bruno et al., 2017). Analyses of onshore seismic and ground deformation data show a clear decoupling of the shallow and deep strain regimes beneath the eastern flank at a depth of 2 km during an inflation period (Alparone et al., 2011). Inflation and dyke intrusions can thus favor episodic accelerations of flank movement in addition to largescale continuous gravitational sliding. Both processes may well interact with and influence each other, as demon strated by analog models (Le Corvec et al., 2014).

Crossing baseline	Baseline length (m)	Length change (cm)	1 - σ (cm)	α_1 (°)	α_2 (°)	α_{mean} (°)	Slip$_1$ (cm)	Slip$_2$ (cm)	Mean Slip (cm)
1–2	368.357	1.09	0.55	67.2	72.2	69.7	2.82	3.57	3.15
2–4	804.192	3.32	0.83	34.4	39.4	36.9	4.02	4.30	4.15
4–5	688.623	2.88	0.66	43.6	48.6	46.1	3.98	4.36	4.16
1–5	350.719	0.62	0.51	94.9	99.9	97.4	7.22	3.59	4.79
3–4	1253.642	3.46	1.54	5.5	10.5	8.0	3.47	3.51	3.49
1–3	699.045	3.86	1.61	0.5	5.5	3.0	3.86	3.87	3.86
						Mean slip:	**4.23**	**3.87**	**3.93**

Table 8.1: Morphologic map of Mount Etna including tectonic features of the southeastern flank. Onshore topography in gray and offshore bathymetry in green to blue colors. Contour line interval is 300 m. Main features are shown as dashed (Gross et al., 2016) and solid (Barreca et al., 2013) black lines. The thick gray line delineates the coastline. The orange rectangle marks the location of the seafloor geodetic network.

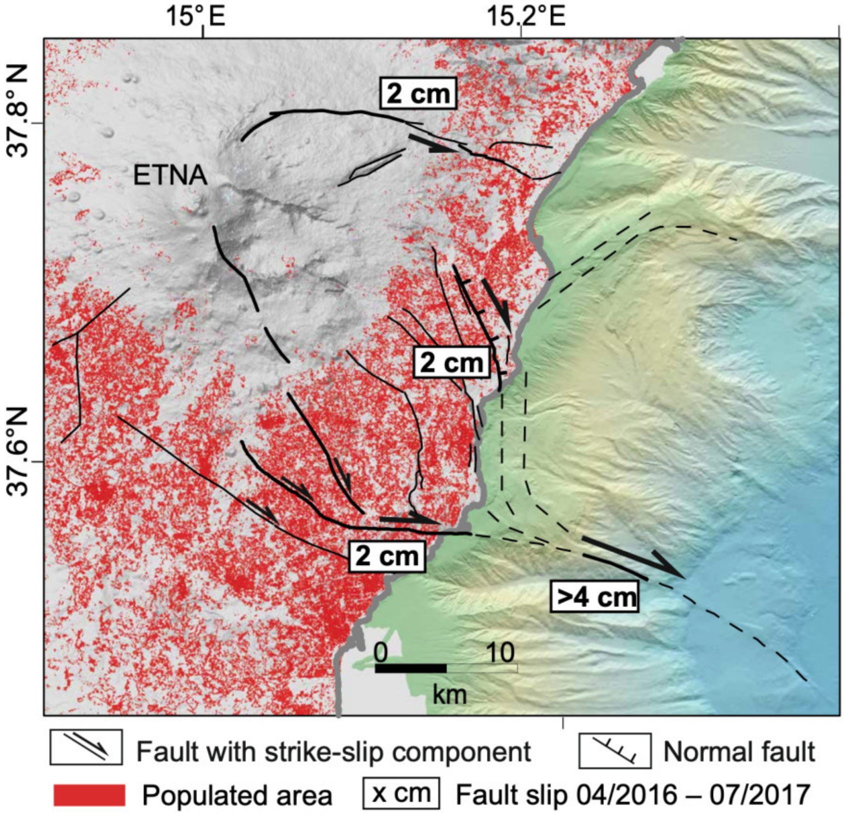

Figure 8.4: Populated areas are obtained from a Landsat-8 classification on a 30 m by 30 m grid (Landsat-8 image courtesy of the U.S. Geological Survey). Bold lines represent main active features during the observation period.

Marine geological records off the Canary Islands document that largescale submarine flank failures occurred in multiple stages, all preceding explosive eruptions (Hunt et al., 2018). A similar pattern is recorded in sediment cores at Etna's submerged flank, where ash layers overlie landslide deposits (Gross et al., 2014). These observations further support a close interaction of flank movement and magmatic activity. However, eruptions do not trigger catastrophic flank collapses, implying that gravitational sliding is the governing process.

Our results show that only the combination of onshore and off shore ground deformation data gives a clear picture of overall volcano flank dynamics, from which the hazard of catastrophic flank collapse can be assessed. In the case of Mount Etna, our shoreline crossing deformation analysis implies a greater hazard for flank collapse than previously assumed, as deepseated gravitational sliding can potentially lead to catastrophic collapse (Morgan et al., 2000; Denlinger and Morgan, 2014; Karstens et al., 2019). Onshore ground deformation analyses reveal signs of ongoing flank instability at numerous coastal and ocean island volcanoes today (Poland et al., 2017). Volcanoes, including those in Hawaii, the Canary Islands, and La Réunion, are potentially liable to collapse, but shoreline-crossing ground defor mation analyses are needed to obtain a comprehensive view of the dynamics and constrain the hazard. Our results demonstrate both that seafloor geodetic investigations are capable of characterizing the dynamics of submerged volcanic flanks and that such investigations provide deformation data at a resolution comparable to GPS.

Acknowledgments

We thank the captains, crews, and scientific parties of the cruises POS496, POS515, and Tethys-II (CRACK) for deployment of seafloor instruments and recovery of the data set. We also thank the INGV researchers and technicians for maintaining the GPS monitoring network and data and C. Hammersley and T. Bennetts from Sonardyne for technical support related to the AMTs. We thank C. Berndt and J. Geersen for discussions. Seafloor geodetic stations were positioned using the procedure patented under *DE 102016107558 A1 2017.10.26*.

Funding

The GeoSEA Array is funded through grant 03F0658I of the BMBF (German Federal Ministry of Education and Research). Part of this work was funded by grant CP1635 of the Cluster of Excellence 80 “The Future Ocean.” The Future Ocean is funded within the framework of the Excellence Initiative by the Deutsche Forschungsgemeinschaft on behalf of the German federal and state governments.

Author contributions

M.U., F. Gross, and G.P. were responsible for the conception of this study. H.K., D.L., M.U., and F.P. are responsible for the design of the seafloor network and formal data analysis. F.P., F. Gross, and S.K. participated in the acquisition of marine data. A.B., F. Guglielmino, and G.P. formally analyzed the onshore data. M.U., F.P., F. Gross, A.B., and G.P. interpreted the data. M.U. drafted and prepared the article, and all authors critically reviewed it.

Competing interests

D.L., H.K., and F.P. are inventors on a patent related to this work (no. DE 10 2016 107 558.2, filed on 22 April 2016, published on 26 October 2017). All other authors declare that they have no competing interests.

Data and materials availability

The seafloor geodetic data are archived in the World Data Center PANGAEA and can be accessed under `doi.pangaea.de/10.1594/PANGAEA.893036`. Copernicus Sentinel-1 data (2016 – 2017) are available at the Copernicus Open Access Hub (`https://scihub.copernicus.eu`). All data needed to evaluate the conclusions in the paper are present in the paper and/or the Supplementary Materials. Additional data related to this paper may be requested from the authors.

References

Acocella, V., Behncke, B., Neri, M., & D'Amico, S. (2003). Link between major flank slip and 2002-2003 eruption at mt. etna (italy). *Geophysical Research Letters*, *30*(24), `https://doi.org/10.1029/2003gl018642`.

Alparone, S., Barberi, G., Bonforte, A., Maiolino, V., & Ursino, A. (2011). Evidence of multiple strain fields beneath the eastern flank of mt. etna volcano (sicily, italy) deduced from seismic and geodetic data during 2003–2004. *Bulletin of Volcanology*, *73*(7), 869–885, `https://doi.org/10.1007/s00445-011-0456-1`.

Alparone, S., Bonaccorso, A., Bonforte, A., & Currenti, G. (2013). Long-term stress-strain analysis of volcano flank instability: The eastern sector of etna from 1980 to 2012. *Journal of Geophysical Research: Solid Earth*, *118*(9), 5098–5108, `https://doi.org/10.1002/jgrb.50364`.

Barreca, G., Bonforte, A., & Neri, M. (2013). A pilot gis database of active faults of mt. etna (sicily): A tool for integrated hazard evaluation. *Journal of Volcanology and Geothermal Research*, *251*, 170–186, `https://doi.org/10.1016/j.jvolgeores.2012.08.013`.

Bonforte, A., Bonaccorso, A., Guglielmino, F., Palano, M., & Puglisi, G. (2008). Feeding system and magma storage beneath mt. etna as revealed by recent inflation/deflation cycles. *Journal of Geophysical Research*, *113*(B5), `https://doi.org/10.1029/2007jb005334`.

Bonforte, A. & Guglielmino, F. (2015). Very shallow dyke intrusion and potential slope failure imaged by ground deformation: The 28 december 2014 eruption on mount etna. *Geophysical Research Letters*, *42*(8), 2727–2733, `https://doi.org/10.1002/2015gl063462`.

Bonforte, A., Guglielmino, F., Coltelli, M., Ferretti, A., & Puglisi, G. (2011). Structural assessment of mount etna volcano from permanent scatterers analysis. *Geochemistry, Geophysics, Geosystems*, *12*(2), `https://doi.org/10.1029/2010gc003213`.

Bonforte, A., Guglielmino, F., & Puglisi, G. (2013). Interaction between magma intrusion and flank dynamics at mt. etna in 2008, imaged by integrated dense gps and dinsar data. *Geochemistry, Geophysics, Geosystems*, *14*(8), 2818–2835, `https://doi.org/10.1002/ggge.20190`.

Borgia, A., Ferrari, L., & Pasquarè, G. (1992). Importance of gravitational spreading in the tectonic and volcanic evolution of mount etna. *Nature*, *357*(6375), 231–235, `https://doi.org/10.1038/357231a0`.

Brooks, B. A., Foster, J. H., McGuire, J. J., & Behn, M. (2011). *Submarine Landslides and Slow Earthquakes: Monitoring Motion with GPS and Seafloor Geodesy*, book section Chapter 48, (pp. 889–907).

Bruno, V., Mattia, M., Montgomery-Brown, E., Rossi, M., & Scandura, D. (2017). Inflation leading to a slow slip event and volcanic unrest at mount etna in 2016: Insights from cgps data. *Geophysical Research Letters*, *44*(24), `https://doi.org/10.1002/2017gl075744`.

Bürgmann, R. & Chadwell, D. (2014). Seafloor geodesy. *Annual Review of Earth and Planetary Sciences*, *42*(1), 509–534, `https://doi.org/10.1146/annurev-earth-060313-054953`.

Chiocci, F. L., Coltelli, M., Bosman, A., & Cavallaro, D. (2011). Continental margin large-scale instability controlling the flank sliding of etna volcano. *Earth and Planetary Science Letters*, *305*(1-2), 57–64, `https://doi.org/10.1016/j.epsl.2011.02.040`.

Chiocci, F. L. & Ridente, D. (2011). Regional-scale seafloor mapping and geohazard assessment. the experience from the italian project magic (marine geohazards along the italian coasts). *Marine Geophysical Research*, *32*(1-2), 13–23, `https://doi.org/10.1007/s11001-011-9120-6`.

Denlinger, R. P. & Morgan, J. K. (2014). *Instability of Hawaiian volcanoes, in Characteristics of Hawaiian Volcanoes.* Professional Paper 1801. U.S. Geological Survey,.

Elsworth, D. & Voight, B. (1995). Dike intrusion as a trigger for large earthquakes and the failure of volcano flanks. *Journal of Geophysical Research: Solid Earth*, *100*(B4), 6005–6024, `https://doi.org/10.1029/94jb02884`.

Gross, F., Krastel, S., Chiocci, F. L., Ridente, D., Bialas, J., Schwab, J., Beier, J., Cukur, D., & Winkelmann, D. (2014). Evidence for submarine landslides offshore mt. etna, italy. *Advances in Natural and Technological Hazards Research*, *37*, `https://doi.org/10.1007/978-3-319-00972-8`.

Gross, F., Krastel, S., Geersen, J., Behrmann, J. H., Ridente, D., Chiocci, F. L., Bialas, J., Papenberg, C., Cukur, D., Urlaub, M., & Micallef, A. (2016). The limits of seaward spreading and slope instability at the continental margin offshore mt etna, imaged by high-resolution 2d seismic data. *Tectonophysics*, *667*, 63–76, `https://doi.org/10.1016/j.tecto.2015.11.011`.

Guglielmino, F., Bignami, C., Bonforte, A., Briole, P., Obrizzo, F., Puglisi, G., Stramondo, S., & Wegmüller, U. (2011). Analysis of satellite and in situ ground deformation data integrated by the sistem approach: The april 3, 2010 earthquake along the pernicana fault (mt. etna - italy) case study. *Earth and Planetary Science Letters*, *312*(3-4), 327–336, `https://doi.org/10.1016/j.epsl.2011.10.028`.

Hanks, T. C. & Kanamori, H. (1979). A moment magnitude scale. *Journal of Geophysical Research*, *84*(B5), `https://doi.org/10.1029/JB084iB05p02348`.

Houlié, N., Briole, P., Bonforte, A., & Puglisi, G. (2006). Large scale ground deformation of etna observed by gps between 1994 and 2001. *Geophysical Research Letters*, *33*(2), `https://doi.org/10.1029/2005gl024414`.

Hunt, J. E., Cassidy, M., & Talling, P. J. (2018). Multi-stage volcanic island flank collapses with coeval explosive caldera-forming eruptions. *Sci Rep*, *8*(1), 1146, `https://doi.org/10.1038/s41598-018-19285-2`.

Hutton, L. K. & Boore, D. M. (1987). The ml scale in southern california. *Bulletin of the Seismological Society of America*, *77*(6), 2074–2094.

Ide, S., Beroza, G. C., Shelly, D. R., & Uchide, T. (2007). A scaling law for slow earthquakes. *Nature*, *447*(7140), 76–9, `https://doi.org/10.1038/nature05780`.

Jokat, W., Geissler, W., & Voss, M. (2008). Basement structure of the north-western yermak plateau. *Geophysical Research Letters*, *35*(5), `https://doi.org/10.1029/2007gl032892`.

Karstens, J., Berndt, C., Urlaub, M., Watt, S. F. L., Micallef, A., Ray, M., Klaucke, I., Muff, S., Klaeschen, D., Kühn, M., Roth, T., Böttner, C., Schramm, B., Elger, J., & Brune, S. (2019). From gradual spreading to catastrophic collapse – reconstruction of the 1888 ritter island volcanic sector collapse from high-resolution 3d seismic data. *Earth and Planetary Science Letters*, *517*, 1–13, `https://doi.org/10.1016/j.epsl.2019.04.009`.

Keating, B. H. & McGuire, W. J. (2000). Island edifice failures and associated tsunami hazards. *Pure and Applied Geophysics*, *157*(6-8), 899–955, `https://doi.org/10.1007/s000240050011`.

Le Corvec, N., Walter, T. R., Ruch, J., Bonforte, A., & Puglisi, G. (2014). Experimental study of the interplay between magmatic rift intrusion and flank instability with application to the 2001 mount etna eruption. *Journal of Geophysical Research: Solid Earth*, *119*(7), 5356–5368, `https://doi.org/10.1002/2014jb011224`.

Leroy, C. C., Robinson, S. P., & Goldsmith, M. J. (2008). A new equation for the accurate calculation of sound speed in all oceans. *J Acoust Soc Am*, *124*(5), 2774–82, `https://doi.org/10.1121/1.2988296`.

Lundgren, P., Casu, F., Manzo, M., Pepe, A., Berardino, P., Sansosti, E., & Lanari, R. (2004). Gravity and magma induced spreading of mount etna volcano revealed by satellite radar interferometry. *Geophysical Research Letters*, *31*(4), `https://doi.org/10.1029/2003gl018736`.

Massonnet, D. & Feigl, K. L. (1998). Radar interferometry and its application to changes in the earth's surface. *Reviews of Geophysics*, *36*(4), 441–500, `https://doi.org/10.1029/97rg03139`.

McGuire, J. J. & Collins, J. A. (2013). Millimeter-level precision in a seafloor geodesy experiment at the discovery transform fault, east pacific rise. *Geochemistry, Geophysics, Geosystems*, *14*(10), 4392–4402, `https://doi.org/10.1002/ggge.20225`.

Merle, O. & Borgia, A. (1996). Scaled experiments of volcanic spreading. *Journal of Geophysical Research: Solid Earth*, *101*(B6), 13805–13817, `https://doi.org/10.1029/95jb03736`.

Montgomery-Brown, E. K., Segall, P., & Miklius, A. (2009). Kilauea slow slip events: Identification, source inversions, and relation to seismicity. *Journal of Geophysical Research*, *114*, `https://doi.org/10.1029/2008jb006074`.

Moore, J. G., Clague, D. A., Holcomb, R. T., Lipman, P. W., Normark, W. R., & Torresan, M. E. (1989). Prodigious submarine landslides on the hawaiian ridge. *Journal of Geophysical Research*, *94*(B12), `https://doi.org/10.1029/JB094iB12p17465`.

Morgan, J. K., Moore, G. F., Hills, D. J., & Leslie, S. (2000). Overthrusting and sediment accretion along kilauea's mobile south flank, hawaii: Evidence for volcanic spreading from marine seismic reflection data. *Geology*, *28*(7), `https://doi.org/10.1130/0091-7613(2000)28<667:Oasaak>2.0.Co;2`.

Patanè, D., De Gori, P., Chiarabba, C., & Bonaccorso, A. (2003). Magma ascent and the pressurization of mount etna's volcanic system. *Science*, *299*(5615), 2061–3, `https://doi.org/10.1126/science.1080653`.

Poland, M. P., Peltier, A., Bonforte, A., & Puglisi, G. (2017). The spectrum of persistent volcanic flank instability: A review and proposed framework based on kīlauea, piton de la fournaise, and etna. *Journal of Volcanology and Geothermal Research*, *339*, 63–80, `https://doi.org/10.1016/j.jvolgeores.2017.05.004`.

Ramalho, R. S., Winckler, G., Madeira, J., Helffrich, G. R., Hipolito, A., Quartau, R., Adena, K., & Schaefer, J. M. (2015). Hazard potential of volcanic flank collapses raised by new megatsunami evidence. *Sci Adv*, *1*(9), e1500456, `https://doi.org/10.1126/sciadv.1500456`.

Scholz, C. H. (2018). *The Mechanics of Earthquakes and Faulting.* Cambridge University Press.

Stewart, I., McGuire, W. J., Vita-Finzi, C., Firth, C., Holmes, R., & Saunders, S. (1993). Active faulting and neotectonic deformation on the eastern flank of mount etna, sicily. *Zeits. Geomorph.*, *94*, 73–94.

van Wyk de Vries, B. & Francis, P. W. (1997). Catastrophic collapse at stratovolcanoes induced by gradual volcano spreading. *Nature*, *387*, 387–390, `https://doi.org/10.1038/387387a0`.

Wang, Z., Bucholz, C., Skinner, B., Shimizu, N., & Eiler, J. (2011). Oxygen isotope constraints on the origin of high-cr garnets from kimberlites. *Earth and Planetary Science Letters*, *312*(3-4), 337–347, `https://doi.org/10.1016/j.epsl.2011.09.061`.

Supplementary Materials

Seismic and bathymetric characteristics of the offshore boundaries of Mount Etna's unstable flank

The northern boundary of the onshore unstable sector is the seismically active left-lateral Pernicana Fault, which splits up into several smaller scale fault systems near the coast (Hanks and Kanamori, 1979; Bonforte et al., 2011). The latter fault systems are aseismic and deformation appears diffuse. This is similar offshore, where no clear structure is evident, but Riposto Ridge forms a morphological boundary (Gross et al., 2016). In the south, the right-lateral Tremestieri-Trecastagni fault zone, which appears to merge near the coastline to the Acitrezza fault (Gross et al., 2016), transfers extension to the East (Bonforte et al., 2011). The fault outcrop extends beyond the coast (Chiocci et al., 2011) and on to a morphologically prominent structural feature north of Catania Canyon (e.g. Figure 8.1), termed 'lineament' (Chiocci et al., 2011; Gross et al., 2016).

Regional seismic reflection lines reveal that the lineament coincides with discontinuous strata in the shallow subsurface indicating active tectonic deformation (Gross et al., 2016). The deformation pattern has been interpreted as a positive flower structure indicative of a right-lateral oblique transpressive fault system (Gross et al., 2016). New closely spaced high resolution seismic profiles across the lineament, which were collected in 2016 during RV POSEIDON expedition POS496 support this interpretation. Figure 8.1 shows a seismic line from the POS496 survey, which crosses the lineament in the area of the seafloor geodetic array. At kilometer 3.3, i.e. the location of the lineament, seismic reflectors are sharply truncated. Whereas reflectors to the south appear predominantly horizontally layered, reflectors to the north are slightly tilted northwards. The structural discontinuity and the truncation of seismic reflectors lend support to the interpretation that the lineament is the surface expression of an active underlying strike slip fault. The data recorded by the geodetic array that measures across this strike slip fault confirm this observation and we therefore interpret the lineament north of Catania Canyon as the southern boundary of the unstable flank.

Results of seafloor displacement monitoring campaign

Data download in July 2017 during RV Poseidon expedition POS515 provides continuous time series for an observation period of almost 16 months without interrupting the long-term monitoring campaign. The stations were recording all parameters (travel times, sound speed, pressure, temperature, tilt) with the exception of transponder 2 that shows a data gap in June-July 2016. Transponder 1 recorded data correctly but data download was corrupt. However, both transponders were continuously answering to incoming acoustic signals resulting in one- directional baselines.

Distance changes

Changes in the acoustic measurements of distances may result from a combination of true length variations and drift in the computed sound speeds used in the time-to-distance conversion. This makes it hard to differentiate very long period displacement signals from drift. However, it is with large certainty that the length changes recorded in May represent deformation on a strike-slip fault because it is observed in all of the six fault-crossing baselines (Figure 8.6). The changes in lengths clearly stand out of the background noise level and data scatter. Standard deviations range between 2 mm for the shortest baseline (transponder pair 2 - 5) and 20 mm for one of the longer baselines (pair 2 - 3) (Figure 8.3) and is smaller than the observed baseline change.

For some transponder pairs we note a change in distances to the opposite direction prior to the main May 2017 event as well as an overshoot to more extreme distance changes during the event (e.g. 1 - 3, 2 - 4, 3 - 4, 4 - 5 in Figure 8.6). The same pattern also shows up in the pressure baselines (Figure 8.8). Such a signal has been observed during slow-slip events elsewhere (Montgomery-Brown et al., 2009). A possible explanation is that sliding of the southern side of the fault is triggered during the slow-slip event. This may well affect only the very shallow sediments, but we do not have any constraints on that. We therefore do not consider the overshoot, which is the common consensus (Montgomery-Brown et al., 2009).

The changes in distance between two transponders are the sum of horizontal and vertical movements of both transponders. Acoustic distances are not sensitive to height changes and therefore changes in acoustic distances reflect horizontal displacement. For example, for an original transponder pair distance of 1000 m with height difference of 100 m (approximate averages in the geodetic network), a relative change in depth of one transponder of 0.1 m is required to explain a distance change of 0.01 m.

Cosine relationship of displacement and fault angle

Relative distance changes during the May 2017 event range between 6 mm and -39 mm for different transponder pairs. These variations are in line with the network geometry and the strike direction of the fault relative to the baselines. The measured relative distance changes between transponder pairs are a function of the slip on the fault and the angle at which the baseline crosses the fault. A very small angle provides a minimum estimate of fault slip. Our data show that the fault trends between transponders 1 and 3. Owing to the network geometry, the baseline between these stations and the fault itself cross at very small angle, so that the change in acoustic distance between transponders 1 - 3 may be regarded as the best estimate of fault slip. Figure 8.7 shows that the acoustic distance changes recorded by other transponder pairs that cross the fault fit extremely well with the expected cosine relationship.

Estimated magnitude and characteristics of the May 2017 offshore event

The cumulative aseismic moment released in the May 2017 offshore event is M_w 4.3 - 5.37 assuming fault plane lengths ranging between 5 - 15 km, fault depths between 0.5 and 5 km, and a shear modulus of 30 GPa (Alparone et al., 2013). With its duration of eight days and an estimated moment magnitude between 4.3 and 5.3 the Mount Etna offshore event in May 2017 classifies as a slow slip event (Ide et al., 2007). The phenomena of slow earthquakes or 'slow slip events' (SSE) are mainly observed at convergent plate boundaries. Observations of SSE on strike-slip faults are extremely rare. Under water as yet only the vertical component has been detected by pressure gauges.

Onshore data

Data from the permanent GPS monitoring network of Etna acquired during the first week of April 2016 and the last week of July 2017 were processed for calculating the cumulative displacements (Figure 8.9). To investigate the deformation during the observation period, we also performed a Differential Interferometry Synthetic Aperture Radar (DInSAR) analysis of ascending and descending Sentinel 1A/1B TOPSAR images. We analyzed the ascending 31 March 2016 - 30 July 2017 and the descending 06 April 2016 – 30 July 2017 pairs (Figure 8.10). The SISTEM results (Figure 8.11) depict the 3D ground deformation occurring during the April 2016 - July2017 time span; they show an inflation affecting the summit central area of the volcano (with an uplift of about 5 cm), coupled with an eastward movement of the eastern flank (maximum value of about 7 cm recorded along the Pernicana fault). Another important feature of the 3D deformation pattern obtained by integrating GPS and InSAR data is the clear control of the main fault system (Pernicana fault, at the northern flank, and Acicastello fault, in the south) on horizontal displacements.

Supplementary Figures

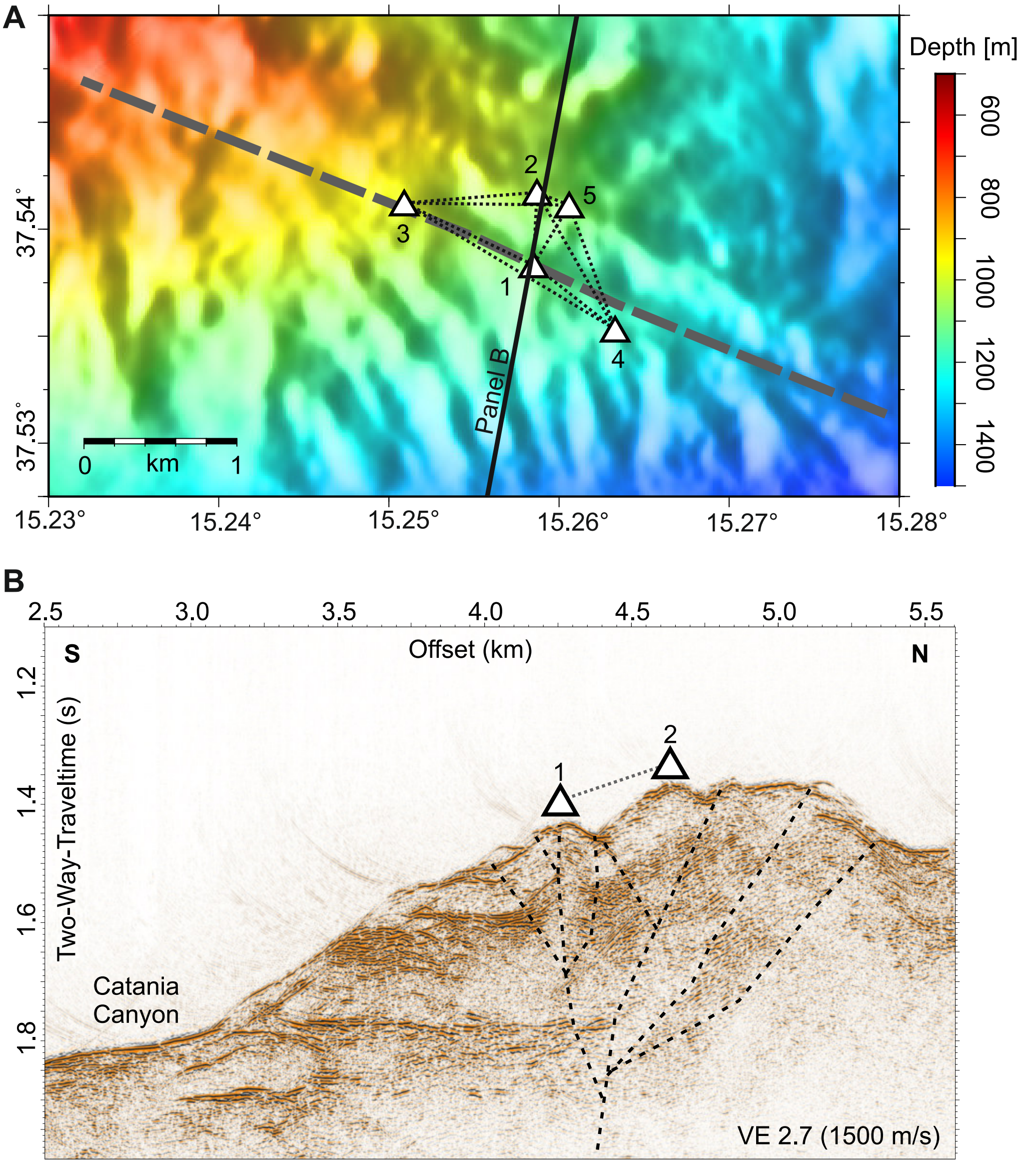

Figure 8.5: Transponder locations shown on local bathymetry (A) and high resolution seismics (B). (A) Triangles represent transponders with individual numbers. (B) Part of seismic profile p500 crossing the seafloor geodetic array recorded with a Geometrics GeoEel streamer consisting of 11 solid state sections (each 12.5 m). One standard 2 x 0.2l Mini-GI-gun was used as source. Triangles above the seafloor indicate projected transponder locations.

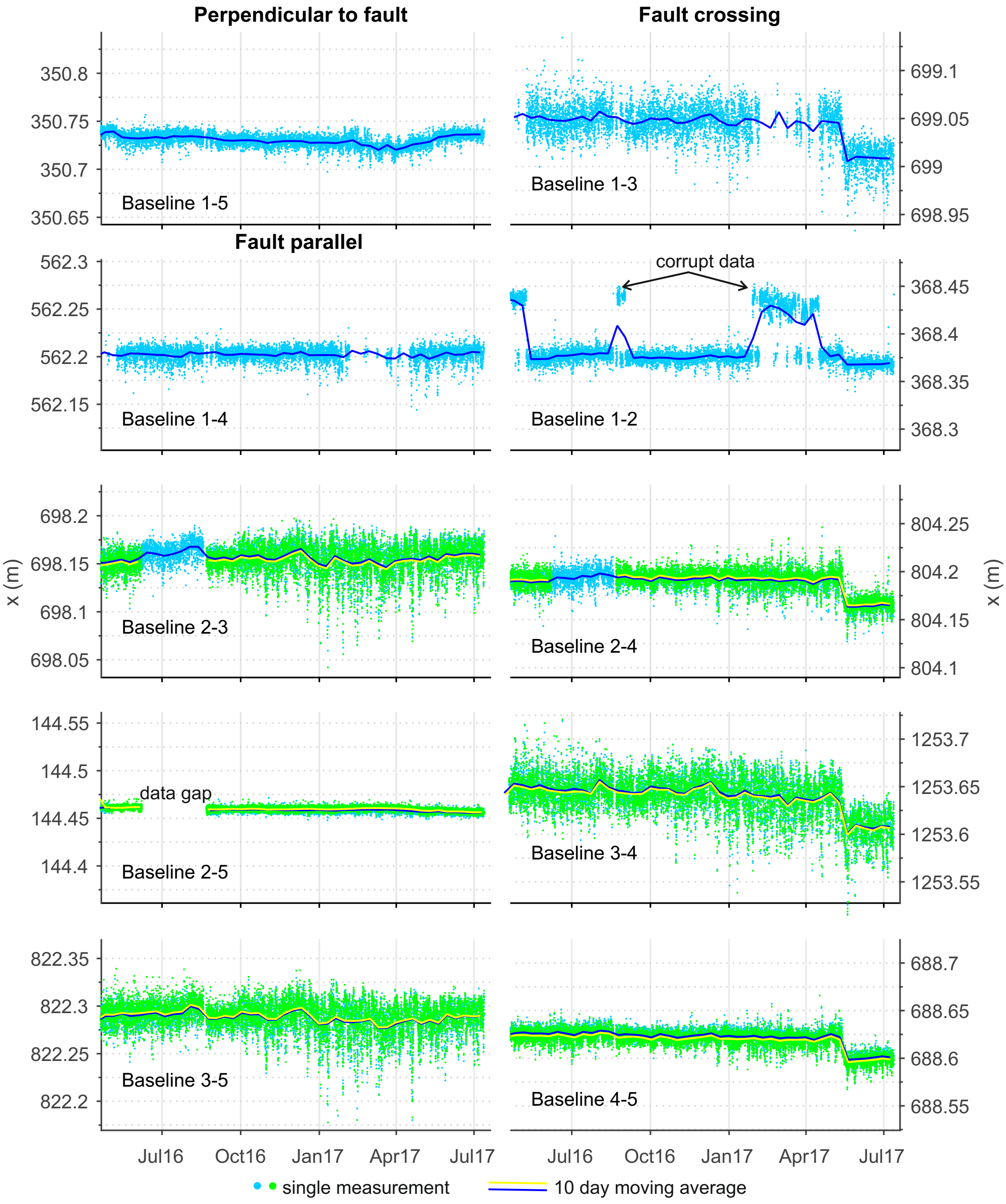

Figure 8.6: Relative changes in distances for all 10 baselines during the entire observation period from April 2016 to July 2017. Blue and green markers indicate active interrogation and passive response of acoustic signals, respectively. Due to high sampling frequency individual measurements partly overlap. Dark blue and yellow lines show a 10 day moving average also for interrogation and response. Transponder 1 did not record any data but was still responding to the interrogations of all other transponders. All plots show a range of 0.2 m. For transponder locations see Figure 8.5A.

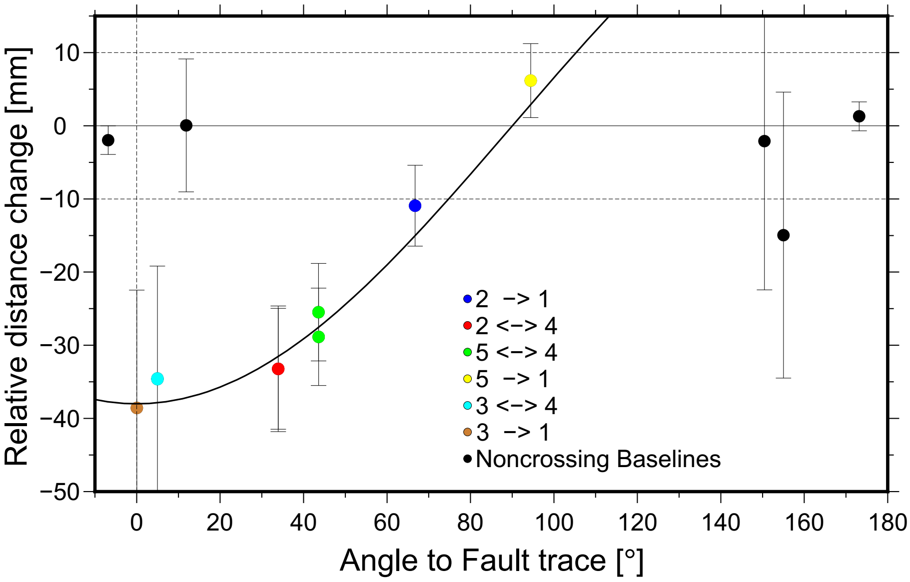

Figure 8.7: Cosine relationship between the relative distance shortening and lengthening during the May 2017 event and the angle at which the baselines cut the fault trace. Error bars represent the standard deviation of the baseline time series before 10 May 2017. For transponder locations see Figure 8.5A.

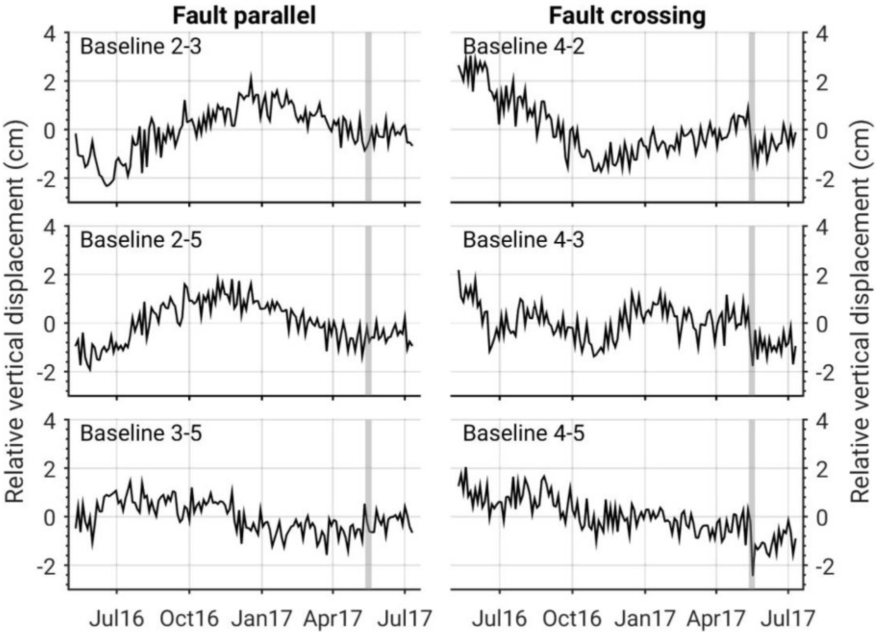

Figure 8.8: Relative pressure differences for the entire observation period (10-day moving average) between individual transponder pairs. The displacement of the second transponder relative to the first is shown (e.g. in A the vertical displacement of transponder 3 relative to transponder 2 is shown, i.e. transponder 2 is assumed fixed). Left panels show transponder pairs north of the fault and right panels show transponder pairs crossing the fault. Grey vertical bars represent the time period of the May 2017 event. We do not show time series for baselines of transponder 1 because it recorded corrupt data. The May 2017 event is evident in all fault crossing transponder pairs in that all stations on the northern side of the fault move downward by approximately 10 mm with respect to transponder 4. Long period signals occur in all transponder pairs and do not reflect true vertical displacement but are the result of seasonal temperature variations. For transponder locations see Figure 8.5A.

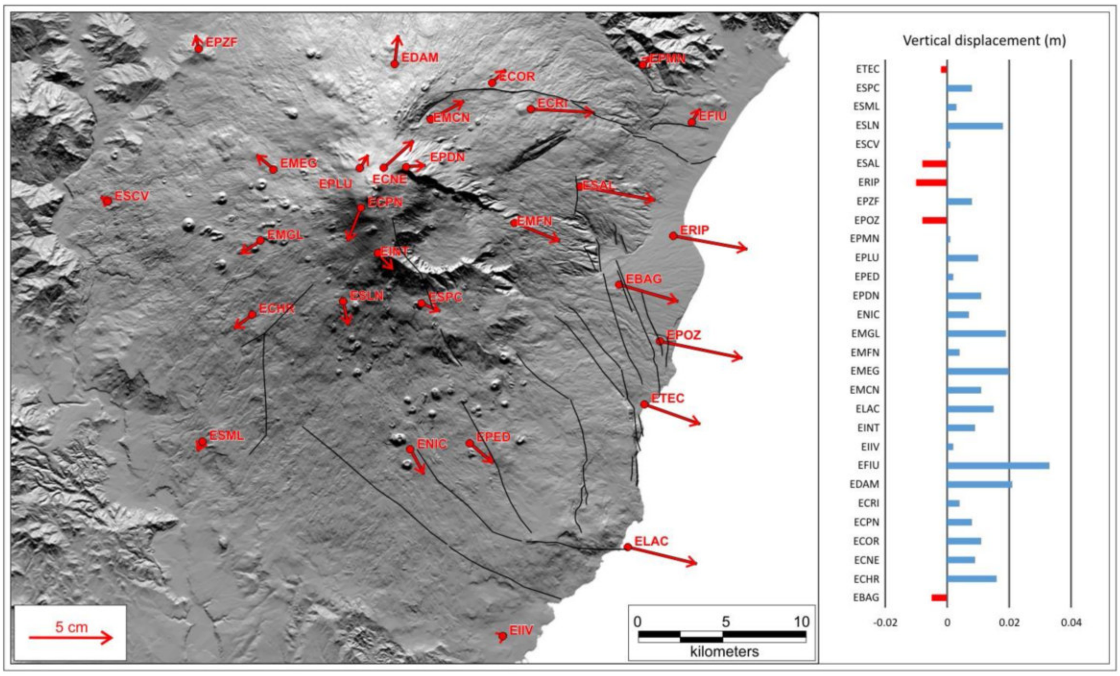

Figure 8.9: GPS displacements referring to the April 2016 to July 2017 comparison. Red vectors in the map indicate the observed horizontal displacements. On the right, vertical displacement is reported for each station.

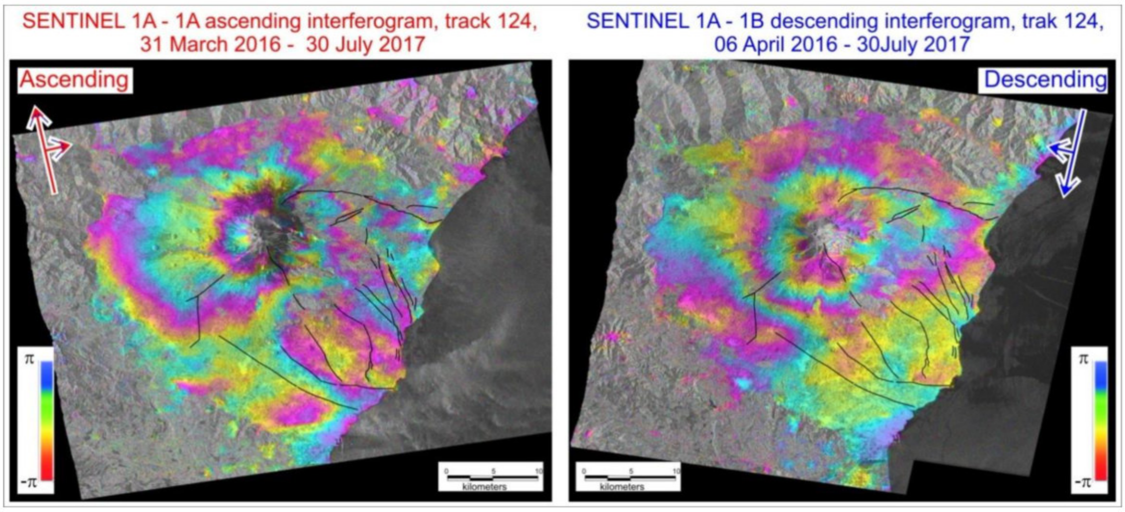
SENTINEL 1A - 1A ascending interferogram, track 124, 31 March 2016 - 30 July 2017

SENTINEL 1A - 1B descending interferogram, trak 124, 06 April 2016 - 30July 2017

Figure 8.10: Ascending 31 March 2016 to 30 July 2017 and descending 6 April 2016 to 30 July 2017 Sentinel-1 phase interferograms. Ascending 31 March 2016 to 30 July 2017 (left) and descending 06 April 2016 to 30 July 2017 (right) Sentinel-1 phase interferograms. Fault traces (Hanks and Kanamori, 1979) are reported in the figure in order to demonstrate how the main discontinuities in the ground deformation field are controlled by the local fault systems.

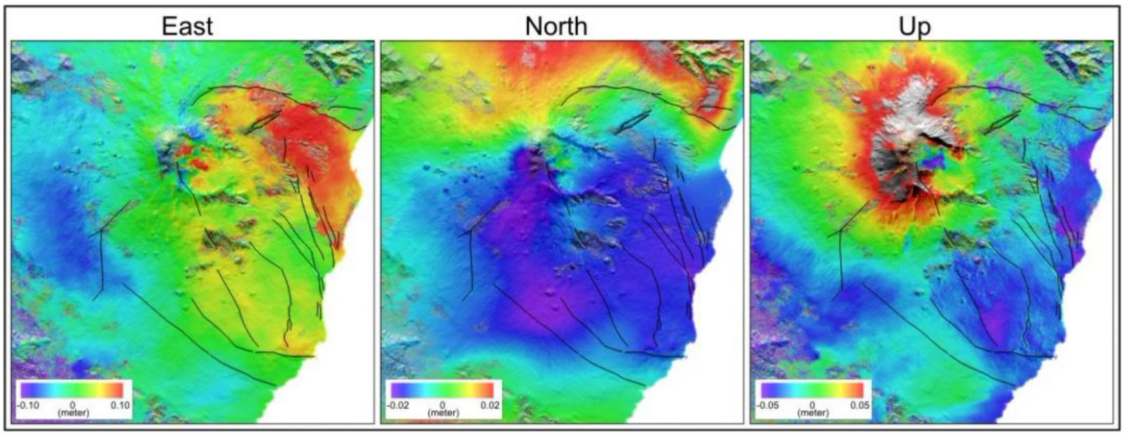

Figure 8.11: East, north, and up displacement components resulting from the SISTEM integration. Fault traces (Hanks and Kanamori, 1979) are reported in the figure in order to evidence how the main discontinuities in the ground deformation field are controlled by the local fault systems.

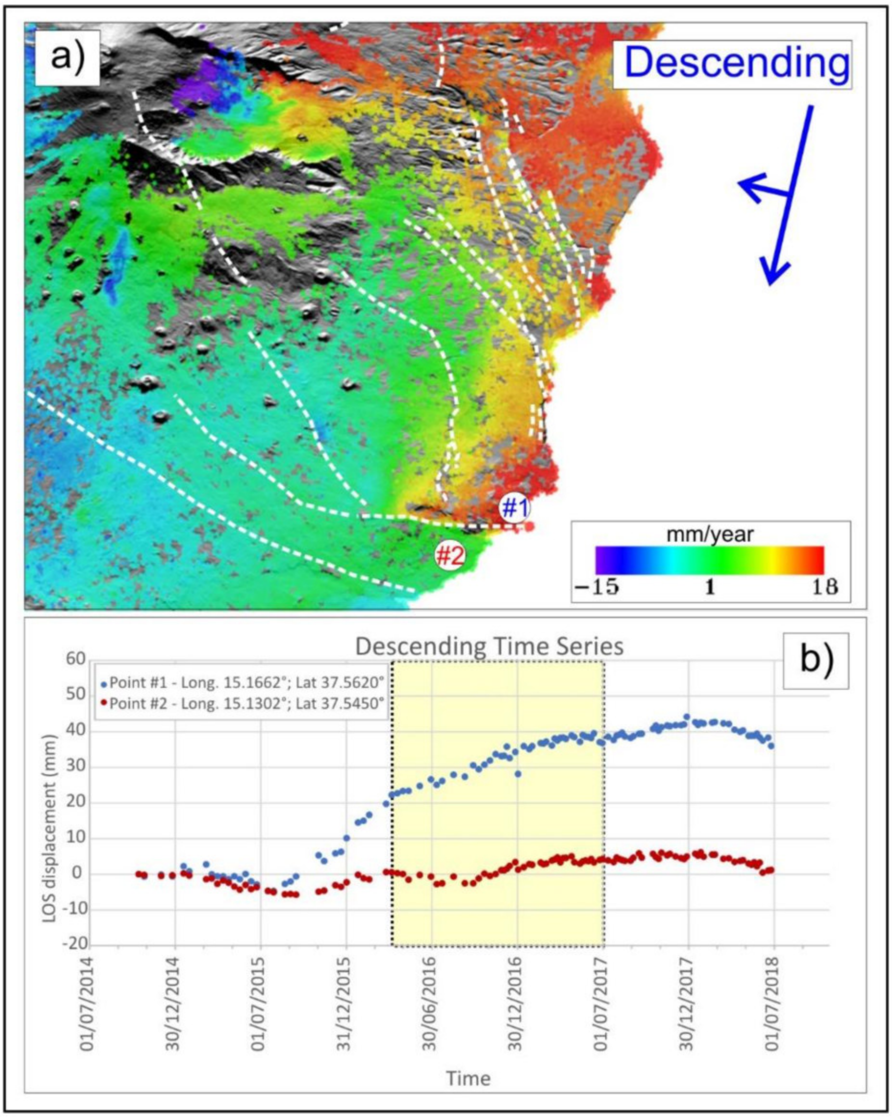

Figure 8.12: Ground displacements along the LOS across the study area measured by both Sentinel 1A and 1B satellites with a 6-day interval. (a) Descending Sentinel 1A-B mean LOS velocity (2014 - 2018); positive values approaching to the sensor. (b) Time Series of two selected points located on to northern and southern side of Acitrezza fault, respectively. The yellow rectangle represents the time period investigated by the offshore array.

9 Conclusion and Outlook

9.1 Conclusion

The analyses of seismic and aseismic deformation at offshore located fault zones is important to understand the physics of earthquake nucleation and enable us to improve our understanding of the strength of plate boundary faults. Many fault zones are located offshore and cannot be investigated using conventional space-based methods or land-based instrumentation. Combining data from shoreline-crossing studies, in particular connecting ocean-bottom seismometers, acoustic seafloor geodesy, long-offset multi-channel seismic data with onshore broadband seismometers, InSAR and GNSS data, this thesis demonstrates how the offshore analysis of seismic and aseismic deformation significantly improves our knowledge in frictional behaviors of fault zones. Furthermore, better constraints on the spatio-temporal distribution of fault slip allows to understand the underlying processes that drive frictional properties in different fault zones and to improve adequate assessments of potential geohazards, especially for the coastal areas.

At the North Chilean subduction zone, the erosional underthrusting of the oceanic Nazca plate under the continental South American plate zone poses a significant risk to the coastal populations in the circum-Pacific belt due to the absence of a large earthquake since 1877. In 2014, the Iquique earthquake ruptured a central segment of the north Chilean seismic gap and has released elastic energy with a magnitude 8.1 earthquake, but the remaining portions along the north Chilean margin persist in a combination of high and lower plate interface coupling. The understanding of the variability of fault slip behaviors in shallow subduction zones is essential to discern internal stress and changes throughout the seismic cycle. Therefore, the analysis of aftershocks following the 2014 Iquique megathrust event recorded by two subsequent OBS deployments and land seismometers in combination with long-offset multi-channel seismic data indicates a relationship between the abundant occurrence of aftershocks at the seismogenic up-dip limit and the long-term process of subduction erosion of the overriding plate (Chapter 3). Despite the stress redistribution as a consequence of the large seismic rupture, expressed as aftershocks, intense seismicity up-dip of the seismogenic zone, with the majority near the plate interface and a significant number of aftershocks above, support the model of subduction erosion, which removes forearc material over long periods of time. Active fracturing at the base of the upper plate at the updip limit of the seismogenic zone induces seismicity and removes material of the upper plate. The provoked upper plate deformation is manifested in seismic deformation along seaward dipping planes. Multi-channel seismic data show an overall increase in reflection amplitudes, which is indicative of a high degree of fracturing and the presence of fluids. Large-scale faulting above the seismogenic up-dip limit matches the aftershock seismicity. This seismic deformation results in permanent deformation and erosion of the overriding plate, seaward of the 2014 Iquique earthquake, over several earthquake cycles.

The decrease of the coherent plate boundary reflection amplitude correlates spatially to the up-dip extent of the seismic rupture area (Chapter 3 and 4). This compelling observation has significant impact on our understanding of seismic deformation. If the seismic reflection technique is able to resolve seismic rupture asperities and to discriminate between seismic and aseismic slip behavior at other subduction zones, then possible other prominent asperities can be revealed. Aseismic deformation is difficult to constrain using solely seismic instrumentation on the seafloor (Chapter 2), however, small asperities on faults that are repeatedly caused to slip by the surrounding aseismic deformation can be used as a proxy for the total cumulative slip (Chapter 5). To expand our investigation of time-dependent stress variations within the marine forearc, we analyzed the behavior of repeating earthquakes from the interseismic to the postseismic phase of the 2014 Iquique earthquake in Chapter 5. The search for repeaters revealed the evident occurrence of seismic and aseismic deformation on large faults above the seismogenic up-dip limit since the foreshock period of the 2014 Iquique earthquake. Comparing the average cumulative slip of the plate interface and within the upper plate, we find that the gradual unlocking of the plate interface forced extensional faults in the upper plate to reverse the slip mode one week before the main earthquake. Taking the results of Chapter 3 into account, we provide evidence for an emerging process that leads to the erosion of the upper plate from the pre-seismic to the postseismic phase. Concluding the results of Chapter 3 to 5, the accumulated strain as a result of basal erosion of the upper plate at the seismogenic up-dip boundary requires gradual relaxation that transitions to an extensional state and favors slow extensional faulting as observed in multi-channel seismic data (Chapter 3 and 4). Such normal faulting and associated subsidence of the marine forearc occurs over long-time scales and is related to aseismic deformation.

To measure long-term aseismic sub-seafloor deformation processes, seafloor measurements techniques are beneficial (Chapter 6). The emerging field of seafloor geodesy aims to monitor either relative or absolute deformation, according to the research target. Acoustic direct-ranging has proven to be powerful to identify aseismic deformation and to determine the locking state of fault portions. Uncertainty analyses of environmental effects on measurements and network configurations, discussed in Chapter 6, indicated that fault geometries (strike-slip or normal) and slip partitioning, i.e., over several fault branches, need to be considered in the conception of the network geometry. Analysis of the slip behavior at the continental North Anatolian strike-slip fault in the Sea of Marmara contributed to the understanding of frictional properties of faults. The central Marmara segment is characterized by sparse seismicity including patches that lack seismicity altogether. Chapter 7 evaluates offshore geodetic observations and reveals that during the monitoring period no significant deformation has occurred. According to a concurrent seafloor geodetic measurement on a western segment, which revealed partial fault creep, the results of Chapter 7 indicate a complex fault locking pattern that infers the accumulation of strain equivalent to an earthquake of magnitude 7.1 to 7.4.

Drivers for aseismic deformation are not necessarily accommodated tectonic plate motion, but also gravitational forces that can lead to slow aseismic deformation. In particular, the southeastern flank of Etna volcano, which slides into the Ionian Sea at rates of centimeters per year, has been continuously monitored using onshore geodetic measurements. The shoreline-crossing study in Chapter 8 applies a similar approach to reveal the slip behavior of the southern submarine landslide limit, including acoustic direct-path ranging combined with onshore geodetic measurements. The analysis revealed that aseismic deformation, expressed as a slow-slip event, increases away from the volcano summit into the Ionian Sea. Simultaneously, no volcanic activity such as inflation of the volcanic edifice caused by uprising magma was recorded, implying a secondary origin that causes fault displacement. Such a deformation pattern has been observed at other volcanic edifices and has been associated with gravitational sliding. In summary, the studies of Chapters 7 and 8 demonstrate clearly that only the combination of onshore and offshore deformation analysis allows the determination of fault slip behavior in these settings.

9.2 Outlook

Over the past decade, the employment of marine geophysical techniques to decipher sub-seafloor processes through the analysis of seismic and aseismic deformation has increased. This thesis, as part of a recent effort using shoreline-crossing observations to analyze fault slip behaviors, demonstrates that numerous underlying processes, such as subduction erosion on the marine forearc or the state of locking on an offshore strike-slip fault zone that poses a significant geohazard, are poorly understood. However, the monitoring of spatial and temporal variabilities of seismic and aseismic displacement along subduction margins or strike-slip fault zones, including seafloor geodetic monitoring have been used selectively and remain still in their infancy (compare Chapter 6). In addition, the analysis of deformation at divergent plate boundaries, where the majority of plate motion is accommodated aseismically, was beyond the scope of this thesis. To enhance our knowledge of the processes that drive the partitioning between aseismic and seismic slip and promote the nucleation of earthquakes, I recommend the following proposals:

Mid-ocean ridges form where tectonic plates spread apart and create new oceanic crust and lithosphere through magmatism and extension. These spreading ridges are interrupted by transform faults which generally have a less heterogeneous composition than continental strike-slip faults, but the rotation of normal stress from the ridge into transform strike-slip displacement comprises increasingly oblique shearing, resulting in a two-stage crustal accretion process involving thinning and magmatism (Grevemeyer et al., 2021). At the transform faults, plate motion is accommodated on average 85 % aseismically, and only 15 % of deformation is related to high-frequency acoustic emissions, such as seismicity or tremors (Boettcher and Jordan, 2004). Moreover, earthquake monitoring of transform faults in intermediate and fast-spreading contexts have revealed high foreshock rates preceding mainshocks, compared to continental strike-slip faults, suggesting a linkage between foreshocks and mainshocks that leads to short-term predictability (McGuire, 2008; McGuire et al., 2012). To study such stress changes driven by slip partitioning, particularly the relationship between seismicity and displacement, a multidisciplinary approach combining seafloor geodesy, seafloor hydroacoustics, seismic monitoring, and repeated high-resolution seafloor mapping using an autonomous underwater vehicle (AUV) is needed. At the Southeast Indian Ridge, the intermediate spreading-rate that splits the Australian and Antarctic plates apart is offset by the large Amsterdam transform fault, which causes $M_w > 5$ earthquakes every year over the past two decades. The intersection between the Amsterdam St Paul hotspot and the Southeast Indian Ridge is bounded to the west by two short and active transform faults (Boomerang and Hillegom) and is an appropriate research area to expand the analyses of seismic and aseismic deformation. The nearby located Amsterdam and St Paul islands, equipped with permanent GNSS and broadband seismometers, allow the collaboration between French and German research institutes to combine resources and know-how of acoustic direct-path ranging (Lange et al., 2019; Petersen et al., 2019) and GNSS-A (Sakic et al., 2018, 2020) methods. I propose to focus on two deployments sites, covering the Boomerang transform fault and spreading ridge segment, where each site independently comprises an acoustic ranging network, GNSS-A, and long-term pressure gauges, surrounded by a network of OBS. A study at the East Pacific Rise considers ratios of the average slip of transform fault earthquakes ($M_w \leq 6$) to the plate motion rate and suggests that the repetitive time of seismic cycles is in the range of ten years (McGuire et al., 2005). Considering the current battery capacities of up to ten years, deployment may have the ability to capture the stress transfer from spreading to strike-slip faulting during the entire seismic cycle.

Building on the experience of the Southeast Indian Ridge seafloor geodesy experiment and recent numerical modeling of mid-ocean ridge transform earthquake sequences (Liu et al., 2020), I recommend to initiate a similar interdisciplinary seafloor geodesy experiment at the fast-spreading East Pacific Rise. The Quebrada-Discovery-Gofar transform fault system is located south of the Galapagos Triple Junction and exhibits a range of different fault slip behavior. The seismically active Gofar and Discovery transforms which repeatedly rupture in quasi-periods every 5 to 6 years in a magnitude 6 earthquake contrasts the Quebrada transform that generates only one magnitude 5.5 earthquake every five years (McGuire, 2008). This distinct contrast in earthquake behavior demonstrates an along-strike change in mechanical properties and implies a variation in fault coupling of discrete transform segments that requires in situ seafloor measurements to reveal the underlying processes. Building on an early acoustic direct-path ranging experiment that was conducted at the western Discovery transform fault segment (McGuire and Collins, 2013); also discussed in Chapter 6, a joint multinational experiment encompassing US, French and German research institutes, will provide the capability to manage such a long-term (up to 10 years) project in this remote location.

The third proposal I recommend is to initiate an integrated interdisciplinary approach, similar to Chapter 7, at the Queen Charlotte Fault (QCF) to complement the ongoing joint U.S. Geological Survey / Geological Survey of Canada program to investigate the seismic/aseismic deformation pattern and the tectonic structure of the Queen Charlotte Fault in North America (e.g., Riedel et al., 2020). The Queen Charlotte Fault ruptured twice in the last decade (2012 and 2013) with moment magnitudes between 7.5 and 7.8, including detectable tsunamis, raising concerns about its potential to damage coastal and seafloor infrastructure (James et al., 2013). The highly seismically active QCF displaces with rates of ~55 mm/yr (Brothers et al., 2020) and represents a model area to address the following research questions: What is the relationship between the ratio of foreshocks to aftershocks and fault displacement?; Are there precursors that precede the mainshocks? In addition, the coastal location simplifies and reduces project costs through the use of coastal vessels. Building on the joined forces of Canada and the USA that have been used to map the surface expression of the Queen Charlotte Fault with high-resolution AUV bathymetry, a direct-path ranging network encircled by long-term OBS can monitor the accumulation of strain and discern between fully locked or fully creeping fault behavior. This proposal may allow to contribute to an adequate basis for an assessment of potential geohazards affecting adjacent coastal population.

Besides applying seafloor measurement techniques to analyze fault slip behavior and to answer research questions, which I have discussed in this thesis, the development of new methods and data analysis techniques can lead to progress in the detection and quantification of strain transients. Regions with complex seafloor deformation (across a distinct fault or diffusive over a large area), such as the North Anatolian Fault in the Sea of Marmara (Chapter 7), where slip partitioned across a pull-apart basin, impedes the precise measurement of strain accumulation. Such complex distribution of strain can be resolved by integrating the analytical method of network adjustment. This technique calculates the individual station locations with the specified distance changes of the acoustic measurement network over time (compare Free Network Adjustment). The development of a modified land-established algorithm using existing field data from Chapters 7 and 8 are appropriate data sets to improve the technique for seafloor geodetic use. The implementation of an error analysis based on Bayesian statistics to solve the inverse problem will foster the network adjustment algorithm.

Another challenge of underwater acoustic distance measurements is the reliance on the exact sound speed in water. In Chapters 6, 7 and 8, I have shown that direct measurements of sound speed are less accurate than individual measurements of temperature, pressure, and salinity (Chapter 6). However, measuring the physical properties of the water column at the seafloor and converting sound speed and travel-time into distance remains challenging, as the acoustic ray path is influenced by tides, ocean currents, weather incidents and sensor drift. Improvements in acoustic distance measurements are critical for identifying and quantifying long-term strain transients, and distinguishing such slow deformation from ocean environmental noise and fault rupture. I intend to improve acoustic measurements by developing new processing methods by, i.e., stacking all normalized distance measurements to identify mutual environmental influences.

Overall, the field of seafloor measurements will increase over the next decades and more countries exposed to geohazards near their coasts begin to investigate sub-seafloor deformation. Due to the mounting interest in accurate acoustic monitoring for the offshore industry and advances in technology development of sea-going instrumentation, the seafloor is now becoming more accessible.

References

Boettcher, M. S. & Jordan, T. H. (2004). Earthquake scaling relations for mid-ocean ridge transform faults. *Journal of Geophysical Research*, *109*(B12), `https://doi.org/10.1029/2004jb003110`.

Brothers, D. S., Miller, N. C., Barrie, J. V., Haeussler, P. J., Greene, H. G., Andrews, B. D., Zielke, O., Watt, J., & Dartnell, P. (2020). Plate boundary localization, slip-rates and rupture segmentation of the queen charlotte fault based on submarine tectonic geomorphology. *Earth and Planetary Science Letters*, *530*, `https://doi.org/10.1016/j.epsl.2019.115882`.

Grevemeyer, I., Rüpke, L., Morgen, J. P., Iyker, K., & Devey, C. W. (2021). Extensional tectonics and two-stage crustal accretion at oceanic transform faults. *Nature*, *591*, `https://doi.org/10.1038/s41586-021-03278-9`.

James, T., Rogers, G., Cassidy, J., Dragert, H., Hyndman, R., Leonard, L., Nykolaishen, L., Riedel, M., Schmidt, M., & Wang, K. (2013). Field studies target 2012 haida gwaii earthquake. *Eos, Transactions American Geophysical Union*, *94*(22), 197, `https://doi.org/10.1002/2013eo090001`.

Lange, D., Kopp, H., Royer, J. Y., Henry, P., Cakir, Z., Petersen, F., Sakic, P., Ballu, V., Bialas, J., Ozeren, M. S., Ergintav, S., & Geli, L. (2019). Interseismic strain build-up on the submarine north anatolian fault offshore istanbul. *Nat Commun*, *10*(1), 3006, `https://doi.org/10.1038/s41467-019-11016-z`.

Liu, Y., McGuire, J. J., & Behn, M. D. (2020). Aseismic transient slip on the gofar transform fault, east pacific rise. *Proc Natl Acad Sci U S A*, *117*(19), 10188–10194, `https://doi.org/10.1073/pnas.1913625117`.

McGuire, J. J. (2008). Seismic cycles and earthquake predictability on east pacific rise transform faults. *Bulletin of the Seismological Society of America*, *98*(3), 1067–1084, `https://doi.org/10.1785/0120070154`.

McGuire, J. J., Boettcher, M. S., & Jordan, T. H. (2005). Foreshock sequences and short-term earthquake predictability on east pacific rise transform faults. *Nature*, *434*(7032), 457–61, `https://doi.org/10.1038/nature03377`.

McGuire, J. J. & Collins, J. A. (2013). Millimeter-level precision in a seafloor geodesy experiment at the discovery transform fault, east pacific rise. *Geochemistry, Geophysics, Geosystems*, *14*(10), 4392–4402, `https://doi.org/10.1002/ggge.20225`.

McGuire, J. J., Collins, J. A., Gouédard, P., Roland, E., Lizarralde, D., Boettcher, M. S., Behn, M. D., & van der Hilst, R. D. (2012). Variations in earthquake rupture properties along the gofar transform fault, east pacific rise. *Nature Geoscience*, *5*(5), 336–341, `https://doi.org/10.1038/ngeo1454`.

Petersen, F., Kopp, H., Lange, D., Hannemann, K., & Urlaub, M. (2019). Measuring tectonic seafloor deformation and strain-build up with acoustic direct-path ranging. *Journal of Geodynamics*, *124*, 14–24, `https://doi.org/10.1016/j.jog.2019.01.002`.

Riedel, M., Yelisetti, S., Papenberg, C., Rohr, K. M. M., Côté, M. M., Spence, G. D., Hyndman, R. D., & James, T. (2020). Seismic velocity structure of the queen charlotte terrace off western canada in the region of the 2012 haida gwaii mw 7.8 thrust earthquake. *Geosphere*, *17*(1), 23–38, `https://doi.org/10.1130/ges02258.1`.

Sakic, P., Ballu, V., Crawford, W. C., & Wöppelmann, G. (2018). Acoustic ray tracing comparisons in the context of geodetic precise off-shore positioning experiments. *Marine Geodesy*, *41*(4), 315–330, `https://doi.org/10.1080/01490419.2018.1438322`.

Sakic, P., Ballu, V., & Royer, J.-Y. (2020). A multi-observation least-squares inversion for gnss-acoustic seafloor positioning. *Remote Sensing*, *12*(3), `https://doi.org/10.3390/rs12030448`.

List of Figures

List of Tables

Acknowledgments

First and foremost, I am very grateful for the supervision over the last three years from Heidrun Kopp and Dietrich Lange. Thank you, Heidrun, for your mentoring and advice for my scientific career, for giving me the opportunity to discover the field of marine geodesy. You have always supported me and encouraged me to question existing knowledge and to develop my own ideas. Dietrich Lange, thank you for the fruitful and inspiring discussions, encouragement and reading of my drafts. It was a pleasure to spend time with you on research cruises around the world and to work with you over these last three years. I look forward to ongoing and future collaborations with you.

I would like to thank Ingo Grevemeyer for being my co-supervisior within the PhD project. Thank you for your helpful advices, your constructive input, opinions on scientific work, ideas on career planning and motivation.

A special thanks to Felix Wolf, who shared last three years the office with me. Thank you for all the nice conversations, the good working climate, memorable vacations and your patience in tolerating my messy desk and erratic mind.

Thanks to Bettina Schramm, Gesa Franz, Anke Dannowski, Anouk Beniest for many shared research cruises around the world and memorable vacations, Morelia Urlaub and Jacob Geersen for the constant support during my doctorate, the insightful discussions and mentoring of the last years. Many thanks to Michael Riedel for the discussions, the morning coffee and the time together on research cruises.

I would like to thank the GEOMAR and German Research Association (DFG) for financing my doctorate. Many thanks to the captains and crews of research cruises MARSITE, SO244, POS496, POS497, MGL1610, CRACK, T-443, SO277 for making this exciting scientific work possible.

Many thanks to Jasmin Mögeltönder, Anne Völsch, and Julia Schätzel, who helped me greatly throughout the seven years at GEOMAR in dealing with all the paperwork and travel preparation. Additional thanks to Patrick Schröder for your technical guidance during the last decade.

I would like to thank Moana Kraj for brightening my days and the good times we have. Many thanks to my friends Christoph Böttner, Felix and Sandra Gross, Peter Haas, Lena Runge, Rachel Barrett and Jdith Elger for the time we spend together, the guidance and unforgettable holidays.

I would like to thank Wolfgang Richter for awakening my interest in earth sciences and encouraging me to take that path. I thank my family, Kai Petersen, Karin Warkentien, Nicole Bitkin, Ann-Christine Rehpenning and Katrin Petersen for their support, backing and advice during the long way to my doctorate.

Curriculum Vitae

Removed according to data protection regulations.
Aus datenschutzrechtlichen Gründen entfernt.

List of Publications

ResearcherID: D-6125-2019; ORCID ID: 0000-0002-3526-6541

Peer Reviewed

11. **Petersen, F.**, Lange, D., Grevemeyer, I., Barrientos, S. and Kopp, H. (in review for JGR Solid Earth). Repeating earthquakes reveal pre-seismic upper plate weakening by the 2014 Iquique foreshock sequence.

10. Ma B., Geersen, J., Lange, D., Klaeschen, D., Grevemeyer, I., **Petersen, F.**, Riedel, M., Xia, Y., Tréhu, A. M., Contreras-Reyes, E., and Kopp, H. (in review for Nature Communications). Megathrust reflectivity matches the 2014 Iquique earthquake rupture.

9. Thorwart, M., Dannowski, A., Grevemeyer, I., Lange, D., Kopp, H., **Petersen, F.**, Crawford W., and Paul A. (2021, accepted). Basin inversion: Reactivated rift structures in the Ligurian Sea revealed by OBS. *Solid Earth*, DOI 10.5194/se-2021-9

8. **Petersen F.**, Lange D., Ma B., Grevemeyer I., Geersen J., Klaeschen, D., Contreras-Reyes E., Barrientos S., Vera. E, Tréhu A. M. and Kopp H. (2021). Relationship between subduction erosion and the up-dip limit of the 2014 Mw 8.1 Iquique earthquake. *Geophysical Reseach Letters*, *48* (9). DOI 10.1029/2020GL092207

7. Schmid F., Cremanns M., Augustin N., Lange D., **Petersen F.** and Kopp H. (2021) Microseismicity and lava flows constrain magmato-tectonic processes near the southern tip of the Fonualei Rift and Spreading Center in the Lau Basin. *Journal of Geophysical Research Solid Earth.* DOI 10.1029/2020JB021340

6. Lange D., Kopp H., Royer J. Y., Henry P., Çakir Z., **Petersen, F.**, Sakic P., Ballu V., Bialas J., Özeren M. S., Ergintav S. and Géli L. (2019) Interseismic strain build-up on the submarine North Anatolian Fault offshore Istanbul. *Nature Communications.* DOI 10.1038/s41467-019-11016-z.

5. **Petersen F.**, Kopp H., Lange D., Hannemann K. und Urlaub M. (2019) Invited review article: Measuring tectonic seafloor deformation and strain-build up with acoustic direct-path ranging. *Journal of Geodynamics*, 124. pp. 14-24. DOI 10.1016/j.jog.2019.01.002.

4. Urlaub, M., **Petersen F.**, Gross F., Bonforte A., Puglisi G., Guglielmino F., Krastel S., Lange D. and Kopp H. (2018) Gravitational collapse of Mount Etna's southeastern flank. *Science Advances*, 4 (10). eaat9700. DOI 10.1126/sciadv.aat9700.

3. Hetenyi G., Molinari I., Clinton J., Bokelmann G., Bondár I., Crawford W. C., Dessa J. X., Doubre C., Friederich W., Fuchs F., Giardini D., Graczer Z., Handy M. R., Herak M., Jia Y., Kissling E., Kopp H. , Korn M., Margheriti L., Meier T., Mucciarelli M., Paul A., Pesaresi D., Piromallo C., Plenefisch T., Plomerova J., Ritter J., Rümpker G., Sipka V., Spallarossa D. Thomas C., Tilmann F., Wassermann, J., Weber, M., Weber Z., Wesztergom V., Zivcic M., Dannowski A. , **Petersen F.**, Wolf F. and Lange D. and AlpArray OBS Cruise Crew (2018) The AlpArray Seismic Network: A Large-Scale European Experiment to Image the Alpine Orogen. *Surveys in Geophysics*, 39 (5). pp. 1009-1033. DOI 10.1007/s10712-018-9472-4.

2. Sakic P., Piété H., Ballu V., Royer J. Y., Kopp H., Lange D , **Petersen, F.**, Özeren M. S., Ergintav S., Geli L., Henry P. and Deschamps, A. (2016) No significant steady state surface creep along the North Anatolian Fault offshore Istanbul: Results of 6 months of seafloor acoustic ranging. *Geophysical Research Letters*, 43 (13). pp. 6817-6825. DOI 10.1002/2016GL069600.

1. Kaminski M. A., Niessen F., Bazhenova E., De La Guardia L. C., Coakley B., De Vernal H., Eagles G., Eisermann H., Forwick M., Gebhardt C., Geissler W., Horner T., Jensen L., Jin H., Jokat W., Kabot, S., Kimmel B., Kolling H., Kopsc, C., Kudriavtsev, A., Matthiessen J., Nam S. I., **Petersen F.** , Prim, A. K., Riefstahl F., Sauermilch I., Schreck M., Spielhagen R., Stein R., Stolle C. and Zwick, M. and PS87 Shipboard Geoscience Party (2015) Modern agglutinated foraminifera from the Hovgård ridge, fram strait, west of Spitsbergen: Evidence for a deep bottom current. *Annales Societatis Geologorum Poloniae*, 85. pp. 309-320.

Non-Peer Reviewed

3. Gutscher, M. A., Royer, J. Y., Graindorge, D., Murphy, S., Klingelhoefer, F., Aiken, C., Cattaneo, A., Barreca, G., Quetel, L., Riccobene, G., **Petersen, F.**, Urlaub, M., Krastel, S., Gross, F., Kopp, H., Margheriti, L. and Beranzoli, L. (2019) Fiber Optic Monitoring of Active Faults at the Seafloor: the FOCUS project . Open Access Photoniques, 2019 (Special EOS Issue). pp. 32-36. DOI 10.1051/photon/2019S432.

2. Kopp, H., Lange, D., Thorwart, M., Paul, A., Dannowski, A., **Petersen, F.**, Aubert, C., Beek, F., Beniest, A., Besancon, S., Brotzer, A., Caielli, G., Crawford, W., Deen, M., Lehmann, C., Marquardt, K., Neckel, M., Papanagnou, L., Schramm, B., Schröder, P., Steffen, K. P., Wolf, F. N. and Xia, Y., eds. (2018) RV MARIA S. MERIAN Fahrtbericht / Cruise Report MSM71 LOBSTER: Ligurian Ocean Bottom Seismology and Tectonics Research, Las Palmas (Spain) – Heraklion (Greece) 07.02.-27.02.2018. Open Access. GEOMAR Report, N. Ser. 041. GEOMAR Helmholtz-Zentrum für Ozeanforschung Kiel, Kiel, Germany, 47 pp. DOI

1. Kopp, H., Lange, D., Hannemann, K., Krabbenhoeft, A., **Petersen, F.** and Timmermann, A. and Scientific Crew SO244-II (2016) RV SONNE Fahrtbericht / Cruise Report SO244/2, GeoSEA: Geodetic Earthquake Observatory on the Seafloor, Antofagasta (Chile) – Antofagasta (Chile), 27.11.-13.12.2015. Open Access. GEOMAR Report, N. Ser. 034. GEOMAR Helmholtz Centre for Ocean Research, Kiel, 86 pp. DOI

Patent

Kopp, H., Lange, D., Steffen, K. P. and **Petersen, F.**, Holder: GEOMAR Helmholtz Centre for Ocean Research (2017). Mechanism to deploy cable decoupled equipment in deep water. *Patent*: DE 102016107558 A1 2017.10.26

Invited Talks

Dannowski, A., Wolf, F. N., Kopp, H., Grevemeyer, I., Lange, D., Thorwart, M., Crawford, W., Caielli, G., de Franco, R., Paul, A., **Petersen, F.** and Schramm, B. and MSM71 Cruise participants, AlpArray Working Group (2019) Investigations of the crust and upper mantle in the Ligurian Basin using refraction seismic data and ambient noise – LOBSTER. AlpArray and 4D MB Scientific Meeting 2019, Frankfurt am Main, Germany.

Kopp, H., Lange, D., Urlaub, M., **Petersen, F.** and Hannemann, K. (2018) The GeoSEA Array: in-situ monitoring of seafloor deformation. Seafloor Sensors Workshop, 2018, Oregon, USA.

Kopp, H., Lange, D., Urlaub, M., **Petersen, F.** and Hannemann, K. (2018) From no slip to slow slip: How seafloor geodesy reveals crustal deformation at mm-scales. Geological Survey of Canada, 2018, Sidney, British Columbia, Canada.

Kopp, H., Lange, D., Urlaub, M., **Petersen, F.** and Hannemann, K. (2018) From no slip to slow slip: How seafloor geodesy reveals crustal deformation at mm-scales. Ocean Networks Canada Symposium. 2018, Canada.

Petersen, F., Kopp, H., Lange, D., Hannemann, K. und Urlaub, M. (2017) Monitoring submarine fault deformation using direct-path ranging. IAG-IASPEI, Kobe, Japan.

Urlaub, M., **Petersen, F.**, Gross, F., Lange, D. and Kopp, H. (2017) Monitoring Underwater Landslides Using Seafloor Geodesy: Evidence for Active Sliding of Mount Etna's Submerged Flank. AGU Fall Meeting 2017, New Orleans.

Conference Contributions (first author only)

Petersen, F., Lange, D., Ma B., Grevemeyer, I., Geersen, J., Klaeschen, D., E. Contreras-Reyes, S. Barrientos, A. M. Tréhu, E. Vera, H. Kopp (2021). Subduction Erosion and Upper Plate Deformation at the Up-Dip Limit of the 2014 Mw 8.1 Iquique Earthquake. SSA Annual Meeting 2021, Online, USA.

Petersen, F., Lange, D., Ma B., Grevemeyer, I., Geersen, J., Klaeschen, D., E. Contreras-Reyes, S. Barrientos, A. M. Tréhu, E. Vera, H. Kopp (2021). Subduction erosion and upper plate deformation induced by the 2014 Mw 8.1 Iquique earthquake. Virtual Marine Seismology Symposium 2021, Online, USA.

Petersen, F., Lange, D., Ma B., Grevemeyer, I., Geersen, J., Kläschen, D., E. Contreras-Reyes, S. Barrientos, A. M. Tréhu, E. Vera, H. Kopp (2021). Seismogenic up-dip limit of the 2014 Mw 8.1 Iquique earthquake links subduction erosion and upper plate deformation. DGG Jahrestagung 2021, Online, Kiel, Germany.

Petersen, F., Lange, D., , Ma B., Grevemeyer, I., Kopp, H., Contreras-Reyes, E., Barrientos, S., Tréhu, A. and the PICTURES Working Group (2020). Marine forearc structure at the seismogenic up-dip end of the 2014 Iquique Mw 8.1 earthquake. AGU Fall Meeting 2020, San Francisco, USA.

Petersen, F., Lange, D., Ma, B., Geersen, J., Grevemeyer, I., Klaeschen, D., Conteras-Reyes, E., Barrientos, S., Tréhu, A. M. and Kopp, H. (2020) Active subduction erosion at the updip end of the 2014 Mw 8.1 Iquique earthquake in North Chile. IPOC Workshop 2020. 25.11.2020, Online, Potsdam, Germany.

Petersen, F., Lange, D., Grevemeyer, I., Kopp, H., Trehu, A. M., Contreras-Reyes, E. and Barrientos, S. (2019) Marine forearc structure of the 2014 Mw 8.1 Iquique earthquake in Northern Chile revealed by relocated hypocenter locations from offshore observations. AGU Fall Meeting 2019, San Francisco, USA.

Petersen, F., Lange, D., Grevemeyer, I., Kopp, H., Contreras-Reyes, E., Barrientos, S. and Tréhu, A. M. (2019) Marine forearc structure of the 2014 Mw 8.1 Iquique earthquake revealed by hypocenter locations from offshore observations. 25. Latin-American Colloquium of Geosciences, 2019, Hamburg, Germany.

Petersen, F., Lange, D., Grevemeyer, I., Kopp, H., Contreras-Reyes, E., Barrientos, S. and Tréhu, A. (2019) The structure of the 2014 Mw 8.1 Iquique earthquake revealed by offshore observations. EGU General Assembly 2019, Vienna, Austria.

Petersen, F., Kopp, H., Lange, D., Hannemann, K. and Urlaub, M. (2018) Monitoring Seafloor Deformation: Acoustic Ranging Geodesy with Millimeter Precision. EGU General Assembly 2018, Vienna, Austria.

Petersen, F., Urlaub, M., Kopp, H., Lange, D. and Gross, F. (2018) Monitoring seafloor displacement offshore Mount Etna: Evidence for active deformation from acoustic geodesy. Physics of Volcanoes 2018, Kiel, Germany.

Petersen, F., Kopp, H., Lange, D., Hannemann, K. and Urlaub, M. (2017) Seafloor geodesy: Acoustic direct-path ranging for monitoring seafloor deformation. MarFluid Symposium 2017, Brest, France.

Petersen, F., Urlaub, M., Lange, D., Kopp, H., Hannemann, K., Krabbenhoeft, A., Gross, F., Krastel, S. and Gutscher, M. A. (2017) Monitoring deformation offshore Mount Etna: First results from seafloor geodetic measurements. EGU General Assembly 2017, Vienna, Austria.